Investigating the preparation of sterically-stabilised latexes and polymer/graphene oxide nanocomposite particles

A thesis submitted to

The University of Manchester

for the degree of Doctor of Philosophy

in the Faculty of

Science and Engineering

2021

Shang-Pin Wen

School of Natural Sciences

Department of Materials

Contents

Word Count: 62,025

List of Figures

List of Tables

List of Abbreviations

ACVA	4,4′-azobis(4-cyanovaleric acid)
AIBA	2,2′-azodiisobutyramidine dihydrochloride
AIBN	azobisisobutyronitrile
ATRP	atom-transfer radical polymerisation
BzMA	benzyl methacrylate
CMC	critical micelle concentration
CTA	chain transfer agent
D	mean spherical diameter
DCP	disc centrifuge photosedimentometry
D_h	hydrodynamic diameters
DP	degree of polymerisation
D_{SAXS}	SAXS diameters
D_{TEM}	mean TEM particle diameters
DVB	divinylbenzene
GO	graphene oxide
GPC	gel permeation chromatography
HD	hexadecane
IFT	surface interfacial tension
KSPMA	sulfopropyl methacrylate potassium salt
macro-CTA	macromolecular chain transfer agent
MAMs	more-activated monomers
M_n	number-average molar mass
M_w	weight-average molar mass
MWCO	molecular weight cut-off
N_{agg}	mean aggregation number
NMP	nitroxide-mediated polymerisation
NMR	nuclear magnetic resonance spectroscopy
N_p	number of particles per unit volume
P2VP	poly(2-vinyl pyridine)
P2VP–PBzMA	poly(2-vinyl pyridine)-poly(benzyl methacrylate)
PBzMA	poly(benzyl methacrylate)
PDI	polydispersity index
PEGMA	poly(ethylene glycol) methacrylate
PEGVP	PEGMA-stabilised P2VP
PETTC	4-cyano-4-(2-phenylethane sulfanylthiocarbonyl) sulfanylpentanoic acid

PETTCCP	2-cyano-2-propyl phenethyl trithiocarbonate
PISA	polymerisation-induced self-assembly
PKSPMA	poly(potassium 3-sulfopropyl methacrylate)
PKSPMA–PBzMA	poly(potassium 3-sulfopropyl methacrylate)-poly(benzyl methacrylate)
PSS	poly(4-styrene sulfonate)
q	scattering vector
RAFT	reversible addition-fragmentation chain transfer
R_{core}	mean radius of core
RDRP	reversible-deactivation radical polymerisation
R_g	gyration of the stabiliser chains
RI	refractive index
R_N	polymerisation rate per particle
R_p	rate of polymerisation
S_{agg}	average number of copolymer chains per unit surface area
SAXS	small-angle X-ray scattering
TEM	transmission electron microscopy
THF	tetrahydrofuran
V_{co}	volume of a core-forming polymer chains
VOCs	volatile organic compounds
X_{sol}	solvent fraction in the core
2VP	2-vinyl pyridine
y	DP of the core-forming block
α	scaling exponent
θ	half of the scattering angle
λ	wavelength of X-ray radiation
ξ	X-ray scattering length density
ρ	density
σR_{core}	standard deviation of the core radius
[CTA]	concentration of chain transfer agent
[I]	concentration of initiator
[M]	concentration of monomer

Abstract

This thesis describes the preparation of anionic, non-ionic and cationic sterically-stabilised poly(benzyl methacrylate) latex nanoparticles *via* reversible addition-fragmentation chain transfer (RAFT) polymerisation and polymer/graphene oxide nanocomposite particles *via* heteroflocculation.

Anionic sterically-stabilised poly(potassium 3-sulfopropyl methacrylate)-poly(benzyl methacrylate) (PKSPMA–PBzMA) diblock copolymer nanoparticles were prepared *via* RAFT-mediated polymerisation-induced self-assembly (PISA) in alcohol/water mixtures. The effect of solvent quality (alcohol/water ratio and co-solvent composition) on the formation of these nanoparticles was investigated. Generally, particles with larger diameter were obtained using higher alcohol content, indicating the solvency of stabiliser and core-forming block can influence the aggregation of polymer chains during self-assembly. Small-angle X-ray scattering (SAXS) studies showed that these particles had diverse structural parameters. This protocol was successfully extended for the preparation of anionic sterically-stabilised poly(4-styrene sulfonate)-poly(benzyl methacrylate) (PSS–PBzMA) diblock copolymer nanoparticles.

It was demonstrated for the first time that non-ionic sterically-stabilised poly(benzyl methacrylate) (PBzMA) nanoparticles can be prepared *via* RAFT miniemulsion polymerisation. This was achieved using relatively hydrophobic RAFT agent and non-ionic Lutensol TO 20 surfactant. The effects of hydrophobe, initiator and RAFT agent concentrations on particle diameter, particle number, rate of polymerisation (R_p) and molar mass of the final latexes were investigated. Increasing hydrophobe increased number of particles, but decreased latex diameter. Increasing initiator increased overall R_p and followed a power-law relationship $R_p \alpha [\text{initiator}]^{1/2}$, but negligible differences in molar mass and particle diameter were observed. In contrast, increasing RAFT agent increased the latex diameter and the overall R_p. In most cases, well-controlled RAFT polymerisations were achieved, as judged by kinetic studies.

Cationic sterically-stabilised poly(2-vinyl pyridine)-poly(benzyl methacrylate) (P2VP–PBzMA) diblock copolymer nanoparticles were prepared *via* RAFT-mediated PISA under emulsion polymerisation conditions. Nanoparticles with tuneable diameters could be prepared by altering the DP of the stabiliser (P2VP) and/or the core-forming block (PBzMA), or simply by varying the solution pH for a fixed target copolymer composition. Varying the solution pH resulted in the P2VP stabiliser having different solubilities due to protonation/deprotonation of the pyridine groups, leading to a noticeable effect on the aggregation of polymer chains during PISA process. These P2VP–PBzMA nanoparticles had good colloidal stability and high cationic charge below pH 5 and can be dispersed over a wide pH range.

Finally, polymer/GO nanocomposite aggregates with core/shell morphologies were prepared *via* electrostatically-induced heteroflocculation at room temperature in either acidic (pH 2) or basic (pH 9) conditions. Control heteroflocculation experiments were conducted using the previously prepared anionic PKSPMA–PBzMA and non-ionic PBzMA nanoparticles to demonstrate no adsorption of GO nanosheets. In contrast, positively charged P2VP–PBzMA and poly(ethylene glycol) methacrylate (PEGMA)-stabilised P2VP latexes were used for the adsorption of negatively charged GO nanosheets. The degree of flocculation and the strength of electrostatic interaction of the polymer/GO nanocomposite particles were assessed using disc centrifuge photosedimentometry (DCP). DCP and TEM studies suggested that the optimal GO loading was approximately 20% w/w based on latex and P2VP–PBzMA/GO may have stronger electrostatic attraction.

Declaration

No portion of the work referred to in the thesis has been submitted in support of an application for another degree or qualification of this or any other university or other institute of learning.

Copyright Statement

Acknowledgements

Firstly, I would like to thank my supervisor, Dr Lee Fielding, for his guidance, inspiration and support during my studies. He always positively encourages me to interpret experiment results profoundly and provides me very useful ideas whenever I encountered a bottleneck. I want to thank the National Chung-Shan Institute of Science and Technology (NCSIST) for funding a PhD studentship. I also want to thank my managers and colleagues in NCSIST for encouraging me to study abroad and sharing out my work during these years.

I am also grateful to all past and present Fielding group members, Jack, Chi, Vicky, Sergio, Beth, Mo, Haoyang, Ruiling and Xueyuan, for their discussion and help. As an international student, their friendship and help let me feel at home. Particularly, I want to thank Chi for letting me be familiar with the surroundings and culture of Manchester at the very start of my arrival. I want to thank Jack for teaching me to use numerous facilities in the lab and taking several TEM images for me. I want to thank Beth for the preparation of PEGVP latexes and Vicky for the synthesis of PETTCCP CTA. Without these materials, I cannot progress my experiments. I want to thank the MSc students that I supervised, including Hugh, Chung-Peng, Ruiqi and Weiyu, for working with me. Without you guys kept asking me queries, I think I would not deeply think and learn how to explain those theories and concepts behind my research.

I want to thank those friends for doing research together and kindly sharing chemicals and facilities in the MSS Tower these years, including people in Edmondson Group (Oli, Yunzhang and Jackson), Jones Group (Lorraine, Shiyu, Elana and Rob), Saunders Group (James and Tong) and Shaver Group (Tom and Utku).

A thank you to University staff for their incredible work over the past four years. Especially, I thank our professional technicians, Polly, Jasmine, Chloe and Damindi, in the Department of Materials for maintaining all the facilities in our building. Without your hard work, I cannot do any experiments. I thank Dr Duc-The Ngo in EM Bunker for TEM training and problem solving. I thank Dr Ralph W. Adams, Mr. Daryl Bamber and Mr. Carlo Bawn in the Department of Chemistry for always keeping NMR facilities in good conditions and make it possible to run our NMR samples 24 hours a day, 7 days a week. I also thank those post-docs who taught me to conduct certain experiments or use

specific facilities, including Dr Kate Thompson, Dr Nam Nguyen, Dr Amirhossein Milani, Dr Mitchell Perry, Dr Michael Bennison, Dr Thomas Bennett, Dr Meng Wang and Dr Muhamad Zulhasif Mokhtar. Beside those staff in the University of Manchester, I want to thank Mr. Nikul Khunti at beamline B21 in the Diamond Light Source (Didcot, UK) for SAXS data acquisition.

I want to thank all my entire family for supporting me over these years. Especially, to my sister, thank you for taking care of Mum when I studied abroad. To my Mum, thank you for encouraging me to study abroad and preparing what we need during this COVID-19 pandemic period. To my father-in-law, mother-in-law and brother-in-law, thank you for preparing Taiwanese groceries and sending them to us. The final thank you is to my wife (Annie) and my son (Henry) for their constant loving support and living with me in the UK for four years. It is hard to image how can I finish my PhD abroad in the UK without you.

Publications

Primary publications resulting from work in this thesis

(1) "Investigating the influence of solvent quality on RAFT-mediated PISA of sulfonated-functional diblock copolymer nanoparticles." S.-P Wen, J. G Saunders, L. A. Fielding, *Polymer Chemistry*, **2020**, 11, 3416-3426. doi.org/10.1039/C9PY01912J

(2) "RAFT miniemulsion polymerisation of benzyl methacrylate using non-ionic surfactant" S.-P Wen, Q. Yue, L. A. Fielding, *Polymer Chemistry*, **2021**, 12(14), 2122-2131. doi.org/10.1039/D1PY00048A

(3) "Investigating the influence of solution pH on RAFT-mediated PISA of pyridine-functional diblock copolymer nanoparticles" S.-P Wen, L. A. Fielding, *to be submitted to macromolecules, 2021.*

(4) "Physical adsorption of graphene oxide onto polymer latexes *via* electrostatic interaction and characterisation of the resulting nanocomposite particles" S.-P Wen, E. Trinh, L. A. Fielding, *manuscript in preparation.*

Oral presentations at conferences

(1) "Preparation of Polymer Particles by RAFT Miniemulsion Polymerisation" S.-P Wen, L. A. Fielding, School of Materials postgraduate student conference, 10th May **2018**, Manchester, UK.

(2) "Investigating the influence of solvent quality on RAFT-mediated PISA of sulfonated-functional diblock copolymer nanoparticles." S.-P Wen, J. G Saunders, L. A. Fielding, Polymers and composites seminar, 15th October **2020**, Manchester, UK.

Poster presentations at conferences:

(1) "Investigation of block copolymer nanoparticles: the transition from RAFT aqueous emulsion to alcoholic dispersion polymerisation" S.-P Wen, L. A. Fielding, School of Materials 2019 PGR conference, 9th-10th May **2019**, Manchester, UK.

(2) “Investigating the transition from RAFT aqueous emulsion polymerisation to alcoholic dispersion polymerisation” S.-P Wen, L. A. Fielding, 14th International conference on materials chemistry (MC14), 8th-11th July **2019**, Birmingham, UK.

(3) “Investigating the influence of solvent quality on RAFT-mediated PISA of sulfonate-functional diblock copolymer nanoparticles” S.-P Wen, J. G Saunders, L. A. Fielding, Fourth MaRMN annual symposium, 6th February **2020**, Manchester, UK.

Chapter One

Introduction

1.1. Introduction

Polymer nanoparticles with various surface charge have attracted wide attention. These nanoparticles can be cationic, anionic, zwitterionic or non-ionic depending on the nature of the monomers and stabilisers used. Recently, amphiphilic block copolymers comprising a hydrophilic and a hydrophobic block have attracted significant attention.[1-3] They have potential applications in various fields, such as coatings,[4] sensing[5] and drug delivery.[6] In the past two decades, polymerisation-induced self-assembly (PISA) *via* reversible addition-fragmentation chain transfer (RAFT) polymerisation has proven to be a versatile and efficient technique for the preparation of diblock copolymer nanoparticles with controlled size, morphology (e.g. spheres, worms or vesicles) and surface functionality.[7-10] Furthermore, the surface chemistry of such nanoparticles can be readily controlled by utilising anionic,[11,12] cationic,[13] non-ionic[14-20] or zwitterionic[21-23] blocks as steric stabilisers for the PISA formulation. More importantly, RAFT-mediated PISA can be conducted in a wide range of media such as alcohols,[24-26] water[15,22,27] and non-polar solvents.[28-30] Briefly, in this technique, a RAFT macromolecular chain transfer agent (macro-CTA) is used as a soluble stabiliser block, which is chain-extended utilising a solvent-immiscible or a solvent-miscible monomer *via* RAFT (mini)emulsion or dispersion polymerisation, respectively, to form a second block.

1.2. Outline of this thesis

In this thesis, sterically-stabilised polymer nanoparticles with different surface charge prepared *via* RAFT polymerisation have been investigated. **Chapter Two** presents the synthesis of anionic sterically-stabilised poly(potassium 3-sulfopropyl methacrylate)-poly(benzyl methacrylate) (PKSPMA–PBzMA) diblock copolymer nanoparticles *via* RAFT-mediated PISA. The hypothesis that the solvent quality should have a marked impact on both the aggregation of polymer chains during self-assembly and the resulting copolymer nanoparticle morphology is studied. The solvent quality is judiciously changed by altering the ratio of alcohol/water mixtures, and the resulting block copolymer nanoparticles are systematically characterised. In particular, SAXS analysis reveals that nanoparticles with same copolymer composition have different structural parameters in terms of particle diameter, stabiliser density and solvent fraction in the core. This further

demonstrated that the RAFT-mediated PISA approach is highly versatile and provides the ability to obtain desired copolymer compositions with various particle sizes.

Chapter Three describes the synthesis of non-ionic poly(benzyl methacrylate) (PBzMA) latexes *via* RAFT miniemulsion polymerisation using a non-ionic surfactant for the first time. Various types of surfactant and chain transfer agent are screened for use in RAFT miniemulsion polymerisation of benzyl methacrylate. The influence of hydrophobe, initiator and RAFT agent concentration on particle diameter, particle number, rate of polymerisation and molar mass are investigated systematically. The following self-blocking experiments indicate that these synthesised PBzMA obtain high chain-end stability and fidelity after storage for over a 12-month period at room temperature. This implies that these PBzMA latexes could undergo efficient chain extension to form second blocks with other monomers and form more complex latex morphologies.

Chapter Four presents the synthesis of cationic sterically-stabilised poly(2-vinyl pyridine)-poly(benzyl methacrylate) (P2VP–PBzMA) diblock copolymer nanoparticles *via* RAFT-mediated PISA. P2VP is a pH-stimuli responsive polymer due to protonation/deprotonation of the pyridine functional groups at varying pH. The effect of solution pH on the formation of block copolymer chains and the aggregation of polymer chains during self-assembly is investigated. Generally, at lower pH, relatively well-controlled RAFT polymerisation can be achieved and block copolymer nanoparticles with smaller particle diameters can be obtained using a fixed target copolymer composition. Furthermore, aqueous electrophoresis studies show that these diblock copolymer nanoparticles were highly positively charged with high colloidal stability below pH 5.

In **Chapter Five**, the adsorption of graphene oxide (GO) nanosheets onto the surface of cationic latex nanoparticles in aqueous media *via* electrostatic interaction is investigated. Two type of cationic polymer latex nanoparticles (P2VP–PBzMA and PEGMA-stabilised P2VP) are prepared. The heteroflocculation experiments indicated that the anionic GO nanosheets can incorporate with cationic latexes and form polymer/GO nanocomposite aggregates with core/shell morphologies. Substantial differences of morphology and electrostatic interaction strength are observed with GO

and these two types of cationic nanoparticles. This is rationalised in terms of differing surface charge of nanoparticles.

Finally, **Chapter Six** briefly concludes the work presented in this thesis and suggestions for possible future research are made in the field of sterically-stabilised polymer nanoparticles and nanocomposite particles.

In the subsequent sections of this Chapter, several fundamental aspects of polymer science, such as free-radical polymerisation, reversible-deactivation radical polymerisation, emulsion polymerisation and miniemulsion polymerisation will be briefly discussed before an overview of the approaches to prepare nanocomposite particles is given.

1.3. Free radical polymerisation (FRP)

Polymerisation is the chemical process of joining numerous small molecules (monomers) together to form a single macromolecule (polymer). A polymer has high molar mass and its molecular structure is composed of repeating smaller molecules to form long chains. Polymers can be synthesised *via* step-growth and chain-growth polymerisation using many types of monomers under various conditions.[31] More specific, polymers (e.g. polyesters or polyamides) synthesised *via* step-growth polymerisation (e.g. polycondensation) involving reaction of bifunctional or multifunctional monomers and expelling out small molecules as by-product during polymerisation. In contrast, polymers (e.g. polypropylene oxide or polystyrene) synthesised *via* chain-growth polymerisation involving monomers with cyclic or vinyl chemical structures react with the active centre of a growing chain during polymerisation. The most widely utilised form of chain-growth polymerisation is free radical polymerisation (FRP) of unsaturated vinyl monomers.[32,33]

1.3.1. Mechanism of free radical polymerisation

The mechanism of free radical polymerisation (FRP) involves four distinct stages, named as decomposition, initiation, propagation and termination (**Figure 1.1**). The decomposition stage in free radical polymerisation is the generation of primary free radicals ($R^{\bullet}$), which are usually generated by thermal, ultra-violet (UV) radiation or γ radiation to a peroxide (-O-O-) or azo (-N=N-) initiator (I). The initiator undergoes homolytic decomposition to create reactive radicals, where k_d is the rate constant for dissociation (**Figure 1.1a**). Normally, k_d is in the range of 10^{-6}–10^{-5} s^{-1} with half-lives of approximately 10 hours.[34] In the initiation stage, a primary free radical ($R^{\bullet}$) reacts with a vinyl group on a monomer unit (M) to form a new chain-initiating radical centre ($RM_1^{\bullet}$, **Figure 1.1b**), where k_i is the rate constant of initiation. Propagation proceeds *via* adding monomer units to the active radical centres rapidly (**Figure 1.1c**), where k_p is the rate constant. In the termination stage, active radical species are eliminated, which means further growth of the propagating polymer chains is inhibited. **Figure 1.1d** shows two main types of termination mechanisms, named combination and disproportionation. Termination *via* combination (rate constant k_{tc}) involves two radical chain ends coupling together to form a long dead polymer. In contrast, termination *via* disproportionation

(a) Decomposition stage

$$\mathrm{I} \xrightarrow{k_\mathrm{d}} 2\mathrm{R}^\bullet \qquad R_\mathrm{d} = -\frac{\mathrm{d[I]}}{\mathrm{dt}} = k_\mathrm{d}[\mathrm{I}]$$

(b) Initiation stage

$$\mathrm{R}^\bullet + \mathrm{M} \xrightarrow{k_\mathrm{i}} \mathrm{RM_1}^\bullet \qquad R_\mathrm{i} = \frac{\mathrm{d[RM_1^\bullet]}}{\mathrm{dt}} = k_\mathrm{i}[\mathrm{R}^\bullet][\mathrm{M}]$$

(c) Propagation stage

$$\mathrm{RM_1}^\bullet + \mathrm{nM} \xrightarrow{k_\mathrm{p}} \mathrm{RM_{(n+1)}}^\bullet \qquad R_\mathrm{p} = -\frac{\mathrm{d[M]}}{\mathrm{dt}} = k_\mathrm{p}[\mathrm{M}][\mathrm{RM_n}^\bullet]$$

(d) Termination stage

$$\mathrm{RM_n}^\bullet + \mathrm{R'M_m}^\bullet \xrightarrow{k_\mathrm{tc}} \mathrm{RM_{(n+m)}R'} \qquad R_\mathrm{tc} = k_\mathrm{tc}[\mathrm{RM_n}^\bullet][\mathrm{R'M_m}^\bullet]$$

$$\mathrm{RM_n}^\bullet + \mathrm{R'M_m}^\bullet \xrightarrow{k_\mathrm{td}} \mathrm{RM_n} + \mathrm{R'M_m} \qquad R_\mathrm{td} = k_\mathrm{td}[\mathrm{RM_n}^\bullet][\mathrm{R'M_m}^\bullet]$$

Figure 1.1. The mechanism of free radical polymerisation (FRP) and the corresponding rate equations of each stage: (a) decomposition, (b) initiation, (c) propagation and (d) termination by either combination or disproportionation. I, M, R$^\bullet$, *R* and *k* represent initiator, monomer, free radical, rate of reaction and rate constant, respectively.[35,36]

$$\mathrm{RM_n}^\bullet + \mathrm{I} \xrightarrow{k_\mathrm{trI}} \mathrm{M_n\text{-}I} + \mathrm{R}^\bullet \qquad R_\mathrm{trI} = k_\mathrm{trI}[\mathrm{RM_n}^\bullet][\mathrm{I}]$$

$$\mathrm{RM_n}^\bullet + \mathrm{M} \xrightarrow{k_\mathrm{trM}} \mathrm{M_n} + \mathrm{MR}^\bullet \qquad R_\mathrm{trM} = k_\mathrm{trM}[\mathrm{RM_n}^\bullet][\mathrm{M}]$$

$$\mathrm{RM_n}^\bullet + \mathrm{M_x} \xrightarrow{k_\mathrm{trP}} \mathrm{M_n} + \mathrm{M_xR}^\bullet \qquad R_\mathrm{trP} = k_\mathrm{trP}[\mathrm{RM_n}^\bullet][\mathrm{M_x}]$$

$$\mathrm{RM_n}^\bullet + \mathrm{S} \xrightarrow{k_\mathrm{trS}} \mathrm{M_n} + \mathrm{SR}^\bullet \qquad R_\mathrm{trS} = k_\mathrm{trS}[\mathrm{RM_n}^\bullet][\mathrm{S}]$$

$$\mathrm{RM_n}^\bullet + \mathrm{T} \xrightarrow{k_\mathrm{trT}} \mathrm{M_n} + \mathrm{TR}^\bullet \qquad R_\mathrm{trS} = k_\mathrm{trS}[\mathrm{RM_n}^\bullet][\mathrm{T}]$$

Figure 1.2. Chain transfer mechanisms in free radical polymerisation involving a labile hydrogen abstracted by a polymer radical from another chemical, such as initiator (I), monomer (M), polymer chain (M_x), solvent (S) or chain transfer agent (T). R$^\bullet$, *R* and *k* represent free radical, rate of reaction and rate constant respectively.[35,36]

(rate constant k_{td}) involves a hydrogen atom of one radical centre shifting to another, producing a dead polymer with an unsaturated chain end and the other with a saturated chain end. The overall effective rate constant for termination (k_t) can be described using the sum of k_{tc} and k_{td}. Furthermore, the tendency for propagating polymer chains to suffer termination *via* combination or disproportionation is based on steric factors. For instance, polystyrene normally suffers combination termination, whereas poly(methyl methacrylate) generally undergoes disproportionation termination due to larger steric congestion of the active centre.[32]

Besides combination and disproportionation termination, the other main type of reaction in addition polymerisation is chain transfer reactions, which can be attributed to side-reactions not contributing towards polymer chain growth. Normally, chain transfer reactions occur when a labile hydrogen is abstracted by a polymer radical from another chemical, such as initiator (I), monomer (M), polymer chain (M_x), solvent (S) or chain transfer agent (T) (**Figure 1.2**). Therefore, the original radical polymer chain is terminated, and a new radical species is generated. This radical species can react with unreacted monomer to grow as a new polymer chain. Generally, chain transfer reactions are usually undesirable processes because they reduce the degree of control over polymer structure.

1.3.2. Kinetics of free radical polymerisation

The general kinetic equations for each stage in free radical polymerisation are depicted in **Figure 1.1**. Generally, initiation, propagation and termination may all occur simultaneously during free radical polymerisation. However, the overall kinetics of the polymerisation is related to the rate of each stage. Simply, the rate of polymerisation (R) can be defined as the consumptions of monomer and expressed as **Equation 1.1**:

$$R = R_{\mathrm{i}} + R_{\mathrm{P}} = k_{\mathrm{i}}[\mathrm{R}^{\bullet}][\mathrm{M}] + k_{\mathrm{p}}[\mathrm{RM_n}^{\bullet}][\mathrm{M}] \qquad \textbf{Equation 1.1}$$

Assuming monomer consumed during the initiation stage is negligible compared to those consumed in propagation, R can be simplified as **Equation 1.2**:

$$R = k_{\mathrm{p}}[\mathrm{RM_n}^{\bullet}][\mathrm{M}] \qquad \textbf{Equation 1.2}$$

Therefore, the rate of polymerisation is first-order kinetics with respect to the monomer concentration ([M]). Assuming chain transfer reactions are negligible and the

"steady-state approximation" is applied, which means the rate of radical generation (R_i) is quickly equal to radical destruction (R_t),[37] the instantaneous radical concentration will efficiently remain constant, and can be expressed as **Equation 1.3**:

$$R_i - R_t = \frac{d[RM_n^\bullet]}{dt} = 0 \qquad \textbf{Equation 1.3}$$

where R_t stands for the sum of the rates of both combination and disproportionation termination with the composite rate constant (k_t). Therefore, the **Equation 1.3** can be rewritten and expressed as **Equation 1.4**

$$R_i = R_t = 2k_t[RM_n^\bullet]^2 \qquad \textbf{Equation 1.4}$$

Substitution of **Equation 1.4** into **Equation 1.2** provides the rate of polymerisation (R) can be expressed as **Equation 1.5**:

$$R = k_p[M]\left(\frac{R_i}{2k_t}\right)^{\frac{1}{2}} \qquad \textbf{Equation 1.5}$$

From this perspective, the rate of polymerisation is proportional to monomer concentration and to the square root of the rate of initiation. Furthermore, for free radical polymerisation using a thermal initiator, the initiator normally homolytically decomposes to generate two primary free radicals (**Figure 1.1a**). The rate of initiator decomposition (e.g. R_d = 4.85 x 10^{-5} s^{-1} for 4,4'-azobis(4-cyanovaleric acid) (ACVA) at 70 °C)[34] is much slower than that of a primary free radical reacting with a monomer unit to form a chain-initiating radical centre.[7] This indicates that the initiator thermolysis is the rate determining step, and hence R_i can be expressed as **Equation 1.6**:

$$R_i = 2fR_d = 2fk_d[I] \qquad \textbf{Equation 1.6}$$

where f is the initiator efficiency, which is defined as the fraction of primary radicals produced and those that successfully initiate polymer chains. Generally, f is in the range between 0.3 and 0.8 due to side reactions such as chain transfer.[33] Substitution of **Equation 1.6** into **Equation 1.5** provides the rate of polymerisation (R) can be expressed as **Equation 1.7**:

$$R = k_p[M]\left(\frac{fk_d[I]}{k_t}\right)^{\frac{1}{2}} \qquad \textbf{Equation 1.7}$$

From this perspective, R is proportional to $[M][I]^{1/2}$, indicating that the rate of free radical polymerisation follows first order kinetics with respect to monomer

concentration([M]), and depends on the square root of the initiator concentration ([I]). Generally, k_p for most monomers is very high (e.g. k_p = 100 - 2000 $dm^3\ mol^{-1}\ s^{-1}$ for BzMA monomer).[33] This means that thousands of monomers are added onto polymer chains within few seconds during propagation stage. However, the fast polymerisation rate and various types of termination and chain transfer reactions, which occur in free radical polymerisation normally results in (i) high molar masses; (ii) broad molar mass distributions; (iii) short lifetimes for the propagating polymer radical; (iv) poor control of polymer architecture; and (v) inability to produce block copolymers due to the lack of active chain ends on the final polymers.[32] Actually, the problems above may be overcome by using reversible-deactivation radical polymerisation (RDRP) techniques, such as nitroxide-mediated polymerisation (NMP), atom transfer radical polymerisation (ATRP) and reversible addition-fragmentation chain transfer (RAFT) polymerisation. Thus, these techniques are described in the following pages.

1.4. Reversible-deactivation radical polymerisation (RDRP)

RDRP techniques have been developed to overcome the disadvantages of conventional free radical polymerisation. There are several characteristics of RDRP, such as (i) predictable molar masses; (ii) controllable molar mass distributions; (iii) controllable polymer structures; and (iv) polymer chains end-capped with a reactive moiety. The latter characteristic enables polymers with chain extension ability to produce block copolymers, a key “living” characteristic.[38] Although, different RDRP techniques achieve living character *via* different reaction mechanisms, the fundamental principles of each technique are similar. Specifically, propagating radicals are reversibly formed, which have a long lifetime and allow polymer chains to propagate. Furthermore, highly favourable deactivation process leads to low radical concentrations in the system, minimising irreversible radical–radical termination and chain transfer reaction. The most widely used RDRP techniques are nitroxide-mediated polymerisation (NMP), atom transfer radical polymerisation (ATRP) and reversible addition−fragmentation chain transfer (RAFT) polymerisation.[38,39] Therefore, more detailed overviews of these techniques are outlined below.

1.4.1. Nitroxide-mediated polymerisation (NMP)

NMP was first reported by Solomon and Rizzardo in 1986[40] and sometimes termed stable free radical polymerisation (SFRP). NMP involves a reversible reaction of a stable nitroxide free radical with a propagating polymer chain (**Figure 1.3**).[41] Specifically, the nitroxide radical can reversibly cap the propagating polymer chain ($P_n^{\bullet}$) to form dormant polymer chains. The equilibrium lies heavily in favour of the nitroxide-capped dormant polymer chains, resulting in a low concentration of propagating polymer radicals. The low radical concentration supresses irreversible radical-radical termination reactions, and therefore polymers with well-control molar mass and molar mass distribution can be achieved.[42,43] However, polymerisation generally needs to be performed at a high temperature (e.g. 120 °C) with long reaction times to achieve high monomer conversion.[44,45] Recently, some nitroxide initiators were designed and successfully used to perform NMP with higher conversions at lower temperatures in a short period of time.[46,47] Although the feasibility for polymerisation of styrenic monomers *via* NMP has been improved, it is still very challenging for methacrylic monomers.[47] Furthermore, blocking efficiency of NMP is also quite sensitive to the monomer sequence.[42,47] For example, the blocking efficiency for the preparation of poly(*n*-butyl acrylate)-polystyrene block copolymers is high for chain-extension by styrene from poly(*n*-butyl acrylate). However, if using the reverse strategy (styrene first, then *n*-butyl acrylate), it results in significant amount of dead chains and high molar mass polydispersity. Therefore, NMP is still not a particularly versatile technique for the synthesis of block polymers.

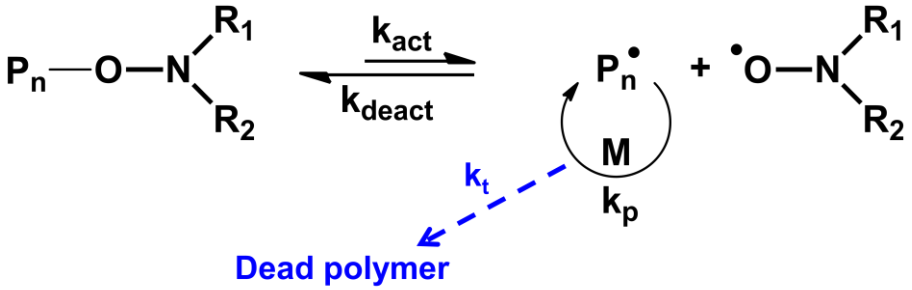

Figure 1.3. Typical mechanism of reversible deactivation/activation equilibration for nitroxide-mediated polymerisation (NMP).[41]

1.4.2. Atom transfer radical polymerisation (ATRP)

ATRP was independently reported by Sawamoto[48] and Matyjaszewski[49] in 1995 and has attracted wide attention for the synthesis well-defined polymeric materials with controlled molar mass and narrow molar mass distribution using a wide range of functional monomers and end groups.[50-52] A typical ATRP reaction is based on a dynamic deactivation/activation equilibrium between the dormant species (e.g. alkyl halides, R-X) and active species (radicals). A well-accepted mechanism for Cu(I)-mediated ATRP is represented in **Figure 1.4**.[53]

The dormant species (R-X) is activated by a transition metal complex in its lower oxidation state [Cu(I)-X/Ligand] to generate an active radical chain end ($R^{\bullet}$) and a transition metal complex in a higher oxidation state [Cu(II)-X_2/Ligand].[53] The active radical chain ends react with monomers (M) to form active living propagating polymer radicals ($P_n^{\bullet}$), which then cap with the transition metal halide to form deactivated dormant species (P_n–X). This reversible activation/deactivation process is rapid and the equilibrium lies heavily in favour of the deactivated halogen-capped polymer chains (dormant species).[54] This leads to the polymer radicals only being active for a short period before becoming dormant, and low radical concentrations during polymerisation.

A successful ATRP needs fast and quantitative transition metal catalysts as an activator for activating species and starting propagation at the same time.[32] However, ATRP reactions are usually air-sensitive and the relatively large amounts of transition metal catalysts are toxic and require removal after polymerisation.[50,55] Therefore, recent ATRP researches have led to *in situ* regeneration of the transition metal catalysts, which essentially limit the catalyst concentration to ppm levels, and increase the tolerance to oxygen and humidity.[56] Such approaches include initiators for continuous activator regeneration (ICAR) ATRP,[57] electrochemically-mediated ATRP (eATRP),[39] supplemental activator and reducing agent (SARA) ATRP[58] and activators regenerated by electron transfer (ARGET) ATRP[59,60] However, these techniques are normally achieved using selected monomers or transition metal catalysts.[61] Furthermore, the trace amount of transition metal catalyst is a potential problem for future applications, and the removal of the trace amount of transition metal catalyst after polymer is still costly.[50,55] Therefore, these drawbacks potentially limit ATRP techniques for use in the commercial areas and the synthesis of block copolymer nanoparticles.

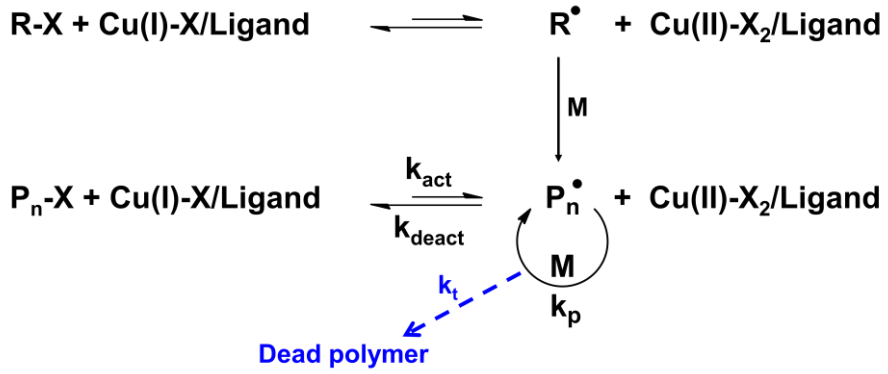

Figure 1.4. Typical mechanism of reversible deactivation/activation equilibration for Cu(I)-mediated atom transfer radical polymerisation (ATRP).[53]

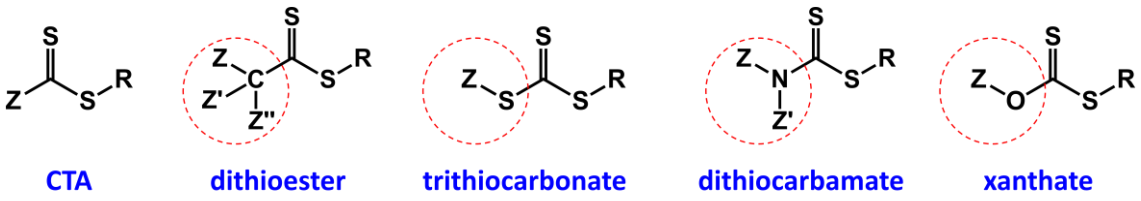

Figure 1.5. Chemical structures of various types of RAFT chain transfer agent (CTA).[62]

1.4.3. Reversible addition–fragmentation chain transfer (RAFT) polymerisation

RAFT polymerisation was first introduced by Moad and co-workers of CSIRO in Australia.[63] Simultaneously, a similar process named 'macromolecular design *via* the interchange of xanthate (MADIX)' was patented by Rhodia and co-workers in France.[64-66] Both RAFT polymerisation and MADIX use chain transfer agents (CTA) with thiocarbonylthio [RS(Z)C=S] moieties to control the polymerisation through a similar mechanism. However, MADIX is limited to xanthates whereas several types of CTA (e.g. dithioester, trithiocarbonate, dithiocarbamate and xanthate) can be utilised in RAFT polymerisation (**Figure 1.5**). Therefore, 'RAFT polymerisation' is the most widely used terminology to describe the polymerisation process using thiocarbonylthio species as CTAs. This technique has revolutionised the field of polymer synthesis because it affords a robust tool to prepare well-defined polymers with desired compositions and complex architectures,[67] such as homo,[68] diblock,[69,70] triblock,[71,72] gradient,[73,74] star,[75,76] polymer brush[77,78] and microgel.[79,80] Since the first introduction of RAFT polymerisation, this synthesis technique has attracted wide attention and numerous review papers have been published in the past two decades.[67,81-87]

1.4.3.1. Mechanism of RAFT polymerisation

The mechanism for RAFT polymerisation to successfully control polymer chain growth is different from NMP and ATRP. For NMP, the control process involves a reversible reaction of a stable nitroxide free radical with a propagating polymer chain, whereas ATRP is based on a dynamic deactivation/activation equilibrium between the dormant species (e.g. alkyl halides, R-X) and active species (radicals). The dormant species of NMP (e.g. alkoxyamine) and ATRP (e.g. halo-compound) are also the source of radicals. Therefore, the deactivation–activation equilibrium and the persistent radical effect determine the rate of polymerisation.[88,89] In contrast, the control process of RAFT polymerisation is achieved by an equilibrium between polymer chains led by a reversible chain-transfer reaction using a thiocarbonylthio CTA.[83]

A generally accepted mechanism of RAFT polymerisation proposed by Moad and co-workers is presented in **Figure 1.6**.[83] The mechanism of RAFT polymerisation not only involves the stages of conventional free radical polymerisation (e.g. initiation, propagation and termination) but also comprises extra stages, such as reversible chain transfer and equilibration. In the initiation stage (**Figure 1.6a**), initiator normally undergoes thermal decomposition to generate radicals ($I^{\bullet}$), which then react with monomer to form propagating radicals ($P_n^{\bullet}$).[90,91] In the early stage of polymerisation (**Figure 1.6b**), these propagating radicals ($P_n^{\bullet}$) are capped with thiocarbonylthio chain transfer agent [RS(Z)C=S, **1**] to generate intermediate radicals (**2**). It is noteworthy that the RAFT agents should be fully consumed before any propagation commences because the thiocarbonyl double bond (C=S) is highly reactive, resulting in the radical addition to form intermediate radicals (**2**) being favoured over addition to vinyl monomer.[63] The intermediate radical (**2**) then undergoes fragmentation to generate a polymeric thiocarbonylthio compound [$P_nS(Z)C=S$, **3**] and a new leaving group radical ($R^{\bullet}$). At the reinitiation stage (**Figure 1.6c**), the new radical ($R^{\bullet}$) reacts with monomers to form another propagating polymer radical ($P_m^{\bullet}$), which then react with the polymeric thiocarbonylthio compound [$P_nS(Z)C=S$, **3**] to generate an intermediate radical (**4**). The intermediate radical (**4**) then undergoes fragmentation to generate a polymeric thiocarbonylthio compound [$S=C(Z)SP_m$, **5**] and a propagating polymer radical ($P_n^{\bullet}$).

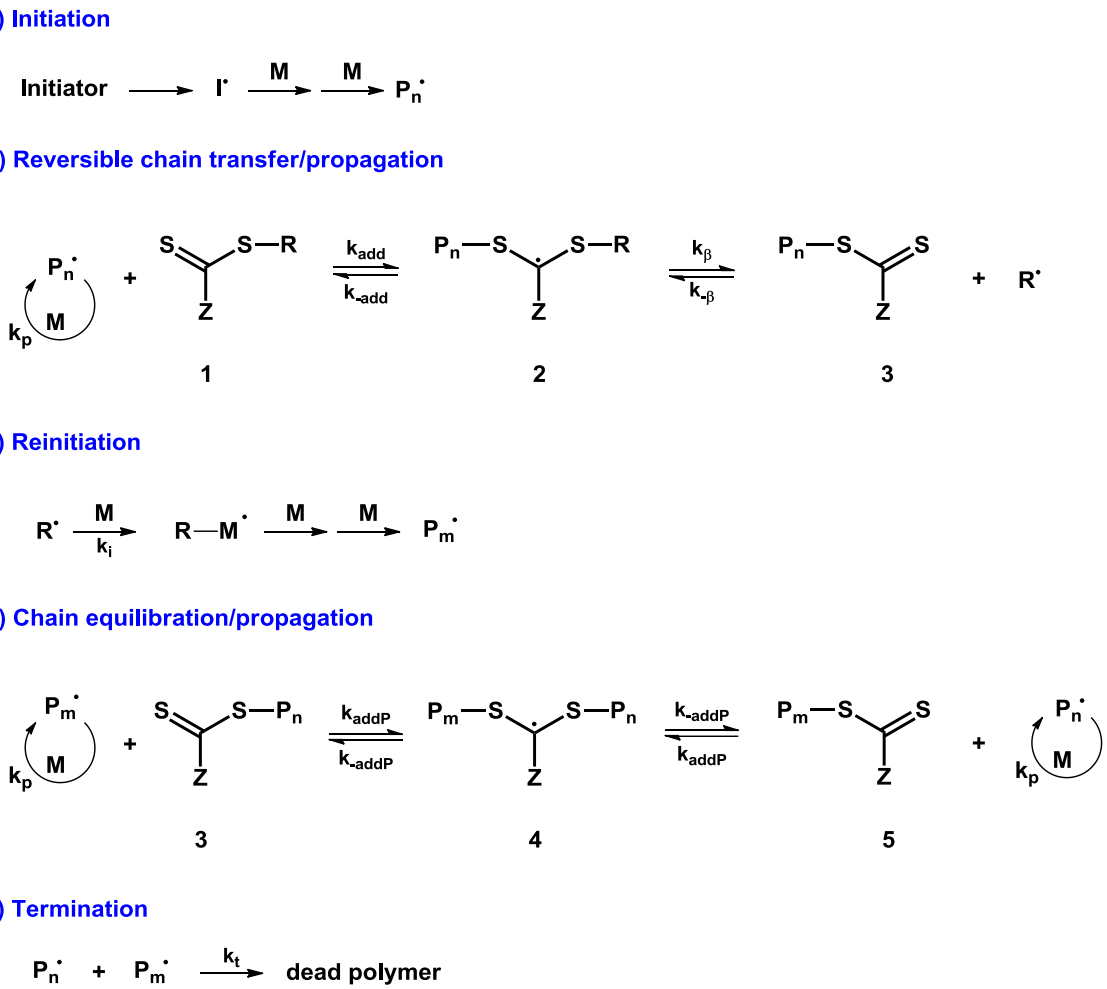

Figure 1.6. Mechanism of reversible addition-fragmentation chain transfer (RAFT) polymerisation proposed by Moad and co-workers.[83]

During the propagation stage, the addition/fragmentation rate between the active propagating radicals ($P_n^{\bullet}$ and $P_m^{\bullet}$) and thiocarbonylthio capped dormant species (**3** and **5**) is higher than that of the propagation, and thus less than one monomer unit is added per activation cycle. This rapid equilibrium suppresses termination and results in all polymer chains having a similar degree of polymerisation (DP). Although termination can be minimised by using chain transfer agents with high transfer efficiency and a high molar ratio of CTA to initiator, it may still occur *via* combination or disproportionation (**Figure 1.6e**). Nevertheless, based on the mechanism of RAFT polymerisation, most of the trithiocarbonate RAFT chain-ends remain intact on polymer chain ends after the polymerisation is completed (or quenched at intermediate conversion).

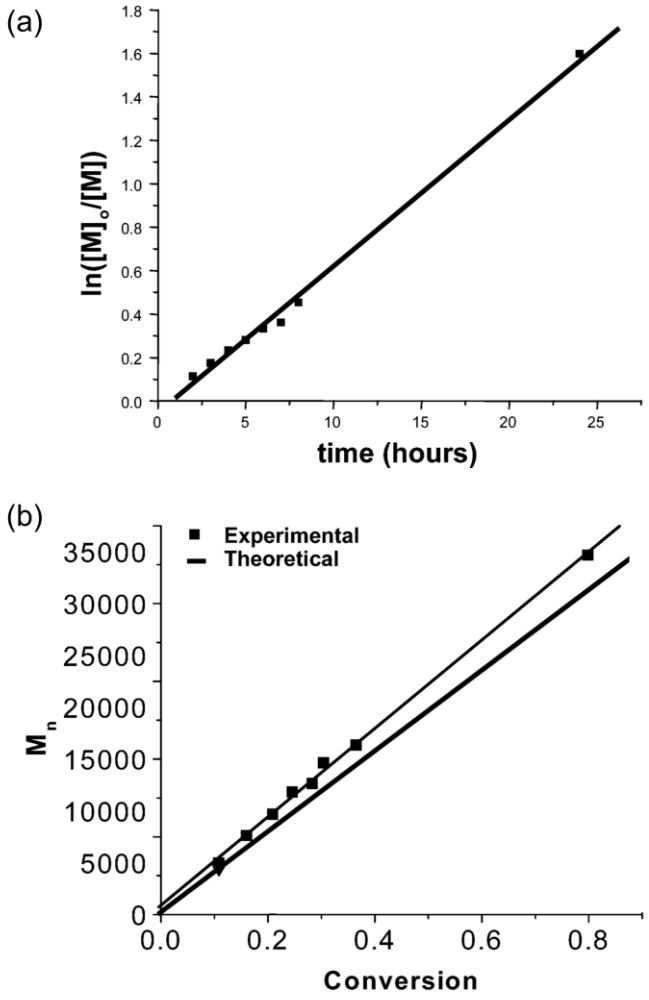

Figure 1.7. Kinetic studies for RAFT-mediated bulk polymerisation of 2-vinyl pyridine (2VP) using cumyl dithiobenzoate (CDB) as a CTA at 60 °C: (a) *pseudo* first-order rate plot and (b) plot of molar mass versus monomer conversion. (Reproduced from Ref. 92 with permission from the American Chemical Society)

For an effective RAFT polymerisation, the polymerisation rate is *pseudo* first-order and the molar mass of polymer increases linearly with conversion in the propagation stage (**Figure 1.7**).[62,92,93] Therefore, the theoretical molar mass can be predicted from the initial stoichiometry using **Equation 1.8**.[82]

$$M_{\mathrm{n,theo}} = \frac{[\mathrm{M}]_0 - [\mathrm{M}]_\mathrm{t}}{[\mathrm{CTA}]_0} \times M_{\mathrm{w,M}} + M_{\mathrm{w,CTA}} \qquad \textbf{Equation 1.8}$$

where $M_{\mathrm{n,theo}}$ represents the theoretical number-average molar mass, $[\mathrm{M}]_0$ and $[\mathrm{M}]_\mathrm{t}$ represent the concentration of monomer at time zero and t, respectively, $M_{\mathrm{w,M}}$ and $M_{\mathrm{w,CTA}}$ represent the molar mass of monomer and CTA, respectively, and $[\mathrm{CTA}]_0$ represents the initial concentration of CTA.

For an ideal RAFT polymerisation, RAFT chain transfer agents can be fully consumed at the commencement of polymerisation and every propagating chain has one trithiocarbonate RAFT chain-end. Therefore, if the CTA has 100% transfer efficiency, the theoretical degree of polymerisation at specific monomer conversion can be predicted from initial stoichiometry using **Equation 1.9**.[62]

$$\mathrm{DP_{theo}} = \frac{[\mathrm{M}]_0}{[\mathrm{CTA}]_0} \times C_\mathrm{T} \qquad \textbf{Equation 1.9}$$

where DP_{theo} represents the theoretical degree of polymerisation, C_T represents monomer conversion at time T, $[M]_0$ and $[CTA]_0$ represent the initial concentration of monomer and CTA, respectively.

1.4.3.2. Choice of RAFT Agents

The RAFT polymerisation technique can be utilised to prepare well-defined polymers with various functionalities and architectures using a wide range of vinyl monomers, such as styrene, acrylates and methacrylates. The choice of CTA is crucial in RAFT polymerisation because it has significant effects on the polymerisation kinetics and control.[94,95] CTAs are organic compounds with thiocarbonylthio [RS(Z)C=S] moieties and the four main types are dithioester, trithiocarbonate, dithiocarbamate and xanthate (**Figure 1.5**). Structural features of thiocarbonylthio RAFT chain transfer agents and the intermediate radicals are presented in **Figure 1.8**. Generally, RAFT agents (**1**, **3** and **5** in **Figure 1.6**) should have a reactive thiocarbonyl double bond (high k_{add}). An efficient RAFT polymerisation also depends on the monomer being polymerised and the nature properties of R and Z groups on the CTA.[96,97] More specifically, the R group should be a better homolytic leaving group than the attacking propagating radical ($P_n^\bullet$), and it should also efficiently reinitiate polymerisation. The Z group influences the activity of the thiocarbonyl double bond (C=S) toward radical addition and modify the stability of the intermediate radicals. The stability of the intermediate radicals (**2** and **4** in **Figure 1.6**) should be modest and fragment rapidly (weak S–R bond and high k_β) to generate the reinitiating radical leaving group ($R^\bullet$) without side reactions. Additionally, the intermediate **2** should prefer products ($k_\beta \geq k_{\text{-add}}$) and likely form polymeric thiocarbonylthio compounds [$P_nS(Z)C=S$, **3** in **Figure 1.6**]. Subsequently, the generated radical leaving group ($R^\bullet$) should efficiently reinitiate polymerisation and form another

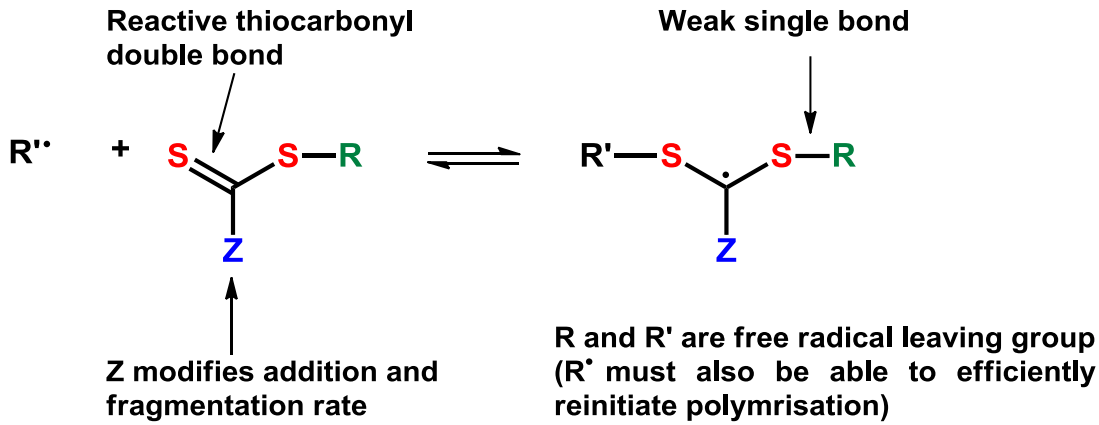

Figure 1.8. Structural features of thiocarbonylthio RAFT chain transfer agents and the intermediate radical. (Reproduced from Ref. 82 with permission from the Australian Journal of Chemistry)

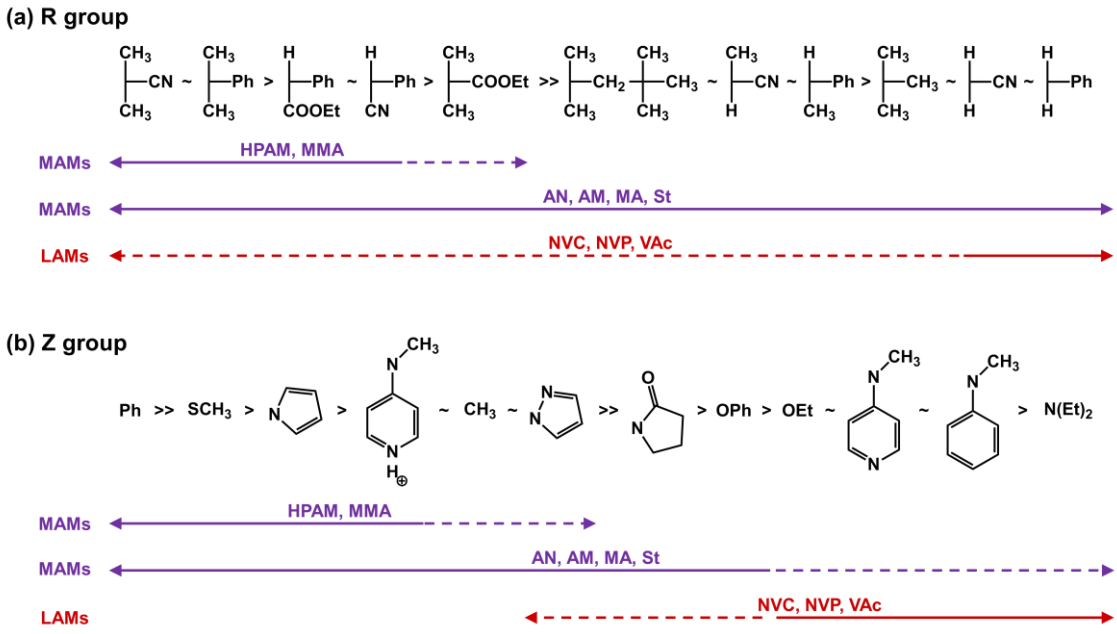

Figure 1.9. Guidelines for selection of RAFT chain transfer agents (ZC(=S)SR) for polymerisation of selected monomers (a) R-group and (b) Z-group. Solid lines represent good control of polymerisation can be achieved, whereas dashed lines indicate only partial or pool control (e.g. broad molar mass distribution or substantial retardation). For R-groups, fragmentation rates and transfer coefficients decrease from left to right. For Z groups, addition rates decrease, and fragmentation rates increase from left to right. Abbreviations: MAMs = more activated monomers, LAMs = less activated monomers, HPMAM = *n*-(2-hydroxypropyl)methacrylamide, MMA = methyl methacrylate, AN = acrylonitrile, AM = acrylamide, MA = methyl acrylate, St = styrene, NVC = *n*-vinylcarbazole, NVP = *n*-vinylpyrrolidone and VAc = vinyl acetate. (Reproduced from Ref. 98 with permission from the Australian Journal of Chemistry)

propagating polymer radical ($P_m^{\bullet}$). Therefore, the reversible and rapid equilibrium between the active propagating radicals ($P_n^{\bullet}$ and $P_m^{\bullet}$) and thiocarbonylthio capped dormant species (**3** and **5** in **Figure 1.6**) in the propagation stage ensures all polymer chains possess an equal possibility for growth, leading to polymer with low molar mass distribution.

Recently, an increasing number of RAFT agents have been synthesised and are commercially available.[94,99,100] An extensive set of guidelines for how to select an appropriate RAFT agent for polymerisation of more activated monomers (MAMs) and less activated monomers (LAMs) is shown in **Figure 1.9**.[98] This guideline clearly indicates that the addition rate decreases and fragmentation rate increases from left to right for the rank of Z group, whereas the fragmentation rate decreases from left to right for the rank of R group. This guideline also provides a judicious way to select an appropriate RAFT agent for polymerisation of selected monomers. For example, in order to have good control for RAFT polymerisation of styrene, the Z group of RAFT agents should select from aryl dithioester to o-aryl xanthate, while R group should be selected from tertiary cyanoalkyl to cumyl.

1.5. Emulsion polymerisation

Emulsion polymerisation was developed in the 1920s[101] and has attracted wide attention in the past decades. The fundamental theory of the emulsion polymerisation mechanism was proposed by Harkins,[102,103] and the polymerisation rate equations were derived by Smith and Ewart,[104] and modified by Gardon in 1940s.[105] Compared to other free radical polymerisation techniques, emulsion polymerisation has several significant advantages,[33] such as (i) high molecular weights can be achieved at fast polymerisation rates; (ii) high monomer conversions can be achieved; (iii) reactions can be performed in cheap, non-toxic and non-flammable solvents (e.g. water); and (iv) a wide range of water-immiscible vinyl monomers (e.g. styrene, benzyl methacrylate) can be used. Therefore, emulsion polymerisation has been widely employed in industry to produce a broad range of polymer latexes (e.g. polymethyl acrylate, poly(2-vinyl pyridine), and polybutadiene) due to financial and environmental reasons.[106,107] As such, a more detailed overview of the emulsion polymerisation mechanism is discussed below.

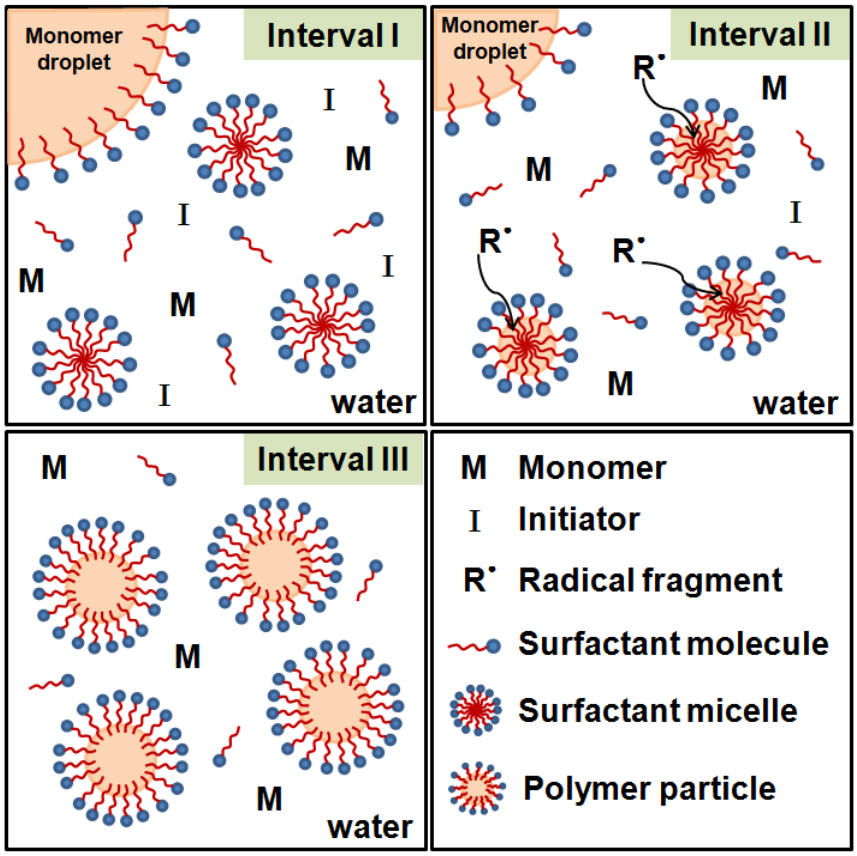

Figure 1.10. Schematic representation of surfactant-stabilised aqueous emulsion polymerisation and its three distinct intervals (I, II and III).[33,106]

Figure 1.10 depicts a generally accepted mechanism of conventional emulsion polymerisation proposed by Harkins. It is typically divided into three distinct intervals, including particle nucleation stage (interval I) and particle growth stages (intervals II and III).[33,106] A typical emulsion polymerisation formulation comprises water, water-immiscible monomer, water-soluble initiator and water-soluble surfactant. The presence of surfactant in the aqueous phase leads to a lower interfacial tension of the polymer/water interface. After the mixture is emulsified using mechanical shear or ultrasonication, surfactant-stabilised monomer droplets (1–10 μm) and micelles (5–15 nm) are formed and dispersed in the aqueous phase.[106] Although most of the monomer is water-insoluble, a very small proportion of monomer molecules are nonetheless dissolved in the aqueous phase. During interval I, these small amounts of monomer molecules are initiated by free radicals to form oligomeric radicals. Subsequently, these water-soluble oligoradicals can enter pre-existing micelles (micellar or heterogeneous nucleation), or continually react with dissolved monomer in the

solution until they reach the critical chain length and become insoluble oligoradicals (homogeneous nucleation).[108] Homogeneous nucleation depends on the critical chain length of a given monomer and surfactant concentration in the system. More specifically, homogeneous nucleation may occur readily when using hydrophobic monomers with slightly higher water solubilities, which can obtain higher critical chain lengths.[109,110] For example, the possibility for vinyl acetate (relatively hydrophilic) to undergo homogeneous nucleation is higher than for styrene (relatively hydrophobic). Furthermore, when the surfactant concentration is less than the critical micelle concentration (CMC), micelles are absent and only homogeneous nucleation occurs.[33]

In contrast, heterogeneous nucleation is dominant when the surfactant concentration is above the CMC, where excess surfactant is present in aqueous phase to form micelles. Free radicals are captured by monomer swollen micelles to form particle nuclei. Furthermore, the number of particles per unit volume of water (N_p) is proportional to the surfactant concentration and initiator concentration to the powers of 0.6 and 0.4, respectively.[102,104] In both homogeneous and heterogeneous nucleation cases, polymer particles continually grow by acquiring monomer diffused from the large monomer droplet reservoirs and form monomer swollen micelles. These growing polymer particles also considerably enlarge their polymer/water interfacial area, so further adsorption of surfactant is needed to maintain the adequate colloidal stability. Furthermore, during the particle nucleation stage, the number of particles and polymerisation rate increase as a function of time (interval I, **Figure 1.11**).[106] Interval I is completed until there are no surfactant micelles present in the aqueous phase, and then the polymerisation enters interval II.

During interval II, particle nucleation has completed, and no new particle formation occurs. There are only surfactant-stabilised monomer droplets and monomer-swollen micelles with free radicals are present in the solution. The polymerisation continually progresses inside the monomer-swollen particles, while the monomer droplets act as reservoirs, which keep diffusing monomer through the continuous aqueous phase into the monomer-swollen growing particles. Furthermore, if radicals in the continuous phase enter the radical-containing monomer-swollen particles, termination may occur. In contrast, if radicals enter an inactive monomer-swollen

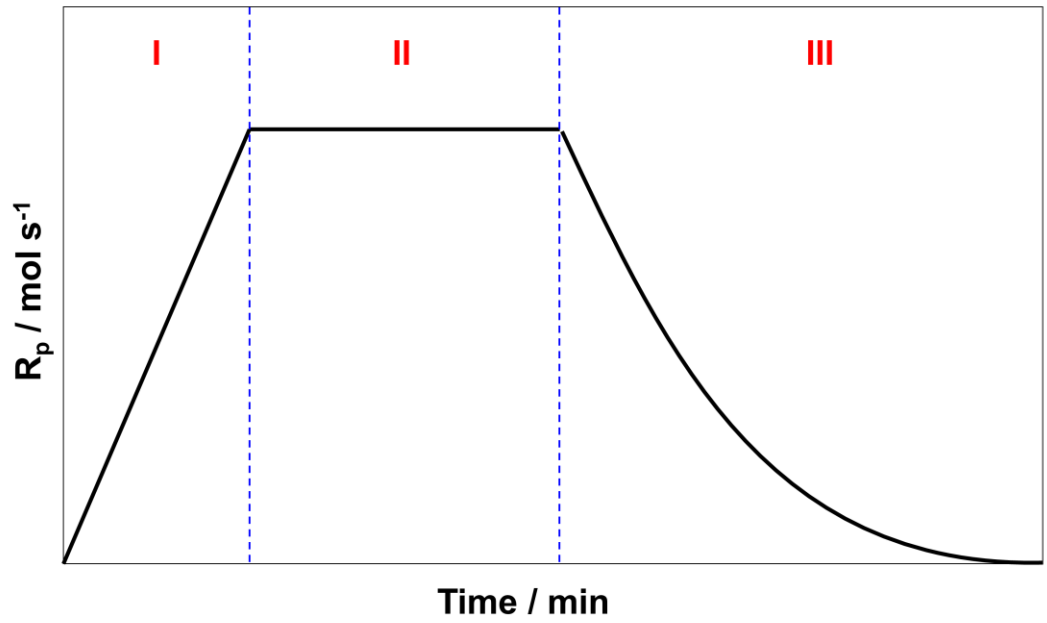

Figure 1.11. Schematic presentation of typical polymerisation rate and the three distinct intervals (I, II and III) in an emulsion polymerisaiton process.[106]

particle reinitiation may occur, and propagation can progress. Nonetheless, during the diffusion process, the monomer concentration inside the growing particles is saturated and relatively constant. Therefore, the polymerisation rate is relatively constant in interval II (**Figure 1.11**). Ideally, polymerisation can continue until all the monomer droplets are completely depleted and only monomer-swollen particles remain in the solution.[33,106] At this point, the polymerisation is said to enter interval III.

During interval III, there are no monomer droplet reservoirs and only a small amount of dissolved monomer remains in the aqueous phase (**Figure 1.10**). These dissolved monomers are diffuse into the polymer particles and are depleted by polymerisation. However, the amount of monomer diffusion is insufficient to saturate the monomer-swollen particles. Therefore, the polymerisation rate decreases (interval III, **Figure 1.11**). It is noteworthy that the reaction time of particle nucleation stage (interval I) is relatively short and most of particles are formed during this period. These particles keep depleting monomer during emulsion polymerisation, resulting in the growth of particle size. Therefore, the particle size of the monomer-swollen micelles and final latexes is significantly different.[106] In contrast, a one-to-one copy of emulsion droplets to latex can be achieved *via* miniemulsion polymerisation[111,112] and this technique it is briefly introduced in the following section.

1.6. Miniemulsion polymerisation

The term “miniemulsion" was coined to describe submicron (50–500 nm) oil in water dispersions, which can be stable for long periods, ranging from hours to months.[113] The first report of miniemulsion polymerisation was proposed by Ugelstad *et al*. in 1973.[114] In this early research, styrene (St) monomer was emulsified with a mixed emulsifier system, containing cetyl alcohol (CA) and sodium dodecyl sulfate (SDS), to obtain stabilised monomer droplets. Furthermore, the droplets had a small size and were stable for months, and polymerisation primarily occurred inside the emulsion droplets. This indicated that each of the stabilised monomer droplets may act as an individual nano-scale reactor and lead to monodisperse latex particles. Since the first introduction of miniemulsion polymerisation, this technique has been developed as a versatile method to synthesize complex polymer materials using monomers with low water solubility.[115,116] These materials have a wide range of applications, including adhesives,[117-120] anticorrosive coatings,[115,116] textile pigments,[121] anti-viral therapy[122] and drug delivery.[123-125] Therefore, this synthesis technique has attracted extensive attention and several highlighted review papers have been published in the past decades[126-129] and is hence briefly introduced here.

1.6.1. Miniemulsion formulations

A typical miniemulsion polymerisation formulation comprises water (continuous phase), water-insoluble monomer, initiator, surfactant (also referred as emulsifier or stabiliser) and hydrophobe (also referred as cosurfactant or costabiliser).[126,130] The use of a highly hydrophobic species (hydrophobe) in miniemulsion formulations is the main difference compared to emulsion formulations. After the emulsification process using high shear or ultrasonication, stable submicron-size miniemulsion droplets with monomer, surfactant and hydrophobe are formed and dispersed in the aqueous phase. The appropriate use of a surfactant can prevent coalescence of droplets, whereas a highly water-insoluble hydrophobe can retard Ostwald ripening.[131] Emulsion droplet coalescence is caused by the collision of droplets with Brownian motion, whereas Ostwald ripening occurs due to the diffusion of monomer from small droplets to larger ones (**Figure 1.12**).[33] More specifically, if a miniemulsion polymerisation system is susceptible to the random nature of the coalescence, the final latexes would consist of

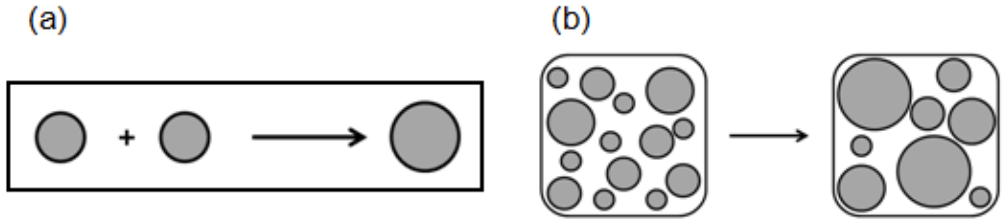

Figure 1.12. Schematic representation of (a) coalescence of two droplets and (b) Ostwald ripening in miniemulsion polymerisation.[33]

non-uniform particle sizes. If a miniemulsion polymerisation system is susceptible to Ostwald ripening, the larger size monomer droplets expand by absorbing the monomer diffused from the smaller droplets. Ostwald ripening results from the driving force for decreasing interfacial energy by forming large monomer droplets from the degradation of small ones.[132] The driving force can be reduced by using a highly hydrophobic and low-molecular-weight hydrophobe. The hydrophobe creates osmotic pressure in each droplet and suppress monomer diffusion from smaller droplets to larger ones. Therefore, a successful miniemulsion formulation should suppress droplet coalescence and Ostwald ripening. This leads the formation of polymer chains to be confined within pre-formed miniemulsion droplets, resulting in latex particles, which are one-to-one copies of the initial droplets.[111]

It is noteworthy that the surfactant is a crucial component for both emulsion and miniemulsion formulations because it facilitates the formation of monomer droplets from the initial emulsion. The appropriate use of surfactant decisively leads to nucleation process and colloidal stability of polymer particles and the final latexes.[126,130] The role of surfactants for miniemulsion formulations is the same as for conventional emulsion polymerisation, and surfactants should meet certain requirements as follows:[127,133-135] (i) have specific chemical structures with polar and non-polar groups; (ii) have higher solubility in the aqueous phase than in oil phase and be readily adsorbed on the droplet/particle surface; (iii) have strong adsorption and not be easily displaced when two droplets/particles collide; (iv) can reduce the interfacial tension and work effectively at low concentrations; and (v) are relatively inexpensive and non-toxic.

There are various commercially available surfactants that satisfy the requirements above, and they can be generally classified into two categories based on the polar head group:[106,136]

(i) Ionic surfactants

Ionic surfactants have a net negative charge (anionic, e.g. sulfate, sulfonate, phosphate and carboxylates), positive charge (cationic, e.g. amine) or both negatively and positively charged (zwitterionic) head groups. Ionic surfactants can prevent coalescence by electrostatic repulsion generated from the charges located on the particle surface and related electrical double layer. Commonly used anionic and cationic surfactants are sodium dodecyl sulfate (SDS) and cetyltrimethylammonium bromide (CTAB), respectively.[137,138] However, latexes stabilised with ionic surfactant are often unstable in the presence of electrolytes.[139,140] Therefore, non-ionic surfactants have attracted wide interest for the preparation of latexes with higher stability in electrolytes.

(ii) Non-ionic surfactants

Non-ionic surfactants typically have covalently bonded oxygen-containing hydrophilic head groups (no charge), such as ethoxylate and alkoxylate groups. Non-ionic surfactants prevent coalescence *via* the entropic repulsion resulting from chains trying to pack in the same space.[141-143] Due to not carrying a charge on their hydrophilic head groups, they are milder in nature and therefore can be used not only in conventional industry (e.g. petroleum) but also throughout the personal care markets and agrochemical industry.[136] Furthermore, the lack of charge leads to non-ionic surfactants readily being able to emulsify oil, organic monomers (e.g. styrenic and acrylic monomers) and aromatic solvents (e.g. benzene, toluene and xylene). Some of the commonly used non-ionic surfactants include lecithin, Tween and Lutensol surfactants. The Lutensol series surfactants have a saturated iso-C_{13} alcohol with a differing ethoxylation block length [iso-$C_{13}H_{27}O(CH_2CH_2O)_xH$], and they were chosen as surfactants for miniemulsion polymerisation study in this thesis (see **Chapter Three**).

1.6.2. Mechanism of miniemulsion polymerisation

Miniemulsion polymerisation can be successfully achieved when polymerisation only occurs in miniemulsion droplets. The process for the preparation of miniemulsion droplets (also named miniemulsification) is the first crucial step for miniemulsion polymerisation. In a typical protocol, dispersed (includes monomer, initiator and hydrophobe) and aqueous (includes water and surfactant) phases are prepared

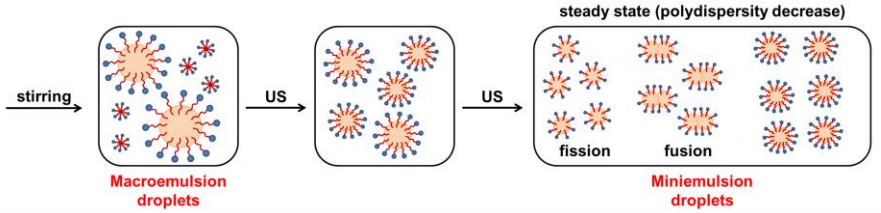

Figure 1.13. Schematic representation of miniemulsification process using ultrasonication (US) in aqueous solution.[133]

separately. The dispersed phase is added to the aqueous solution of surfactant under vigorous stirring to form a coarse emulsion. This coarse emulsion is then subjected to a highly efficient homogenisation process, using rotor-stator devices, high-pressure homogenizers or ultrasonication to obtain miniemulsion droplets.[127] During the miniemulsification process, the number of droplets increases, and the total surface area of droplets become very large. These droplets absorb most of the surfactant and hydrophobe and can prevent coalescence and Ostwald ripening. Therefore, these droplets capture most of the oligomeric free radicals, which then reside inside the monomer droplets. However, during the miniemulsification process, the size distribution of the droplets is still very high at the beginning. The droplets will undergo dynamic equilibrium *via* droplet fission and fusion processes until reach a steady state (**Figure 1.13**).[133]

It is noteworthy that ideally no monomer droplet reservoirs are formed, which is a significant difference from conventional emulsion polymerisation. Therefore, nucleation and polymerisation occur only in the miniemulsion droplets.[144] Specifically, for emulsion polymerisation, the nucleation mechanism is *via* either homogeneous or heterogeneous nucleation, whereas droplet nucleation is dominant in miniemulsion polymerisation.[145] Furthermore, the use of oil dissolved initiator (e.g. AIBN) can promote droplet nucleation and prevent secondary nucleation occurring in the aqueous phase.[146,147]

There are three distinct intervals (interval I, III and IV), which can be identified throughout the process of miniemulsion polymerisation.[148] **Figure 1.14** shows the polymerisation rate of a typical miniemulsion polymerisation of styrene in an aqueous continuous phase using sodium dodecyl sulfate (SDS) as surfactant and hexadecane (HD) as hydrophobe. During interval I, the average number of radicals per particle increase significantly and every droplet can be seen as a separate nanoreactor.[149] The

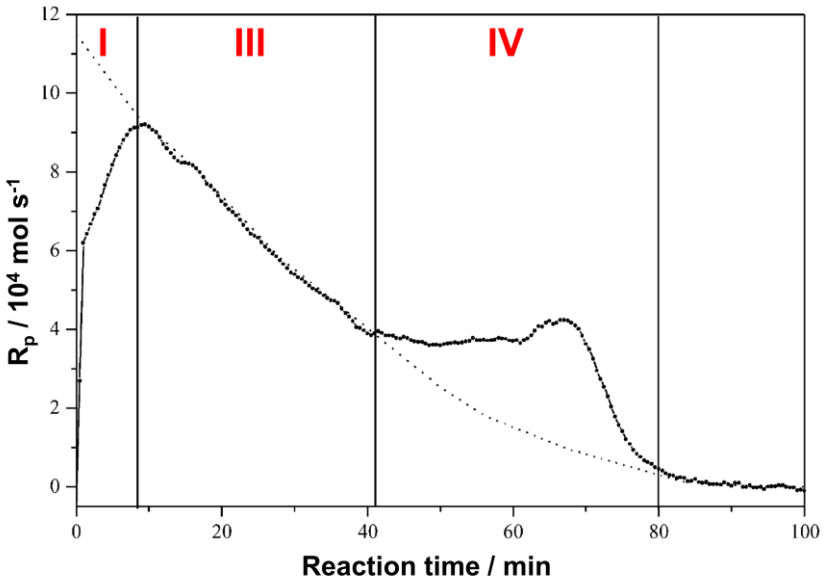

Figure 1.14 Typical polymerisation rate and the three distinct intervals (I, III and IV) in a typical miniemulsion polymerisation of styrene using sodium dodecyl sulfate (SDS) as surfactant and hexadecane (HD) as hydrophobe. (Reproduced from Ref. 148 with permission from the American Chemical Society)

nanoreactors do not interact with each other, and the evolution of monomer conversion in each droplet is different.[149] Compared the distinct intervals of emulsion polymerisation proposed by Harkins (**Figure 1.11**),[106] only intervals I and III can be found in the miniemulsion process. For miniemulsion polymerisation, there is no interval II, which is the stage of polymerisation with constant reaction rate. This indicates that the diffusion of monomer from droplet reservoirs to nucleation droplet does not occur in miniemulsion polymerisation.

During interval III, the polymerisation follows exponential kinetics, which occurs in interval III of emulsion polymerisation as well.[106] Due to the droplet nucleation mechanism, only monomer in the miniemulsion droplets can be polymerised and is exponentially depleted in the nanoreactors. Furthermore, the average number of radicals is quite accurately kept the same during interval III. This suggests that additional radicals do not enter the nanoreactors, and the on/off mechanism in emulsion polymerisation does not occur in miniemulsion polymerisation.[106]

During interval IV, the polymerisation does not follow exponential kinetics with a sudden peak at a period between 60 and 70 minutes (**Figure 1.14**). This gel-peak occurs due to the increase of viscosity inside the particles and the coupled kinetic hindrance of the radical recombination.[148]

1.6.3. Miniemulsion polymerisation vs. emulsion polymerisation

Miniemulsion polymerisation provides several advantages over emulsion or dispersion polymerisation such as smaller particle size of the final latex particles, efficient use of surfactant, production of dispersions with low viscosity and high solids content, and production of particles, which are one-to-one copies of the original miniemulsion droplets.[150,151] Several comparisons between conventional emulsion and miniemulsion polymerisation have been reported,[126,133,152,153] and crucial differences are as follows.

(i) The size difference between monomer droplets and latex particles is a key feature to distinguish emulsion and miniemulsion polymerisation.[133] More specifically, in emulsion polymerisation, the primary emulsion droplets are much larger than latex particles, whereas in miniemulsion polymerisation the latexes are ideally one-to-one copies of the droplets (**Figure 1.15**).

(ii) The size of emulsion droplets is much larger (1–100 μm) than miniemulsion droplets (50–500 nm).

(iii) Droplets/particles in emulsion polymerisation are stabilised by surfactant only, whereas, in miniemulsion polymerisation, they are stabilised by surfactant and hydrophobe, which creates osmotic pressure and retards droplet degradation.

(iv) The mechanism of nucleation and polymerisation are different.[144] More specifically, for emulsion polymerisation, homogeneous and heterogeneous nucleation are the dominant mechanisms, and micelles are the predominant loci of nucleation. In contrast, for miniemulsion polymerisation, droplet nucleation is the dominant mechanism.

(v) The propagation mechanism is different. During emulsion polymerisation, the monomer diffuses from monomer droplet reservoirs through the aqueous phase into micelles, but this does not occur in miniemulsion polymerisation.

(vi) In emulsion polymerisation, the size of latex particles is significantly influenced by kinetic parameters, such as temperature, initiator concentration and surfactant concentration. In contrast, the size of latex particle prepared *via* miniemulsion polymerisation is determined by the emulsification process (e.g. ultrasonication) and droplet stability, and the kinetic parameters mentioned above only have a minor influence.

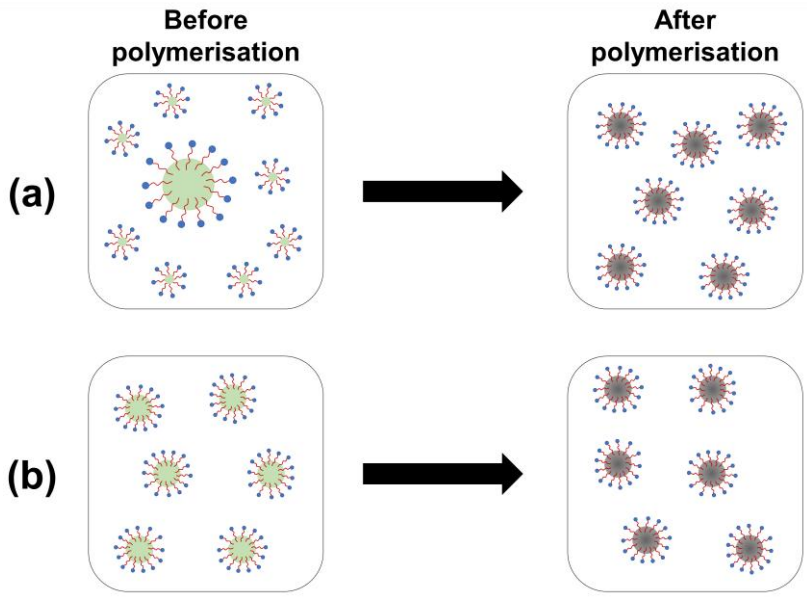

Figure 1.15. Comparison of different polymerisation processes before and after polymerisation: (a) emulsion polymerisation and (b) miniemulsion polymerisation.[128]

1.6.4. RAFT miniemulsion polymerisation

It has been reported that RAFT miniemulsion polymerisation can be used to prepare polymers with low molar mass distributions and well-defined polymer nano-objects.[96,97,154-159] RAFT miniemulsion formulations generally comprise water, hydrophobic monomer, surfactant, hydrophobe and chain transfer agent (CTA). In RAFT miniemulsion polymerisation, the CTA is dissolved in the monomer phase prior to emulsification and located inside the tiny miniemulsion droplets after emulsification. Furthermore, the addition of CTA enables the formation of polymers with controllable molar mass and living characteristics.[114]

However, the use of RAFT agents in miniemulsion polymerisation is sometimes problematic, leading to colloidal instability,[160,161] lower polymerisation rates,[162,163] lower monomer conversions,[159,164,165] broader particle size distributions,[154,166] broad molar mass distributions[167-169] and retardation of the polymerisation.[154,162] Lansalot *et al.* proposed that poor control over polymerisation and retardation may be attributed to the escape of radicals formed after addition and the fragmentation of the initial RAFT agent, which can be terminated in the aqueous phase or re-enter polymer particles and terminate growing chains.[154] This can be minimised and the control of polymerisation and the latex stability in RAFT miniemulsion polymerisation can be improved using relatively high concentrations of surfactant and hydrophobe.[170-172] Furthermore,

Miller *et al.* reported that the presence of a minor amount of high molar mass polystyrene in the miniemulsion polymerisation of styrene resulted in higher polymerisation rates and smaller particle sizes.[111,173] Butté *et al.* achieved RAFT miniemulsion polymerisations of styrene with high conversions using a poly(methyl methacrylate) (PMMA) macro-CTA.[171] However, the reported molar mass dispersities were typically high (>1.9). Pham *et al.* reported that relatively stable polystyrene and poly(*n*-butyl acrylate) latexes can be obtained *via* surfactant-free RAFT miniemulsion polymerisation using diblock macro-RAFT agents.[174] This process minimised secondary nucleation of new particles, leading to latexes with no labile surfactant and good control of particle size. However, these were achieved only when using amphipathic diblock macro-RAFT agents, such as poly(acrylic acid)-polystyrene, which located at the monomer droplet/water interface and performed as both stabiliser and chain transfer agent.[175-177]

In fact, polymers with low molar mass distributions and the resulting latexes with good stability and can be successfully prepared *via* RAFT miniemulsion polymerisation using conventional RAFT agents.[126,154,172,178-180] Moad *et al.* prepared polystyrene with narrow molar mass distribution (<1.2) *via* RAFT miniemulsion polymerisation simply using phenylethyl dithiobenzoate (PEDB) RAFT agents, but retardation was observed.[179] The retardation can be markedly reduced by using aliphatic dithioesters[154] or trithiocarbonate RAFT agents.[174]

1.7. Self-assembly

Self-assembly is a process whereby a disordered system of components forms an ordered structure or pattern. The self-assembly of surfactant amphiphiles has been investigated for over a century.[181] In 1913, McBain was the first to investigate the formation of micelles using soap solutions.[182] However, research into block copolymer self-assembly started in the early 1960s.[183,184] In the following sections, surfactant molecule self-assembly, block copolymer self-assembly and polymerisation-induced self-assembly (PISA) will be briefly introduced.

1.7.1. Surfactant molecule self-assembly

Surfactant molecules are organic amphiphilic compounds comprised a hydrophilic (or polar) head and a hydrophobic (or non-polar) tail. This amphiphilic character leads the surfactant to undergo self-assembly spontaneously to reduce the interfacial tension between two phases.[185,186] Israelachvili *et al*. developed the theory of amphiphilic self-assembly *via* investigating the interaction free energy between surfactant molecules (e.g. lipids) as a function of hydrophilic/hydrophobic interfacial surface area.[187-191] More specifically, hydrophilic repulsion forces are inversely proportional to interfacial surface area, whereas hydrophobic attraction increases in a linear manner (**Figure 1.16a**). Additionally, the total interaction free energy (dashed line) obtains a minimum interaction free energy at an optimum headgroup area, indicating the structure formed by the amphiphiles.

The morphologies of colloidal aggregation can generally be determined by the packing of amphiphiles, which commonly referred as the packing parameter (*P*, **Equation 1.10**).[187,191-193]

$$P = \frac{V}{A_0 L_c} \qquad \textbf{Equation 1.10}$$

where *P* represents packing parameter, *V* represents the volume of the hydrophobic chain, A_0 represents the optimal area of the head group and L_c represents the length of the hydrophobic segment.

The relationship between packing parameter and expected morphologies of self-assembly are presented in **Figure 1.17**.[191] At $P < 1/3$, spherical micelles are obtained; for $1/3 < P < 1/2$, cylindrical micelles are formed; at $1/2 < P < 1$, flexible bilayers or vesicles are produced; for $P = 1$, planar bilayers are obtained; and at $P < 1$, inverted micelles are observed.

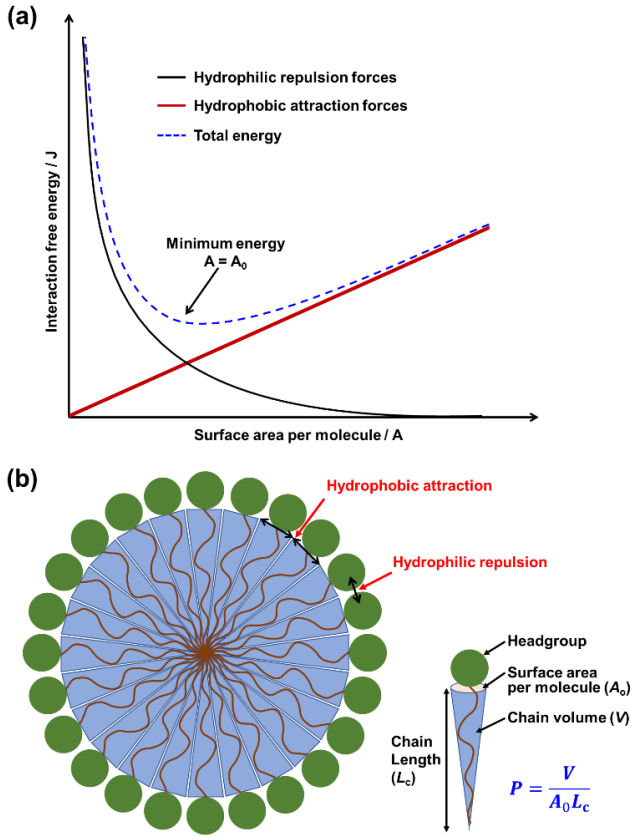

Figure 1.16. (a) Interaction free energy change with surface area per molecule. The total energy (dashed line) is contributed from the hydrophilic repulsion force and the hydrophobic attraction forces between neighbouring amphiphiles. (b) Schematic representation of the aggregation of amphiphiles based on a balance of hydrophilic repulsive and hydrophobic attractive forces. The packing parameter (*P*) is defined by the equation. (Reproduced from Ref. 191 with permission from the Elsevier)

Packing parameter (*P*)	$< \frac{1}{3}$	$\frac{1}{3}$ - $\frac{1}{2}$	$\frac{1}{2}$ - 1	~ 1	> 1
Packing shape	Cone	Truncated cone	Truncated cone	Cylinder	Inverted truncated cone
Formed morphology	Spherical micelles	Cylindrical micelles	Flexible bilayers, vesicles	Planar bilayers	Inverted micelles

Figure 1.17. Relationship between packing parameter, packing shape and expected morphologies of self-assembly. (Reproduced from Ref. 191 with permission from the Elsevier)

1.7.2. Self-assembly of block copolymers

Self-assembly of amphiphilic block copolymers, comprising a hydrophilic and a hydrophobic block in selective solvents has attracted significant attention in the past two decades.[1,2,194,195] Compared to the self-assembly of small molecules, self-assembled copolymers exhibit higher stability and durability.[2] Therefore, these amphiphilic block copolymers have potential applications in various fields, such as catalysis, cosmetics and drug delivery.[5,194] Similar to the self-assembly of small surfactant molecules (e.g. lipids), amphiphilic diblock copolymers can also aggregate and form various morphologies, such as sphere, worm, vesicle, cylinder, bicontinuous structure and lamellae.[1,5,196-199] Eisenberg *et al.* reported that self-assembly of polystyrene-poly(acrylic acid) (PS–PAA) diblock copolymers in selected solvents can result in a wide range of morphologies, such as spherical micelles, rods, bicontinuous rods, vesicles, lamellae and hexagonally packed hollow hoops (HHHs) (**Figure 1.18**).[194] The morphologies of these PS–PAA diblock copolymers can be seen as core/shell structures. The hydrophobic PS block is hidden in the core to reduce the unfavourable interactions energy with solution. In contrast, the hydrophilic PAA block is present in the shell to stabilise the aggregates in solution, and thus the total free energy can be lower.

Principally, self-assembly of block copolymers is affected by many factors, such as copolymer composition,[195] copolymer concentration,[200] nature of solvent[201] and water content.[202] Various self-assembly techniques for amphiphilic block copolymers have been reported *via* post polymerisation methods, such as pH switch,[203] thin film rehydration[204] or solvent exchange.[205] However, for these approaches, block copolymers are generally prepared first, and then self-assembled using a second process. Furthermore, well-defined morphologies can be obtained only in dilute solution (<1%), which considerably limits their practical applications in large-scale preparation. Therefore, extensive attention has been focused on developing an alternative strategy, named polymerisation-induced self-assembly (PISA), to produce self-assembled block copolymers, and is described in the following section.

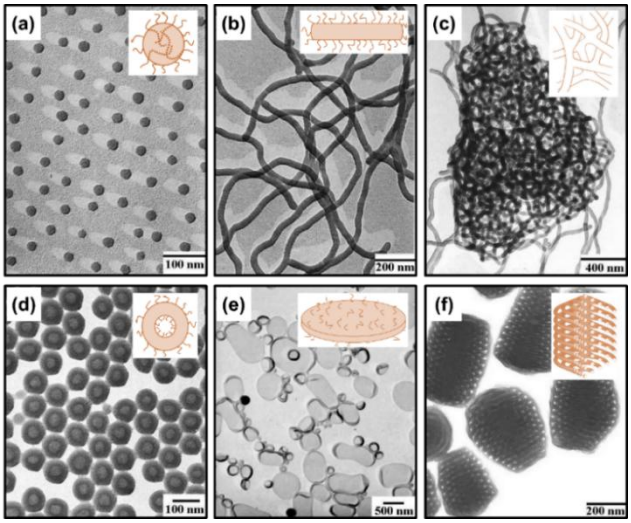

Figure 1.18. Representative TEM images and corresponding cartoons for a wide range of morphologies for amphiphilic polystyrene-poly(acrylic acid) (PS–PAA) diblock copolymer obtained *via* self-assembly in selective solvents. (a) Spherical micelles, (b) rods, (c) bicontinuous rods, (d) vesicles, (e) lamellaes and (f) hexagonally packed hollow hoops (HHHs). (Reproduced from Ref. 194 with permission from Canadian Journal of Chemistry)

1.7.3. Polymerisation-induced self-assembly (PISA)

In recent years, PISA has received considerable attention and become widely recognised as a versatile and efficient route to prepare a wide range of diblock copolymer nanoparticles with controlled size, morphology and surface functionality.[7-10] PISA has enormous advantages in that: (i) it enables the preparation of block copolymer nanoparticles without the requirement for conventional post polymerisation processing techniques; (ii) it can be conducted using formations with high solids, making this method amenable to scale-up for industrial production; (iii) it is capable of obtaining nanoparticles with a wide range of morphologies (e.g. sphere, worm or vesicle) simply by varying the DP of the stabiliser or core-forming blocks; and (iv) it enables the formation of nanoparticles with a wide range of surface chemistries by using stabiliser chains with different chemical nature.

Principally, PISA can be achieved *via* any type of living polymerisation,[206-211] but the majority of literature examples are based on RAFT polymerisation.[7,8,14,212-218] **Figure 1.19** shows a schematic depiction of diblock copolymer nanoparticles with varying morphologies (sphere, worm and vesicle) synthesised *via* RAFT-mediated PISA.[3] More specifically, a RAFT macromolecular chain transfer agent (macro-CTA) is utilised as a soluble stabiliser block to chain-extend with second monomer in an appropriate solvent

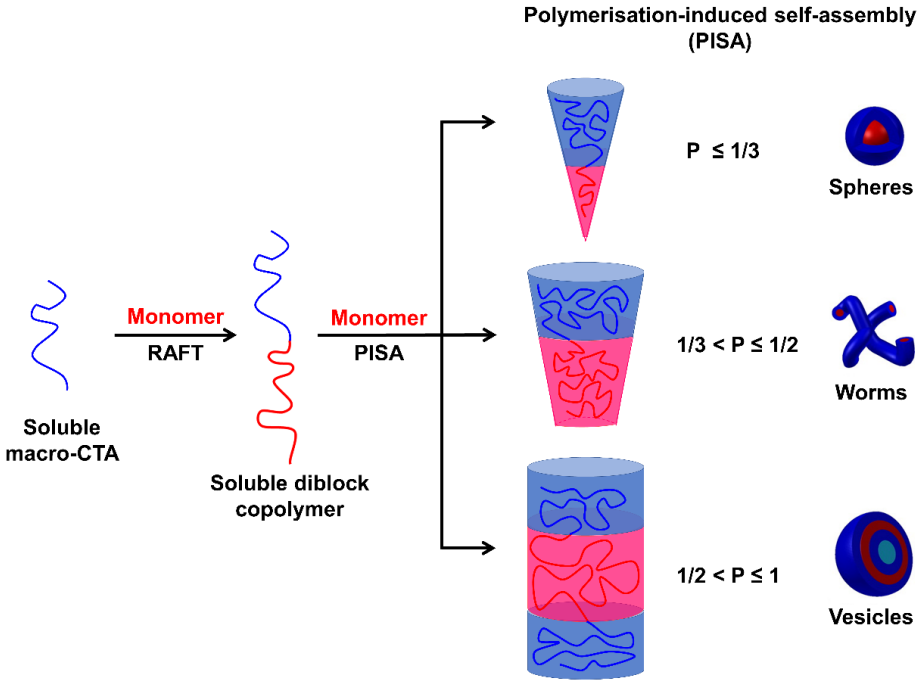

Figure 1.19. Schematic representation of the preparation of diblock copolymer nano-objects *via* RAFT-mediated PISA. Soluble macro-CTA is synthesised *via* RAFT solution polymerisation, followed by RAFT-mediated PISA of solvent-immiscible or solvent-miscible monomer to form a second block *via* RAFT emulsion polymerisation or RAFT dispersion polymerisation. (Reproduced from Ref. 3 with permission from the American Chemical Society)

to form a core-forming block. As the polymerisation progress, the DP of the core-forming block increases with monomer conversion and gradually forms an insoluble block. *In situ* self-assembly enables to form sterically-stabilised nanoparticles such as spherical micelles (spheres), worm-like micelles (worms) and vesicles.[3,215,219]

In principle, block copolymer nanoparticles with varying surface chemistry (e.g. anionic,[11,12] cationic,[13] non-ionic[14-20] or zwitterionic[21-23]) can be prepared *via* RAFT-mediated PISA using appropriate macro-CTAs. Furthermore, the morphologies and morphology transitions of polymers in the PISA process are influenced by numerous factors, such as monomer,[3,8,9] DP of stabiliser/core-forming blocks[220] and solvent.[213] In principle, RAFT-mediated PISA can be performed in a wide range of media, such as alcohols,[24-26] water[15,22,27] and non-polar solvents.[28-30] Based on the initial solubility of the core-forming monomer, the macro-CTA can be chain-extended using solvent-immiscible or solvent-miscible monomer to form a second block *via* RAFT emulsion polymerisation or RAFT dispersion polymerisation, respectively.

1.7.4. PISA *via* RAFT aqueous emulsion polymerisation

As discussed in **section 1.5**, a conventional aqueous emulsion polymerisation formulation comprises water, water-immiscible monomer, water-soluble initiator and water-soluble surfactant. However, for RAFT aqueous emulsion polymerisation formulation, a water-soluble macro-CTA is used as a stabiliser rather than surfactant.[221] This enables the formation of block copolymer nanoparticles without the requirement for post polymerisation processing techniques (e.g. centrifugation or dialysis) to remove excess surfactant, making this approach more cost-effective and amenable to scale-up for industrial production.[222,223] However, RAFT emulsion polymerisation using a water-soluble macro-CTA may suffer from competition between the desired self-assembly nucleation and the undesired homogeneous nucleation.[7] Homogeneous nucleation may occur especially when using macro-CTAs with low reactivity or concentration. Under such conditions, most of the primary radicals may rapidly react with the hydrophobic monomer before reacting with the macro-CTA, resulting in the nascent polymer chains precipitating to form nuclei. This results in poor control over the RAFT polymerisation (i.e. higher molar mass and broader molar mass distribution), and the unreacted macro-CTA being present in the polymer latex.[7]

In 2002, Hawkett and coworkers reported the first *ab initio* RAFT aqueous emulsion polymerisation of *n*-butyl acrylate.[224-226] More specifically, a hydrophilic poly(acrylic acid) (PAA) macro-CTA was prepared using a trithiocarbonate RAFT agent. The PAA was subsequently chain-extended with *n*-butyl acrylate, and the resulting poly(acrylic acid)-poly(*n*-butyl acrylate) chains self-assembled to form micelles as the poly(*n*-butyl acrylate) block reached its critical DP. This RAFT aqueous emulsion polymerisation exhibited good living character (well-control molar mass and molar mass distribution), and the resulting latexes, stabilised by hydrophilic PAA block, had good colloidal stability.

Charleux and co-workers reported the first example for the preparation of block copolymer latexes with higher order morphologies *via* RAFT aqueous emulsion polymerisation in 2010.[227] More specifically, a series of hydrophilic poly(acrylic acid-co-poly(ethylene oxide) methyl ether acrylate) [P(AA-co-PEGA)] polymers with varying AA/PEGA ratio were synthesised. These macro-CTAs were chain-extended with styrene (hydrophobic monomer) at various conditions, including composition [(AA/PEGA ratio of

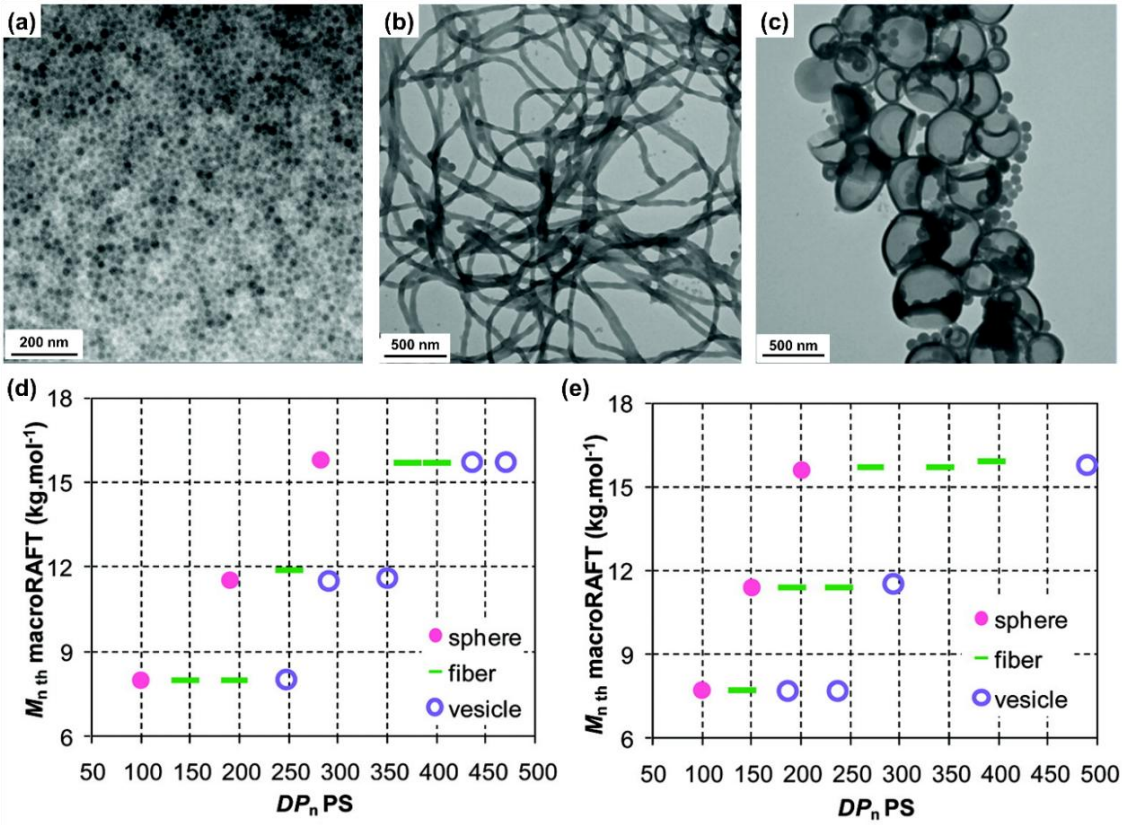

Figure 1.20. Representative TEM images for block copolymer nano-objects: (a) spherical micelles, (b) nanofibres and (c) vesicles. Morphology diagrams constructed for poly(methacrylic acid-co-poly(ethylene oxide) methyl ether acrylate)-polystyrene [P(MAA-co-PEOMA)–PS] block copolymer nano-objects prepared *via* RAFT aqueous emulsion polymerisation at pH = 5 using P(MAA-co-PEOMA) as macro-CTA with (d) MAA/PEOMA = 50/50 and (e) MAA/PEOMA = 67/33. (Reproduced from Ref. 228 with permission from the American Chemical Society)

P(AA-co-PEGA)], solution pH and salt ($NaHCO_3$) concentration. They showed that nano-objects with various morphologies (sphere, fibre and vesicle) can be obtained under appropriate synthetic conditions. For example, only spherical micelles were obtained when using PAA or PEGA macro-CTA. In contrast, higher order morphologies (fibre and vesicle) can be achieved using P(AA-co-PEGA) macro-CTA with 50/50 molar composition at acidic pH or in the presence of added salt ($NaHCO_3$).[227] Recently, the same research group reported that block copolymer nano-objects can be prepared *via* RAFT aqueous emulsion polymerisation using a wide range hydrophilic stabiliser blocks based on acrylamide,[229] methacrylic acid,[230] poly(ethylene oxide)[231,232] or poly(ethylene oxide) methyl ether acrylate,[228] and hydrophobic monomers (e.g. benzyl methacrylate,[233] methyl methacrylate[234] or styrene[228]). **Figure 1.20** shows morphology diagrams

constructed for poly(methacrylic acid-co-poly((ethylene oxide) methyl ether acrylate)-polystyrene [P(MAA-co-PEOMA)–PS] block copolymer nano-objects prepared *via* RAFT aqueous emulsion polymerisation using P(MAA-co-PEOMA) macro-CTAs.[228] The diagrams indicated that spheres, fibres and vesicles can be obtained using P(MAA-co-PEOMA) macro-CTA with MAA/PEOMA composition of either 50/50 or 67/33. It was also found that these P(MAA-co-PEOMA) macro-CTAs may become partially ionised at pH 5, resulting in a stronger segregation between the hydrophilic and hydrophobic blocks to form higher order morphologies.[228]

Armes and co-workers reported the preparation of poly(glycerol monomethacrylate)−poly(benzyl methacrylate) (PGMA-PBzMA) diblock copolymer nanoparticles *via* RAFT aqueous emulsion polymerisation using a non-ionic PGMA macro-CTA.[233] A series of PGMA-PBzMA diblock copolymer spherical nanoparticles ranging from 30 to 230 nm were readily prepared by simply altering the DP of core-forming PBzMA block (**Figure 1.21**). More specifically, for a fixed $PGMA_{51}$ macro-CTA, a monotonic increase in mean hydrodynamic diameter was observed when increasing the DP of PBzMA from 50 to 1000. Furthermore, this approach can be used to prepare spherical diblock copolymer nanoparticles with a fixed PGMA-PBzMA copolymer composition at up to 50% solids.[233]

Ma *et al.*[235] reported the preparation of cationic poly(2-(methacryloyloxy) ethyl trimethylammonium iodide)-poly(benzyl methacrylate) (PQDMA–PBzMA) and anionic poly(potassium 3-sulfopropyl methacrylate)-poly(benzyl methacrylate) (PKSPMA–PBzMA) diblock copolymer nanoparticles *via* RAFT aqueous emulsion polymerisation. In both cases, purely spherical nanoparticles with small diameter (approximately 50 nm) and good colloidal stability were obtained. Furthermore, both the cationic PQDMA–PBzMA and the anionic PKSPMA–PBzMA diblock copolymer nanoparticles exhibited high surface charge with the zeta potential values of +35 mV and -43 mV, respectively. These two oppositely charged spherical nanoparticles were utilised to prepare thin film membranes by sequential deposition using spray coating (**Figure 1.22**). The thickness of the film membranes could be readily altered by varying the number of the deposited cycles. Furthermore, the electrostatic attraction between the nanoparticles with opposite surface charge ensured the good cohesion and formed stable thin film membranes.[235]

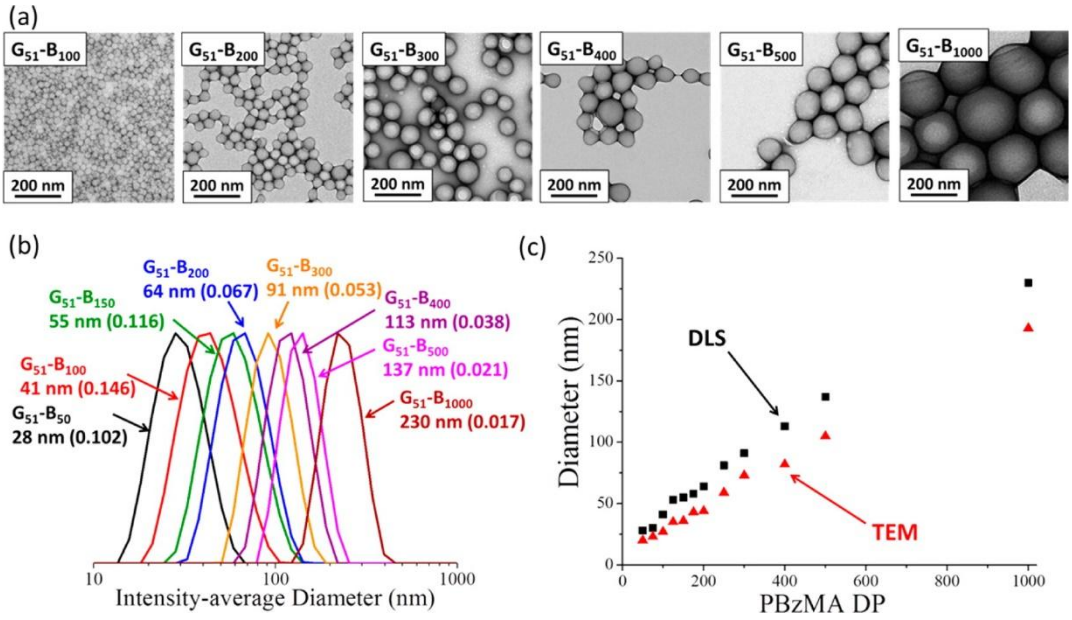

Figure 1.21. Poly(glycerol monomethacrylate)$_{51}$-poly(benzyl methacrylate)$_x$ (G_{51}–B_x) diblock copolymer nanoparticles prepared *via* RAFT aqueous emulsion polymerisation at 10% w/w solids. (a) TEM images of $PGMA_{51}$–$PBzMA_x$ (x = 100, 200, 300, 400, 500 and 1000), (b) corresponding DLS intensity-average size distributions (the number in brackets represents the DLS polydispersity index) and (c) mean particle diameter versus degree of polymerisation of the PBzMA core-forming block. (Reproduced from Ref. 233 with permission from the American Chemical Society)

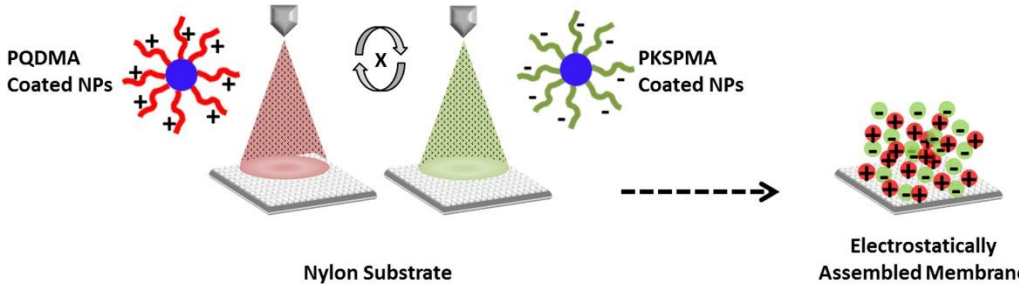

Figure 1.22. Schematic representation of the sequential deposition of the thin film membrane using spray coating. (Reproduced from Ref. 235 with permission from Journal of Membrane Science)

1.7.5. PISA *via* RAFT Dispersion Polymerisation

PISA *via* RAFT dispersion polymerisation is a type of precipitation polymerisations conducted in a selected solvent, which is a good solvent for the macro-CTA, core-forming monomer and initiator, but is a non-solvent for block copolymer once the core-forming block reached its critical DP.[8] More specifically, a solvent-miscible monomer chain extends a soluble macro-CTA during polymerisation and gradually forms an insoluble block as its DP increases.[215,219] Subsequently, *in situ* self-assembly occurs to form

sterically-stabilised nanoparticles such as spheres, worms and vesicles.[215,219] In fact, it has been shown this RAFT-mediated PISA technique can be conducted in a wide range of solvents, such as polar solvents (e.g. water,[9,15,16,236-238] methanol,[25,239,240] ethanol[25,241-243] and isopropanol[244]), non-polar solvents (e.g. *n*-alkanes,[30,245] isododecane[28] and mineral oil[222]) and exotic media (e.g. ionic liquids[246,247]).

RAFT dispersion polymerisation can also be conducted in alcohol/water mixtures.[248-252] It has been shown that the co-solvent composition can affect the polymerisation kinetics and the resulting copolymer morphology.[250,251] Jones *et al.* reported the preparation of poly(2-(dimethylamino)ethyl methacrylate)-poly(benzyl methacrylate) (PDMA–PBzMA) diblock copolymer nanoparticles *via* RAFT-mediated PISA in varying ethanol/water mixtures.[251] Significantly faster polymerisation rates were observed for the RAFT-mediated PISA conducted at higher water content. Furthermore, for a fixed diblock copolymer composition, nano-objects with higher order morphologies (worms and vesicles) were obtained when using relatively lower water or higher ethanol contents (**Figure 1.23**).[251] This can be attributed to the build-up of cationic charge on the PDMA stabiliser in the presence of water, leading to higher inter-particle repulsion and preventing the sphere-sphere fusion to form higher order morphologies.

Ning *et al.* reported the preparation of anionic poly(ammonium 2-sulfatoethyl methacrylate)-poly(benzyl methacrylate) (PSEM–PBzMA) diblock copolymer nanoparticles *via* RAFT dispersion polymerisation in a 2/1 v/v ethanol/water mixture and RAFT aqueous emulsion polymerisation (**Figure 1.24**).[252] In both cases, well-defined spherical nanoparticles were obtained. For a fixed diblock copolymer composition, the nanoparticles prepared *via* RAFT dispersion polymerisation in ethanol/water mixture were significantly larger (80–126 nm) than those prepared *via* aqueous emulsion polymerisation (31–36 nm). Furthermore, the former case had higher mean aggregation number (1200–4100 versus 40–70) and higher PSEM stabilizer surface density (0.06–0.12 versus 0.02–0.04 chain per nm^2). This can be attributed to repulsive interactions between neighbouring anionic PSEM stabiliser chains being significantly weaker in a 2/1 v/v ethanol/water mixture compared to pure water.[252] Furthermore, the PBzMA chains may be more solvated when grown in the ethanol/water mixture, leading to more stretched configuration, and thus more closely packed copolymer chains can be aggregated in the nanoparticle cores.

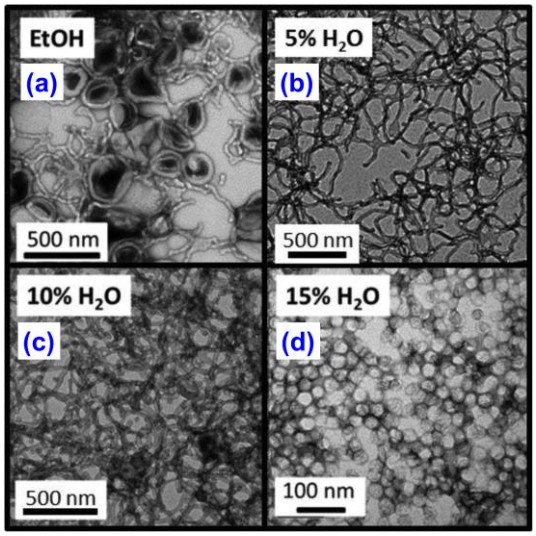

Figure 1.23. Representative TEM images of poly(2-(dimethylamino)ethyl methacrylate)$_{43}$-poly(benzyl methacrylate)$_{120}$ (PDMA$_{43}$–PBzMA$_{120}$) nano-objects prepared *via* RAFT dispersion polymerisation at 70 °C in varying ethanol/water mixtures (a) 100% ethanol, (b) 95/5 w/w ethanol/water, (c) 90/10 w/w ethanol/water, (d) 85/15 w/w ethanol/water. (Reproduced from Ref. 251 with permission from the Royal Society of Chemistry)

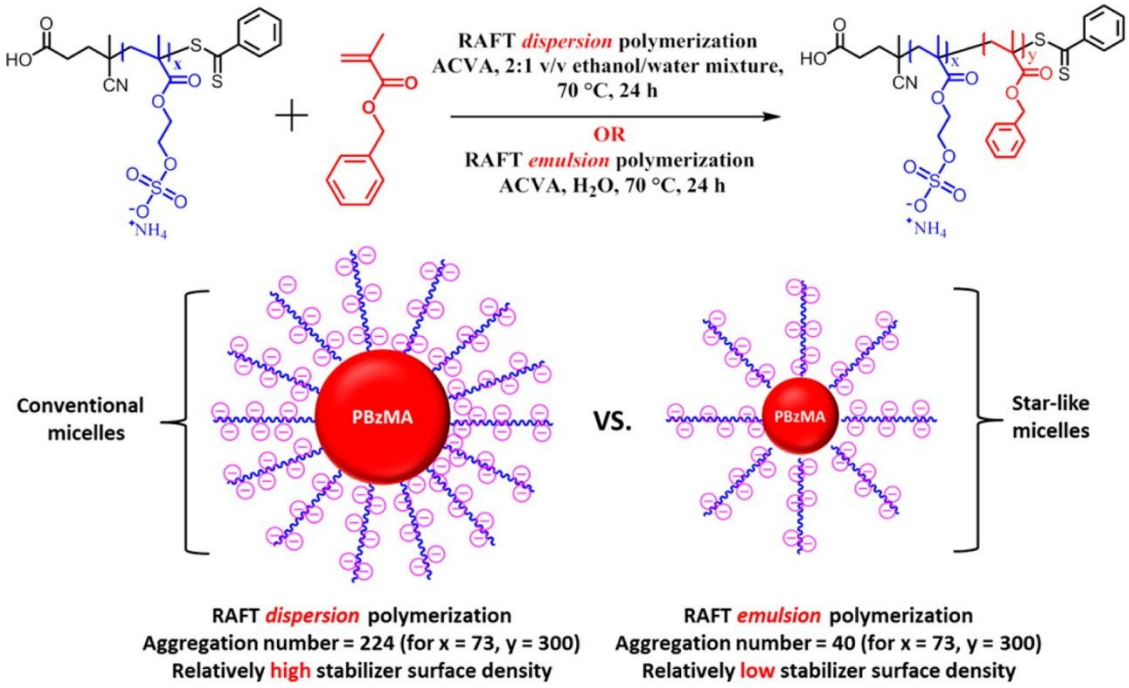

Figure 1.24. (a) Synthesis of poly(ammonium 2-sulfatoethyl methacrylate)-poly(benzyl methacrylate) (PSEM–PBzMA) diblock copolymer nanoparticles at 10% w/w *via* RAFT dispersion polymerisation in a 2/1 v/v ethanol/water mixture and RAFT aqueous emulsion polymerisation at 70 °C for 24 h. (b) Schematic representation of how solvent quality affects the resulting nanoparticle diameter, mean aggregation number and stabiliser surface density for a fixed target PSEM–PBzMA composition. (Reproduced from Ref. 252 with permission from the American Chemical Society)

1.8. Graphene-based polymer nanocomposite particle

Nanocomposites are hybrid materials where two or more components with different physical or chemical properties are combined and one or more components are at the nanometre (nm) scale. Recently, polymer/inorganic nanocomposites have attracted extensive attention by both academic and industrial researchers.[253-257] Particularly, nanocomposites comprising polymer and graphene have received much attention.[258-262] They have potential applications in areas, such as sensors,[263,264] electrode materials,[265] catalytic materials[266,267] and supercapacitors.[268-270]

Numerous approaches have been reported to prepare polymer/inorganic composite materials using inorganic materials as a filler *via* solution blending[271,272] and melt processing.[272,273] In solution blending, the polymer is dissolved in a selected solvent, and the nano fillers are dispersed in the polymer solution. Generally, solution blending can be utilised to prepare more homogeneous polymer/inorganic nanocomposites. However, it is difficult to remove trace residual solvents in nanocomposites.[271,272] From an industrial standpoint, melt processing is a preferred approach for the preparation of polymer/inorganic nanocomposites as it is direct and can be applied to a wide range of polymers and nano fillers.[272,273] However, this approach needs to be conducted at relatively high temperature (>180°C)[274] and the nano fillers readily aggregate due to high surface areas, leading to poor dispersion of the nano fillers and phase separation of the polymer/inorganic phase.[275] Therefore, both the solution blending and melt processing approaches are relatively irreproducible for the preparation of polymer/inorganic nanocomposite.

Alternatively, various strategies have been developed for the preparation of polymer/inorganic nanocomposite through hybrid latex particles on the nanoscale. These methods can generally be classified into four distinct routes as follows:[276]

(i) Polymerisation of organic monomer in the presence of pre-formed inorganic oxide particles (e.g. *in situ* polymerisation).[277-279]

(ii) Preparation of an inorganic oxide phase in the presence of pre-formed polymer latex particles.[252,280]

(iii) Preparation of both polymer and inorganic phases simultaneously.[281,282]

(iv) Heteroflocculation between pre-formed polymer latexes and pre-formed inorganic oxide particles.[283-285]

Among those four routes, heteroflocculation strategy (route iv) is the simplest route to prepare polymer/inorganic nanocomposite particles, achieved simply by mixing pre-formed polymer latex with pre-formed inorganic sol at room temperature. Therefore, the heteroflocculation strategy is employed for the preparation of polymer/graphene oxide (GO) nanocomposite particles in this thesis, as reported in **Chapter Five**. Hence, graphene oxide and the heteroflocculation strategy are briefly described in the following sections.

1.8.1. Graphene oxide (GO)

Graphene is a single atomic layer of graphite with sp^2-bonded carbon atoms arranged in a two-dimensional hexagonal or honeycomb lattice. In 2004, Geim, Novoselov and co-workers at the University of Manchester reported a novel method to isolate a single sheet of graphene (approximately 0.8 nm) using micromechanical cleavage (also named Scotch tape technique).[286,287] Due to this breakthrough finding, both Andre Geim and Konstantin Novoselov were awarded the Nobel Prize for Physics in 2010. Furthermore, it has been reported that graphene has excellent electrical conductivities, thermal conductivities, mechanical properties and high surface area.[288-291] Thus, graphene has attracted great attention in both academic and industrial labs to develop economically available approaches for manufacturing of graphene-based composites in the past two decades. However, the reported approaches for the preparation of mass produced high-quality graphene are usually costly and require tedious purification, which are normally associate with high energy consumption.[292,293] Furthermore, graphene has a relatively hydrophobic surface with high Van der Waals attraction between graphene sheets. This leads to the tendency for irreversible stacking-induced aggregation, hindering production, processing and storage for research and industrial manufacturing.[294-296]

Recently, graphene oxide (GO) has attracted great attention as it is a highly oxidised chemically derived graphene with various oxygen-containing functional groups, such as carboxyl, hydroxyl and epoxy.[297-299] These oxygen-containing groups make GO highly attractive as they can be readily functionalised for a wide range of applications.[300] Brodie reported the first preparation of GO in 1859 *via* oxidation of graphite precursor using potassium chlorate ($KClO_3$) and nitric acid (HNO_3) mixture.[301] In 1958, Hummers

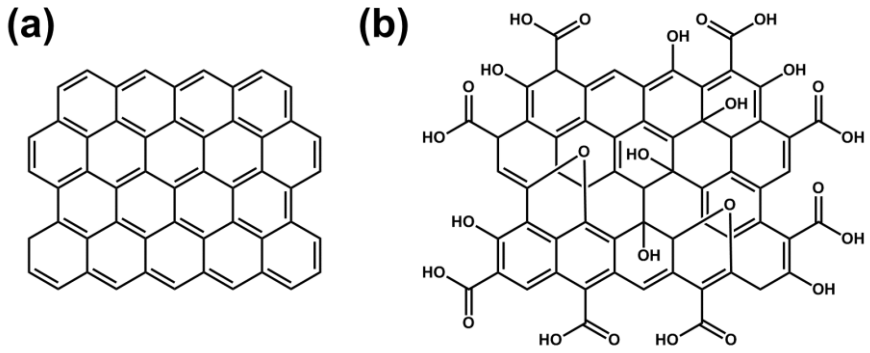

Figure 1.25. Structural model of (a) graphene and (b) graphene oxide.[302,303]

and Offeman reported a more efficient approach to prepared GO, utilising potassium permanganate ($KMnO_4$), sodium nitrate ($NaNO_3$) and concentrated sulfuric acid (H_2SO_4).[304] This approach includes chemical functionalisation *via* strong oxidation and physical exfoliation through vigorous agitation to obtain GO sheets, resulting in oxygen-containing functional groups (e.g. carboxyl, hydroxyl and epoxy groups) being created and covalently attached to the basal carbon plane. More specifically, the carboxylic functionalities are mostly located at the sheet edges, whereas hydroxyl and epoxide functional groups are generally on the surfaces of the GO sheets (**Figure 1.25**).[302,303] These groups result in the GO sheets being negatively charged across a wide pH range, with the zeta potential becoming more negative as the pH increases, due to ionisation of the carboxylic acid and phenolic hydroxyl groups attached to the carbon skeleton.[305,306]

The oxygen-containing functional groups on the GO change the hybridisation of the carbon atoms from sp^2 to sp^3, leading to disrupted delocalised π system and effectively loss of electrical conductivity.[307-309] However, these oxygen-containing groups can increase the distance between graphitic layers and increase hydrophilic and polar character, resulting in GO sheets being able to be readily dispersed in a variety of solvents (e.g. water, tetrahydrofuran and *N*,*N*-dimethylformamide) and exfoliated using ultrasonication.[305,310,311] Furthermore, the oxygen-containing groups on the GO surface can also be functionalised *via* covalent bonding or non-covalent interactions to prepare polymer/GO nanocomposites.[312-315]

1.8.2. Graphene-based polymer nanocomposite particles preparation *via* heteroflocculation

Heteroflocculation has been reported as a versatile approach for the formation of nanocomposite particles and requires a mutual attraction (e.g. electrostatic interaction) between the polymer latex and inorganic component to form nanocomposite particles, rather than a binary mixture of noninteracting particles.[316-318] It has been reported that polymer/silica (SiO_2) nanocomposite particles can be obtained *via* heteroflocculation between cationic polymer latexes and anionic silica particles.[319-323] Luna-Xavier *et al.* reported the heteroflocculation between large anionic silica (70 nm) and small cationic poly(methyl methacrylate) (PMMA) latex particles (33 nm). Nanocomposite particles with core/shell morphologies were obtained by the adsorption of the pre-formed PMMA latex nanoparticles onto the silica.[319] In contrast, Balmer *et al.* reported a series of studies of heteroflocculation between large cationic poly(ethylene glycol) methacrylate (PEGMA)-stabilised poly(2-vinyl pyridine) (P2VP) latex particles and small anionic colloidal silica sol (20 nm) at pH 10.[320-323] In these cases, the nanocomposite particles comprised a P2VP core with silica forming the shell. It was found that nanocomposite particles with a well-defined monolayer of silica particles surrounding the P2VP latex cores were obtained when using near-monodisperse 463 nm P2VP latexes and 20 nm silica sol at packing density of 69%.[323]

Fielding *et al.* reported the heteroflocculation between PEGMA-stabilised P2VP latex nanoparticles with 'rice grain' alumina–silica coated titania (TiO_2) nanoparticles (**Figure 1.26**).[324] It was found that P2VP/titania nanocomposite particles with core/shell morphologies were obtained and titania particles adsorb strongly at pH 10. Furthermore, the degree of flocculation of the P2VP/titania nanocomposite particles were assessed by disc centrifuge photosedimentometry (DCP, **Figure 1.26e**). The DCP studies showed that the particle size distribution for bare P2VP latexes was relatively narrow, whereas addition of titania led to significantly broader distributions, indicating P2VP/titania nanocomposite particles were formed. However, when adding a small amount of titania (12 and 21 wt.%), the particle size distributions became much broader, implying that titania adsorbs onto the P2VP latex but causes bridging flocculation due to insufficient titania to coat all the latex particles. In contrast, at higher titania contents, the degree of

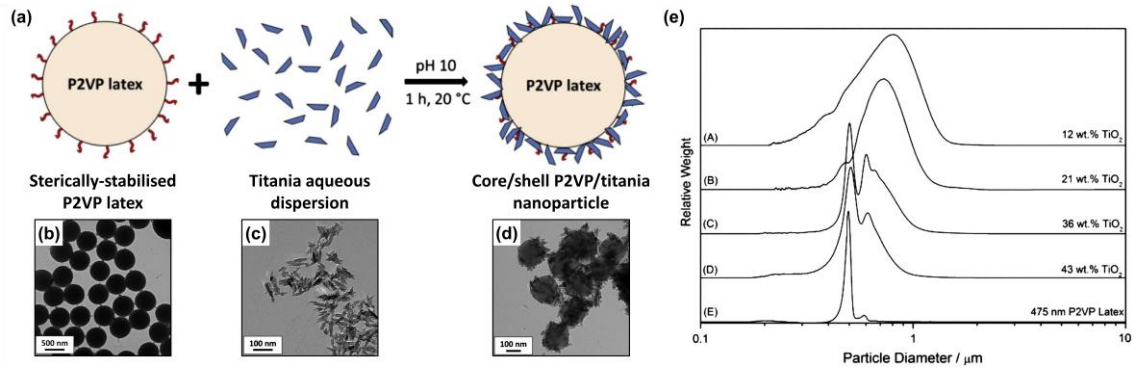

Figure 1.26. (a) Schematic representation of the heteroflocculation between sterically stabilised P2VP latex nanoparticles with 'rice grain' titania nanoparticles. Representative TEM images for (b) (PEGMA)-stabilised P2VP latex, (c) alumina–silica coated 'rice grain' titania particles and (d) P2VP/titania nanocomposite particles. (e) DCP particle size distributions obtained for cationic PEGMA-stabilised P2VP latex (475 nm) before and after heteroflocculation with addition of varying anionic titania content (12 to 43 wt.% relative to latex) at pH 10. (Reproduced from Ref. 324 with permission from Journal of Colloid and Interface Science)

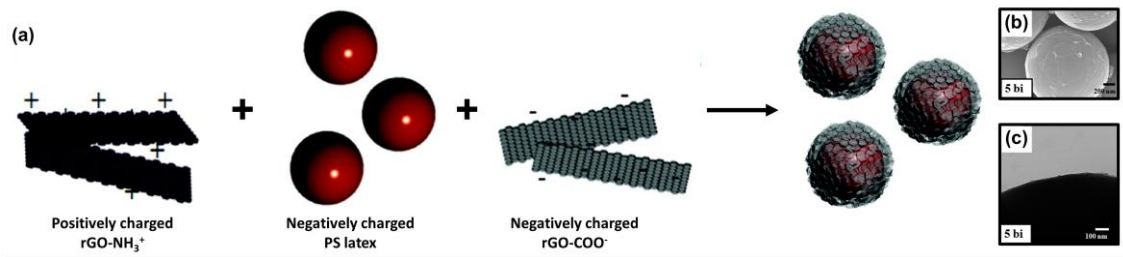

Figure 1.27. (a) Schematic representation of the layer-by-layer heteroflocculation between negatively charged PS and rGO (positively charged rGO-NH_3^+ and negatively charged rGO-COO^-); representative (b) SEM and (c) TEM images of PS/rGO nanocomposite particles with five bilayers of rGO-NH_3^+/rGO-COO^- onto PS colloid particle. (Reproduced from Ref. 325 with permission from the American Chemical Society)

flocculation is reduced and the primary peak for P2VP latexes becomes narrower, indicating that the latex particles are fully covered with titania.

Heteroflocculation has also been utilised to prepare GO-based hybrid nanocomposite particles using negatively charged GO sheets and positively charged polymer latex.[283-285,325-327] Pham *et al.* performed heteroflocculation between positively charged poly(methyl methacrylate) (PMMA) latex nanoparticles (~200 nm) and negatively charged GO sheets (~10 μm) to obtain PMMA/GO nanocomposite.[327] The SEM images indicated that several PMMA particles were wrapped by one GO sheet. This is because the GO sheets were much larger than the size of the PMMA nanoparticles.

Nevertheless, the PMMA/GO nanocomposites were reduced using hydrazine (GO/hydrazine 1:10 w/w) to obtain PMMA/rGO nanocomposite. These PMMA/rGO nanocomposite particles were compression molded to create PMMA/rGO composite pellets. These pellets exhibit excellent electrical and thermomechanical properties.

Hong *et al.* prepared polymer/reduced graphene oxide (rGO) nanocomposite particles *via* layer-by-layer heteroflocculation route, whereby negatively charged polystyrene (PS) latexes (~1.2 μm) were alternatively coated with positively charged rGO-NH_3^+ and negatively charged rGO-COO^- nanosheets (**Figure 1.27**).[325] The thickness of the rGO was increased by increasing the number of rGO-NH_3^+/rGO-COO^- coated layers. Furthermore, the PS colloidal particle substrates inside the nanocomposite particles can be removed using extensive THF solvent to obtain hollow rGO capsules. These hollow capsule of rGO nanosheets exhibited good chemical and physical stabilities during the removal of PS particle templates by THF treatment.

Chapter Two

Investigating the influence of solvent quality on RAFT-mediated PISA of sulfonate-functional diblock copolymer nanoparticles

2.1. Introduction

Self-assembly of amphiphilic block copolymers comprising a hydrophilic and a hydrophobic block in selective solvents has attracted wide attention for decades.[1-3] They have potential applications in various fields, such as coatings,[4] sensing[5] and drug delivery.[6] It is well-known that amphiphilic diblock copolymers self-assemble to form well-defined nanoparticles in appropriate selective solvents for one of the two blocks.[192,328,329] Self-assembly is typically conducted in dilute solution (<1%) using various post-polymerisation methods, such as pH switch,[203] thin film rehydration[204] or solvent exchange.[205] Principally, the nanoparticle morphology and mean diameter depend on the relative volume fractions of the solvophobic and solvophilic blocks, which dictate the packing parameter.[330]

In the past two decades, polymerisation-induced self-assembly (PISA) *via* reversible addition-fragmentation chain transfer (RAFT) polymerisation has attracted considerable interest for the design and preparation of a wide range of complex block copolymer nanoparticles with controlled size, morphology and surface functionality.[7-10] PISA is also a versatile and efficient route to prepare a wide range of diblock copolymer nanoparticles at high solids[331] without the requirement for conventional post polymerisation processing techniques, making this method amenable to scale-up for industrial production.[222] Furthermore, RAFT-mediated PISA can be performed in a wide range of media such as alcohols,[24-26] water[15,22,27] and non-polar solvents.[28-30] Briefly, in this technique, a RAFT macromolecular chain transfer agent (macro-CTA) is utilised as a soluble stabiliser block, which is chain-extended using a solvent-miscible or a solvent-immiscible monomer *via* RAFT dispersion or emulsion polymerisation, respectively, to form a second block.

During RAFT dispersion polymerisation, a solvent-miscible monomer chain-extends a soluble macro-CTA and gradually forms an insoluble block as the degree of polymerisation (DP) increases. *In situ* self-assembly occurs to form sterically-stabilised nanoparticles, such as spherical micelles (spheres), worm-like micelles (worms) and vesicles.[215,219] In contrast, during RAFT emulsion polymerisation, the monomer is solvent-immiscible. Although most of the monomer is water-insoluble, a small proportion of monomer is nevertheless dissolved in the continuous phase and can transport to the locus of polymerisation. Upon the addition of a small number of

monomer units to the macro-CTA, nucleation occurs, and monomer-swollen micelles are formed. Importantly, the low solvation of the growing block copolymer chains hinders the formation of higher-order nanoparticle morphologies during polymerisation and typically only kinetically trapped spheres are obtained *via* RAFT emulsion polymerisation.[7,332,333]

Sulfonate functional groups are frequently present in biologically important macromolecules, which can have potential antibacterial applications,[334,335] and can also be used to modify the growth of inorganic crystals.[336] Thus, the preparation of sulfonate-functional nanoparticles with tuneable sizes and controllable surface chemistries is of great interest. Sulfopropyl methacrylate potassium salt (KSPMA) is a commercially available monomer, which has also been used in previous PISA formulations.[235,337,338] For example, Ma *et al.*[235] prepared poly(potassium 3-sulfopropyl methacrylate)-poly(benzyl methacrylate) (PKSPMA–PBzMA) diblock copolymer nanoparticles *via* RAFT aqueous emulsion polymerisation. Spherical nanoparticles with small diameters (56 nm) were obtained but DLS reported relatively high polydispersity indexes for these particles, which indicates relatively poor control over the PISA process was achieved.

Typically, either a dispersion or emulsion polymerisation formulation is used to probe the assembly of nanoparticles during PISA. This is often achieved by varying the DP of the macro-CTA or core-forming block,[233,339-341] by changing the copolymer concentration[233,339-341] or by varying the macro-CTA chemistry (e.g. using statistical copolymerisation[29,342] or 'mixed macro-CTA' approach[11,343]). However, only a few studies have investigated the role of solvent quality during PISA,[2,344] and there are relatively few detailed investigations of PISA in the intermediate conditions between emulsion and dispersion polymerisation.

Recently, Ning *et al.*[252] prepared poly(ammonium 2-sulfatoethyl methacrylate)-poly(benzyl methacrylate) (PSEM–PBzMA) *via* RAFT aqueous emulsion polymerisation and dispersion polymerisation in a 2:1 v/v ethanol/water mixture. Spherical nanoparticles were obtained in both cases. The nanoparticles synthesised *via* RAFT dispersion polymerisation were significantly larger (80–126 nm versus 31–36 nm) and had higher mean aggregation numbers (1200–4100 versus 40–70) than those prepared *via* aqueous emulsion polymerisation.

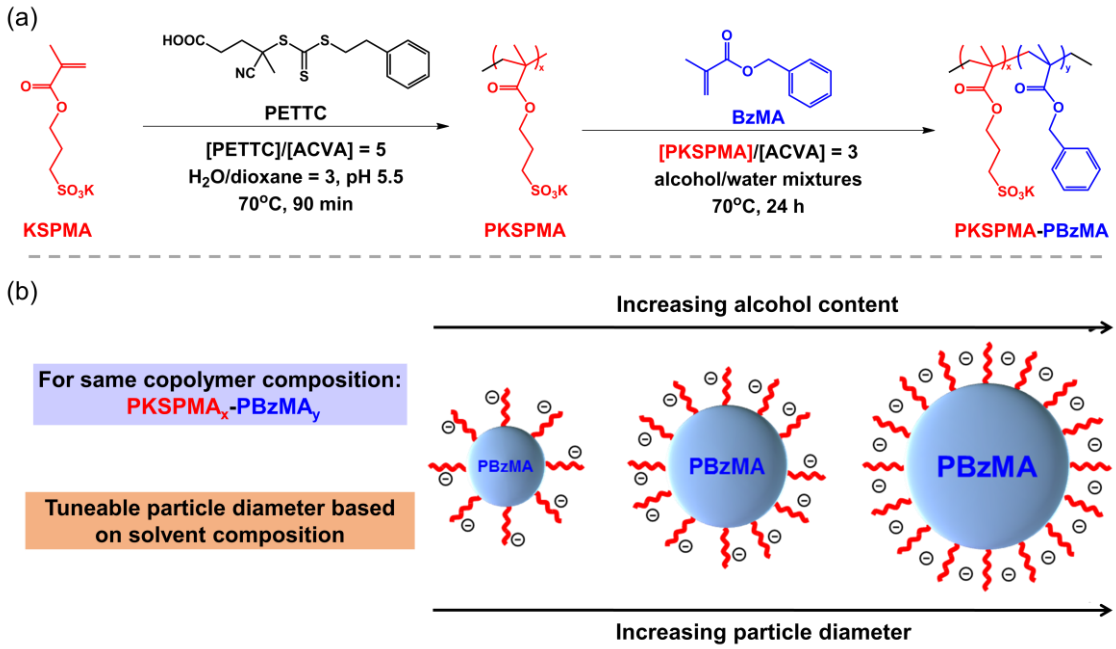

Scheme 2.1. (a) Synthesis of poly(potassium 3-sulfopropyl methacrylate) (PKSPMA) macro-CTA *via* RAFT solution polymerisation at 70 °C (15% w/w, pH 5.5), followed by RAFT-mediated PISA of benzyl methacrylate (BzMA) in alcohol/water mixtures at 70 °C (10% w/w). (b) Schematic representation of how solvent quality affects the resulting nanoparticle diameter for a fixed target PKSPMA–PBzMA copolymer composition.

Herein, the preparation of amphiphilic diblock copolymer nanoparticles in alcohol/water mixtures is reported. More specifically, a series of PKSPMA–PBzMA nanoparticles have been prepared by systematically adjusting the alcohol/water ratio of the continuous phase (**Scheme 2.1**). This has allowed the knowledge of the rules, which govern nanoparticle formation during PISA to be extended. It is demonstrated that nanoparticles with tuneable diameters can be synthesised by altering the co-solvent composition for a fixed stabiliser and/or core-forming block. The resulting nanoparticles were characterised *via* DLS, TEM, SAXS and aqueous electrophoresis. Moreover, the colloidal stability and the ability to redisperse these nanoparticles from a dried state is demonstrated. For the sake of brevity, a shorthand label is used throughout this chapter: PKSPMA and PBzMA or “S” and “B” are utilised to denote the two blocks, respectively.

2.2. Experimental details

2.2.1. Materials

Potassium 3-sulfopropyl methacrylate salt (KSPMA, 98%) and 4,4'-azobis(4-cyanovaleric acid) (ACVA, 99%), sodium hydride (60% dispersion in mineral oil), carbon disulphide (≥99.9%), 2-phenylethanethiol (98%), iodine (≥99%), ethyl acetate (≥99.5%) and diethyl ether (≥99.7%) were purchased from Sigma-Aldrich (UK) and used as received. Benzyl methacrylate (98%) was purchased from Alfa Aesar (UK) and passed through a column of activated basic alumina to remove inhibitors and impurities before use. 1,4-Dioxane was purchased from Honeywell (UK) and used as received. Deuterium oxide (D_2O) and chloroform-*d* ($CDCl_3$) used for NMR studies were purchased from Cambridge Isotope Laboratories (UK). Petroleum ether (36 °C to 60 °C), methanol (99.9%) and ethanol (95%) were purchased from Fisher Scientific (UK) and used as received. 4-Cyano-4-(2-phenylethane sulfanylthiocarbonyl) sulfanylpentanoic acid (PETTC) was prepared in-house.[337] Dialysis tubing (regenerated cellulose, molecular weight cut off (MWCO) = 3.5 kDa and diameter = 29 mm) was received from Fisher Scientific. Deionised water was used in all experiments.

2.2.2. Synthesis of 4-cyano-4-(2-phenylethane sulfanylthiocarbonyl) sulfanylpentanoic acid (PETTC)

The synthesis of the 4-cyano-4-(2-phenylethane sulfanylthiocarbonyl) sulfanylpentanoic acid (PETTC) RAFT agent was conducted according to a modified procedure described by Semsarilar *et al.*[337] The synthetic scheme for the preparation of PETTC chain transfer agent is presented in **Scheme A.1**. Sodium hydride (60% in oil, 3.0 g, 76 mmol) was gradually added to diethyl ether (150 mL) at 5 °C to obtain a grey suspension. 2-Phenylethanethiol (10.0 g, 72 mmol) was added dropwise to the grey suspension and hydrogen gas was observed. A white viscous slurry of sodium phenylethanethiolate formed over a 30 min period. Carbon disulfide (5.8 g, 76 mmol) was added dropwise to the reaction mixture and slowly transformed into a thick yellow precipitate of sodium 2-phenylethanetrithiocarbonate over 30 min. The precipitate was collected by filtration and subsequently used in the next step without further purification. Sodium 2-phenylethanetrithiocarbonate (15.6 g, 66 mmol) was gradually added to

diethyl ether (150 mL) at room temperature to obtain a suspension and then solid iodine (8.8 g, 35 mmol) was added. The reaction mixture was stirred at room temperature for 1 hour and an insoluble white precipitate of sodium iodide was formed and removed by filtration. The yellow−brown filtrate was washed with a sodium thiosulfate aqueous solution to remove excess iodine (three 150 mL portions) and dried over sodium sulfate to remove residual water. The filtrate was further dried under vacuum to evaporate volatiles, and yield bis(2-phenylethane sulfanylthiocarbonyl) disulfide.

A solution of bis(2-phenylethane sulfanylthiocarbonyl) disulfide (9.4 g, 22 mmol) and 4,4'-azobis(4-cyanovaleric acid) (ACVA, 9.3 g, 33 mmol) were dissolved in ethyl acetate (200 mL) and deoxygenated with nitrogen for 30 min. This reaction mixture was immersed in an oil bath at 82 °C and reacted for 18 h under nitrogen. The organic phase was evaporated under vacuum and the crude product was purified by silica chromatography using a mixed eluent (7:3 petroleum ether/ethyl acetate, gradually increasing to 3:7) to isolate 4-cyano-4-(2-phenylethane sulfanylthiocarbonyl) sulfanylpentanoic acid (PETTC) as a viscous yellow oil. The purified yellow oil was further dried under vacuum to obtain a yellow solid (12.1 g, 78% yield).

^{1}H NMR (400 MHz, $CDCl_3$, **Figure A.1**): 7.18−7.36 (m, 5H, aromatic), 3.54-3.62 (t, 2H, $-CH_2$), 2.95-3.04 (t, 2H, $-CH_2$), 2.63-2.75 (t, 2H, $-CH_2$), 2.35−2.60 (m, 2H, $-CH_2$), δ 1.89 (3H, $-CH_3$). ^{13}C NMR (400 MHz, $CDCl_3$): 216.28 (C=S), 176.25 (C=O), 126.75, 128.45, 139.02, 139.02 (Ph), 118.71 (CN), 46.21 ($SCCH_2$), 37.85 (SCH_2CH_2Ph), 33.93 (CH_2CH_2COOH), 33.38 (CH_2Ph), 29.26 (CH_2CH_2COOH), δ 24.74 (CH_3).

2.2.3. Synthesis of poly(potassium 3-sulfopropyl methacrylate) macro-CTA *via* RAFT solution polymerisation

The synthesis of poly(potassium 3-sulfopropyl methacrylate) (PKSPMA) macro-CTAs has been described in detail elsewhere.[235,337] In a typical protocol for the synthesis of $PKSPMA_{30}$, a round-bottomed flask was charged with KSPMA (15.0 g, 60.9 mmol), PETTC (689.1 mg, 2.0 mmol, dissolved in dioxane), ACVA (113.8 mg, 0.4 mmol, PETTC/ACVA molar ratio = 5) and pH 5.5 acetate buffer (66.6 g, final buffer/dioxane ratio = 3). The sealed reaction vessel was deoxygenated with nitrogen for 30 min and placed in a preheated oil bath at 70 °C for 90 min (or 120 min for $PKSPMA_{50}$).

The resulting PKSPMA macro-CTA was purified by dialysis against 10:1 water/methanol and isolated under vacuum overnight.

2.2.4. Synthesis of PKSPMA–PBzMA diblock copolymer nanoparticles

A typical protocol for the synthesis of $PKSPMA_x$–$PBzMA_y$ (S_x–B_y) diblock copolymer nanoparticles at 10% w/w solids in alcohol/water mixtures was as follows. For $PKSPMA_{32}$–$PBzMA_{100}$ synthesised in methanol/water, BzMA (215.3 mg, 1.220 mmol), $PKSPMA_{32}$ macro-CTA (85.2 mg, 0.012 mmol), ACVA (1.1 mg, 0.004 mmol, CTA/initiator molar ratio = 3) and methanol/water (2.7 g) were weighed into a 14 mL vial. The vial was sealed and purged with nitrogen for 10 min before being placed in a preheated oil bath at 70 °C for 24 h to ensure complete conversion of BzMA. Polymerisations were quenched by cooling to room temperature and opening to air. Monomer conversions were determined *via* gravimetry by drying approximately 0.1 g of the final dispersion at 80 °C until constant weight. In subsequent syntheses, the DP of the two blocks and the solvent was varied using methanol/water and ethanol/water mixtures, using the procedure described above. Unfortunately, GPC and NMR cannot readily be utilised to characterise S_x–B_y diblock copolymers as no suitable solvents were available due to the highly amphiphilic nature of these block copolymers. Thus, a relatively low CTA/initiator ratio of 3 was used during the synthesis of these copolymers. This ensured high BzMA conversions (>99% in all cases, as judged by gravimetry of the final reaction dispersion) and is consistent with prior literature on related PISA formulations.[252,345]

2.2.5. Characterisation

2.2.5.1. Nuclear magnetic resonance spectroscopy

Proton (^{1}H) and carbon (^{13}C) nuclear magnetic resonance (NMR) spectra were acquired on a Bruker Advance III 400 MHz spectrometer with 128 scans averaged per spectrum. Samples were dissolved in either D_2O or $CDCl_3$ prior to NMR analysis.

2.2.5.2. Aqueous gel permeation chromatography

Molar masses and molar mass distributions of PKSPMA macro-CTA were determined using an aqueous gel permeation chromatography (GPC) equipped with two PL aquagel-OH MIXED-H 8 µm columns at ambient temperature. Phosphate buffer at

pH 9 with 30% v/v methanol was used as an eluent at a flow rate of 1.0 mL min^{-1}. A refractive index detector (Shodex RI-101) was used and the system was calibrated with a series of near-monodisperse poly(ethylene oxide) standards (ranging from 1.0×10^2 to 1.3×10^6 g mol^{-1}).

2.2.5.3. Dynamic light scattering

Dynamic light scattering (DLS) studies were performed using a Malvern Zetasizer Nano ZS instrument equipped with a He–Ne solid-state laser operating at 633 nm and back-scattered light at a scattering angle of 173°. Copolymer dispersions were diluted to approximately 0.1% w/w using the same alcohol/water mixture used during the synthesis of the particles. DLS samples were analysed at 25 °C using disposable plastic cuvettes and data were averaged over three consecutive measurements. The parameters for calculating hydrodynamic diameters (D_h) were obtained by fitting literature values of reflective index,[346] viscosity[347] and dielectric constant[348] (**Table 2.1**).

Table 2.1. Summary of viscosity, refractive index and dielectric constant values of methanol/water mixtures at 25 °C for DLS hydrodynamic diameter calculations. All parameters were obtained by fitting literature data.[346-348]

Mixture type	Alcohol content / %	Viscosity / cp	Refractive index	Dielectric constant
methanol/water	20	1.394	1.337	69.21
methanol/water	33	1.565	1.339	62.82
methanol/water	50	1.524	1.340	54.78
methanol/water	67	1.269	1.339	46.71
methanol/water	80	0.994	1.336	40.24
ethanol/water	20	1.808	1.344	67.01
ethanol/water	33	2.257	1.351	59.06
ethanol/water	50	2.386	1.357	49.15

2.2.5.4. Aqueous electrophoresis

Aqueous electrophoresis studies for the diblock copolymer nanoparticles were analysed using the same Malvern Zetasizer Nano ZS instrument described above. The solution pH was initially adjusted to 10 using 0.1 M KOH in the presence of 1.0 mM KCl. The solution pH was then manually lowered from 10 to 4 using 0.1 M HCl as required. Aqueous dispersions (approximately 0.1% w/w) were analysed at 25 °C using disposable folded capillary cell (Malvern DTS1017) and data were averaged over three consecutive measurements.

2.2.5.5. Transmission electron microscopy

Transmission electron microscopy (TEM) images were recorded using a Philips CM 20 instrument operating at an accelerating voltage of 200 kV and connected to a Gatan 1k CCD camera. Samples for TEM observations were prepared by depositing 3 µL of diluted copolymer dispersion onto 400 mesh carbon-coated copper grids for 30 min and then carefully blotted with filter paper to remove excess solution. The samples were stained in the vapour space above ruthenium tetroxide (RuO_4) solution for 7 min at room temperature.[349] Mean nanoparticle diameters were determined by ImageJ software and over 200 randomly selected particles were measured for each sample.

2.2.5.6. Small-angle X-ray scattering

Small-angle X-ray scattering (SAXS) patterns were collected in batch mode on beamline B21 at the Diamond Light Source synchrotron facility (Didcot, UK). Data were recorded at 13.1 keV (wavelength 0.0946 nm), at a sample-detector distance of 2694.2 mm using an Eiger 4 M detector. This corresponds to a scattering vector (q) range from 0.0032 to 0.38 $Å^{-1}$, where $q = 4\pi \sin\theta/\lambda$, θ is a half of the scattering angle and λ is the wavelength of X-ray radiation. SAXS samples were prepared using copolymer dispersions diluted with the corresponding alcohol/water mixture to 1.0% w/w. All samples and solvents were loaded into a 96-well plate, and 30 µL of each sample was sequentially injected into a temperature-controlled quartz capillary (10 µm thick) using the BioSAXS robot (designed by the EMBL in Grenoble). The X-ray scattering data were analysed (i.e. averaged, background subtraction, data modelling and fitting) using Irena SAS macros for Igor Pro.[350] Structural parameters were determined by fitting 1D SAXS

patterns using a two-population model of spherical micelles[351] plus Gaussian polymer chains[341] with related fitting parameters shown in **Table 2.2** This approach enabled the determination of structural parameters for the nanoparticles, such as the radius of gyration of the stabiliser chains (R_g), mean radius of core (R_{core}), solvent fraction in the core (X_{sol}), mean aggregation number (N_{agg}) and average number of copolymer chains per unit surface area (S_{agg}).

Table 2.2. Summary of fitting parameters used for modelling SAXS data obtained for $PKSPMA_x$–$PBzMA_y$ nanoparticles. SAXS data were fitted using a two-population spherical micelles[351] plus Gaussian polymer chains[341] model.

X-ray scattering length density (ξ) of polymers[a] / x 10^{10} cm^{-2}		
PKSPMA		11.69
PBzMA		10.71
X-ray scattering length density (ξ) of alcohol/water mixtures[a]		
Mixture type	**Alcohol content / %**	**ξ / x 10^{10} cm^{-2}**
Ethanol/water	33	8.80
	50	8.49
Methanol/water	20	9.05
	33	8.80
	50	8.49
	67	8.17
Calculated volume of polymer chains		
Polymer Chain	**DP**	**V / Å^3**
PKSPMA	32	8470
	53	14029
PBzMA (V_{co})	100	24819
	300	74456
	500	124093
	700	173730
	1000	248185

[a] X-ray scattering length densities were calculated using programming tools within Irena SAS macros for Igor Pro 7. Density values used in these calculations were taken as ρ_{PKSPMA} = 1.300 g cm^{-3}, ρ_{PBzMA} = 1.179 g cm^{-3}, ρ_{Water} = 1.000 g cm^{-3}, $\rho_{Ethanol}$ = 0.789 g cm^{-3}, $\rho_{Methanol}$ = 0.792 g cm^{-3}.

2.3. Results and discussion

2.3.1. Synthesis of PKSPMA macro-CTAs

RAFT solution polymerisation of KSPMA was conducted in 3:1 water/dioxane at 70 °C (**Scheme 2.1**). The DP for PKSPMA macro-CTA was calculated from ^{1}H NMR spectra (**Figure 2.1**) by comparing the integrated proton signals corresponding to the methacrylic polymer backbone at 0.4–2.2 ppm with those corresponding to the aromatic protons of the PETTC chain end at 7.2–7.4 ppm. The calculated DPs for the targeted $PKSPMA_{30}$ and $PKSPMA_{50}$ macro-CTAs were 32 and 53, respectively. **Figure 2.2a** and **Figure 2.3a** show conversion and semi-logarithmic kinetics versus reaction time for $PKSPMA_{32}$ and $PKSPMA_{53}$. Approximately 90% conversion was achieved in both cases and the approximately linear relationship between $\ln([M]_0/[M])$ and reaction time indicated the polymerisation was first-order with respect to monomer concentration.[29]

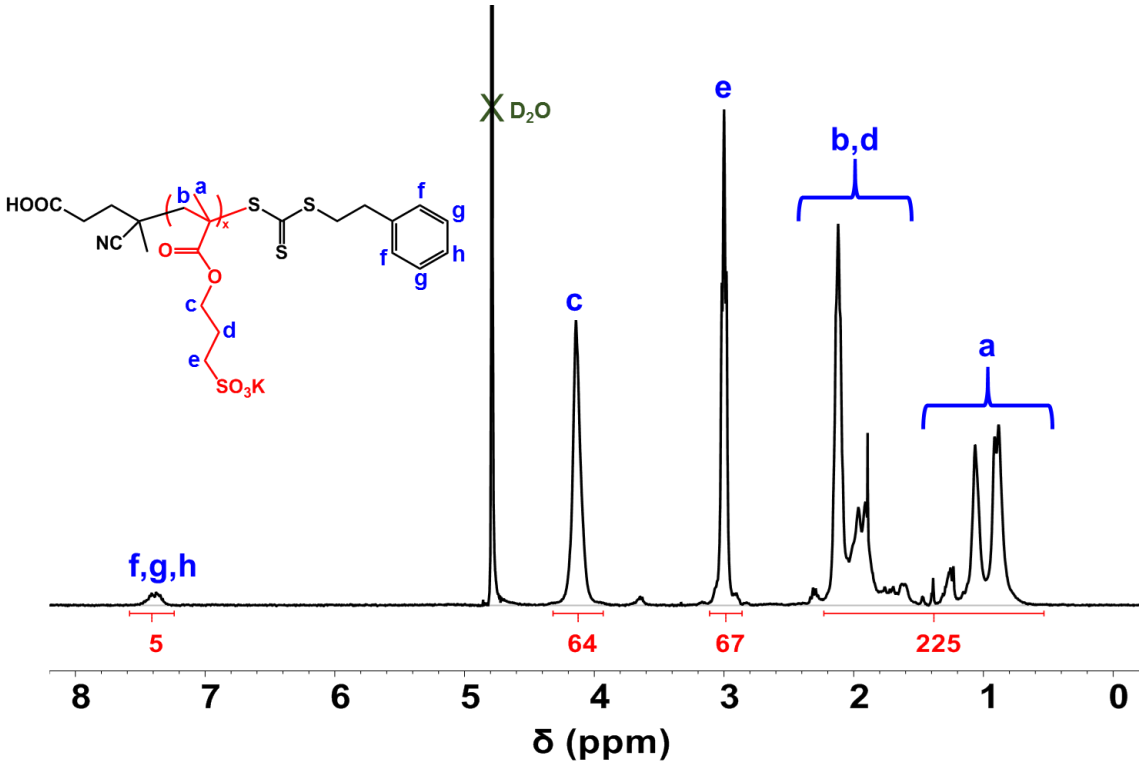

Figure 2.1. ^{1}H NMR spectra of a purified and freeze-dried $PKSPMA_{32}$ macro-CTA. The sample was dissolved in D_2O prior to analysis. The degree of polymerisation (DP) for this macro-CTA was calculated by comparing the integrated proton signals corresponding to the methacrylic polymer backbone at 0.4-2.2 ppm (a,b,d) with that corresponding to the aromatic protons of PETTC chain end at 7.2-7.4 ppm (f,g,h).

It is noteworthy that all GPC chromatograms of samples taken during the preparation of $PKSPMA_{32}$ and $PKSPMA_{53}$ were unimodal and successively shifted to shorter retention times (**Figure 2.2c** and **Figure 2.3.c**). The evolution of molar mass and molar mass dispersity (M_w/M_n) versus monomer conversion for $PKSPMA_{32}$ and $PKSPMA_{53}$ are shown in **Figure 2.2b** and **Figure 2.3b**. As the polymerisations progressed, the corresponding dispersities decreased, and the resulting macro-CTAs had relatively narrow molar mass distributions ($M_w/M_n < 1.13$) at 90% conversion.

The blocking efficiency of the PKSPMA macro-CTAs were examined by self-blocking experiments (**Figure 2.4**). Briefly, addition of a further charge of KSPMA (target DP 300) led to chain extension. GPC analysis of the resulting chain-extended homopolymer confirmed unimodal distributions and relatively low molar mass dispersities ($M_w/M_n < 1.26$) in both cases. This indicates that these macro-CTAs are likely undergo efficient chain extension to form second blocks with other monomers, as desired.[345,352]

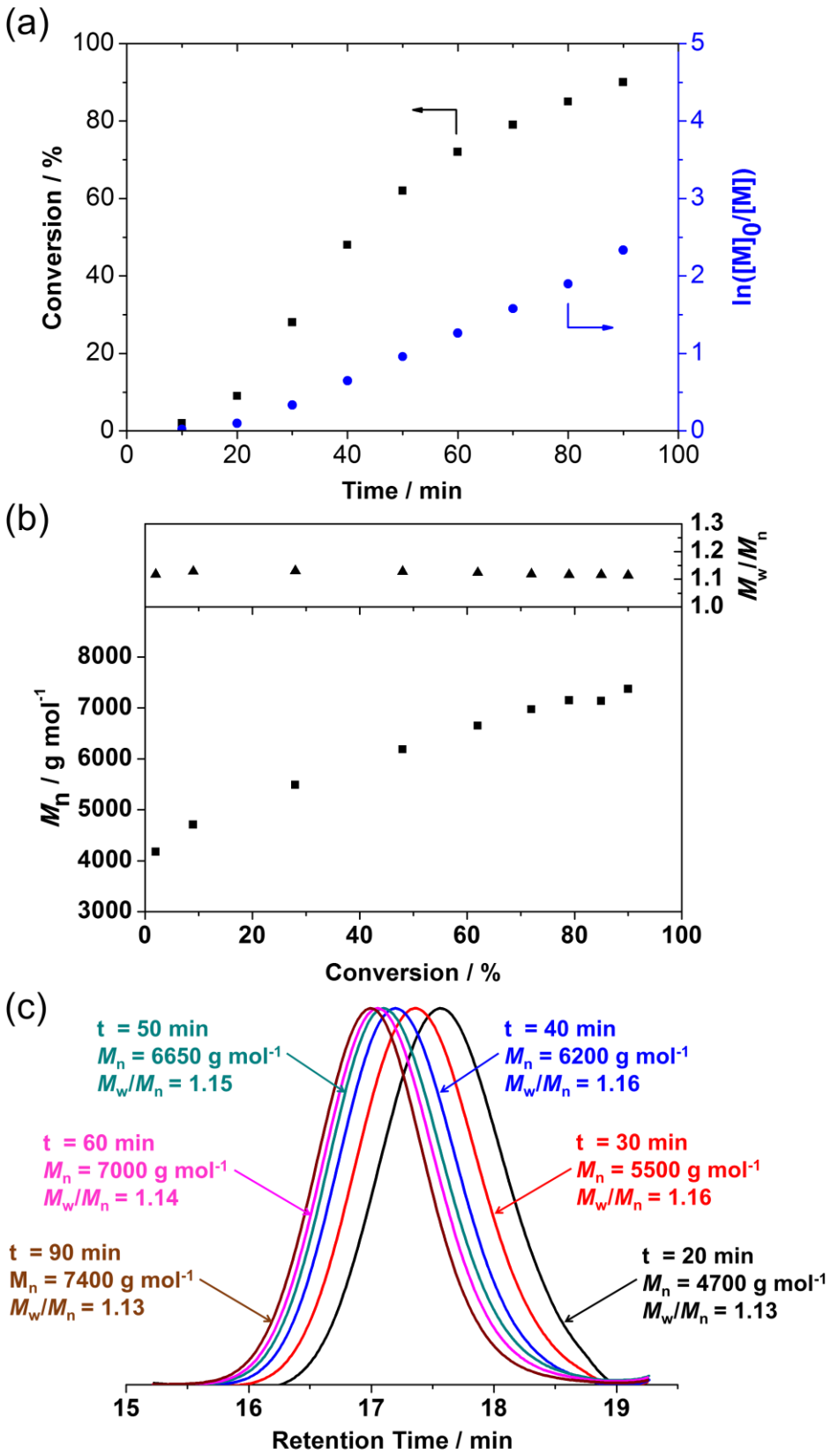

Figure 2.2. Kinetic studies for RAFT solution polymerisation of KSPMA (target DP 30) with PETTC as a CTA in 3:1 water/dioxane at 70 °C: (a) conversion and semi-logarithmic kinetics versus reaction time, (b) M_w/M_n and M_n versus monomer conversion and (c) aqueous GPC chromatograms.

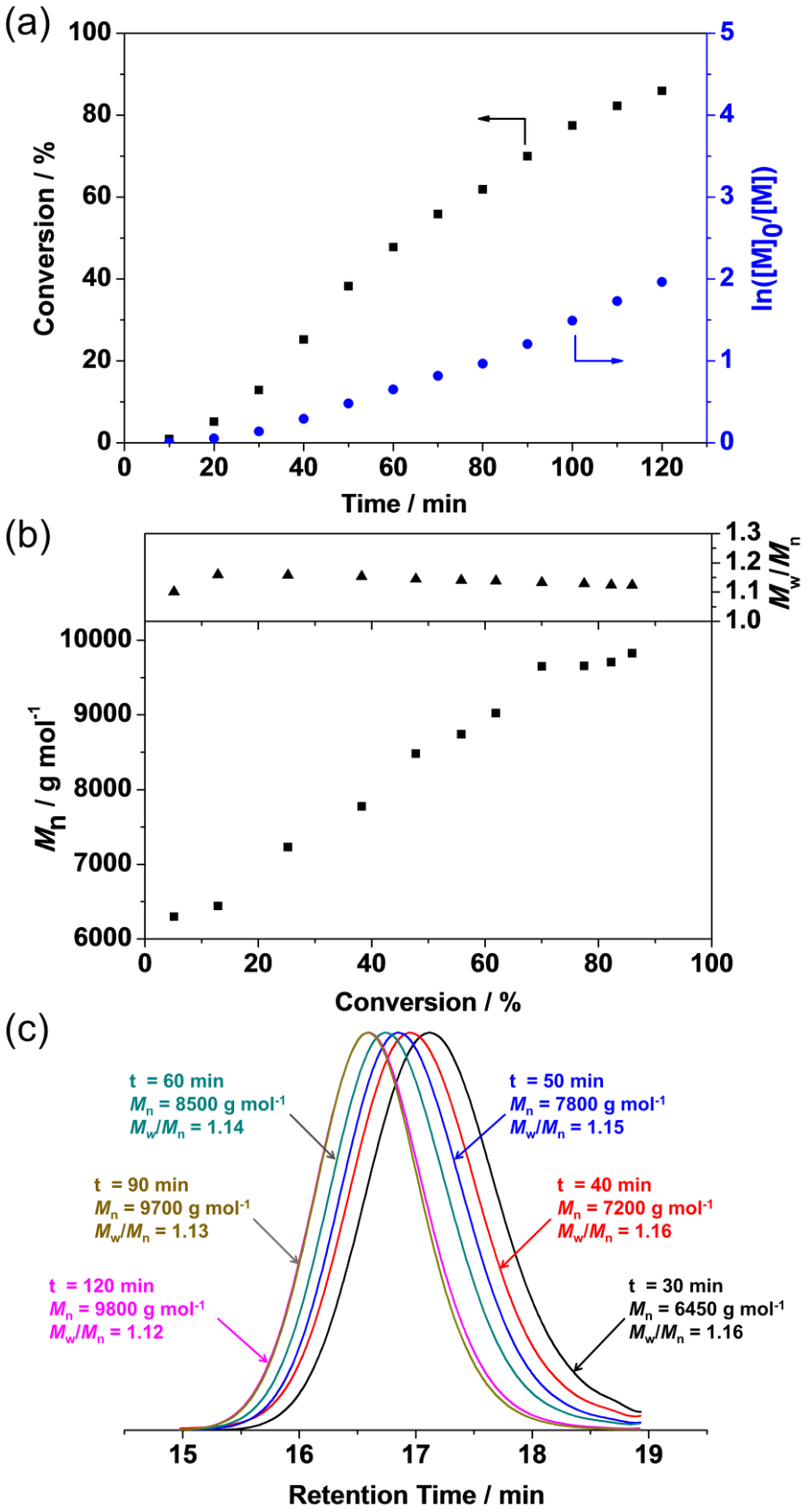

Figure 2.3. Kinetic studies for RAFT solution polymerisation of KSPMA (target DP 50) with PETTC as a CTA in 3:1 water/dioxane at 70 °C: (a) conversion and semi-logarithmic kinetics versus reaction time, (b) M_w/M_n and M_n versus monomer conversion and (c) aqueous GPC chromatograms.

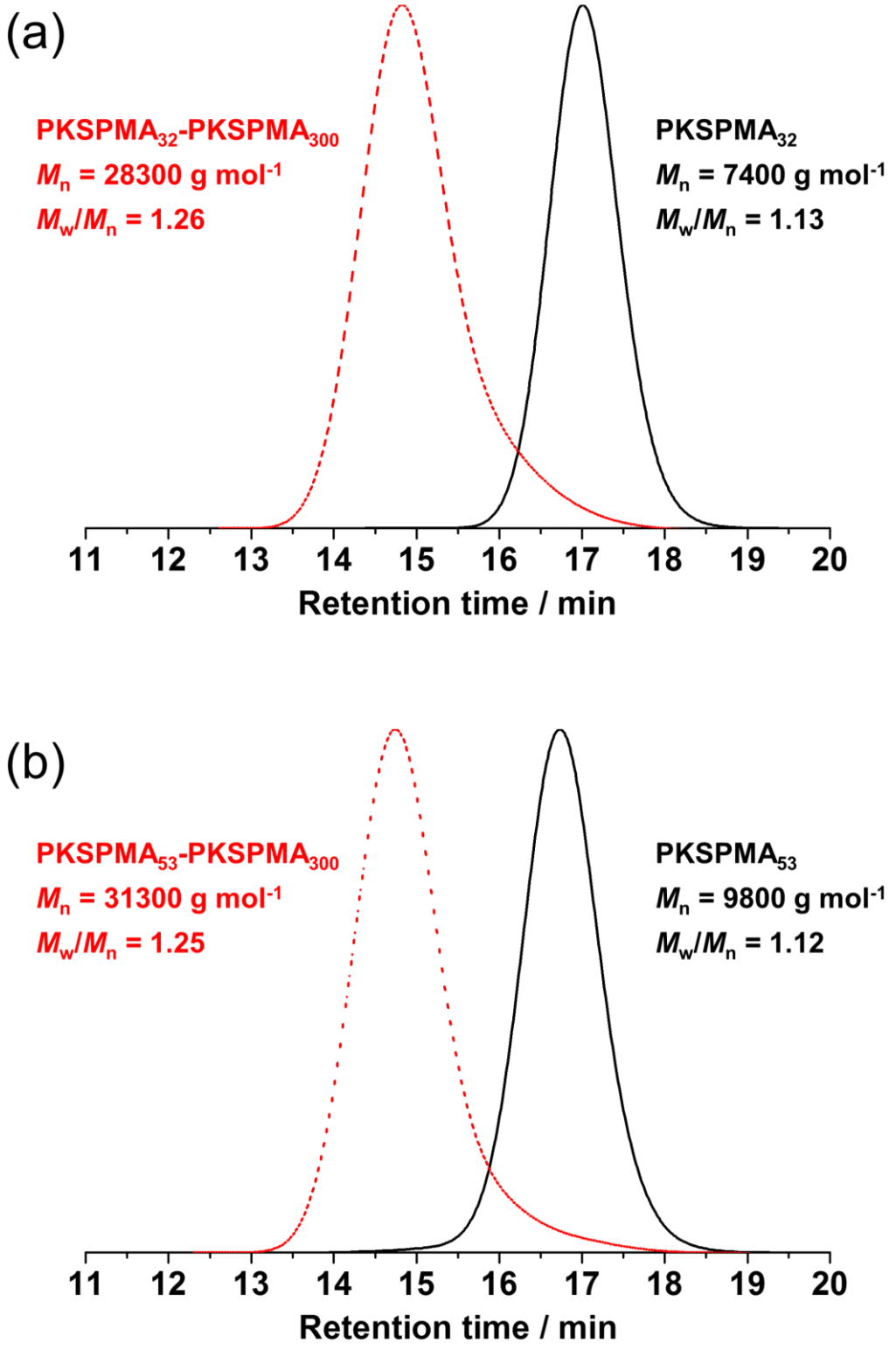

Figure 2.4. Aqueous GPC chromatograms obtained for (a) $PKSPMA_{32}$ and (b) $PKSPMA_{53}$ macro-CTAs and their subsequent chain extension *via* RAFT aqueous solution polymerisation using KSPMA at 70 °C (15% w/w, target DP of second block = 300).

2.3.2. Preparation of PKSPMA–PBzMA nanoparticles in various alcohol/water mixtures

Sulfonate-functional nanoparticles were prepared *via* RAFT mediated PISA in various alcohol/water mixtures. The synthesis of related anionic sterically-stabilised nanoparticles have been conducted *via* RAFT aqueous emulsion polymerisation[235] or RAFT alcoholic dispersion polymerisation.[25] In this work, the core-forming monomer, BzMA, is soluble in alcohol-rich solvent compositions whereas the PKSPMA stabiliser is soluble in water-rich solvent mixtures (**Figure 2.5**). For example, BzMA dissolves at ethanol contents >70% w/w, but visible phase separation occurs at water contents >30% w/w. In contrast, PKSPMA cannot dissolve when the ethanol content is higher than approximately 70% w/w (or ~85% w/w for methanol/water mixtures). Importantly, PBzMA is insoluble in all solvent combinations reported herein.[250] Thus, in this work, PISA at intermediate solvent compositions between wholly aqueous emulsion and alcoholic dispersion polymerisation conditions has been investigated. $PKSPMA_x$–$PBzMA_y$ nanoparticles were therefore prepared under various intermediate alcohol/water mixtures as a mechanism of probing the effect of solvent quality on the particle diameter, morphology and composition of the resulting nanoparticles (**Scheme 2.1**, **Table 2.3** and **Table 2.4**).

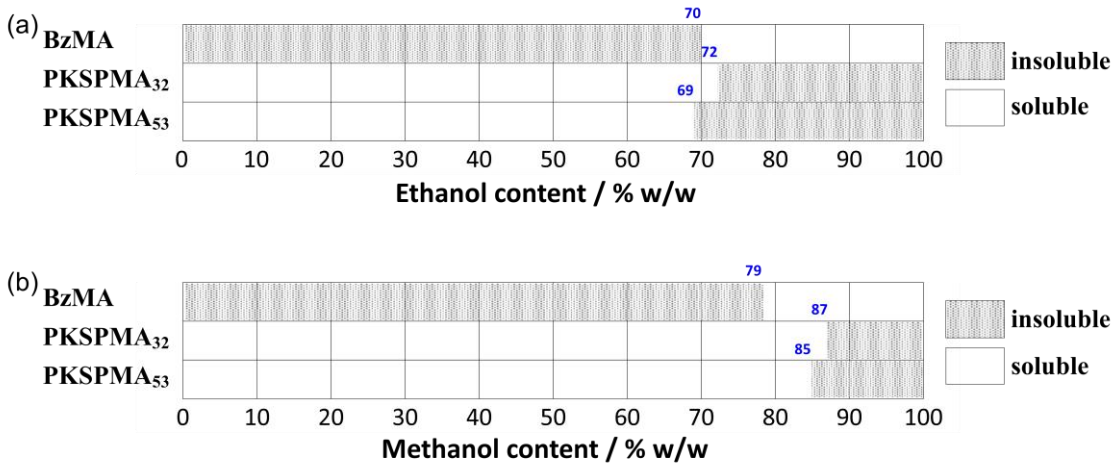

Figure 2.5. Solubility of BzMA, $PKSPMA_{32}$ and $PKSPMA_{53}$ in (a) ethanol/water mixtures and (b) methanol/water mixtures. Solubility tests were conducted at 21 °C and at concentrations of 0.3 g mL^{-1} and 5 mg mL^{-1} for BzMA and $PKSPMA_x$, respectively.

Table 2.3. Summary of target composition, methanol content and mean diameters obtained for PKSPMA$_x$–PBzMA$_y$ (S_x–B_y) diblock copolymer nanoparticles synthesised at 10% w/w solids *via* RAFT-mediated polymerisation in methanol/water mixtures.

Entry	Target[a] S_x–B_y	Methanol content /%w/w	DLS		TEM	SAXS
			$D_{h,\ water}$[b] / nm	$D_{h,\ MeOH/water}$[c] / nm	D_{TEM}[d] / nm	D_{SAXS}[e] / nm
1	S_{32}–B_{100}	0	21 (0.431)	21 (0.431)		
2	S_{32}–B_{100}	20	23 (0.340)	23 (0.317)		
3	S_{32}–B_{100}	33	33 (0.154)	30 (0.169)	23 ± 4	29 ± 3
4	S_{32}–B_{100}	50	93 (0.036)	85 (0.026)	43 ± 7	70 ± 9
5	S_{32}–B_{100}	67	97 (0.026)	88 (0.020)	66 ± 6	73 ± 8
6	S_{32}–B_{300}	0	40 (0.435)	40 (0.435)		
7	S_{32}–B_{300}	20	48 (0.192)	42 (0.214)	25 ± 2	40 ± 5
8	S_{32}–B_{300}	33	96 (0.053)	86 (0.030)	52 ± 5	74 ± 6
9	S_{32}–B_{300}	50	192 (0.018)	181 (0.061)	147 ± 14	161 ± 9
10	S_{32}–B_{300}	67	211 (0.016)	204 (0.021)	159 ± 12	179 ± 8
11	S_{32}–B_{300}	80	197 (0.063)	181 (0.048)	194 ± 17	
12	S_{53}–B_{100}	0	24 (0.266)	24 (0.266)		
13	S_{53}–B_{100}	20	26 (0.302)	24 (0.377)		
14	S_{53}–B_{100}	33	31 (0.237)	30 (0.228)		
15	S_{53}–B_{100}	50	100 (0.065)	76 (0.049)	60 ± 6	70 ± 10
16	S_{53}–B_{100}	67	114 (0.364)	89 (0.037)		43 ± 6
17	S_{53}–B_{300}	0	39 (0.270)	39 (0.270)		
18	S_{53}–B_{300}	20	57 (0.164)	46 (0.173)	31 ± 4	39 ± 5
19	S_{53}–B_{300}	33	89 (0.052)	78 (0.066)	51 ± 7	62 ± 9
20	S_{53}–B_{300}	50	131 (0.070)	119 (0.077)	59 ± 6	65 ± 6
21	S_{53}–B_{300}	67	174 (0.014)	164 (0.021)	130 ± 13	147 ± 8
22	S_{53}–B_{300}	80	165 (0.016)	181 (0.086)	145 ± 14	
23	S_{32}–B_{500}	33	119 (0.014)	113 (0.017)	81 ± 8	101 ± 8
24	S_{32}–B_{700}	33	158 (0.017)	150 (0.035)	92 ± 11	131 ± 11

[a] All conversions were determined to be >99% *via* gravimetry thus the target composition is assumed to be the actual obtained copolymer composition. [b] DLS analysis using water as dispersant. DLS polydispersity index vales are indicated in brackets. [c] DLS analysis using methanol/water mixtures corresponding to the synthetic conditions. DLS polydispersity index vales are indicated in brackets. [d] Mean TEM particle diameters were calculated by analysing 200 particles using ImageJ software. [e] SAXS diameters were calculated using $D_{SAXS} = 2R_{core} + 4R_g$.

Table 2.4. Summary of target composition, ethanol content and mean diameters obtained for PKSPMA$_x$–PBzMA$_y$ (S_x–B_y) diblock copolymer nanoparticles synthesised at 10% w/w *via* RAFT-mediated polymerisation in ethanol/water mixtures.

Entry	Target[a] S_x–B_y	Ethanol content /%w/w	DLS		TEM	SAXS
			$D_{h,\ water}$[b] / nm	$D_{h,\ EtOH/water}$[c] / nm	D_{TEM}[d] / nm	D_{SAXS}[e] / nm
1	S_{32}–B_{100}	0	21 (0.431)	21 (0.431)		
2	S_{32}–B_{100}	20	32 (0.243)	28 (0.288)		
3	S_{32}–B_{100}	33	68 (0.051)	61 (0.029)	38 ± 4	52 ± 5
4	S_{32}–B_{100}	50	139 (0.032)	123 (0.071)	113 ± 10	
5	S_{32}–B_{300}	0	40 (0.435)	40 (0.435)		
6	S_{32}–B_{300}	20	71 (0.152)	58 (0.159)	32 ± 4	
7	S_{32}–B_{300}	33	157 (0.011)	150 (0.078)	01 ± 8	132 ± 7
8	S_{32}–B_{300}	50	196 (0.059)	164 (0.057)	156 ± 34	
9	S_{53}–B_{100}	0	24 (0.266)	24 (0.266)		
10	S_{53}–B_{100}	20	26 (0.379)	24 (0.339)		
11	S_{53}–B_{100}	33	64 (0.069)	57 (0.062)	29 ± 3	39 ± 5
12	S_{53}–B_{100}	50	140 (0.055)	122 (0.070)	10 ± 7	
13	S_{53}–B_{300}	0	39 (0.270)	39 (0.270)		
14	S_{53}–B_{300}	20	137 (0.017)	132 (0.043)	119 ± 9	
15	S_{53}–B_{300}	33	173 (0.033)	169 (0.040)	139 ± 13	144 ± 9
16	S_{53}–B_{300}	50	214 (0.016)	194 (0.094)	174 ± 23	
17	S_{32}–B_{500}	33	171 (0.016)	153 (0.053)	112 ± 11	144 ± 6
18	S_{32}–B_{1000}	33	180 (0.024)	135 (0.035)	115 ± 9	141 ± 11

[a] All conversions were determined to be >99% *via* gravimetry thus the target composition is assumed to be the actual obtained copolymer composition. [b] DLS analysis using water as dispersant. DLS polydispersity index vales are indicated in brackets. [c] DLS analysis using ethanol/water mixtures corresponding to the synthetic conditions. DLS polydispersity index vales are indicated in brackets. [d] Mean TEM particle diameters were calculated by analysing 200 particles using ImageJ software. [e] SAXS diameters were calculated using $D_{SAXS} = 2R_{core} + 4R_g$.

Figure 2.6 shows mean hydrodynamic diameters of S_x–B_y particles synthesised in methanol/water and ethanol/water mixtures. In **Figure 2.6a**, the mean particle diameters increased with increasing methanol content. For example, in the S_{32}–B_{300} series, the mean hydrodynamic diameter increased five-fold, from approximately 40 to 200 nm for methanol contents in the range 0 to 67% w/w (entries 6–11, **Table 2.3**). On increasing the methanol content to 80% w/w, the mean particle diameter determined by DLS decreased to 181 nm, whereas the mean diameter calculated from TEM image analysis was 194 nm. This discrepancy is likely due to the PKSPMA stabiliser being close to its solubility limit (**Figure 2.5**). When DLS analysis was conducted on particles transferred to wholly aqueous media, the mean particle diameter was determined to be 197 nm, indicating better solvation of the PKSPMA corona. This observation was consistent across all particles studied (**Table 2.3**). Furthermore, the change in particle diameter for a fixed copolymer composition suggests that solvent quality dramatically affects the PISA process.[353] For instance, in a water rich solvent mixture, the hydrophilic PKSPMA block can stretch easily, but the PBzMA block is constrained significantly due to the relatively high hydrophobicity of PBzMA. This constraint at higher water contents results in the observed smaller particle diameters as the copolymer chains are not solvated and unable to exchange.[251] In contrast, the PBzMA block will be more swollen, and thus occupy more volume during PISA at higher alcohol/water ratios, resulting in the larger particle diameters observed. At methanol contents higher than 67–80% w/w, phase separation occurred and no colloidally stable particles were present in the final dispersion.

For ethanol/water mixtures (**Figure 2.6b**) a similar trend was observed as for methanol/water, i.e. with increasing ethanol content the mean hydrodynamic diameter increased up to an ethanol content of 50% w/w. However, phase separation occurred with ethanol contents higher than 67% w/w. This correlates with the solubility of PKSPMA homopolymer, which is soluble in alcohol/water mixtures up to ~70% w/w ethanol or ~85% w/w methanol (**Figure 2.5**). Thus, at higher ethanol contents, this highly anionic macro-CTA can no longer stabilise the nanoparticles and precipitation occurs during polymerisation.

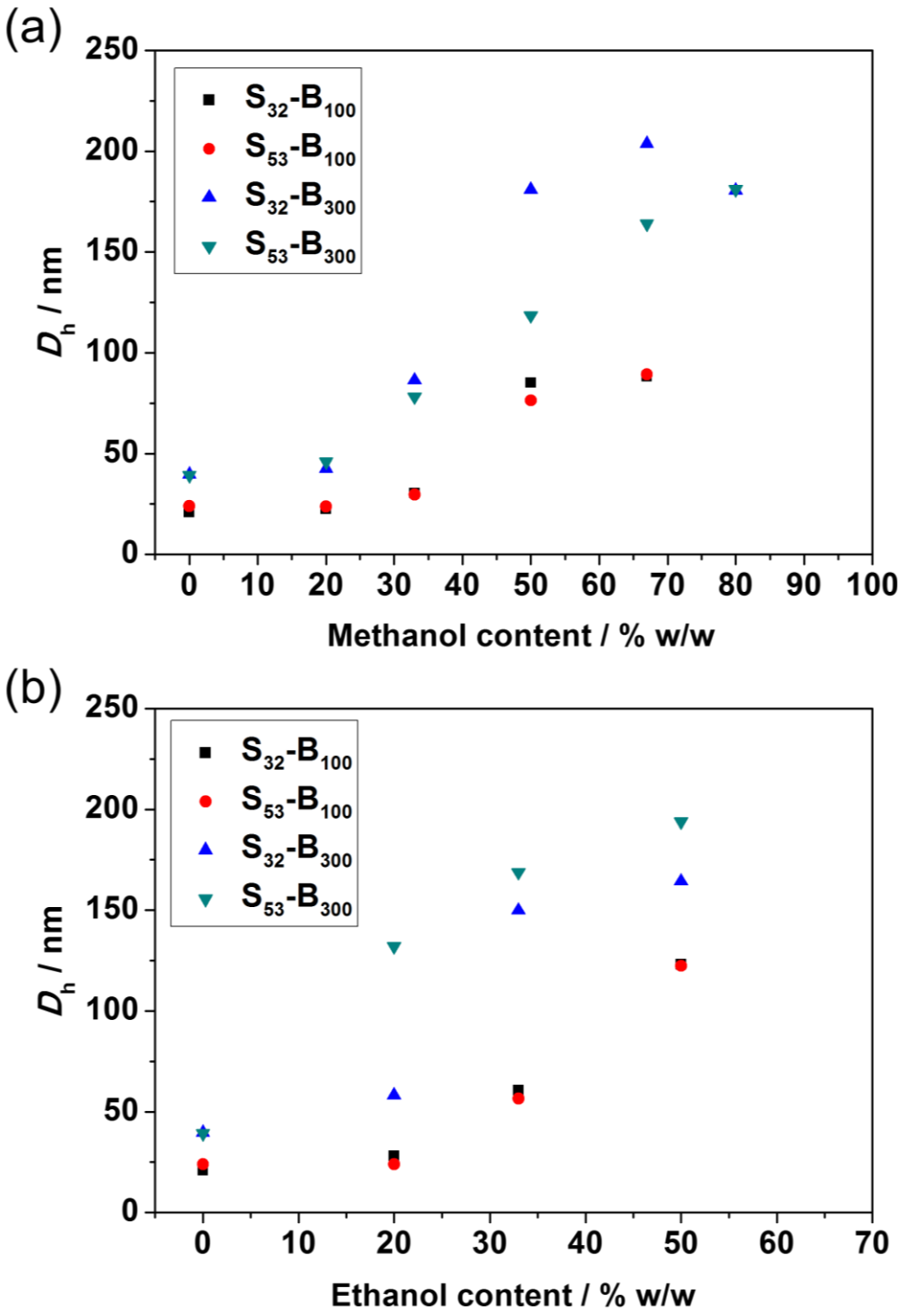

Figure 2.6. Mean hydrodynamic diameters (D_h) of S_x–B_y diblock copolymer nanoparticles synthesised in varying (a) methanol/water and (b) ethanol/water mixtures at 10% w/w solids and 70 °C.

The morphologies of the S_x–B_y diblock copolymer nanoparticles prepared at various ethanol/water (**Figure 2.7** and **Figure A.2**) and methanol/water (**Figure 2.8** and **Figure A.3**) ratios were investigated *via* TEM after staining with RuO_4. This stain highlights the aromatic PBzMA block in these particles,[354] hence some of the images appear to have a distinct core–shell morphology. In all cases, spherical micelles were obtained, with diameters generally in agreement with DLS (**Figure 2.6**, **Table 2.3** and **Table 2.4**). This observation agrees with previous studies, which also only obtained spheres for PKSPMA–PBzMA[235] and PSEM–PBzMA[252] PISA formulations. This is likely due to the highly anionic character of PKSPMA preventing higher order morphology formation.[235,252]

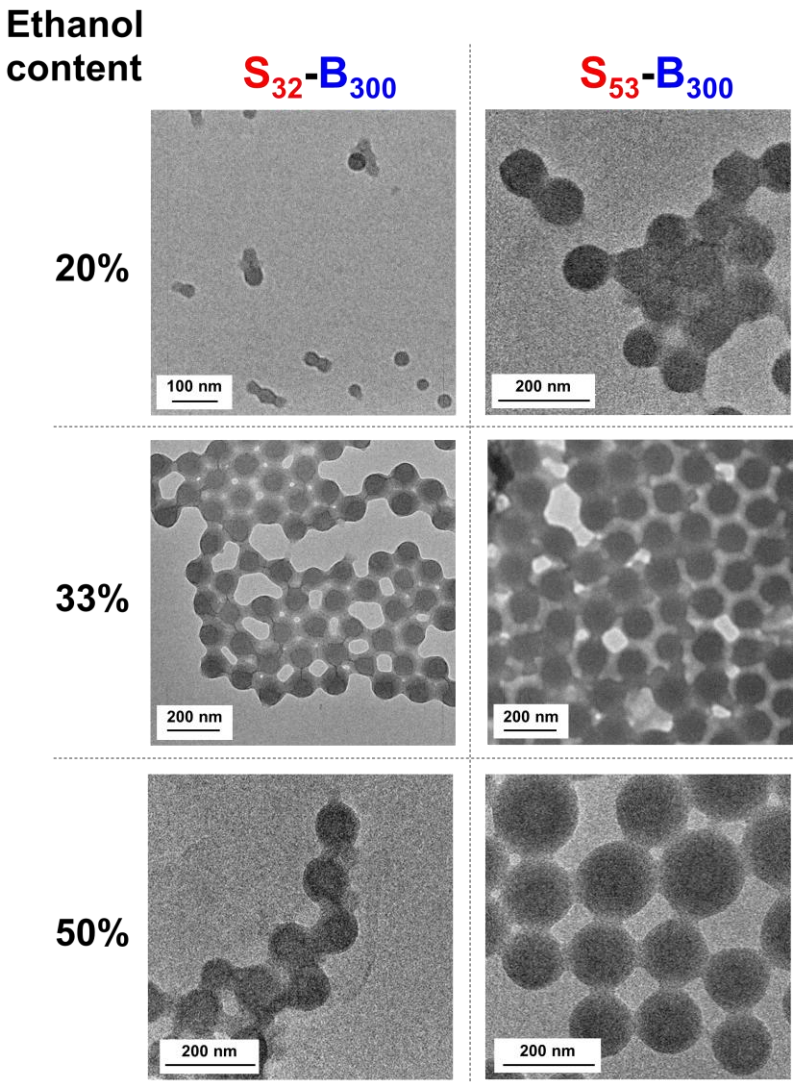

Figure 2.7. Representative TEM images of S_{32}–B_{300} and S_{53}–B_{300} diblock copolymer nanoparticles prepared at 10% w/w solids *via* RAFT-mediated PISA in ethanol/water mixtures at 70 °C.

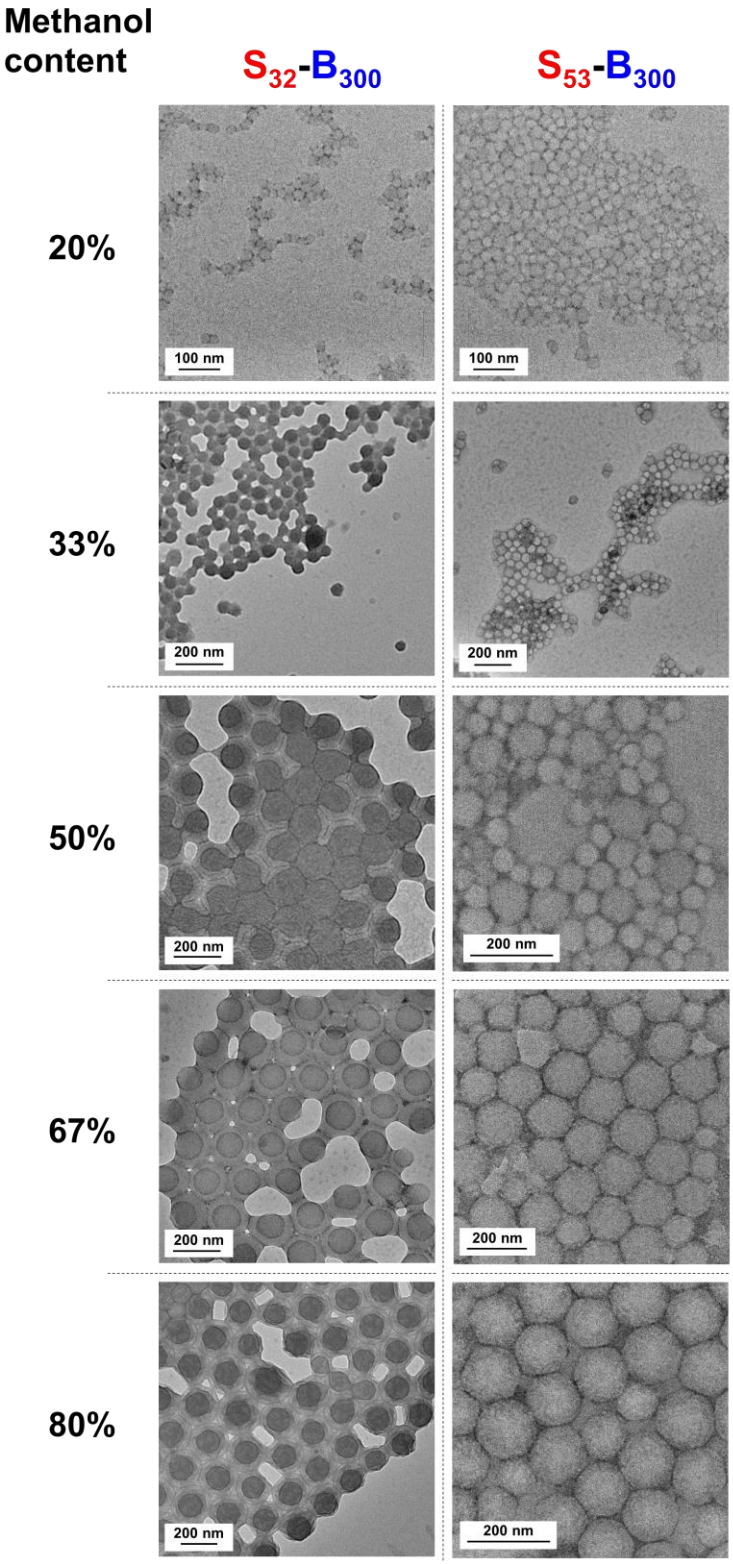

Figure 2.8. Representative TEM images of S_{32}–B_{300} and S_{53}–B_{300} diblock copolymer nanoparticles prepared at 10% w/w solids *via* RAFT-mediated PISA in methanol/water mixtures at 70 °C.

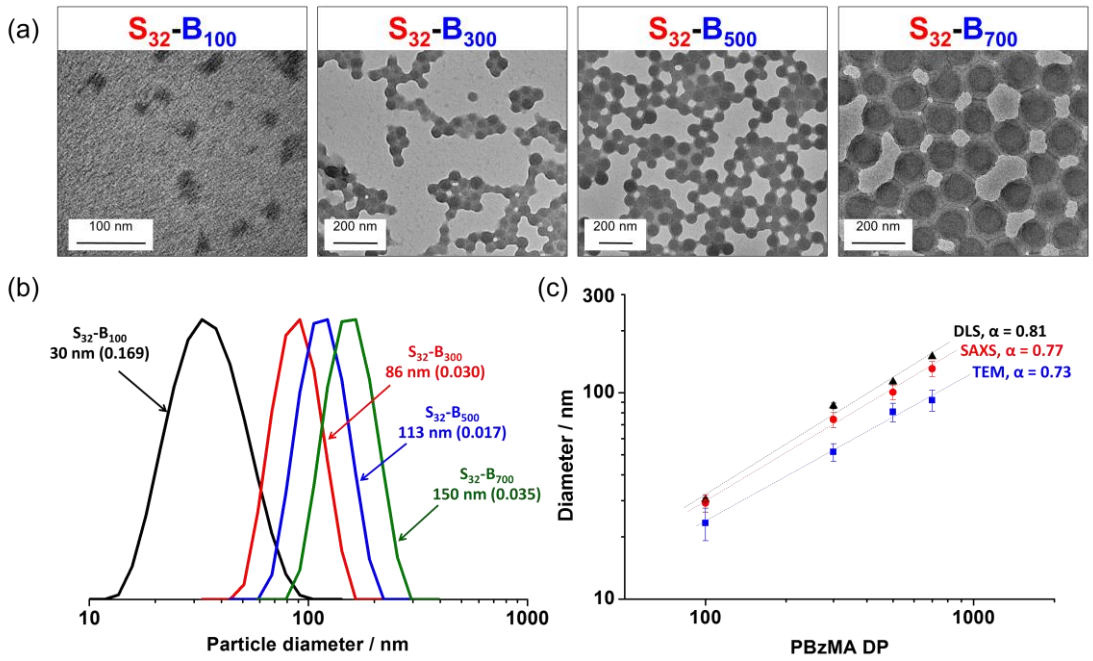

Figure 2.9. S_{32}–B_y diblock copolymers nanoparticles prepared at 10% w/w solids *via* RAFT-mediated polymerisation of BzMA in methanol/water mixture at 33% w/w methanol content. (a) TEM images of S_{32}–B_y (y = 100, 300, 500 and 700); (b) corresponding DLS intensity-average size distributions (the number in brackets represents the DLS polydispersity index); and (c) mean particle diameter versus degree of polymerisation of the PBzMA core-forming block.

2.3.3. Preparation of $PKSPMA_x$–$PBzMA_y$ diblock copolymer nanoparticles with varying PBzMA DP

The mean diameters of $PKSPMA_x$–$PBzMA_y$ (S_x–B_y) nanoparticles can also be tuned by simply altering the DP of PBzMA. Specifically, for a fixed $PKSPMA_{32}$ macro-CTA, a monotonic increase in mean hydrodynamic diameter was observed when increasing the DP of PBzMA from 100 to 700 (**Figure 2.9**). For instance, the mean hydrodynamic diameter of S_{32}–B_{100} was 30 nm, while S_{32}–B_{700} formed nanoparticles with diameters of 150 nm. The spherical morphology and particle diameters reported by DLS (**Figure 2.9b**) and SAXS (**Table 2.5**) were also verified by TEM images (**Figure 2.9a**). DLS particle size distributions remained relatively narrow for nanoparticles with PBzMA DP >100, even when targeting highly asymmetric core-forming block compositions, such as S_{32}–B_{700}. It is worth noting that whilst the S_{32}–B_{100} particles were very difficult to image *via* TEM (**Figure 2.9a**), both DLS and SAXS data support that the objects observed are spherical nanoparticles.

The mean spherical diameter (*D*) can be related to the DP of the core-forming block (*y*) by a scaling exponent (α), as described by the equation $D = ky^{\alpha}$, where *k* is a constant.[355,356] **Figure 2.9c** shows a double-logarithmic plot of *D* against *y* for S_{32}–B_y nanoparticles prepared at 33% w/w methanol. In all cases, a linear relationship is evident, with determined α values of 0.81, 0.77 and 0.73 for DLS, SAXS (see section below), and TEM analysis, respectively. These α values (>2/3) suggest strong copolymer segregation and that the PBzMA chains are in a relatively stretched configuration.[355-357]

2.3.4. SAXS analysis of $PKSPMA_x$–$PBzMA_y$ diblock copolymer nanoparticles

SAXS data were recorded for $PKSPMA_x$–$PBzMA_y$ (S_x–B_y) nanoparticles and the resulting scattering patterns modelled using a spherical micelles[351] plus Gaussian polymer chains[341] model (**Table 2.2**). From these SAXS patterns (**Figure 2.10** and **Figure 2.11**), it was possible to determine the mean radius of the micelle core (R_{core}), radius of gyration of the PKSPMA stabiliser chains (R_g), average solvent fraction in the core (X_{sol}), mean aggregation number (N_{agg}), average number of copolymer chains per unit surface area (S_{agg}) and the volume fraction of the two populations. The mean particle diameters were calculated by SAXS fitting ($D_{SAXS} = 2R_{core} + 4R_g$) and are consistent with both DLS and TEM data (**Table 2.3**, **Table 2.4** and **Table 2.5**).

In all cases, the second population, representing dissolved polymer chains, had negligible volume fractions on fitting. This resulted in fits that were not particularly sensitive to the R_g of these dissolved chains. Nevertheless, this population was included for consistency with previously published data[70] and the fitted R_g values were in the range 3 to 10 Å. This indicates that the low concentration of these dissolved chains is PKSPMA homopolymer (calculated R_g of 14.4 and 18.6 Å for DP 32 and 53, respectively) rather than S_x–B_y copolymer chains.

The SAXS fitting parameters of S_{32}–B_{300} nanoparticles prepared in different methanol/water mixtures are shown in **Table 2.5** (entries 1–4). As the alcohol content increased, R_g of the PKSPMA stabiliser block slightly decreases. This is presumably because at higher methanol contents, the solvent has a lower polarity, resulting in the shrinkage of the highly hydrophilic PKSPMA chains. As the methanol content is increased, the particle diameter becomes significantly larger. This is consistent with DLS (**Figure 2.6a**)

and TEM (**Figure 2.8** and **Figure A.3**). As the alcohol content increases from 20 to 67% w/w, X_{sol} increases significantly from 0 to 0.44. This indicates that methanol occupies more volume in the micelle cores at higher alcohol contents during the PISA process. Thus, the core-forming PBzMA chains are swollen and consequently larger particle diameters are obtained.

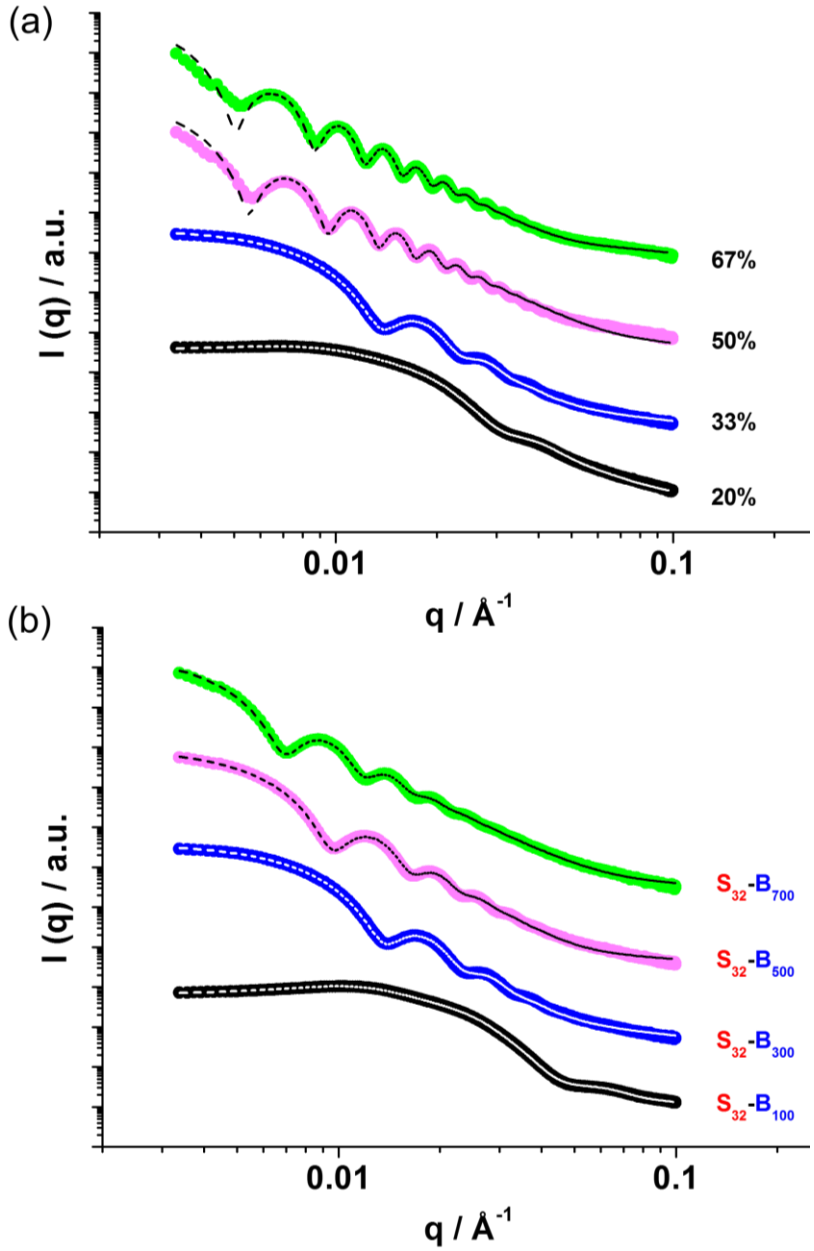

Figure 2.10. Selected small-angle X-ray scattering data (coloured circles) recorded for 1.0% w/w copolymer dispersions for nanoparticles prepared at 10% w/w solids *via* RAFT-mediated PISA of (a) S_{32}–B_{300} synthesised at various methanol contents (indicated on Figure) and (b) S_{32}–$B_{100\text{-}700}$ nanoparticles prepared in 33% w/w methanol/water mixtures. Dashed lines represent fits to the data using a spherical micelles[351] plus Gaussian polymer chains[341] model.

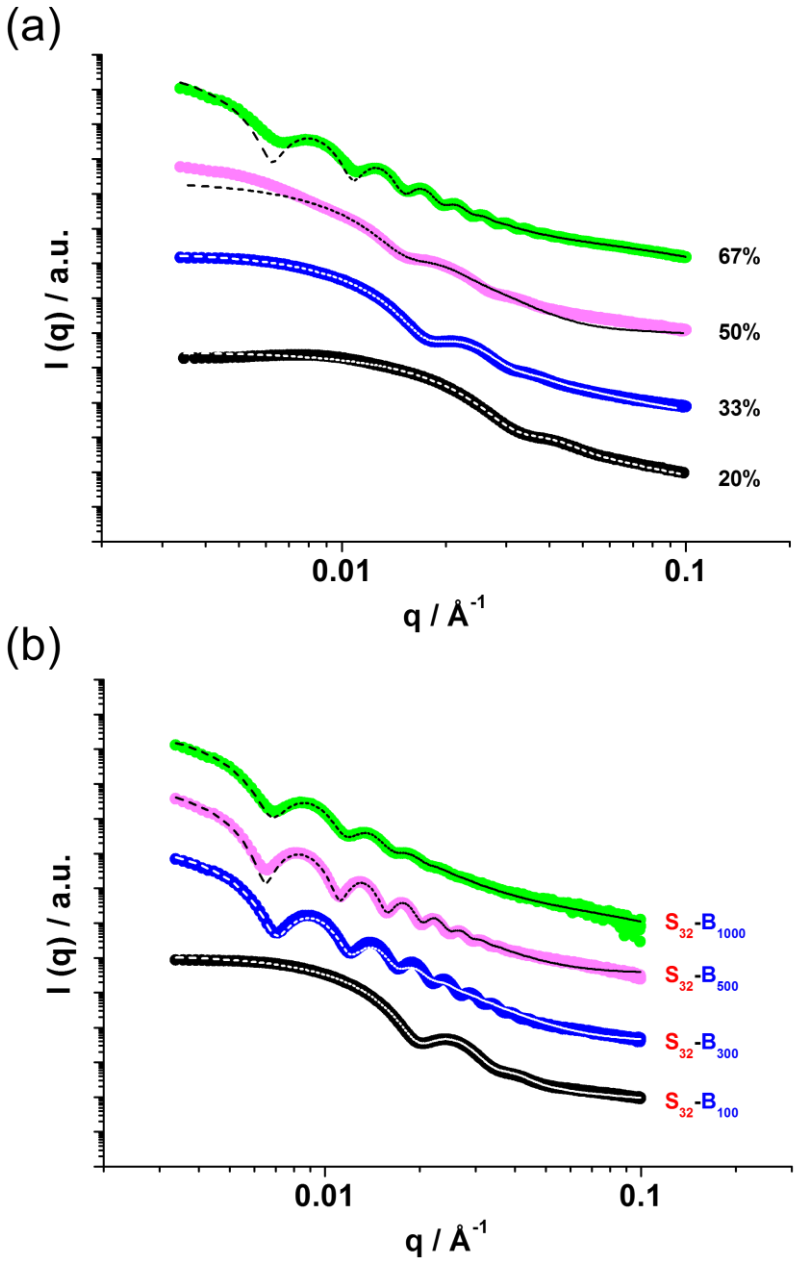

Figure 2.11. Selected small-angle X-ray scattering data (coloured circles) recorded for 1.0% w/w copolymer dispersions of S_x–B_y nanoparticles prepared at 10% w/w solids *via* RAFT-mediated PISA. (a) S_{53}–B_{300} nanoparticles synthesised at 20-67% w/w methanol content and (b) S_{32}–$B_{100\text{-}1000}$ nanoparticles prepared in a 33% w/w ethanol/water mixture. Dashed lines represent fits to the data using a spherical micelles[351] plus Gaussian polymer chains[341] model.

Table 2.5. Summary of mean particle diameters and SAXS structural parameters for PKSPMA-PBzMA (S_x–B_y) nanoparticles prepared in different alcohol/water mixtures.

Entry	Target Composition	Dispersant	Alcohol content / % w/w	Particle diameter (nm)			Structural parameters					
				D_{DLS}[a]	D_{TEM}[b]	D_{SAXS}[c]	R_{core}[d] (Å)	σR_{core}[e] (Å)	R_g[f] (Å)	X_{sol}[g]	N_{agg}[h]	S_{agg}[i]
1	S_{32}–B_{300}	methanol/water	20	42 ± 0	25 ± 2	40 ± 5	138	26	31.5	0.00	147	0.062
2	S_{32}–B_{300}	methanol/water	33	86 ± 2	52 ± 5	74 ± 6	313	32	28.8	0.17	1430	0.116
3	S_{32}–B_{300}	methanol/water	50	181 ± 3	147 ± 14	161 ± 9	774	44	15.5	0.17	21777	0.289
4	S_{32}–B_{300}	methanol/water	67	204 ± 2	159 ± 12	179 ± 8	849	39	22.9	0.44	19119	0.211
5	S_{32}–B_{100}	methanol/water	33	30 ± 0	23 ± 4	29 ± 3	92	14	27.1	0.07	125	0.116
6	S_{32}–B_{500}	methanol/water	33	113 ± 2	81 ± 8	101 ± 8	455	41	24.4	0.21	2519	0.097
7	S_{32}–B_{700}	methanol/water	33	150 ± 1	92 ± 11	131 ± 11	636	57	9.3	0.34	4081	0.080
8	S_{32}–B_{300}	ethanol/water	33	150 ± 2	101 ± 8	132 ± 7	613	35	22.7	0.02	12762	0.270

[a] Mean hydrodynamic diameter obtained *via* DLS analysis. [b] Mean TEM particle diameters were calculated by analysing 200 particles using ImageJ software. [c] SAXS diameters were calculated using $D_{SAXS} = 2R_{core} + 4R_g$. [d] R_{core} represents mean radius of the spherical core. [e] σR_{core} represents standard deviation of the core radius. [f] R_g represents radius of gyration of the PKSPMA stabiliser. [g] X_{sol} represents solvent fraction in the micelle core. [h] N_{agg} represents mean aggregation number and is calculated using **Equation 2.1**. [i] S_{agg} represents average number of copolymer chains per unit surface area and is calculated using **Equation 2.2**.

The structural parameters of S_x–B_y nanoparticles can also be tuned by altering the DP of the PBzMA block (entries 2 and 5–7, **Table 2.5**). Specifically, for a fixed S_{32} stabiliser block and particles synthesised at 33% w/w methanol content, a monotonic increase in particle diameter was observed while targeting PBzMA DPs up to 700. This observation is consistent with DLS and TEM data discussed earlier (**Figure 2.9**).

The number of polymeric chains present in a micelle can be represented by the mean aggregation number (N_{agg}).[358,359] For the S_x–B_y particles reported herein, there are significant variations in the solvent fraction (X_{sol}) within the particle cores (**Table 2.5**). We have therefore taken this into account when calculating N_{agg}, using **Equation 2.1** (where V_{co} is the calculated volume of a PBzMA chain).

$$N_{\mathrm{agg}} = \frac{\frac{4}{3}\pi {R_{\mathrm{core}}}^3}{V_{\mathrm{co}}} \times (1 - X_{\mathrm{sol}}) \qquad \textbf{Equation 2.1}$$

From the modelled SAXS structural parameters for the series prepared in 33% w/w methanol/water, N_{agg} increases from 125 for S_{32}–B_{100} to 4081 for S_{32}–B_{700} (33-fold). This indicates that the average number of PBzMA chains present in a particle is significantly larger when targeting a higher DP. Furthermore, as both R_{core} and N_{agg} increase when targeting higher DPs of the core-forming PBzMA block (entries 2 and 5–7, **Table 2.5**), it is pertinent to calculate the average number of copolymer chains per unit surface area (S_{agg}, **Equation 2.2**).[359]

$$S_{\mathrm{agg}} = \frac{N_{\mathrm{agg}}}{4\pi {R_{\mathrm{core}}}^2} \qquad \textbf{Equation 2.2}$$

The calculated S_{agg} values for the series prepared in 33% w/w methanol decreased from 0.116 nm^{-2} for S_{32}–B_{100} to 0.080 nm^{-2} when targeting a PBzMA DP of 700. This indicates that the surface density of the hydrophilic PKSPMA stabiliser chains becomes much lower when targeting a higher core DP. At low copolymer chain densities, the relatively hydrophobic methanol molecules can solvate the core-forming block more readily (higher X_{sol}), and thus the core occupies more volume (higher R_{core}).

For a fixed S_{32}–B_{300} copolymer composition and 33% w/w alcohol content (entries 2 and 8, **Table 2.5**), nanoparticles prepared in ethanol/water have significantly larger mean diameters and aggregation numbers than those obtained in methanol/water mixtures. This is presumably because the dielectric constant of the 33% w/w ethanol/water mixture is lower than that of the 33% w/w methanol/water mixture

(**Table 2.1**).[348] The relatively low dielectric constant of the ethanol/water mixture reduces the repulsive interactions between neighbouring anionic PKSPMA stabiliser chains during PISA, allowing more copolymer chains to assemble per unit surface area (S_{agg} in **Table 2.5**).[252,360] Hence X_{sol} is lower for particles prepared in ethanol/water than for methanol/water mixtures. Copolymer chains will therefore be more stretched and assemble in a more compact manner.[361] This results in a higher number of copolymer chains present for particles prepared in ethanol/water mixtures and consequently larger mean diameters.[252]

2.3.5. Colloidal stability of PKSPMA–PBzMA nanoparticles

Figure 2.12 shows DLS and aqueous electrophoresis data for S_{32}–B_{300} diblock copolymer nanoparticles, synthesised in either 33% w/w methanol/water or 33% w/w ethanol/water mixtures, as a function of pH. According to **Figure 2.12a**, the mean hydrodynamic diameter of the nanoparticles is independent of the solution pH, which indicates good colloidal stability over a wide pH range.[345] This is clearly different from related poly(methacrylic acid) (PMAA) stabilised diblock copolymer nanoparticles, where the PMAA is a weak polyelectrolyte, which can be protonated and result in particle aggregation at low pH.[345,362]

Figure 2.12b shows that S_x–B_y diblock copolymer nanoparticles are highly anionic and pH-independent zeta potentials were observed, even at relatively low pH. This pH-independent character confirms that PKSPMA is present within the coronas of the particles. This strong anionic polyelectrolyte stabiliser enables flocculation to be prevented during attempted aggregation by variation of the solution pH.[11,337,345] As previously stated, the strong anionic nature of this stabiliser provides electrostatic repulsion between block copolymer nanoparticles during PISA and prevents the formation of worm, vesicle, or other higher order morphologies.[2]

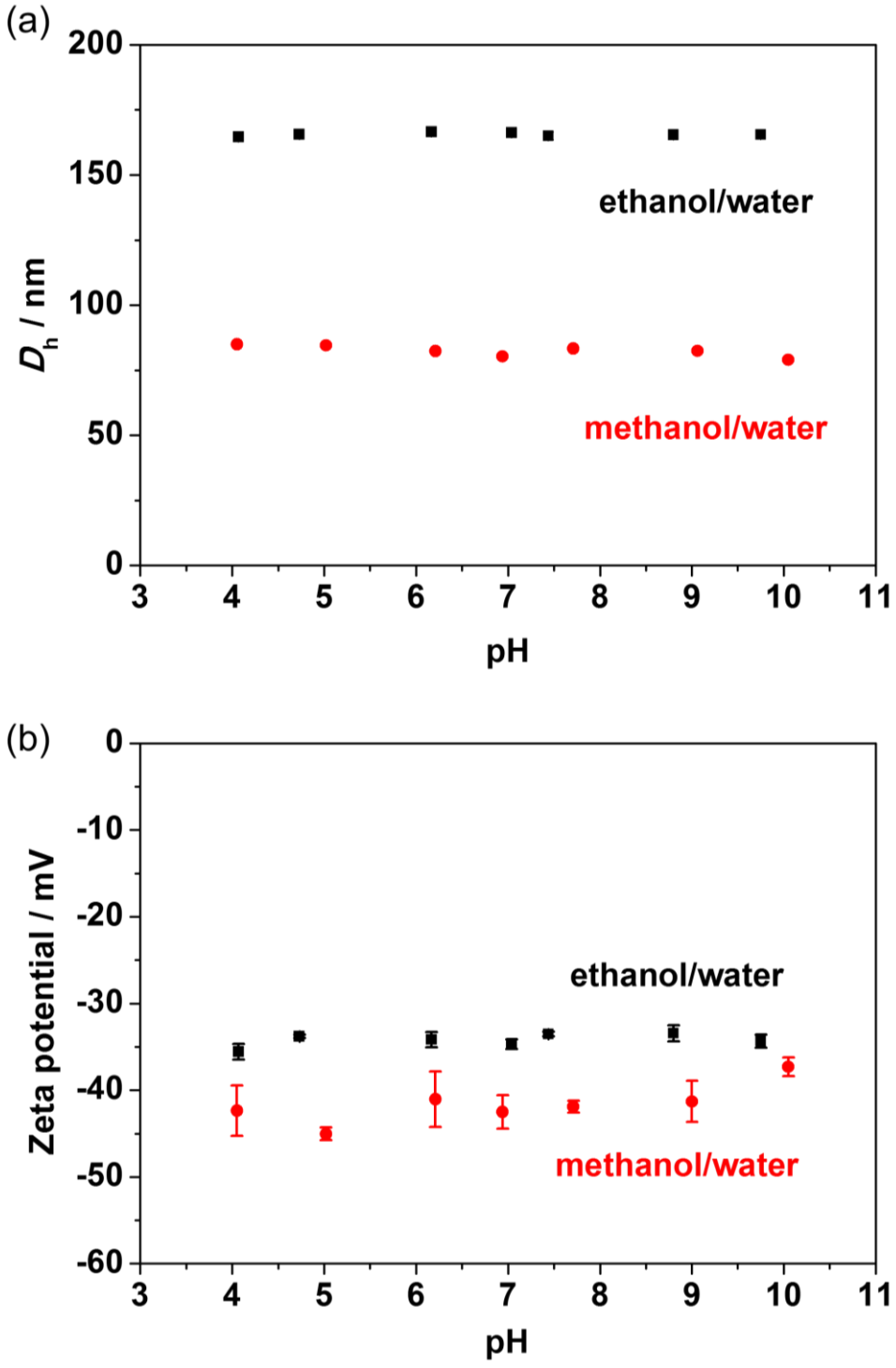

Figure 2.12. Representative (a) dynamic light scattering and (b) aqueous electrophoresis data as a function of pH obtained for S_{32}–B_{300} diblock copolymer nanoparticles prepared in ethanol/water (black squares) and methanol/water (red circles) at an alcohol content of 33% w/w. Measurements were conducted at a copolymer concentration of approximately 0.1% w/w in the presence of 1 mM KCl as a background electrolyte. The solution pH was initially adjusted to pH 10 by the addition of KOH and subsequently titrated to pH 4 using HCl.

To further demonstrate the stability of these nanoparticles, mean hydrodynamic diameters of these particles were measured after: (i) drying under vacuum and redispersion in water with gentle shaking; and (ii) storage at −20 °C and subsequent thawing to ambient temperature (**Figure 2.13**). Only negligible changes in mean hydrodynamic diameter were observed in all cases. This suggested that these S_x–B_y nanoparticles can be used in subsequent studies as a dried powder. This means that they are easy and convenient to weigh precisely, and the influence of residual solvent can also be minimised. This property is especially significant for further bio-related or industrial applications of these copolymer nanoparticles.

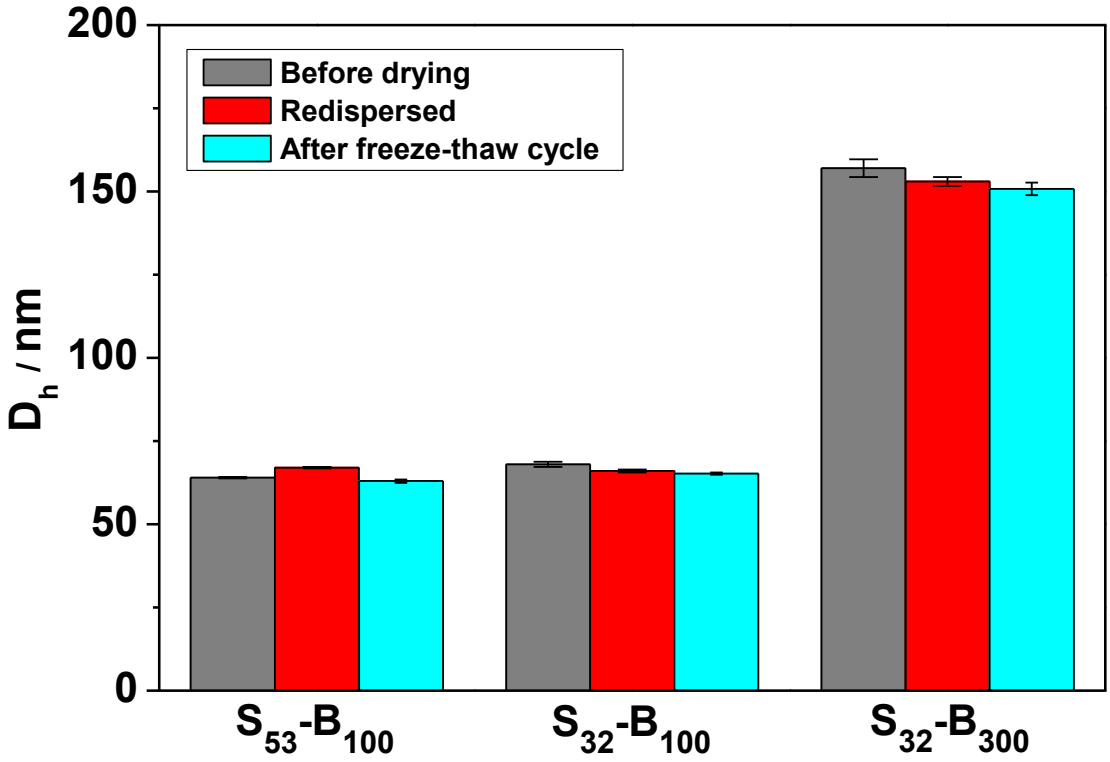

Figure 2.13. Representative hydrodynamic diameters of S_x–B_y diblock copolymer nanoparticles synthesised at an ethanol content of 33% w/w. Grey, red and blue bars represent diluted dispersions before drying; nanoparticles dried and redispersed in water; and after a freeze-thaw cycle, respectively.

2.3.6. Preparation of poly(4-styrene sulfonate)-poly(benzyl methacrylate) (PSS–PBzMA) diblock copolymer nanoparticles

All of the above data in this chapter formed a publication in *Polymer Chemistry*. Subsequently, the PKSPMA–PBzMA nanoparticles described have been used by a collaborator to evaluate their use as anti-viral materials. As part of this collaboration, this RAFT-mediated PISA protocol was extended to prepare a series of anionic, sterically-stabilised, sulfonate-functional poly(4-styrene sulfonate)-poly(benzyl methacrylate) (PSS–PBzMA) nanoparticles using largely the same methodology described above. More specifically, sulfonated aromatic PSS macromolecular chain transfer agents (macro-CTAs) were synthesised *via* RAFT solution polymerisation followed by chain-extension with benzyl methacrylate (BzMA) in alcohol/water mixtures to form PSS–PBzMA nanoparticles. The preparation and analysis of the series of PSS–PBzMA particles prepared as part of this collaboration are described in this section.

PSS macro-CTAs were synthesised *via* RAFT solution polymerisations of 4-styrene sulfonate in 3:1 water/dioxane at 70 °C and quenched at predetermined times. A series PSS macro-CTAs with target DP of 10, 20, 50 and 100 were successfully obtained with high monomer conversions, and the calculated DPs were 13, 23, 54 and 111, respectively (**Table 2.6**). Furthermore, all GPC chromatograms of these macro-CTAs were unimodal with low molar mass dispersities (M_w/M_n < 1.10), and successively shifted to shorter retention times when targeting higher DP (**Figure 2.14**). This indicated that these were well-controlled RAFT solution polymerisations, even when targeting higher DP, such as PSS_{100}. The evolution of molar mass and molar mass dispersity (M_w/M_n) versus monomer conversion for PSS_{32} is shown in **Figure 2.15**. As the polymerisation progressed, the corresponding dispersities decreased, and the resulting macro-CTA had relatively narrow molar mass distributions (M_w/M_n < 1.10) at 93% conversion.

The blocking efficiency of the PSS macro-CTAs was examined by a self-blocking experiment using PSS_{32} (**Figure 2.16**). GPC analysis of the resulting chain-extended homopolymer confirmed a unimodal distribution and relatively low molar mass dispersity (M_w/M_n = 1.22). This indicates that these macro-CTAs are likely undergo efficient chain extension to form second blocks with other monomers, as desired.[345,352]

Table 2.6. Summary of PSS macro-CTAs prepared *via* RAFT solution polymerisation in 3:1 water/dioxane at 70 °C with varying target DP. The [PETTC]:[ACVA] ratio was fixed at 5:1 and polymerisations were conducted at a solids content of 15% w/w.

Entry	Target DP	Polymerisation time / min	Conversion[a] / %	DP[a]	M_n[b] / g mol^{-1}	M_w/M_n[b]
1	10	120	83	13	3100	1.10
2	20	150	93	23	6200	1.04
3	50	180	92	54	9500	1.05
4	100	240	93	111	14700	1.07

[a] Determined *via* ^{1}H NMR. [b] Determined *via* aqueous GPC analysis.

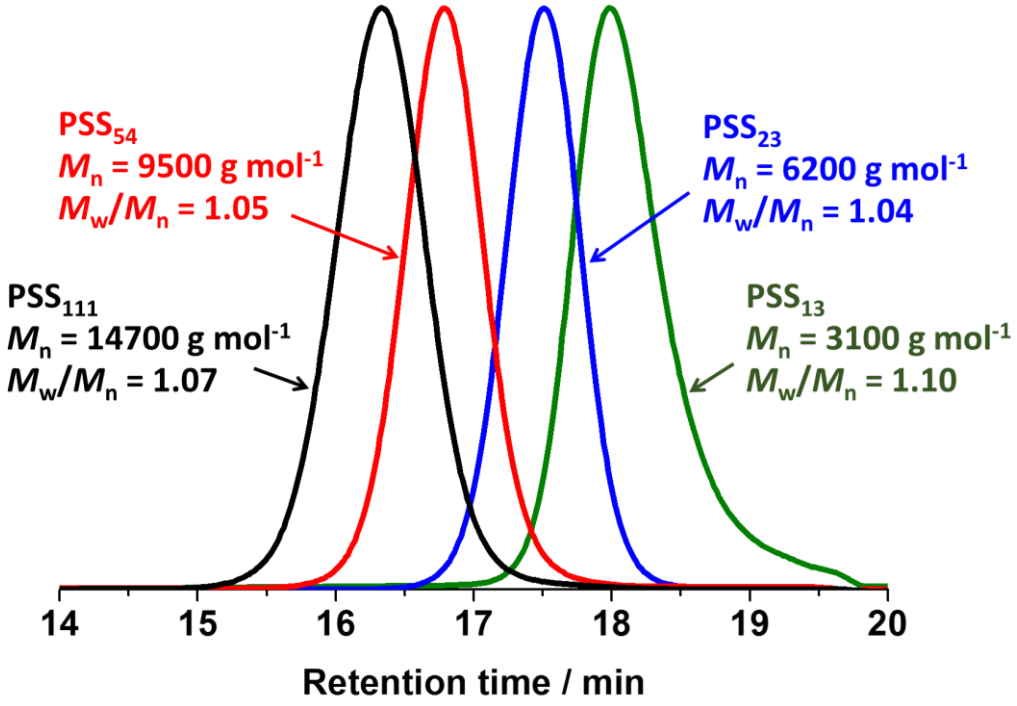

Figure 2.14. Aqueous GPC chromatograms obtained for PSS macro-CTAs (target DP 10, 20, 50 and 100) prepared *via* RAFT solution polymerisation of 4-styrene sulfonate using PETTC as CTA in 3:1 water/dioxane at 70 °C. The [PETTC]:[ACVA] ratio was fixed at 5:1 and polymerisations were conducted at a solids content of 15% w/w. Monomer conversions of PSS_{13}, PSS_{23}, PSS_{54} and PSS_{111}, were 83%, 93%, 92% and 93%, respectively.

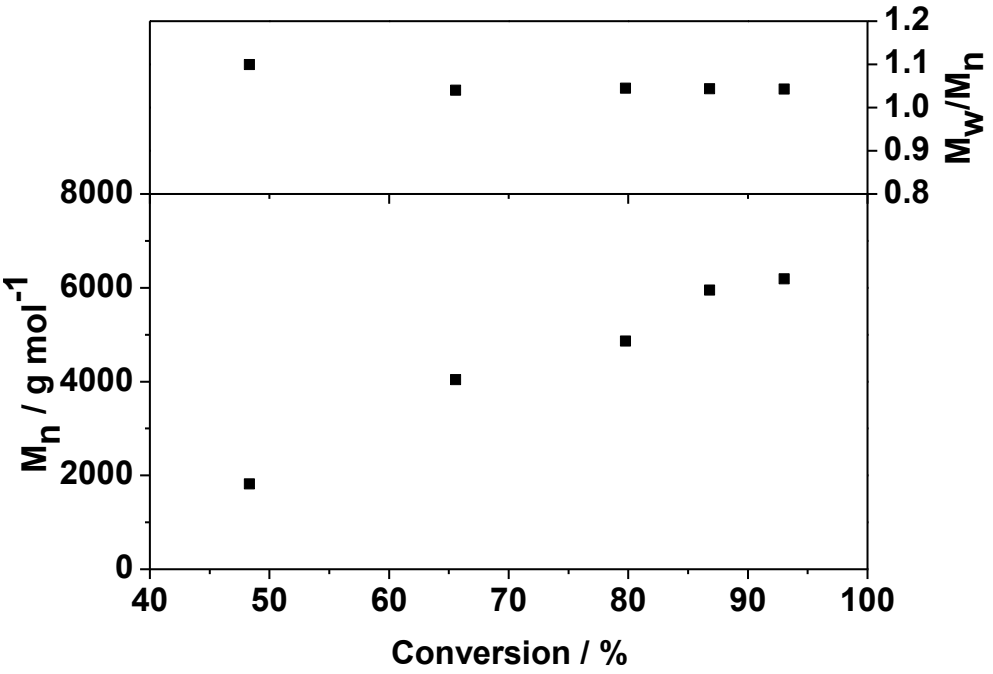

Figure 2.15. M_n and M_w/M_n versus monomer conversion for PSS macro-CTA (target DP 20) synthesised *via* RAFT solution polymerisation of 4-styrene sulfonate with PETTC as CTA in 3:1 water/dioxane at 70 °C. The [PETTC]:[ACVA] ratio was fixed at 5:1 and polymerisations were conducted at a solid content of 15% w/w.

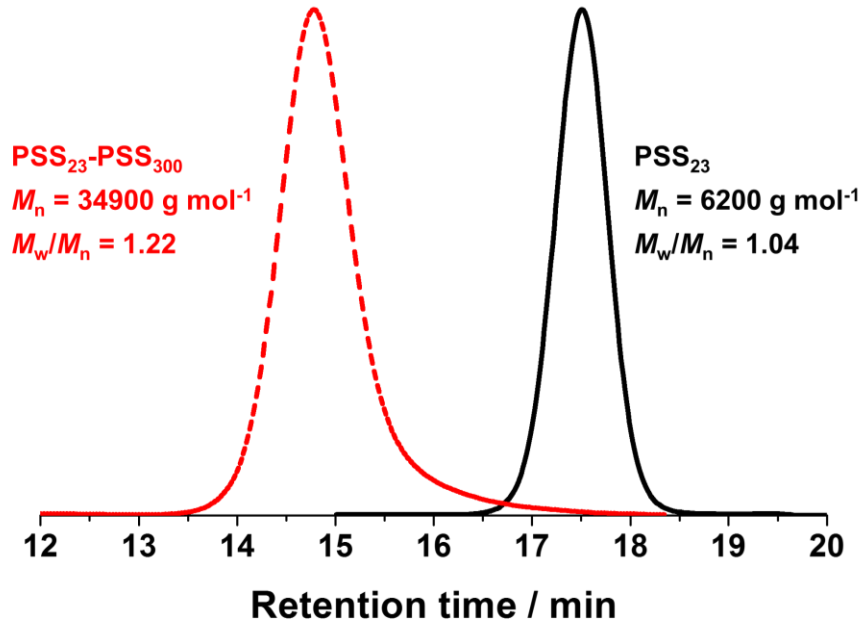

Figure 2.16. Aqueous GPC chromatograms obtained for the PSS_{23} macro-CTA and its subsequent chain extension *via* RAFT aqueous solution polymerisation using 4-styrene sulfonate as monomer at 70 °C. The target DP of second block was 300. The [CTA]:[ACVA] ratio was fixed at 5:1 and polymerisations were conducted at a solid content of 15% w/w.

Sulfonate-functional PSS–PBzMA diblock copolymer nanoparticles were prepared *via* RAFT mediated PISA in various methanol/water (**Figure 2.17**, entries 1–5 in **Table 2.7**) and ethanol/water (**Figure 2.18**, entries 6–9 in **Table 2.7**) mixtures. Similar to the preparation of PKSPMA–PBzMA diblock copolymer nanoparticles, the mean particle diameters increased with increasing alcohol content. For example, the mean hydrodynamic diameter of PSS_{54}–$PBzMA_{100}$ increased approximately nine-fold, from approximately 70 to 660 nm for methanol contents in the range 0 to 80% w/w (**Figure 2.17**). The change in particle diameter for a fixed copolymer composition for this analogues series further confirms that solvent quality dramatically affects the PISA process.[353]

The morphologies of the PSS_x–$PBzMA_{100}$ diblock copolymer nanoparticles (entries 10–13, **Table 2.7**) prepared *via* RAFT-mediated PISA at 20% w/w methanol were investigated *via* TEM after staining with RuO_4. In all cases, spherical micelles were obtained (**Figure 2.19** and **Figure A.4**). This observation agrees with PKSPMA–PBzMA PISA formulations. This is likely due to the highly anionic character of the PSS stabiliser preventing higher order morphology formation.[235,252]

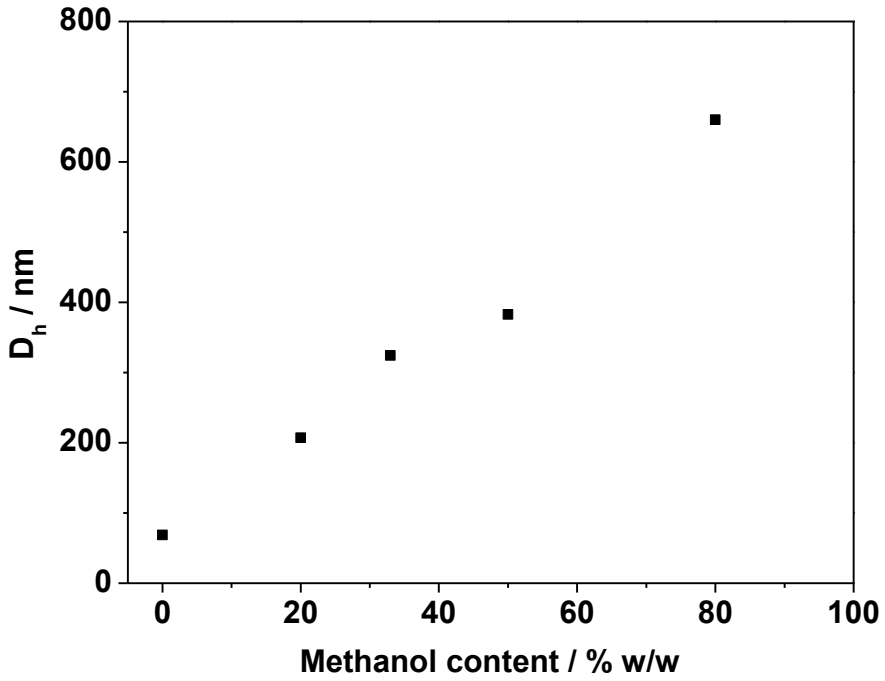

Figure 2.17. Mean hydrodynamic diameters (D_h) of PSS_{54}–$PBzMA_{100}$ diblock copolymer nanoparticles synthesised *via* RAFT-mediated PISA in varying methanol/water mixtures at 70 °C (entries 1–5, **Table 2.7**). The [PSS]:[ACVA] ratio was fixed at 3:1 and polymerisations were conducted at a solids content of 10% w/w.

Table 2.7. Summary of target composition, alcohol content and mean diameters obtained for PSS_x–$PBzMA_y$ (SS_x–B_y) diblock copolymer nanoparticles synthesised at 10% w/w solids *via* RAFT-mediated polymerisation in different alcohol/water mixtures.

Entry	Target composition	Dispersant	Alcohol content / %	D_h / nm[a]
1	SS_{54}-B_{100}	Methanol/water	0	69 (0.071)
2	SS_{54}-B_{100}	Methanol/water	20	207 (0.087)
3	SS_{54}-B_{100}	Methanol/water	33	324 (0.437)
4	SS_{54}-B_{100}	Methanol/water	50	383 (0.077)
5	SS_{54}-B_{100}	Methanol/water	80	660 (0.129)
6	SS_{54}-B_{300}	Ethanol/water	0	82 (0.043)
7	SS_{54}-B_{300}	Ethanol/water	20	307 (0.048)
8	SS_{54}-B_{300}	Ethanol/water	33	575 (0.773)
9	SS_{54}-B_{300}	Ethanol/water	50	641 (0.446)
10	SS_{13}-B_{100}	Methanol/water	20	204 (0.072)
11	SS_{23}-B_{100}	Methanol/water	20	226 (0.073)
12	SS_{54}-B_{100}	Methanol/water	20	207 (0.087)
13	SS_{111}-B_{100}	Methanol/water	20	190 (0.033)

[a] DLS analysis using water as dispersant. DLS polydispersity index vales are indicated in brackets.

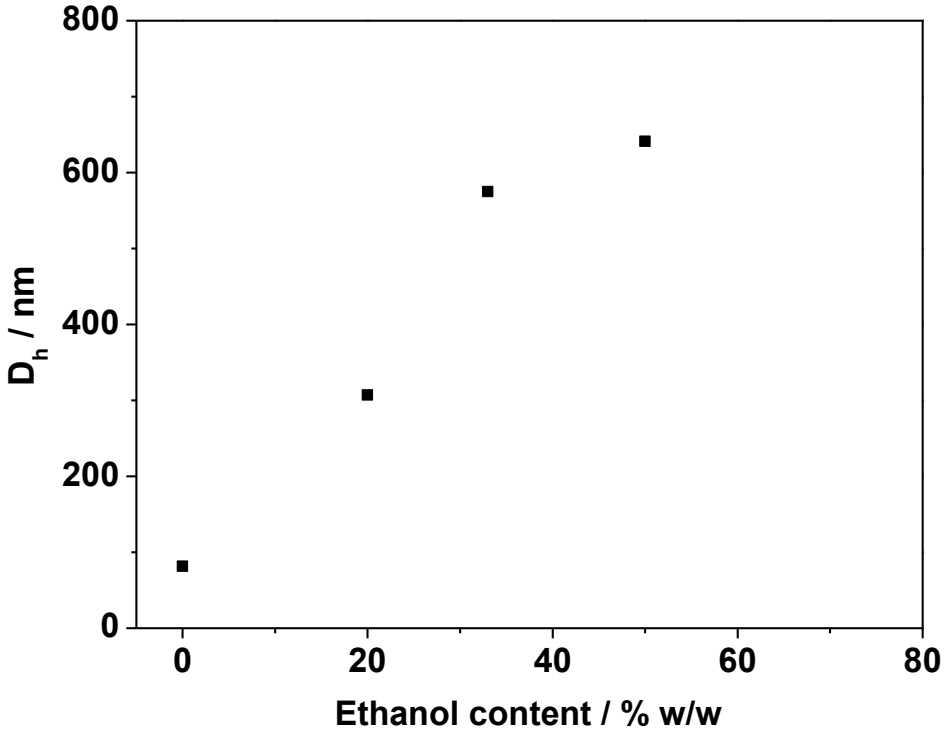

Figure 2.18. Mean hydrodynamic diameters (D_h) of PSS_{54}–$PBzMA_{300}$ diblock copolymer nanoparticles synthesised *via* RAFT-mediated PISA in varying ethanol/water mixtures at 70 °C (entries 6–9, **Table 2.7**). The [PSS]:[ACVA] ratio was fixed at 3:1 and polymerisations were conducted at a solid content of 10% w/w.

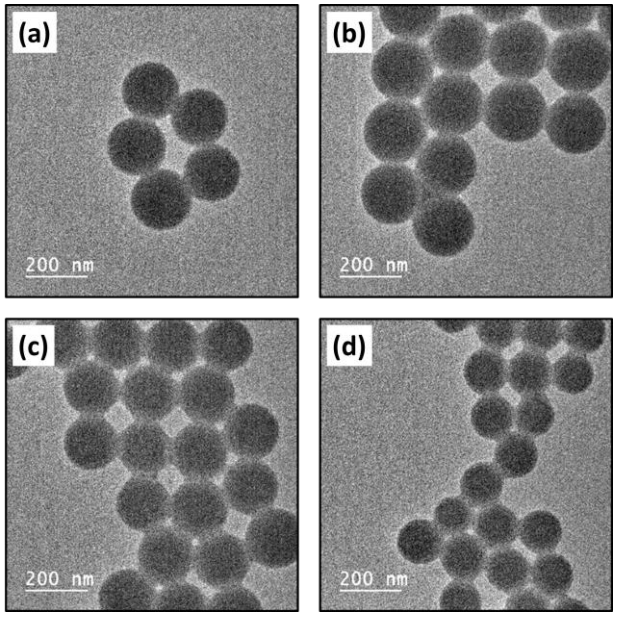

Figure 2.19. Representative TEM images for (a) PSS_{13}–$PBzMA_{100}$, (b) PSS_{23}–$PBzMA_{100}$, (c) PSS_{54}–$PBzMA_{100}$ and (d) PSS_{111}–$PBzMA_{100}$ diblock copolymer nanoparticles synthesised *via* RAFT-mediated PISA at 70 °C in methanol/water at 20% w/w methanol (entries 10–13, **Table 2.7**). The [macro-CTA]:[ACVA] ratio was fixed at 3:1 and polymerisations were conducted at a solids content of 10% w/w.

Figure 2.20 shows DLS and aqueous electrophoresis data for PSS_{54}–$PBzMA_{300}$ diblock copolymer nanoparticles, synthesised in a methanol/water mixture at 20% w/w methanol, as a function of pH. The mean hydrodynamic diameter of the nanoparticles is independent of the solution pH, which indicates good colloidal stability over a wide pH range.[345] Furthermore, PSS–PBzMA diblock copolymer nanoparticles are highly anionic, even at low pH, indicating that PSS is present within the coronas of the particles. This strong anionic polyelectrolyte stabiliser enables flocculation to be prohibited during attempted aggregation by variation of the solution pH.[11,337,345] As previously stated, the strong anionic nature of this stabiliser provides electrostatic repulsion between block copolymer nanoparticles during PISA and prevents the formation of worm, vesicle or other higher order morphologies.[2]

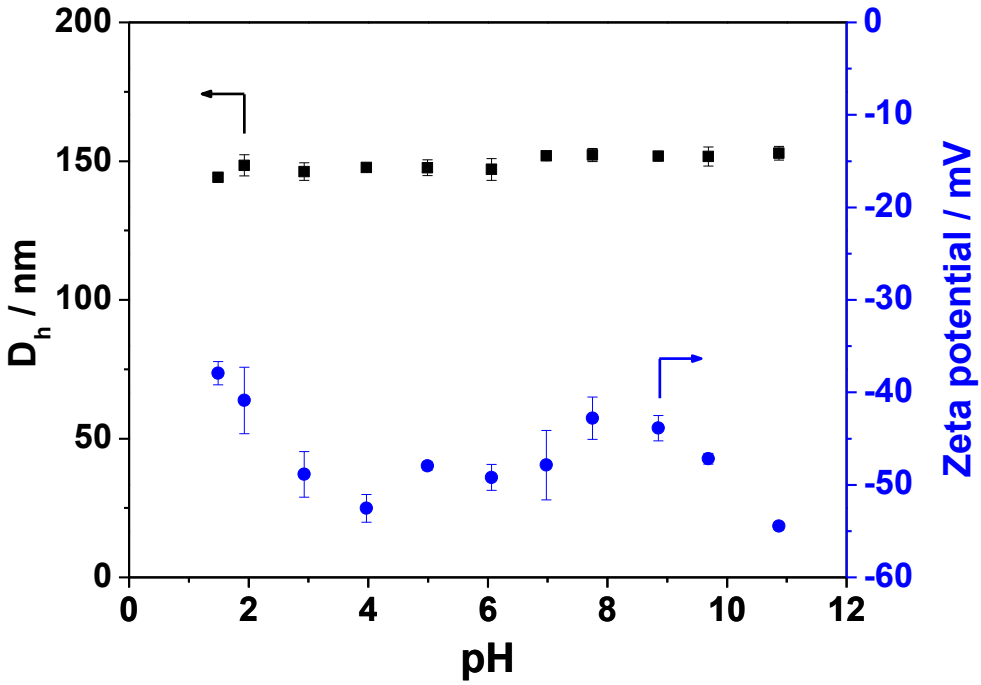

Figure 2.20. Representative dynamic light scattering and aqueous electrophoresis data as a function of pH obtained for PSS_{54}–$PBzMA_{300}$ diblock copolymer nanoparticles synthesised *via* RAFT-mediated PISA at 70 °C in a methanol/water mixture at 20% w/w. Measurements were conducted at a copolymer concentration of approximately 0.1% w/w in the presence of 1 mM KCl as a background electrolyte. The solution pH was initially adjusted to pH 11 by the addition of KOH and subsequently titrated to pH 1 using HCl.

2.4. Conclusions

RAFT solution polymerisation affords sulfonate-functional macro-CTAs, which are subsequently used to prepare sulfonate-bearing spherical nanoparticles *via* RAFT-mediated PISA in alcohol/water mixtures. Nanoparticles with tuneable diameters can be prepared *via* varying the DP of the stabiliser and/or core-forming block, or by simply altering the co-solvent composition for a fixed target copolymer. This indicates that the solvency of both the stabiliser and core-forming block has a marked impact on both the aggregation of polymer chains during self-assembly and the resulting copolymer nanoparticle morphology. This approach is highly versatile and provides the ability to obtain preferred particle diameters with different copolymer compositions, or to prepare a desired copolymer composition with various particle sizes. In addition, these results demonstrate that solvency of both the stabiliser (PKSPMA or PSS) and core-forming block (PBzMA) have a marked impact on both the aggregation of polymer chains during self-assembly and the resulting copolymer nanoparticle morphology. Furthermore, the ability of these highly anionic particles to be easily redispersed after drying is promising for application in future studies.

Chapter Three

RAFT miniemulsion polymerisation of benzyl methacrylate using non-ionic surfactant

3.1. Introduction

Reversible-deactivation radical polymerisation (RDRP) is a versatile technique for the synthesis of well-defined polymers and has attracted both academic and industrial attention in the past two decades.[363-365] The three main RDRP techniques are nitroxide-mediated polymerisation (NMP),[41,46] atom-transfer radical polymerisation (ATRP)[49,366] and reversible addition-fragmentation chain transfer (RAFT) polymerisation.[179,218,367,368] These techniques afford the capability to overcome drawbacks of conventional free radical polymerisation. More specifically, radical polymerisations can be controlled to obtain polymers with desired molar masses, narrow molar mass distributions and complex architectures. However, NMP and ATRP reactions typically have lower polymerisation rates and other associated drawbacks (see **Chapter One**).[156,369] In contrast, RAFT polymerisation has attracted wide attention because the polymerisation rate is high and it can be applied to an extensive range of functional monomers and be performed under moderate conditions.[179]

RDRPs are typically performed in homogeneous media, which often require the use of undesirable volatile organic compounds (VOCs) for the control of heat evolution and viscosity of a given polymerisation. However, RDRP performed in heterogeneous conditions, such as emulsion, miniemulsion or dispersion polymerisation, has gained increasing attention in recent years.[7,370-372] Common advantages of heterogeneous polymerisation include the use of water as a continuous phase (as a more environmentally friendly solvent) and low viscosity of the polymerisation medium due to the formation of discrete polymeric particles.[106] In addition, it has been demonstrated that RAFT polymerisation can be conducted *via* various heterogeneous routes, such as RAFT miniemulsion polymerisation.[154-158]

Miniemulsion polymerisation is a heterogeneous polymerisation technique widely used to prepare well-defined vinyl polymer latexes.[129,373-375] Miniemulsions are normally defined as aqueous dispersions of relatively stable oil droplets (50–500 nm) prepared by applying shear to a system containing water, oil, surfactant and hydrophobe.[33] Miniemulsion droplets are considered metastable but their stability during a miniemulsion polymerisation is crucial because it affects the polymerisation kinetics and resulting latex morphology.[375,376] Typical miniemulsion formulations are based on anionic surfactants (e.g. sodium dodecyl sulfate, SDS[159]) in combination with a

selectively oil-soluble hydrophobe (e.g. hexadecane,[376] dodecyl mercaptan[377] or reactive alkyl methacrylate[378]). Nevertheless, the influence of cationic and non-ionic surfactants on miniemulsion polymerisation has been reported. For example, Landfester *et al.*[137] demonstrated polystyrene latexes synthesised using cetyl trimethylammonium bromide (CTAB) cationic surfactant had similar particle sizes when compared to those prepared using SDS. Hecht *et al.*[138] investigated miniemulsion polymerisation of styrene using a non-ionic surfactant. It was shown that the non-ionic surfactant had slower adsorption and desorption kinetics than SDS, minimising its presence in the continuous phase. This led to newly formed oligomeric species being incorporated within existing droplets before precipitating, and thus nucleation of new particles was not observed.

In RAFT miniemulsion polymerisation, a small amount of hydrophobic chain transfer agent (CTA) is dissolved in the monomer phase prior to emulsification.[96,97] Polymerisation control and latex stability in RAFT miniemulsion polymerisation using conventional RAFT agents has been reported utilising relatively high concentrations of surfactant and hydrophobe.[170-172] However, the use of RAFT agents in miniemulsion polymerisation is sometimes problematic, causing colloidal instability,[160,161] broad particle size distributions,[154,166] low polymerisation rates,[162,163] low monomer conversions[159,164,165] and broad molar mass distributions.[167-169] Furthermore, some RAFT miniemulsion polymerisation systems experience inhibition or retardation of the polymerisation.[154,162]

Acrylic and methacrylic monomers are crucial for manufacturing a wide range of polymeric materials for a variety of applications.[84,379] Among this group of monomers, benzyl methacrylate (BzMA) is a hydrophobic methacrylic monomer, which is often used as a substitute for styrene. For example, in RAFT-mediated PISA,[29,336,380] BzMA acts as water-immiscible monomer, which exhibits higher polymerisation rates than styrene,[9] minimising unreacted monomer in these formulations.[24] Furthermore, a wide range of potential applications of PBzMA have been explored, such as polymeric optical fibres,[381] nanoimprinting lithography,[382,383] contact lenses,[384] coatings and paints,[385] monoliths for capillary electrochromatography,[386] colour filter photoresist materials,[387] stationary phases in liquid chromatography[388,389] and ionic liquids.[390-392] However, to the best of our

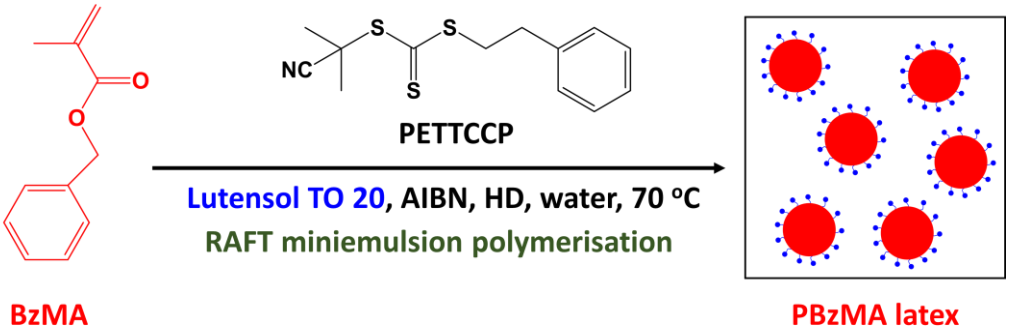

Scheme 3.1. Synthesis of poly(benzyl methacrylate) (PBzMA) latex *via* RAFT miniemulsion polymerisation at 70 °C using Lutensol TO 20 non-ionic surfactant. Polymerisations were conducted at a dispersed phase content of 20% w/w.

knowledge, there are relatively few reports, which investigate the effects of the RAFT process on the kinetics of miniemulsion polymerisation of BzMA.

In **Chapter Two**, the preparation of anionic sulfonate-functional nanoparticles *via* RAFT-mediated PISA was described. Herein the preparation of non-ionic sterically-stabilised PBzMA nanoparticles *via* RAFT miniemulsion polymerisation using a non-ionic surfactant is investigated. More specifically, a series of PBzMA latexes were prepared by systematically adjusting the concentration of hydrophobe, initiator and RAFT agent (**Scheme 3.1**). This allowed the knowledge of the rules, which govern latex formation during RAFT miniemulsion polymerisation to be extended. In this work, chain transfer agents with different hydrophilicity, and surfactants including a conventional anionic surfactant (SDS) and a series of Lutensol TO non-ionic surfactants were screened to ascertain a suitable surfactant for miniemulsion polymerisation of BzMA. The resulting PBzMA latexes were characterised *via* gravimetry, DLS, GPC and TEM. Furthermore, it is demonstrated that miniemulsion polymerisations with tuneable polymerisation rate, PBzMA molar mass, number of particles per unit volume and particle diameter can be conducted by altering the concentration of hydrophobe, initiator or RAFT agent.

3.2. Experimental details

3.2.1. Materials

Sodium dodecyl sulfate (SDS, 98.5%), hexadecane (HD, 99%) and azobisisobutyronitrile (AIBN, 98%) were purchased from Sigma-Aldrich (UK) and used as received. The non-ionic Lutensol surfactants, e.g. Lutensol TO 20, which is a saturated *iso*-C_{13} alcohol with an ethoxylation block length of 20 units (*iso*-$C_{13}H_{27}O(CH_2CH_2O)_{20}H$,

molar mass = 1000 g mol^{-1}), were obtained from BASF (UK) and used as received. Benzyl methacrylate (BzMA, 98%) was purchased from Alfa Aesar (UK) and passed through a column of activated basic alumina to remove inhibitors and impurities before use. Tetrahydrofuran (THF, HPLC grade) was purchased from VWR International (UK) and used as received. Chloroform-*d* ($CDCl_3$) was purchased from Cambridge Isotope Laboratories (UK). 4-Cyano-4-(2-phenylethane sulfanylthiocarbonyl) sulfanylpentanoic acid (PETTC) was prepared as described in **Chapter Two** (see **section 2.2.2**). 2-Cyano-2-propyl phenethyl trithiocarbonate (PETTCCP) was prepared in-house. Deionised water was used in all experiments.

3.2.2. Synthesis of 2-cyano-2-propyl phenethyl trithiocarbonate (PETTCCP)

The synthesis of PETTCCP RAFT CTA was conducted according to a modified procedure described by Kocik *et al.*[393] The synthetic scheme for the preparation of PETTCCP chain transfer agent is presented in **Scheme A.2**. Sodium hydride (60% in oil, 7.6 g, 191 mmol) was gradually added to diethyl ether (350 mL) at 5 °C to obtain a grey suspension. 2-Phenylethanethiol (25.1 g, 182 mmol) was added dropwise to the grey suspension and hydrogen gas was generated. A white viscous slurry of sodium phenylethanethiolate was formed over a 30 min period. Carbon disulfide (14.5 g, 191 mmol) was added dropwise to the reaction mixture and gradually transformed into a thick yellow precipitate of sodium 2-phenylethanetrithiocarbonate over 30 min. The precipitate was collected *via* filtration and then utilised in the next step without further purification. Sodium 2-phenylethanetrithiocarbonate (44.0 g, 186 mmol) was slowly added to diethyl ether (350 mL) at ambient temperature to obtain a suspension and subsequently solid iodine (24.1 g, 95 mmol) was added. The reaction mixture was stirred at ambient temperature for 60 min and an insoluble white precipitate of sodium iodide was formed and removed *via* filtration. The yellow−brown filtrate was washed using a sodium thiosulfate aqueous solution three times to remove excess iodine and subsequently dried over sodium sulfate to remove residual water. The filtrate was further dried under vacuum at 35 °C to remove volatiles and yield bis(2-phenylethane sulfanylthiocarbonyl) disulfide.

Bis(2-phenylethane sulfanylthiocarbonyl) disulfide (6.0 g, 14 mmol) and azobisisobutyronitrile (AIBN, 3.5 g, 21 mmol) were dissolved in ethyl acetate (100 mL)

and deoxygenated *via* purging nitrogen for 30 min. This reaction mixture was immersed into a preheated oil bath at 92 °C and heated for 18 h under nitrogen atmosphere. The organic phase was evaporated under vacuum and the crude product was purified *via* silica chromatography utilising a mixed eluent (7:3 petroleum ether/ethyl acetate, gradually increasing to 3:7) to isolate 2-cyano-2-propyl phenethyl trithiocarbonate (PETTCCP) as a viscous orange oil. The oil was further dried under vacuum at 35 °C to evaporate residual solvent. The purified PETTCCP product was an orange oil at ambient temperature and solidified when stored at 5 °C (6.2g, 74% yield).

^{1}H NMR (400 MHz, $CDCl_3$, **Figure A.5**), d [ppm]: 1.89 (s, 6H), 2.94–3.05 (m, 2H), 2.51–3.63 (m, 2H), 7.17–7.37 (m, 5H). ^{13}C NMR (400 MHz, $CDCl_3$), d [ppm]: 27.18 (CH_3), 34.23 (CH_2Ph), 37.95 (CH_2S), 42.60 ($C(CH_3)_2CN$), 120.53 (CN), 126.95 (p-Ph), 128.70 (o-Ph/m-Ph), 128.81 (o-Ph/m-Ph), 139.36 (Ph–CH_2), 217.49 (CS).

3.2.3. Synthesis of poly(benzyl methacrylate) *via* RAFT miniemulsion polymerisation

In a typical protocol, the synthesis of $PBzMA_{300}$ *via* RAFT miniemulsion polymerisation was conducted at a dispersed phase content of 20% w/w, using: BzMA (7.8 g, 44.087 mmol); PETTCCP (41.4 mg, 0.147 mmol); AIBN (4.8 mg, 0.029 mmol, [CTA]/[initiator] = 5); Lutensol TO 20 (604.0 mg, 7.8% w/w related to BzMA); HD (185.2 mg, 2.4% w/w related to BzMA); and water (31.4 g). The dispersed and the aqueous phases were prepared separately. The dispersed phase was prepared by thoroughly mixing BzMA, HD, AIBN and CTA (PETTC or PETTCCP, if used) by magnetic stirring until homogeneous. The dispersed phase was then added to the aqueous solution of surfactant under vigorous stirring at 800 rpm for 60 min to form a coarse emulsion. This coarse emulsion was ultrasonicated using an ultrasonic processor CPX-750 (Cole Palmer, maximum output power of 750 W) at an amplitude of 70% for 5 min (10 seconds pulse on and 5 seconds pulse off) in an ice-water bath to prevent overheating during miniemulsification. The obtained miniemulsion was then transferred to a 100 mL two-necked round-bottom flask equipped with a condenser and a nitrogen inlet. The reactor contents were deoxygenated by purging with nitrogen for 10 min at room temperature. After deoxygenation, the round-bottomed flask was immersed into a preheated oil bath at 70 °C, corresponding to time zero of the polymerisation. The

reaction was heated for 240 min and magnetically stirred at 150 rpm. Samples were periodically withdrawn with a degassed needle from the bottom of the flask to monitor the conversion of monomer and the evolution of molar mass. Polymerisations were quenched by cooling to room temperature and exposing to air.

3.2.4. Characterisation

3.2.4.1. Gravimetry

Monomer conversions during polymerisations were determined by withdrawing samples from the reactor at different times and weighed (approximately 1.0 g) in 7 mL vials. After weighing, the samples were immediately quenched with approximately 10 µL of 1% w/w hydroquinone in an ice-water bath. The specimens were placed in an oven and dried at 60 °C to constant weight. Conversions were calculated from the measured dry residue.

3.2.4.2. Dynamic light scattering

Dynamic light scattering (DLS) studies were performed using a Malvern Zetasizer Nano ZS instrument equipped with a He–Ne solid-state laser operating at 633 nm using back-scattered light at a scattering angle of 173°. Polymer dispersions without any purification were diluted to approximately 0.1% w/w using deionised water. Samples were analysed using disposable plastic cuvettes at 25 °C. Data were averaged over three consecutive measurements.

3.2.4.3. Gel permeation chromatography

Molar masses and molar mass distributions were assessed using a gel permeation chromatography (GPC) instrument equipped with an Agilent 1260 Infinity pump injection module, an Agilent 1260 Infinity II refractive index detector and three Phenomenex phenogel columns with a mobile phase of THF at 35 °C. Polymer dispersions were dried at 60 °C in an oven to remove water, followed by dissolution in HPLC grade THF to approximately 0.3% w/w prior to GPC analysis. Calibration was achieved using a series of polystyrene standards (ranging from 1×10^3 to 2×10^6 g mol^{-1}).

3.2.4.4. Transmission electron microscopy

Transmission electron microscopy (TEM) images were recorded using a FEI Tecnai G2 20 instrument operating at an accelerating voltage of 200 kV and connected to a Gatan 1k CCD camera. Samples for TEM observation were prepared by depositing 3 µL of diluted copolymer dispersion (approximately 0.1% w/w) onto 400 mesh carbon-coated copper grids for 30 min and then carefully blotted using filter paper to remove excess solution. The samples were stained in a vapour space above ruthenium tetroxide (RuO_4) solution at room temperature for 7 min.[349] Mean nanoparticle diameters were determined using ImageJ software and over 200 randomly selected particles were measured for each sample.

3.2.4.5. Nuclear magnetic resonance spectroscopy

Proton (^1H) and carbon (^{13}C) nuclear magnetic resonance spectroscopy (NMR) spectra were acquired on a Bruker Advance III 400 MHz spectrometer with 128 scans averaged per spectrum. Samples were dissolved in $CDCl_3$ prior to NMR analysis.

3.2.4.6. Surface interfacial tension

Surface interfacial tension (IFT) measurements were determined by the pendant drop technique using a Drop Shape Analyzer DSA-100 from KRÜSS GmBH (Hamburg, Germany) and Drop Shape Analysis software (DSA/V 1.9). Stock solutions were prepared for all surfactants, which were diluted to the required concentration using deionised water. All samples were stirred at 150 rpm for 30 min before analysis. A 15-gauge needle (external diameter of 1.835 mm) was used to produce a drop profile at the tip. A setscrew was used to extract the solution with controlled flow rate and volume at ambient temperature (~23 °C). The pendant drop configuration was fitted using the Young-Laplace model to determine interfacial tension. IFT values were averaged over seven measurements.

3.2.4.7. Number of particles per unit volume

The number of particles per unit volume (N_p) was calculated from the Z-average particle diameter (D_h) obtained *via* DLS and polymer concentration using **Equation 3.1**:[394]

$$N_p = \frac{6m}{\pi \rho {D_h}^3} \qquad \textbf{Equation 3.1}$$

Where ρ represents the density of poly(benzyl methacrylate) (PBzMA, assumed to be 1.179 g mL^{-1})[395,396] and m is the mass of polymer per unit volume.

3.2.4.8. Rate of polymerisation

The conversion-time plots for PBzMA synthesised *via* RAFT miniemulsion polymerisation indicate that these are *pseudo* first-order kinetic reactions. Therefore, the overall polymerisation rate (R_p) was calculated using the concentration change of monomer in a certain polymerisation time using **Equation 3.2**:[6]

$$\boldsymbol{R_p = -\frac{dM}{dt}} \qquad \textbf{Equation 3.2}$$

Where dM represents the disappearance of monomer (benzyl methacrylate, BzMA) calculated using gravimetry and dt represents the polymerisation time.

3.2.4.9. Polymerisation rate per particle

Polymerisation rate per particle (R_N) was calculated using **Equation 3.3**:

$$\boldsymbol{R_N = \frac{R_p}{N_p}} \qquad \textbf{Equation 3.3}$$

Where R_p is rate of polymerisation calculated using **Equation 3.2** and N_p is number of particles per unit volume calculated using **Equation 3.1**.

3.3. Results and discussion

3.3.1. Surfactant selection for miniemulsion polymerisation of BzMA

In order to ascertain a suitable surfactant for miniemulsion polymerisation of BzMA, several surfactants were screened by monitoring the stability of BzMA miniemulsion droplets obtained after ultrasonication. A conventional ionic surfactant (SDS) and a series of Lutensol TO non-ionic surfactants, including TO 3, TO 8, TO 15, TO 20 and TO 109, were evaluated. All of these surfactants allowed the formation of BzMA miniemulsions, which remained stable over the timescale of a typical miniemulsion polymerisation. However, Lutensol TO 20 formed emulsions that were stable for the longest period of time (over 11 days), and thus was chosen as the optimal non-ionic surfactant from this range to investigate further.

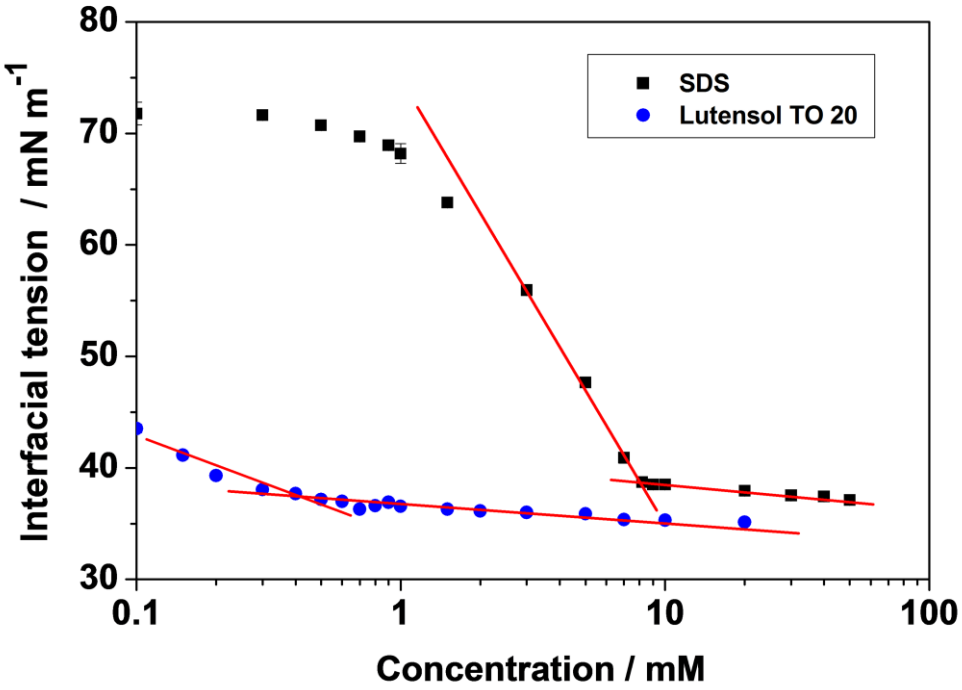

Figure 3.1. Critical micelle concentration (CMC) determination using pendant drop analysis of interfacial tension for sodium dodecyl sulfate (SDS) anionic surfactant and Lutensol TO 20 non-ionic surfactant in deionised water at 23 °C.

Figure 3.1 shows critical micelle concentrations (CMC) determined using pendant drop analysis of interfacial tension for SDS and Lutensol TO 20 in deionised water. The CMC for SDS was approximately 9.2 mM, which is in agreement with the literature (~8 mM).[397,398] In contrast, the CMC of TO 20 (~0.5 mM) was much lower than that of SDS, indicating that TO 20 can act as a more efficient emulsifier.[399,400]

The difference in diameter between the emulsified droplets and resulting latexes can be used to indicate polymerisation type. For example, if the resulting latex size is significantly smaller than the monomer reservoir droplets, it can be classified as emulsion polymerisation. Whereas if the resulting latex is equal in diameter to the initial droplets, it is classified as miniemulsion polymerisation.[146,150] A one-to-one transfer from initial droplets to latexes is possible only when using a suitable surfactant for emulsification in the appropriate concentration range.[150] However, the surfactant concentration used in a miniemulsion formulation is generally above the CMC determined in deionised water. This is because the majority of surfactant molecules locate at the monomer/water droplet interface after the emulsification step.[138] Therefore, only a small proportion of surfactant molecules dissolve in the continuous phase, meaning the surfactant

concentration is actually lower than CMC. This prevents micellar nucleation.[133,401] For example, Landfester and co-workers reported poly(methyl methacrylate) latexes synthesised *via* miniemulsion polymerisation using SDS surfactant at concentrations up to 40 mM, which is much higher than the CMC for SDS in pure deionised water (~8 mM).[138,146] The same research group also demonstrated that polystyrene latexes can be synthesised *via* miniemulsion polymerisation using 0.5–50% w/w SDS surfactant relative to monomer.[133]

A series of experiments were conducted using a relatively wide range of surfactant concentrations (**Table 3.1**) to determine the optimal conditions for miniemulsion polymerisation of BzMA. **Figure 3.2** and **Figure 3.3** show the evolution of hydrodynamic diameter as a function of time for conventional free-radical miniemulsion polymerisation of BzMA using a range of SDS anionic surfactant and HD hydrophobe concentrations. In most cases, the final PBzMA latex diameter was significantly smaller than the initial miniemulsion droplets. This indicated that regular emulsion polymerisation was taking place as opposed to miniemulsion polymerisation.

Figure 3.4 shows the mean diameter of PBzMA latexes synthesised using a wide range of TO 20 non-ionic surfactant concentrations. At surfactant concentrations below 0.5% w/w, a relatively large difference between the monomer droplet and final latex diameters were observed. Above 7.8% w/w surfactant, sub-micron latexes were obtained, which had diameters similar to the initial droplet diameter, indicating successful miniemulsion conditions. On increasing the surfactant concentration from 0.1 to 23.3% w/w, the mean latex diameter decreased from approximately 2400 to 164 nm. As expected, higher surfactant concentrations resulted in smaller polymer particles due to the lower surface tension of the system.[133] It is noteworthy that the sub-500 nm latexes, which had a similar diameter to the initial droplet size were achieved using a TO 20 concentration ≥7.8% w/w (or ≥19 mM). This concentration was approximately 38 times greater than the CMC determined in deionised water (~0.5 mM). Given the suitability of Lutensol TO 20 for miniemulsion polymerisation of BzMA, this surfactant was utilised in all subsequent miniemulsion polymerisations reported herein.

Table 3.1. Monomer, hydrophobe, initiator and surfactant concentration for PBzMA latexes synthesised *via* conventional miniemulsion polymerisation at 70 °C.

Entry	BzMA[a] / % w/w	HD[b] / % w/w	AIBN[b] / % w/w	SDS[b] / % w/w	TO 20[b] / % w/w
1	18.9	4.2	1.7	0.2	—
2	18.9	4.2	1.7	1.3	—
3	18.9	4.2	1.7	8.8	—
4	18.9	1.1	1.7	1.3	—
5	18.9	2.1	1.7	1.3	—
6	18.9	6.4	1.7	1.3	—
7	19.3	2.4	1.2	—	0.1
8	19.3	2.4	1.2	—	0.3
9	19.3	2.4	1.2	—	0.5
10	19.3	2.4	1.2	—	1.0
11	19.3	2.4	1.2	—	1.8
12	19.3	2.4	1.2	—	2.6
13	19.3	2.4	1.2	—	3.6
14	19.3	2.4	1.2	—	5.2
15	19.3	2.4	1.2	—	7.8
16	19.3	2.4	1.2	—	15.5
17	19.3	2.4	1.2	—	23.3

[a] Concentrations given are relative to total weight. [b] Concentrations given are relative to BzMA.

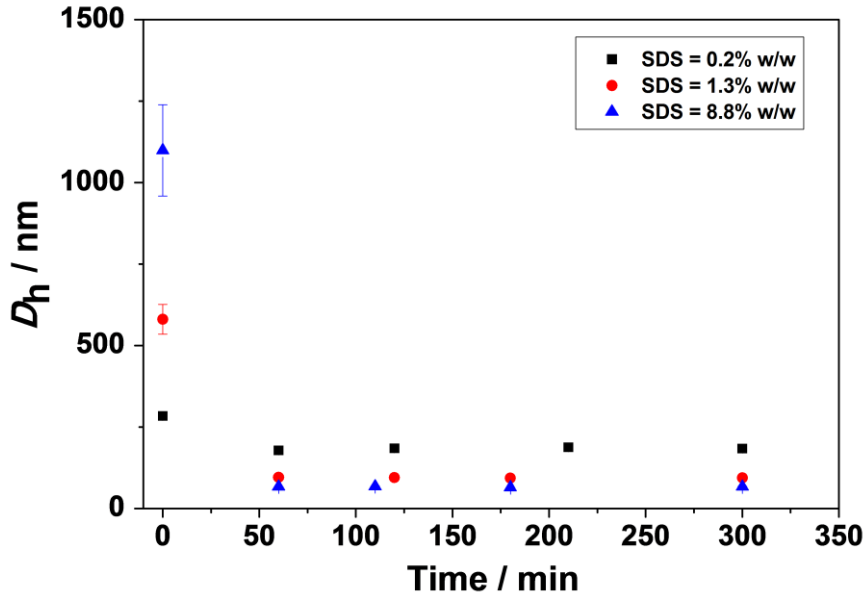

Figure 3.2. Mean hydrodynamic diameter (D_h) versus reaction time for PBzMA latexes synthesised *via* conventional miniemulsion polymerisation with varying SDS concentration at 70 °C. Polymerisations were conducted at a dispersed phase content of 20% w/w with the concentration of HD fixed at 4.2% w/w relative to BzMA (entries 1–3, **Table 3.1**).

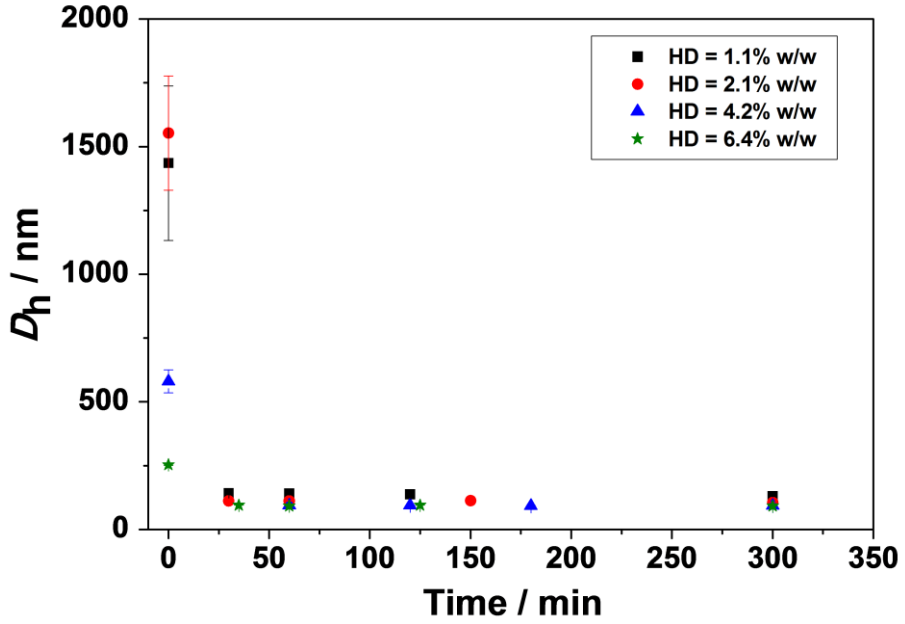

Figure 3.3. Mean hydrodynamic diameter (D_h) versus reaction time for PBzMA latexes synthesised *via* conventional miniemulsion polymerisation with varying HD concentration at 70 °C. The concentration of SDS was fixed at 1.3% w/w relative to BzMA (entries 2 and 4–6, **Table 3.1**).

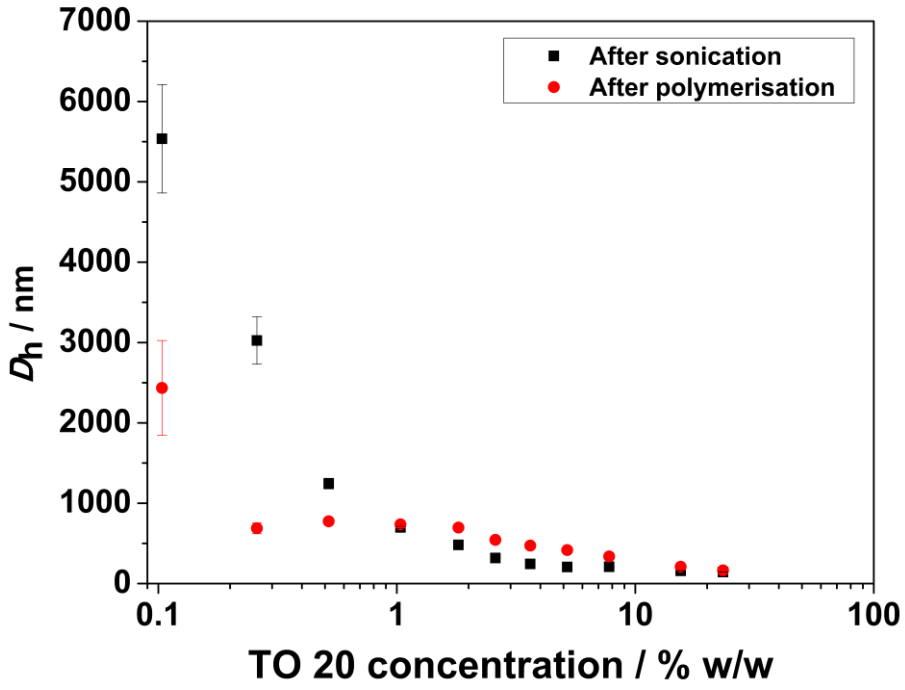

Figure 3.4. Effect of Lutensol TO 20 non-ionic surfactant concentration on the mean hydrodynamic diameter (D_h) of PBzMA latexes synthesised *via* conventional miniemulsion polymerisation at 70 °C for 240 min. Polymerisations were conducted at a dispersed phase content of 20% w/w and the concentration of HD was fixed at 2.4% w/w relative to BzMA (entries 7–17, **Table 3.1**).

3.3.2. Comparison of conventional free-radical miniemulsion polymerisation with RAFT-mediated miniemulsion polymerisation

Miniemulsion polymerisation of BzMA was conducted in the presence of two RAFT CTAs (PETTC and PETTCCP, target DP = 300, see **Figure 3.5** for chemical structures) and without a CTA under otherwise identical conditions. It was observed that PBzMA latexes synthesised *via* conventional free-radical miniemulsion polymerisation achieved full monomer conversion within 40 min (**Figure 3.6**) whereas the two RAFT-mediated reactions took approximately 60–100 min to reach full conversion. Furthermore, the molar mass of PBzMA was much higher and the molar mass distribution was broader ($M_w/M_n > 3.0$) in the absence of a CTA than for the polymers synthesised using the RAFT CTAs (**Figure 3.5**, **Figure 3.6** and **Table 3.2**). This indicates that RAFT control over BzMA polymerisation was achieved in the presence of both PETTC and PETTCCP RAFT agents. Therefore, it is possible to obtain PBzMA with a desired molar mass and relatively low molar mass distribution. Furthermore, the use of a CTA allows the formation of PBzMA which can be subsequently chain extended with other monomers to form block copolymers and other complex architectures.

The mean particle diameter of PBzMA latexes prepared with no CTA and using PETTCCP were 338 nm and 325 nm, respectively. However, the particle diameter was significantly higher (577 nm) when using PETTC. This can be attributed to the PETTC being more hydrophilic than PETTCCP, and thus having an increased ability to cross into the aqueous phase. Therefore, PETTC may form a surfactant/cosurfactant structure at the droplet-water interface and lead to an increased particle diameter.[377] Nevertheless, the minor difference in particle diameter observed for PBzMA latexes prepared by conventional miniemulsion polymerisation and using PETTCCP, as well as the increased control over polymer molar mass afforded, indicates the suitability of PETTCCP for RAFT-mediated miniemulsion polymerisation of BzMA. Thus, the influence of hydrophobe, initiator and CTA concentration were investigated further.

Table 3.2. Summary of latexes and initial droplet diameter ($D_{h,droplet}$) for miniemulsion polymerisation of BzMA at 70 °C for 240 min using various RAFT CTAs. Polymerisations were conducted at a dispersed phase content of 20% w/w with the concentration of HD and TO 20 fixed at 2.4% w/w and 7.8% w/w relative to BzMA, respectively.

Entry	CTA	Conversion[a] / %	D_h[b] / nm	M_n[c] / kg mol^{-1}	M_w/M_n[c]	$D_{h,droplet}$[b] / nm
1	No CTA	99.9	338 (0.14)	255.1	3.06	210 (0.18)
2	PETTC[d]	97.3	577 (0.16)	36.4	1.22	208 (0.19)
3	PETTCCP[d]	99.6	325 (0.12)	36.5	1.27	190 (0.19)

[a] Determined *via* gravimetry. [b] Obtained *via* DLS analysis, where DLS polydispersity index values are indicated in brackets. [c] Determined by THF GPC analysis. [d] Target DP = 300; [CTA]/[AIBN] = 0.4.

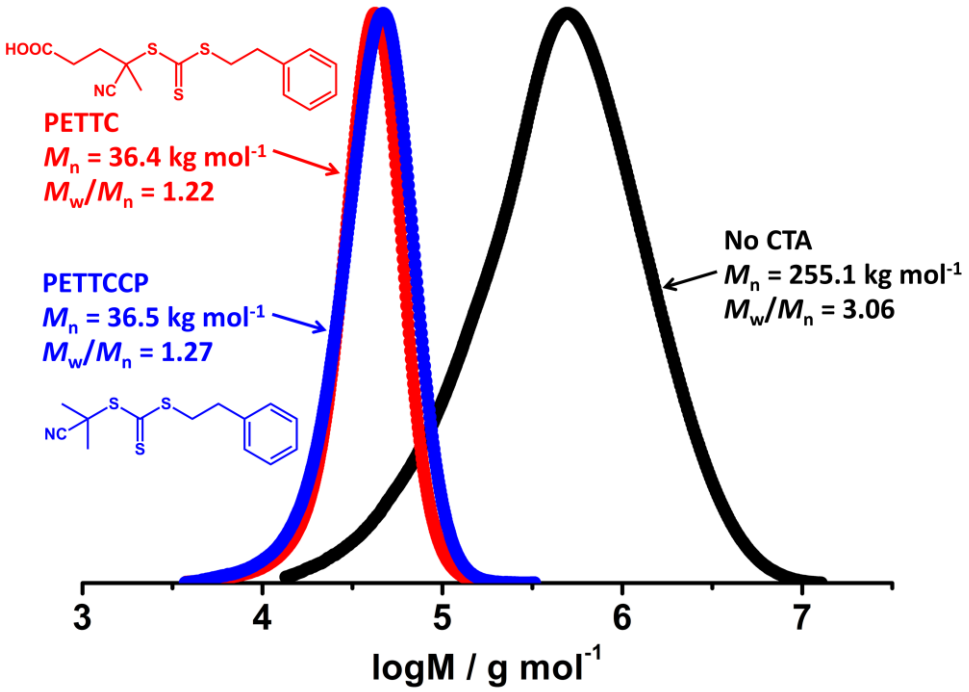

Figure 3.5. GPC chromatograms for PBzMA synthesised *via* RAFT miniemulsion polymerisation in the presence of no CTA (black), PETTC (red) and PETTCCP (blue) at 70 °C. The target PBzMA degree of polymerisation (DP) in the presence of RAFT CTAs was 300 and [CTA]/[AIBN] was 0.4. Polymerisations were conducted at a dispersed phase content of 20% w/w with the concentration of HD and TO 20 fixed at 2.4% w/w and 7.8% w/w relative to BzMA, respectively. Monomer conversions using no CTA, PETTC and PETTCCP CTA were 99.9%, 97.3% and 99.6%, respectively (**Table 3.2**).

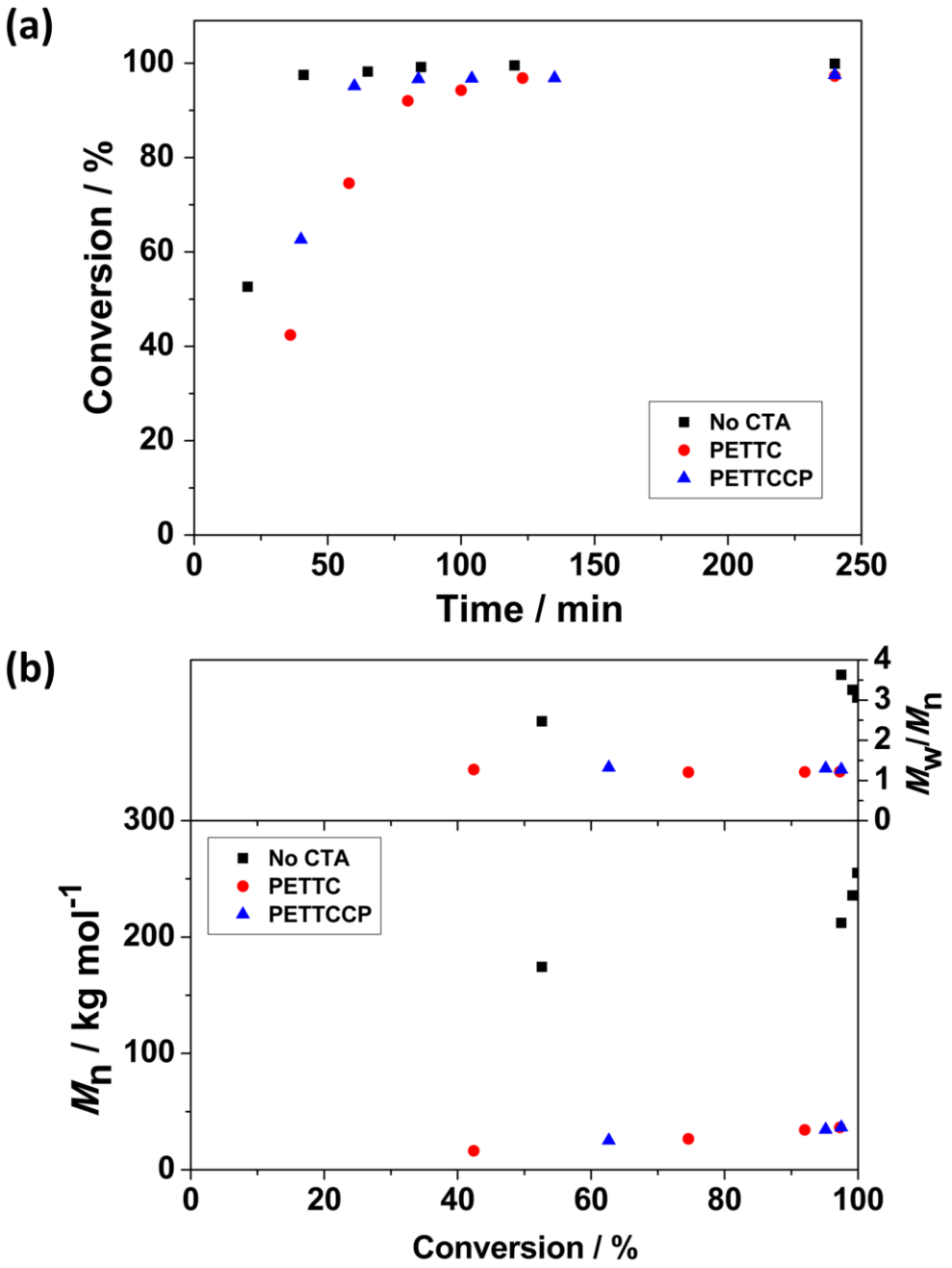

Figure 3.6. (a) Monomer conversion versus reaction time and (b) M_n and M_w/M_n versus monomer conversion for PBzMA synthesised *via* RAFT miniemulsion polymerisation in the presence of no CTA, PETTC and PETTCCP at 70 °C. The target PBzMA degree of polymerisation (DP) in the presence of RAFT CTAs was 300 and [CTA]/[AIBN] was 0.4. Polymerisations were conducted at a dispersed phase content of 20% w/w, with the concentration of HD and TO 20 fixed at 2.4% w/w and 7.8% w/w relative to BzMA, respectively. Monomer conversions using no CTA, PETTC and PETTCCP CTA were 99.9%, 97.3% and 99.6%, respectively (**Table 3.2**).

3.3.3. Influence of hydrophobe concentration

The use of a small quantity of HD as a hydrophobe allows the build-up of osmotic pressure in miniemulsion droplets, providing stability against Ostwald ripening.[131] Thus, the influence of HD concentration on RAFT miniemulsion polymerisation of BzMA was investigated by varying the HD concentration between 1.2–9.5% w/w, based on BzMA, while the concentration of monomer, initiator, surfactant and CTA remained unchanged (**Table 3.3.**). With increasing HD concentration, the measured PBzMA latex diameter (D_h) decreases from 338 to 296 nm, corresponding to a calculated increase in the number of particles per unit volume (N_p). This indicates that with higher HD concentrations, more droplets can be stabilised against Ostwald ripening effects and the average droplet size decreases. However, the influence of HD on polymerisation kinetics was negligible with high monomer conversions being achieved in all cases within 60 min (**Figure 3.7a**). Similarly, no significant differences in PBzMA molar mass evolution were observed (**Figure 3.7b**), with the final latexes having relatively consistent molar masses and molar mass distributions (**Table 3.3.**). These observations suggest that these miniemulsion polymerisations were under good RAFT control. Furthermore, there was no obvious influence of HD concentration on the overall polymerisation rate (R_P in **Table 3.3.**). However, due to the increased number of particles generated with more HD, the mean polymerisation rate per particle (R_N) decreased with increasing HD concentration (**Table 3.3.** and **Figure 3.8**).

Table 3.3. Summary of PBzMA latexes synthesised *via* RAFT miniemulsion polymerisation with varying HD concentration at 70 °C for 240 min. The concentration of Lutensol TO 20 was fixed at 7.8% w/w relative to BzMA and [BzMA]:[PETTCCP]:[AIBN] = 300:1:2.3.

Entry	HD[a] / % w/w	Conversion[b] / %	M_n[c] / kg mol^{-1}	M_w/M_n[c]	D_h[d] / nm	N_p[e] / x 10^{14} mL^{-1}	R_P[f] / M sec^{-1}	R_N[g] / x 10^{-15} M s^{-1}
1	1.2	98.5	36.0	1.31	338 (0.06)	1.40	0.34	2.45
2	2.4	98.9	36.5	1.27	330 (0.12)	1.50	0.34	2.30
3	4.8	94.6	36.0	1.29	325 (0.10)	1.57	0.33	2.10
4	7.2	95.8	34.2	1.29	299 (0.07)	2.02	0.33	1.65
5	9.5	94.3	34.9	1.29	296 (0.09)	2.08	0.33	1.58

[a] Relative to BzMA monomer. [b] Determined by gravimetry. [c] Determined by THF GPC analysis. [d] Obtained *via* DLS analysis, where DLS polydispersity index values are indicated in brackets. [e] Number of particles per unit volume calculated using **Equation 3.1**. [f] Rate of polymerisation calculated using **Equation 3.2**. [g] Polymerisation rate per particle calculated using **Equation 3.3**.

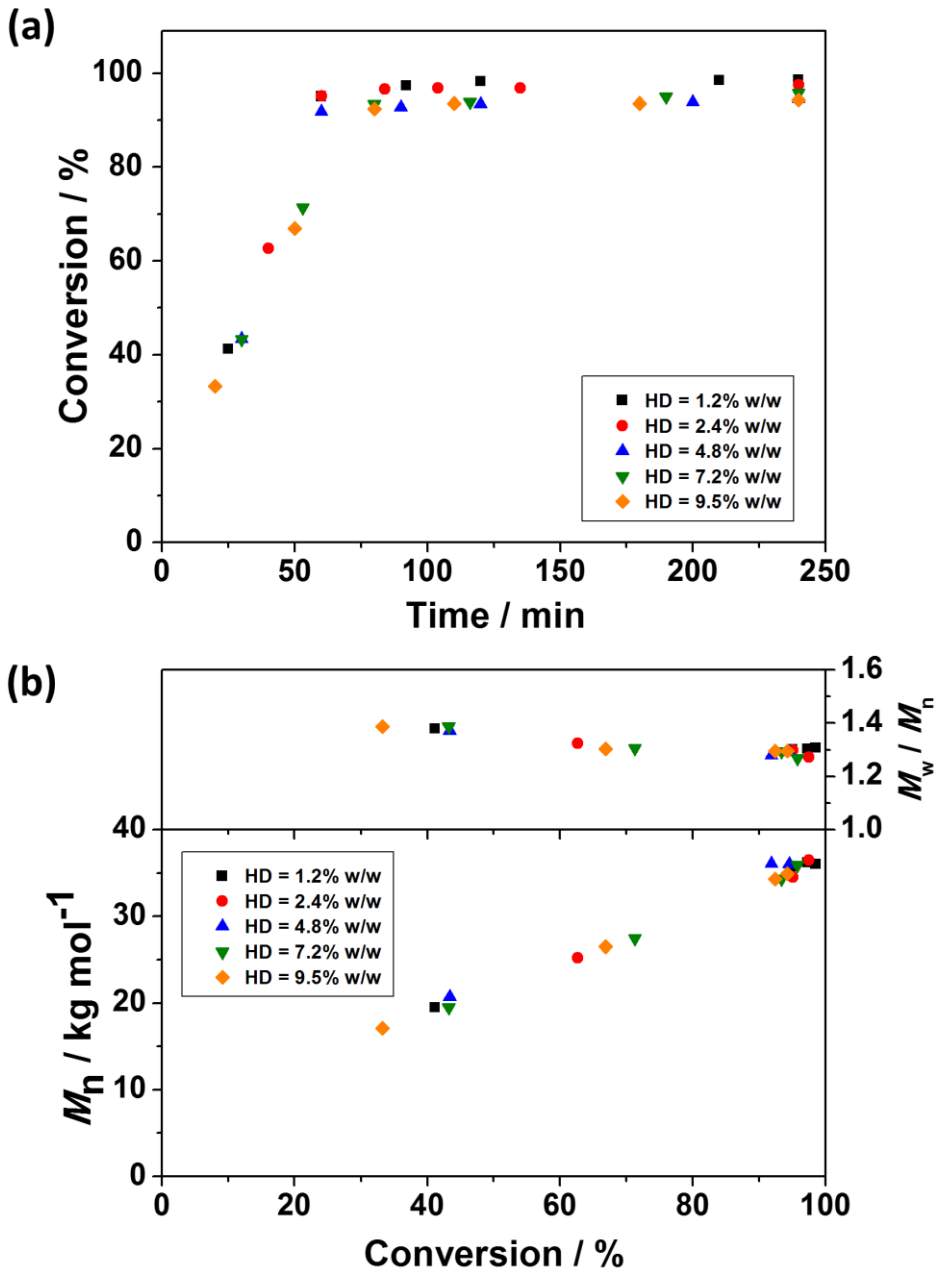

Figure 3.7. (a) Monomer conversion versus reaction time and (b) M_n and M_w/M_n versus monomer conversion for PBzMA synthesised *via* RAFT miniemulsion polymerisation with varying HD concentration relative to BzMA at 70 °C. [BzMA]:[PETTCCP]:[AIBN] = 300:1:2.3 and the concentration of TO 20 surfactant was fixed at 7.8% w/w relative to BzMA.

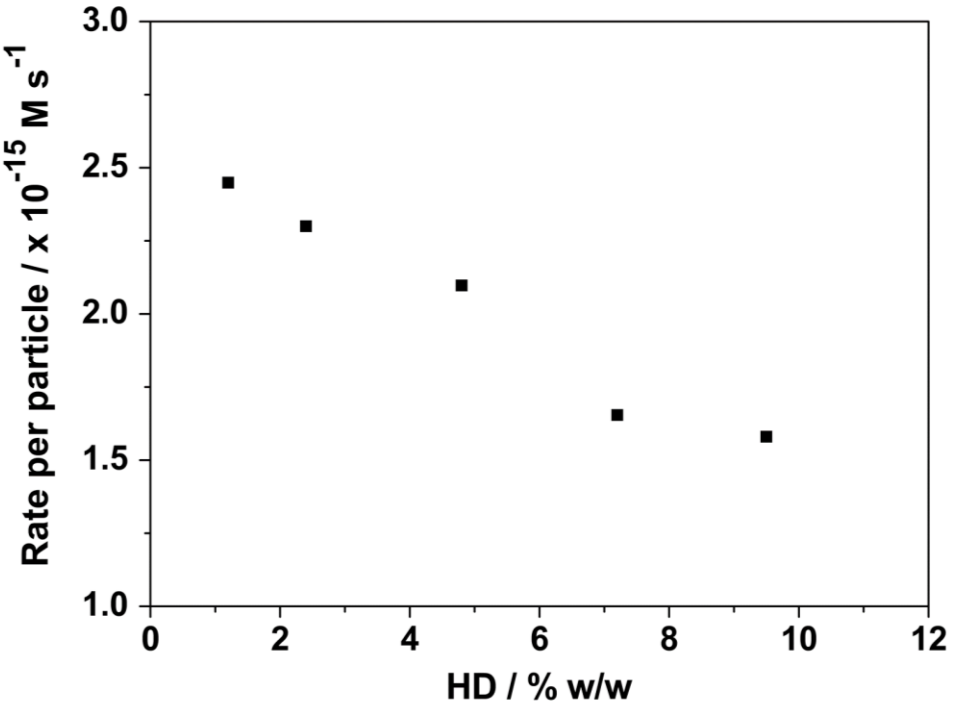

Figure 3.8. Effect of HD concentration on the rate of polymerisation per particle for PBzMA synthesised *via* RAFT miniemulsion polymerisation with varying HD concentration relative to BzMA at 70 °C. [BzMA]:[PETTCCP]:[AIBN] = 300:1:2.3. The concentration of TO 20 surfactant was fixed at 7.8% w/w relative to BzMA.

3.3.4. Influence of initiator concentration

The influence of initiator concentration was investigated by varying the [PETTCCP]:[AIBN] ratio whilst keeping the concentration of monomer, hydrophobe, surfactant and chain transfer agent constant (**Table 3.4**). In most cases, >90% monomer conversion was achieved after 240 min (**Figure 3.9a**). Furthermore, increasing the amount of initiator increases the overall rate of polymerisation (R_p) and follows a power-law relationship $R_p \alpha [AIBN]^{1/2}$.[37,83,93] **Figure 3.9b** shows the approximately linear relationship between $\ln([M]_0/[M])$ and reaction time, indicating the polymerisations were first-order with respect to monomer concentration.[29] **Figure 3.9c** shows the evolution of molar mass and molar mass dispersity (M_w/M_n) versus monomer conversion. It is noteworthy that unlike the polymerisation rate, which was strongly influenced by the initiator concentration, there were negligible differences in the observed molar mass and molar mass dispersity values (**Figure 3.9d**).

Table 3.4. Summary of PBzMA latexes synthesised *via* RAFT miniemulsion polymerisation with varying [PETTCCP]:[AIBN] ratio at 70 °C for 240 min. The target DP was 300. Polymerisations were conducted at a dispersed phase content of 20% w/w with the concentration of HD and TO 20 fixed at 2.4% w/w and 7.8% w/w relative to BzMA, respectively.

Entry	[PETTCCP]:[AIBN] ratio	Conversion[a] / %	M_n[b] / kg mol^{-1}	M_w/M_n[b]	D_h[c] / nm	N_p[d] / x 10^{14} mL^{-1}	R_P[e] / M sec^{-1}	R_N[f] / x 10^{-15} M s^{-1}
1	10	60.0	24.3	1.33	268 (0.08)	2.91	0.21	0.72
2	5	91.8	36.7	1.28	306 (0.15)	1.88	0.32	1.70
3	2	96.4	37.0	1.28	311 (0.08)	1.78	0.34	1.89
4	1	98.5	38.2	1.25	303 (0.11)	1.93	0.34	1.78
5	0.4	98.9	36.5	1.27	330 (0.12)	1.50	0.34	2.30

[a] Determined *via* gravimetry. [b] Determined by THF GPC analysis. [c] Obtained *via* DLS, where DLS polydispersity index values are indicated in brackets. [d] Number of particles per unit volume calculated using **Equation 3.1**. [e] Rate of polymerisation calculated using **Equation 3.2**. [f] Polymerisation rate per particle calculated using **Equation 3.3**.

The relatively linear conversion/time relationships and the *pseudo* first-order kinetic plots (**Figure 3.9**) are reasonably consistent with the features expected for a controlled RAFT polymerisation. This indicates that a rapid main equilibrium between the active propagating radicals and thiocarbonylthio capped dormant species was achieved and a constant number of radical propagating chains was formed during polymerisation.[83] Additionally, no obvious retardation in these formulations was observed and polymerisations proceeded linearly to high monomer conversions (~90% after 240 min, **Figure 3.9a**). In all cases, the evolution of molar mass in relation to monomer conversion was close to linear, with relatively narrow molar mass dispersities obtained (M_w/M_n < 1.3). It is noteworthy that positive y-intercepts were observed in all cases after extrapolating the experimental data for M_n to zero conversion (**Figure 3.9c**). Differences between the GPC calibration standards (polystyrene) and PBzMA may be partially the cause of this positive intercept and deviations from theoretical M_n values.

However, the observed positive y-intercepts may also result from a higher polymerisation rate than that of the addition of growing radicals to the PETTCCP chain transfer agent.[402,403] Therefore, RAFT control was not established instantaneously, resulting in the rapid formation of moderate molar mass species at low monomer conversions. These observations may be considered as hybrid conventional/living behaviour.[43,404] However, this behaviour can be reduced by using a lower ratio of [CTA] to [initiator].[403] For example, the y-intercept was approximately 9 kg mol^{-1} when the [CTA]:[initiator] ratio was 5:1 whereas the y-intercept was approximately 2 kg mol^{-1} (~78% less) when the ratio was 0.4. This indicates that higher initiator concentrations allow more rapid CTA activation, resulting in a shorter time in achieving the main RAFT equilibrium. Nevertheless, the molar mass dispersities of the resultant polymers were relatively low, suggesting this hybrid behaviour had a minor effect on the overall RAFT process.

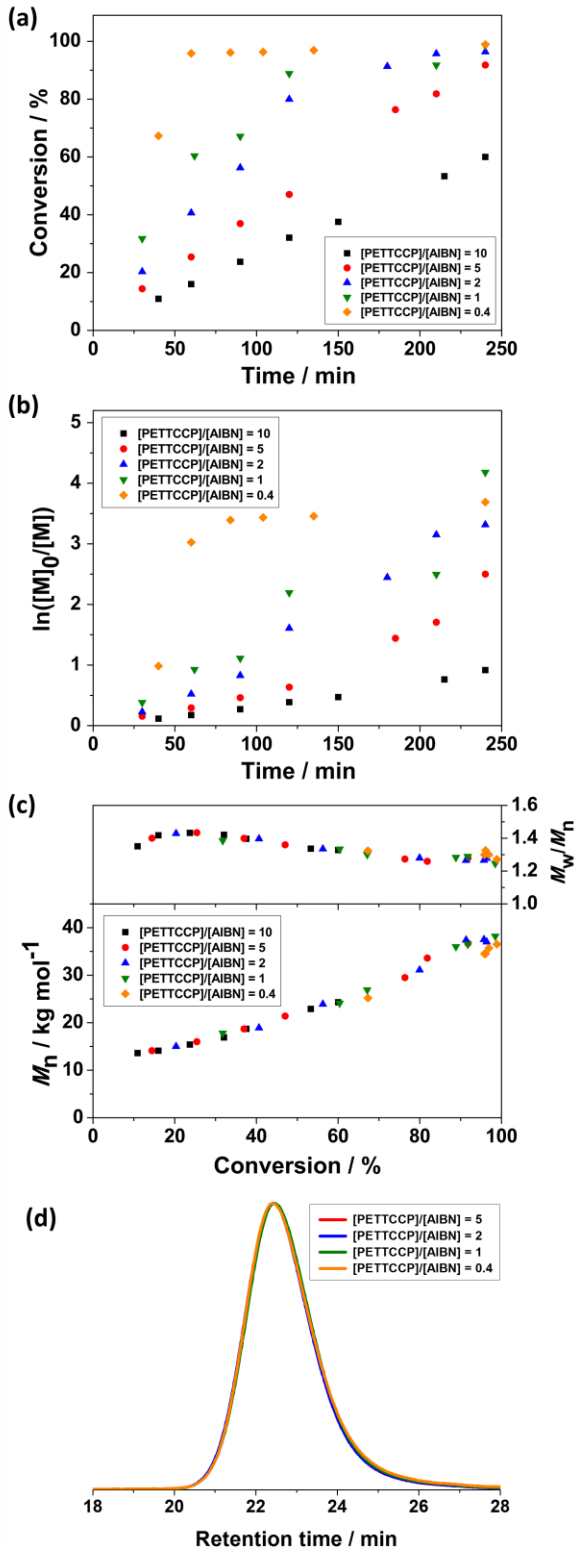

Figure 3.9. (a) Monomer conversion versus reaction time, (b) semi-logarithmic kinetics, (c) M_n and M_w/M_n versus monomer conversion and (d) GPC chromatograms for PBzMA synthesised *via* RAFT miniemulsion polymerisation at 70 °C with varying [PETTCCP]:[AIBN] ratio. The target DP was 300. Polymerisations were conducted at a dispersed phase content of 20% w/w, with the concentration of HD and TO 20 fixed at 2.4% w/w and 7.8% w/w relative to BzMA, respectively.

3.3.5. Influence of RAFT agent concentration

The versatility and limitations of RAFT-mediated miniemulsion polymerisation of BzMA were further investigated by varying the PETTCCP concentration. Specifically, the molar concentration of PETTCCP relative to the dispersed phase was varied from 7.1 mmol L^{-1} (target PBzMA DP = 800) to 28.6 mmol L^{-1} (target PBzMA DP = 200). A [PETTCCP]:[AIBN] ratio of 5:1 was used whilst keeping the concentration of monomer, hydrophobe and surfactant constant (**Table 3.5**). High monomer conversions (~90%) were achieved after 240 min (for DP 200, 300 and 400) or 360 min (for DP 700 and 800, **Figure 3.10a**). Interestingly, the polymerisation rate increased with increasing PETTCCP concentration (or decreasing target DP). For example, the polymerisation rate for PETTCCP at 28.6 mmol L^{-1} (DP = 200) relative to the dispersed phase was approximately 62% faster than for PETTCCP at 7.1 mmol L^{-1} (DP = 800) (**Table 3.5**). In this study, the [CTA]:[initiator] ratio was fixed at 5:1. Thus, increased RAFT CTA concentrations (lower target DP) also meant that the initiator concentration relative to BzMA was also higher. This inevitably led to the faster polymerisation rates observed for lower target DP formulations. It is noteworthy that the rate of polymerisation observed was relatively independent of droplet diameter and rate increases due to compartmentalisation effects were not observed. This can be attributed to the latexes in this work being relatively large (~300 nm).[159,405,406]

$\ln([M]_0/[M])$ versus reaction time for these RAFT miniemulsion polymerisations is shown in **Figure 3.10b**. The approximately linear relationship in all cases indicates that the reactions were first-order with respect to monomer concentration, and thus were well-controlled RAFT polymerisations.[29] GPC chromatograms of PBzMA synthesised with various PETTCCP concentrations at full monomer conversion are shown in **Figure 3.10d**. Unimodal and relatively narrow molar mass distributions ($M_w/M_n < 1.3$) were obtained in all cases, with the M_n clearly increasing with decreasing RAFT agent concentration. The evolution of molar mass and molar mass dispersity (M_w/M_n) versus monomer conversion for PBzMA with various PETTCCP concentrations (target DP 200–800) are shown in **Figure 3.10c**. As the polymerisations progressed, the corresponding dispersity decreased, and the resulting PBzMA had relatively narrow molar mass distributions ($M_w/M_n < 1.3$) at 90% conversion. It is noteworthy that the molar mass increased approximately linear in all cases, even when targeting high DPs.

Table 3.5. Summary of PBzMA latexes synthesised *via* RAFT miniemulsion polymerisation with varying target PBzMA DP at 70 °C. The [PETTCCP]:[AIBN] ratio was fixed at 5:1. Polymerisations were conducted at a dispersed phase content of 20% w/w with the concentration of HD and TO 20 fixed at 2.4% w/w and 7.8% w/w relative to BzMA, respectively.

Entry	Target PBzMA DP	[PETTCCP][a] / mmol L^{-1}	Reaction time / min	Conversion[b] / %	M_n[c] / kg mol^{-1}	M_w/M_n[c]	D_h[d] / nm	N_p[e] / x 10^{14} mL^{-1}	R_P[f] / M sec^{-1}	R_N[g] / x 10^{-15} M s^{-1}
1	200	28.6	240	96.3	25.4	1.24	330 (0.12)	1.49	0.34	2.25
2	300	19.1	240	91.8	36.7	1.28	306 (0.15)	1.88	0.32	1.70
3	400	14.3	240	84.9	43.8	1.27	291 (0.09)	2.18	0.30	1.36
4	700	8.2	360	96.5	78.4	1.29	281 (0.07)	2.67	0.22	0.84
5	800	7.1	360	90.4	78.9	1.31	275 (0.10)	2.84	0.21	0.74

[a] Concentration relative to the dispersed phase. [b] Determined by gravimetry. [c] Determined by THF GPC analysis. [d] Obtained *via* DLS analysis, where DLS polydispersity index values are indicated in brackets. [e] Number of particles per unit volume calculated using **Equation 3.1**. [f] Rate of polymerisation calculated using **Equation 3.2**. [g] Polymerisation rate per particle calculated using **Equation 3.3**.

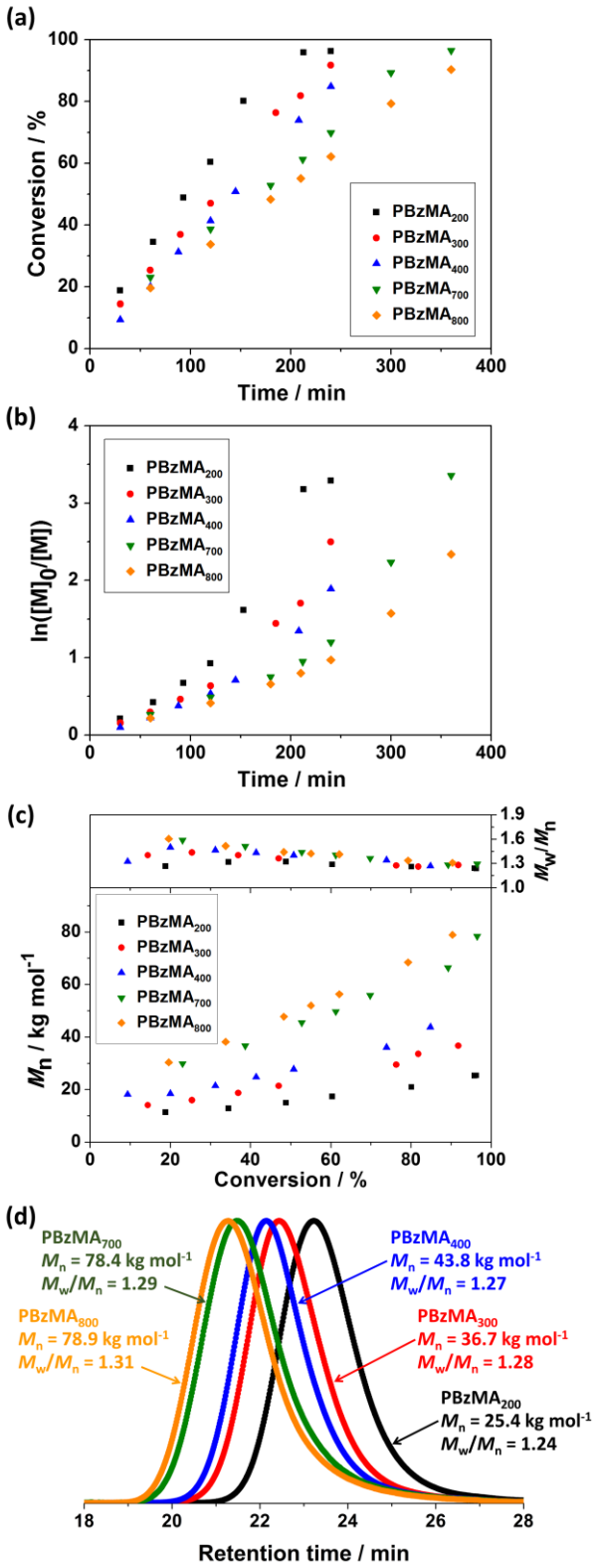

Figure 3.10. (a) Monomer conversion versus reaction time, (b) semi-logarithmic kinetics, (c) M_n and M_w/M_n versus monomer conversion and (d) GPC chromatograms for PBzMA synthesised *via* RAFT miniemulsion polymerisation with varying target DP at 70 °C. The [PETTCCP]:[AIBN] ratio was fixed at 5:1 and polymerisations were conducted at a dispersed phase content of 20% w/w, with the concentration of HD and TO 20 fixed at 2.4% w/w and 7.8% w/w relative to BzMA, respectively.

The measured PBzMA latex diameter (D_h) decreased from 330 to 275 nm with increasing PETTCCP concentration (**Figure 3.11**). This corresponded to a calculated increase in the number of particles per unit volume (N_p) from approximately 1.5 to 2.8×10^{14} mL^{-1}. Furthermore, spherical latexes were obtained in all cases with measured diameters in agreement between TEM (**Figure 3.12** and **Figure A.6**) and DLS (**Table 3.5**). It is noteworthy that the number of particles (N_p) decreased with increasing RAFT agent concentration (**Figure 3.11**). For example, the N_p value for PETTCCP at 28.6 mmol L^{-1} was approximately 48% less than PETTCCP at 7.1 mmol L^{-1}. This is attributed to the increased viscosity of the oil phase.[407] More specifically, formulations with higher PETTCCP concentrations result in droplets, which are more viscous. Thus, fewer droplets are produced using the same ultrasonication procedure and results in larger miniemulsion droplets and final PBzMA latexes.

Finally, PBzMA chain-end stability and fidelity over a 12-month storage period was examined *via* self-blocking experiments (**Figure 3.13**). After being stored at room temperature for over a year, an additional charge of BzMA (target DP of second block = 300) and initiator was added to a dispersion of PBzMA latex (entry 3, **Table 3.4**). GPC analysis indicated a relatively good blocking efficiency and the resulting chain-extended PBzMA homopolymer had a unimodal molar mass distribution and relatively low molar mass dispersity (1.39). This indicates that the majority of the trithiocarbonate RAFT chain-ends remained intact and that these PBzMA latexes could undergo efficient chain extension to form second blocks with other monomers to form more complex latex morphologies.[345,352]

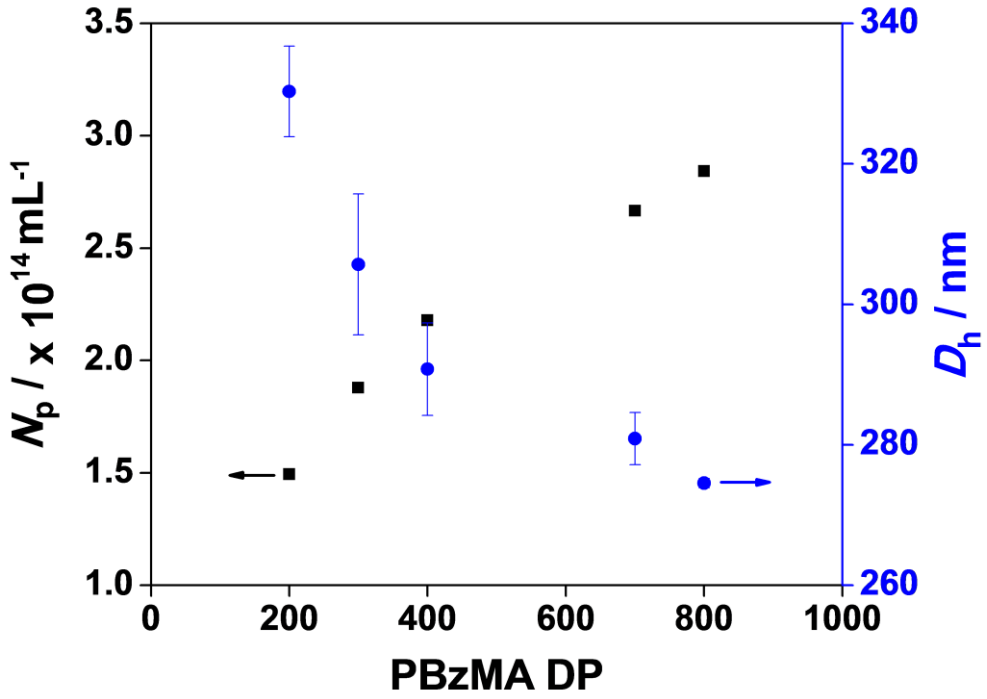

Figure 3.11. Effect of varying target PBzMA DP on the number of particles (N_p) for PBzMA synthesised *via* RAFT miniemulsion polymerisation at 70 °C. The [PETTCCP]:[AIBN] ratio was fixed at 5:1 and polymerisations were conducted at a dispersed phase content of 20% w/w, with the concentration of HD and TO 20 fixed at 2.4% w/w and 7.8% w/w relative to BzMA, respectively.

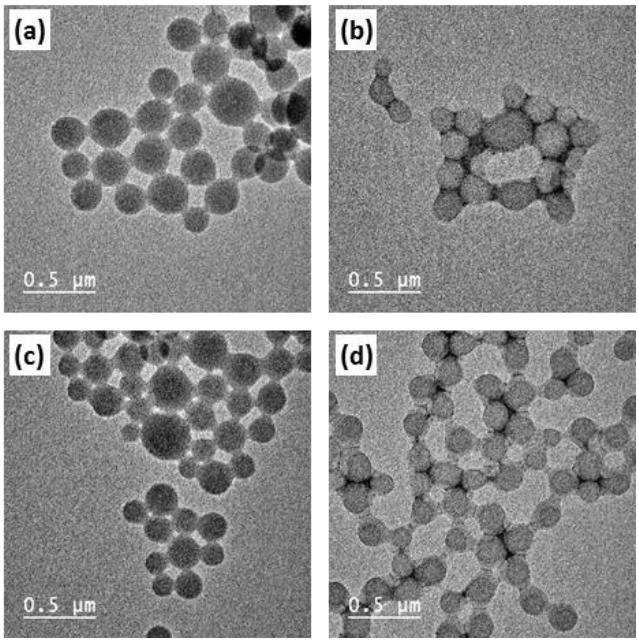

Figure 3.12. Representative TEM images for PBzMA latexes synthesised *via* RAFT miniemulsion polymerisation at 70 °C with varying target DP: (a) 200, (b) 300, (c) 700 and (d) 800. The [PETTCCP]:[AIBN] ratio was fixed at 5:1 and polymerisations were conducted at a dispersed phase content of 20% w/w, with the concentration of HD and TO 20 fixed at 2.4% w/w and 7.8% w/w relative to BzMA, respectively.

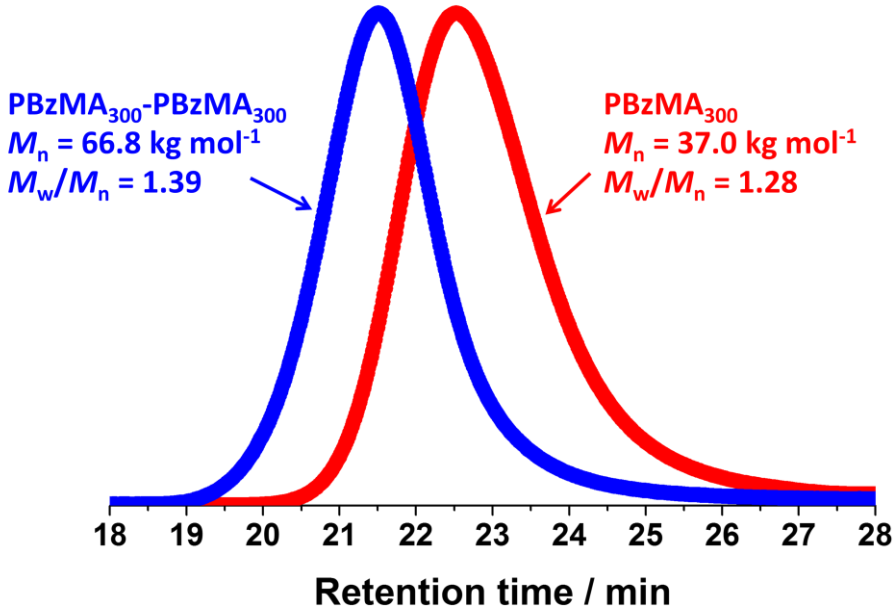

Figure 3.13. GPC chromatograms obtained for a $PBzMA_{300}$ latex prepared *via* RAFT miniemulsion polymerisation and its subsequent chain extension after 12 months of storage using BzMA at 70 °C (20% w/w, target DP of second block = 300).

3.4. Conclusions

Near-monodisperse PBzMA latexes with controlled particle diameters and polymer molar mass were successfully prepared *via* RAFT miniemulsion polymerisation. This was achieved using a relatively hydrophobic chain transfer agent (PETTCCP) and non-ionic Lutensol TO 20 surfactant. Stable miniemulsion droplets were obtained and formed PBzMA latexes upon polymerisation. Much narrower molar mass distributions (M_w/M_n < 1.3) were obtained *via* RAFT miniemulsion polymerisation when compared to conventional miniemulsion polymerisation (M_w/M_n > 3.0). Furthermore, the concentration of hydrophobe, initiator and chain transfer agent were demonstrated to influence the particle diameter, particle number, rate of polymerisation and PBzMA molar mass in the final latexes.

Increasing the hydrophobe (HD) concentration decreased the PBzMA latex diameter (D_h) and increased the number of particles per unit volume (N_p). This indicated that more droplets can be stabilised against Ostwald ripening effects using higher HD concentrations. Furthermore, the mean rate per particle decreased with increasing HD concentration. Increasing initiator (AIBN) concentration increased the overall rate of polymerisation (R_p) and followed a power-law relationship $R_p \alpha [AIBN]^{1/2}$. However, only negligible differences in molar mass, molar mass dispersity and particle diameter values

were observed. Increasing RAFT agent (PETTCCP) concentration increased the measured PBzMA latex diameter (D_h) and the overall rate of polymerisation. The changes in latex diameter can be attributed to the increased viscosity of the oil phase, which results in larger miniemulsion droplets. Furthermore, the approximately linear relationship of $\ln([M]_0/[M])$ versus reaction time, unimodal GPC chromatograms, relatively narrow molar mass distributions ($M_w/M_n < 1.3$) and efficient self-blocking indicated that these were well-controlled RAFT miniemulsion polymerisations.

Chapter Four

Investigating the influence of solution pH on RAFT-mediated PISA of pyridine-functional diblock copolymer nanoparticles

4.1. Introduction

In **Chapter Two** and **Chapter Three**, sterically-stabilised anionic and non-ionic nanoparticles have been successfully prepared *via* RAFT-mediated PISA and RAFT miniemulsion polymerisation, respectively. In this chapter, the RAFT-mediated PISA approach was extended to prepare sterically-stabilised cationic nanoparticles. Furthermore, in order to be consistent with the previous chapters, it was aimed to prepare cationic amphiphilic diblock copolymer nanoparticles with poly(benzyl methacrylate) (PBzMA) as the core-forming block.

In the past two decades, polymerisation-induced self-assembly (PISA) *via* reversible addition-fragmentation chain transfer (RAFT) polymerisation has attracted significant attention for preparation of complex block copolymer nanoparticles with controlled morphology, size and surface functionality.[7-10] PISA has been reported as a versatile and efficient approach to prepare a wide range of diblock copolymer nanoparticles at high solids content without conventional post-polymerisation processing techniques.[228,331] This makes the RAFT-mediated PISA technique amenable to scale-up for industrial production.[222] Furthermore, RAFT-mediated PISA can be conducted in various media, such as aqueous,[9,15,22,27,215,408] alcoholic[24-26] and non-polar solvents.[28-30] Specifically, a solvent soluble RAFT macromolecular chain transfer agent (macro-CTA) is used as a stabiliser block, which chain-extends with a solvent-immiscible or a solvent-miscible monomer to form a second block *via* RAFT emulsion[250,409] or dispersion[6,410] polymerisation, respectively. In comparison to most RAFT dispersion polymerisation formulations, RAFT aqueous emulsion polymerisation has the advantage of being able to polymerise water-immiscible monomers directly in aqueous conditions. Water is a more environmentally friendly solvent than the typical solvents used in dispersion polymerisation formulations, and thus negates the use of undesirable volatile organic compounds (VOCs). In RAFT mediated PISA *via* emulsion polymerisation, the majority of monomer is water-insoluble, but a small percentage of monomer is nonetheless dissolved in the continuous phase and can diffuse to the locus of polymerisation. After adding a small proportion of monomer units to the macro-CTA, nucleation occurs and monomer-swollen micelles are formed. As the polymerisation progresses, the extension of the insoluble block leads to the particle growth. Notably, the low solvation of the growing block copolymer chains inhibits the formation of

higher-order morphologies during PISA process, and generally only kinetically trapped spherical objects are obtained *via* RAFT emulsion polymerisation.[7,332,333]

Stimulus-responsive polymers include those can self-assemble, undergo morphology changes or phase transitions in response to minor external changes in the environment. These responsive polymers are also named smart, intelligent or environmentally responsive polymers and can be responsive to numerous stimuli, such as light, solvent, temperature, chemical agents, ionic strength, electrical field, magnetic field and pH.[411,412] In the past two decades, pH-responsive polymers have attracted great academic and industrial interest as they have wide-span of potential applications, such as sensors, membranes, chromatography and drug delivery.[413-415]

pH-stimuli responsive polymers generally have ionisable basic or acidic functional groups, including sulfonic, carboxyl, phosphate, tertiary amines and pyridine. The ionisation of these functional groups depends on solution pH and can affect polymer structure, surface activity and solubility.[416] Poly(vinyl pyridine)-based block copolymers, e.g. poly(2-vinyl pyridine) (P2VP) or poly(4-vinyl pyridine) (P4VP), are one of the most widely investigated classes of pH-responsive polymers.[416,417] These polymers typically undergo a phase transition above approximately pH 5, resulting from the deprotonation of pyridine groups.[418,419]

Gohy *et al.* synthesised poly(2-vinyl pyridine)-poly((dimethylamino)ethyl methacrylate) diblock copolymers *via* living anionic polymerisation, followed by dissolution of copolymers in aqueous solution at differing pH at 1 g/L to obtain the block copolymer nanoparticles.[420] Armes and coworkers reported poly(ethylene glycol) methacrylate (PEGMA) stabilised P2VP microgels prepared *via* conventional emulsion polymerisation in the presence of divinylbenzene (DVB) cross-linker, and demonstrated that these microgels had swelling behavior below pH 4.5.[320,324,419] However, only a few papers reported the successful preparation of poly(vinyl pyridine) related diblock copolymers *via* RAFT polymerisation. Zamfir *et al.* reported the synthesis of PS–P2VP and PS–P4VP *via* RAFT dispersion polymerisation using PS macro-CTAs.[421] More extensive side reactions and bimodal molar mass distributions were observed for PS–P4VP diblock copolymers than PS–P2VP copolymers due to the greater reactivity and polarity of 4VP than that of 2VP. Convertine *et al.* demonstrated that the synthesis of P2VP and P4VP macro-CTAs can be achieved *via* bulk RAFT polymerisations using cumyl dithiobenzoate

as the CTA in the absence of organic solvents.[92] These macro-CTAs were chain-extended with 4VP or 2VP, and the copolymers had relatively low molar mass distributions, but only low conversions (<40% after polymerisation for 6 h) were achieved. Nieswandt *et al.* successfully prepared P2VP–PS and P4VP–PS *via* RAFT aqueous-alcoholic dispersion polymerisation using P2VP and P4VP as macro-CTAs, respectively.[422] Copolymers with high molar mass (>100 kg mol^{-1}) could be achieved in both cases, but the P4VP–PS had broader molar mass distributions. Nieswandt *et al.* also successfully prepared poly(3-vinyl pyridine)-polystyrene (P3VP–PS) *via* RAFT emulsion polymerisation in DMF/H_2O (50/50, v/v) solvent mixtures. P3VP–PS diblock copolymers with narrow molar mass distribution were obtained.[423] However, in all of the reports described above, block copolymer nanoparticles were formed *via* self-assembly of the copolymers in selective solvents. Although, Nieswandt *et al.* claimed that P2VP–PS,[422] P4VP–PS,[422] and P3VP–PS[423] can be successfully prepared *via* RAFT-mediated PISA, they did not investigate these block copolymer nanoparticles directly. Instead, these copolymers were dissolved in THF and precipitated in an excess of ice-cold *n*-hexane to obtain nanoparticles, and the bulk and surface morphologies of the diblock copolymers were investigated. Therefore, to the best of our knowledge, there are no prior reports on the synthesis and direct characterisation of poly(vinyl pyridine) related block copolymer nanoparticles prepared *via* RAFT-mediated PISA.

Herein, cationic sterically-stabilised poly(2-vinyl pyridine)-poly(benzyl methacrylate) (P2VP–PBzMA) diblock copolymer nanoparticles were prepared *via* RAFT-mediated PISA under aqueous emulsion polymerisation conditions (**Scheme 4.1**). Furthermore, varying the pH of the aqueous continuous phase resulted in the P2VP stabiliser having different solubilities due to protonation/deprotonation of the pyridine groups.[424] This allowed the evaluation of the effect of pH on the formation of P2VP–PBzMA diblock copolymer nanoparticles during PISA. Nanoparticles with tuneable diameters can be prepared *via* varying the solution pH for a fixed stabiliser and/or core-forming block. The resulting nanoparticles were characterised *via* DLS, TEM, aqueous electrophoresis and disc centrifuge photosedimentometry (DCP). Additionally, the P2VP–PBzMA diblock copolymers were characterised by ^{1}H NMR and GPC. For the sake of brevity, shorthand labels are used throughout this chapter: P2VP and PBzMA or "V" and "B" are used to denote the two blocks, respectively.

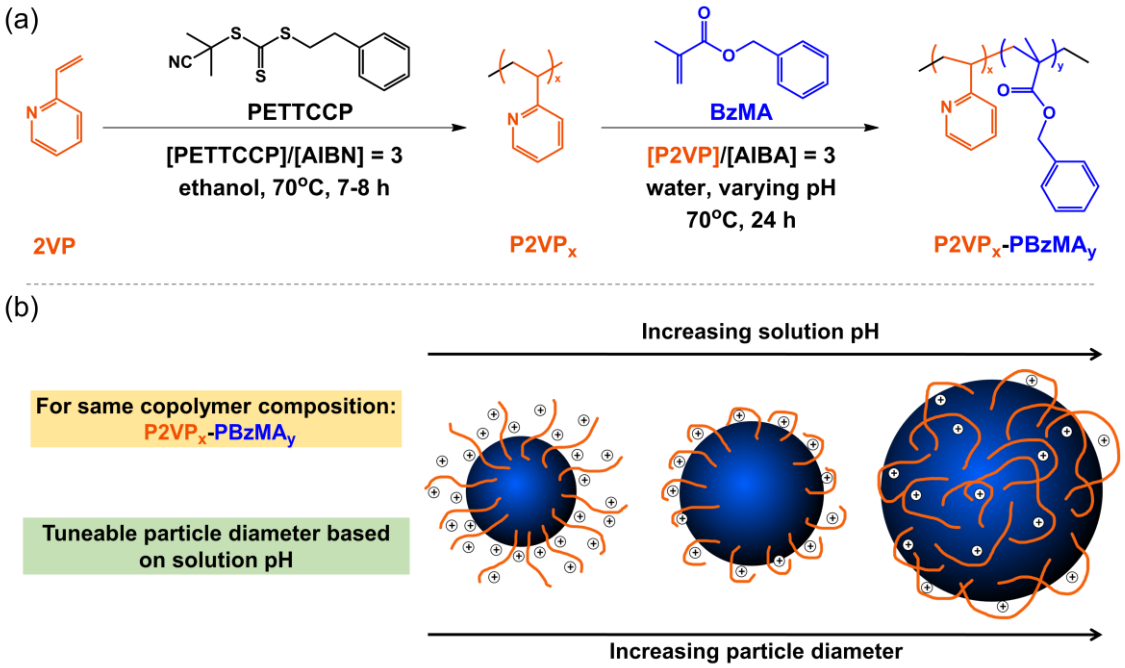

Scheme 4.1. (a) Synthesis of poly(2-vinyl pyridine) (P2VP) macro-CTA *via* RAFT solution polymerisation at 70 °C (15% w/w), followed by RAFT-mediated PISA of benzyl methacrylate (BzMA) in water at varying pH at 70 °C (10% w/w). (b) Schematic representation of how solution pH affects the resulting nanoparticle diameter for a fixed target P2VP–PBzMA composition.

4.2. Experimental details

4.2.1. Materials

2-Vinyl pyridine (2VP; 97%) and benzyl methacrylate (BzMA, 98%) were purchased from Sigma-Aldrich (UK) and Alfa Aesar (UK), respectively, and passed through a column of activated basic alumina to remove inhibitors and impurities before use. Diethyl ether (99%), azobisisobutyronitrile (AIBN, 98%) and 2,2′-azodiisobutyramidine dihydrochloride (AIBA; 97%) were purchased from Sigma-Aldrich (UK) and used as received. Tetrahydrofuran (THF, HPLC grade) was purchased from VWR International (UK) and used as received. Chloroform-*d* ($CDCl_3$) was purchased from Cambridge Isotope Laboratories (UK). 2-Cyano-2-propyl phenethyl trithiocarbonate (PETTCCP) was prepared as described in **Chapter Three**. Ethanol (95%) was purchased from Fisher Scientific (UK) and used as received.

4.2.2. Synthesis of P2VP macro-CTA *via* RAFT solution polymerisation

In a typical protocol for the synthesis of $P2VP_{25}$ macro-CTA *via* RAFT solution polymerisation at 15% solids, 2VP (5.7 g, 54.12 mmol), PETTCCP (609.4 mg, 2.17 mmol), AIBN (118.5 mg, 0.72 mmol, PETTCCP/AIBN molar ratio = 3) and ethanol (35.6 g) were weighed into a 100 mL two-necked round-bottom flask equipped with a condenser and a nitrogen inlet. The reactor contents were deoxygenated by purging nitrogen for 30 min at ambient temperature. After deoxygenation, the round-bottom flask was immersed into a preheated oil bath at 70 °C, corresponding to time zero of the polymerisation. The reaction was heated for 7 hours (or 8 hours for $P2VP_{50}$) and magnetically stirred at 250 rpm. The polymerisation was quenched by rapid cooling in an ice bath and exposure to air. The synthesised polymers were precipitated into an excess of cold diethyl ether and collected by three precipitation/decant cycles. The precipitates were further dried under vacuum at 35 °C to obtain a yellow solid of P2VP macro-CTA.

4.2.3. Synthesis of P2VP–PBzMA diblock copolymer nanoparticles *via* RAFT emulsion polymerisation

A typical protocol for the synthesis of $P2VP_x$–$PBzMA_y$ (V_x–B_y) diblock copolymer nanoparticles *via* RAFT emulsion polymerisation at 10% w/w solids in water was as follows. For $P2VP_{32}$–$PBzMA_{300}$ synthesised in water at pH 2, $P2VP_{32}$ macro-CTA (32.3 mg, 0.009 mmol), AIBA (0.8 mg, 0.003 mmol, CTA/initiator molar ratio = 3) and deionised water were added into a 14 mL vial. The solution pH was slowly adjusted to pH 2 using an aqueous solution of 0.1 M HCl, and then BzMA (467.7 mg, 2.654 mmol) was added. The vial was sealed and deoxygenated by purging nitrogen for 10 min before being placed in a preheated oil bath at 70 °C for 24 h to ensure complete conversion of BzMA. Polymerisations were quenched by cooling to room temperature and exposing to air. Subsequent polymerisations were performed by varying the target copolymer composition and by varying the solution pH from 1.0 to 3.5.

4.2.4. Characterisation

4.2.4.1. Nuclear magnetic resonance spectroscopy

Proton (^{1}H) nuclear magnetic resonance spectroscopy (NMR) spectra were acquired on a Bruker Advance III 400 MHz spectrometer with 128 scans averaged per spectrum. Samples were dissolved in $CDCl_3$ prior to NMR analysis.

4.2.4.2. Gravimetry

Monomer conversions of BzMA for the synthesis of P2VP–PBzMA diblock copolymers were determined *via* gravimetry. Samples (approximately 1.0 g) were withdrawn from the P2VP–PBzMA final dispersions. The specimens were placed in an oven and dried at 60 °C to constant weight. Conversions were calculated from the measured dry residue.

4.2.4.3. Gel permeation chromatography

Molar mass and molar mass distribution were assessed using a gel permeation chromatography (GPC) instrument equipped with an Agilent 1260 Infinity pump injection module, an Agilent 1260 Infinity II refractive index detector and three Phenomenex phenogel columns with a mobile phase of THF at 35 °C. Calibration was achieved using a series of polystyrene standards, ranging from 1 x 10^3 to 2 x 10^6 g mol^{-1}. For P2VP homopolymers, samples were dissolved in THF directly prior to GPC analysis. For P2VP–PBzMA diblock copolymers synthesised below pH 4, samples were diluted in deionised water and then titrated to above pH 7 using 0.1 M KOH, and then dried in an oven at 60 °C to remove water. This specific sample preparation procedure led to a decrease in the protonation of P2VP stabiliser and increased the solubility of P2VP–PBzMA diblock copolymers in THF.

4.2.4.4. Dynamic light scattering

Hydrodynamic diameters of the diblock copolymer nanoparticles were assessed by dynamic light scattering (DLS) using a Malvern Zetasizer Nano ZS instrument equipped with a He–Ne solid-state laser operating at 633 nm and back-scattered light at a scattering angle of 173°. Copolymer dispersions were diluted to approximately 0.1% w/w using water at pH 2 to minimise potential coagulation. DLS samples were analysed using

disposable plastic cuvettes at 25 °C and data were averaged over three consecutive measurements.

4.2.4.5. Aqueous electrophoresis

Aqueous electrophoresis studies for the diblock copolymer nanoparticles were analysed using the same Malvern Zetasizer Nano ZS instrument described above. The solution was initially adjusted to pH 2 using HCl in the presence of 1.0 mM KCl as electrolyte. The solution was then manually raised from pH 2 to pH 11 by addition of KOH as required. Aqueous dispersions (approximately 0.1% w/w) were analysed at 25 °C using disposable folded capillary cells (Malvern DTS1017) and data were averaged over three consecutive measurements.

4.2.4.6. Transmission electron microscopy

Transmission electron microscopy (TEM) images were recorded using a FEI Tecnai G2 20 instrument operating at an accelerating voltage of 200 kV and connected to a Gatan 1k CCD camera. Samples for TEM observations were prepared by depositing 2 μL of diluted copolymer dispersion onto 400 mesh carbon-coated copper grids for 30 min and then carefully blotted with filter paper to remove excess solution. The samples were stained in a vapour space above ruthenium tetroxide (RuO_4) solution for 7 min at ambient temperature.[349] The mean nanoparticle diameters were determined using ImageJ software and over 200 randomly selected particles were measured for each sample.

4.2.4.7. Disc centrifuge photosedimentometry

Disc centrifuge photosedimentometry (DCP) studies were conducted using a CPS DC24000 instrument to obtain particle size distributions. The disc centrifuge was operated at 22,000 rpm. The spin fluid contained a density gradient built from 12 to 4% w/w aqueous sucrose, and then 0.5 ml of *n*-dodecane was injected to prevent surface evaporation and to extend the lifetime of the gradient. The aqueous sucrose solutions and diluted samples were adjusted to pH 2, 5 or 9 (as needed) using HCl or KOH before use. Samples (0.1 mL) were injected into the disc for analysis. The disc centrifuge was calibrated using a polystyrene latex standard with a mean particle diameter of 348 nm.

4.3. Results and discussion

4.3.1. Synthesis of P2VP macro-CTAs

RAFT solution polymerisation of 2VP was conducted in ethanol at 70 °C (**Scheme 4.1**). The polymerisations were quenched at monomer conversions <80% to ensure most of the trithiocarbonate RAFT chain-ends remained intact and minimise bimolecular termination.[86,356] The degree of polymerisation (DP) for P2VP macro-CTAs were calculated using ^{1}H NMR spectroscopy (**Figure 4.1**) by comparing the integrated proton signals corresponding to a proton on pyridine group of P2VP at 8.1-8.6 ppm with those corresponding to the two protons on methylene group of the PETTCCP at 3.4–3.5 ppm. The calculated DPs for $P2VP_{25}$ and $P2VP_{50}$ macro-CTA were 32 and 67, respectively.

Figure 4.2a and **Figure 4.3a** show conversion and semi-logarithmic kinetics versus reaction time for $P2VP_{32}$ and $P2VP_{67}$, respectively. The relatively linear conversion/time relationships and the *pseudo* first-order kinetic plots are reasonably consistent with the features expected for a controlled RAFT polymerisation.[29] However, in order to reach approximately 80% conversion, the polymerisations needed to be allow to proceed for at least 7–8 h. This can be attributed to 2-vinyl pyridine (2VP) being a type of more-activated monomer (MAM), resulting in the intermediate thiocarbonylthio capped radical species having relatively longer half-lives during RAFT polymerisation.[85,221,368,425] Therefore, some of the intermediate radical species may be consumed by side reactions or termination, resulting in slower polymerisation rates and higher than target DPs of the resulting P2VP macro-CTAs.

The evolution of molar mass (M_n) and molar mass dispersity (M_w/M_n) versus monomer conversion for $P2VP_{32}$ and $P2VP_{67}$ are shown in **Figure 4.2b** and **Figure 4.3b**. As the polymerisations progressed, the evolution of molar mass in relation to monomer conversion was close to linear, with relatively narrow molar mass dispersities obtained. However, the molar masses of $P2VP_{32}$ and $P2VP_{67}$ macro-CTAs determined *via* THF GPC analysis were 1200 and 2200 g mol^{-1}, respectively. These values were much lower than the calculated theoretical molar mass, which should be approximately 3600 and 7300 g mol^{-1}, respectively. The low values of molar mass reported by THF GPC analysis were not unexpected and are in good agreement with Nieswandt *et al.*,[422] who prepared

P2VP *via* RAFT bulk polymerisation and observed obviously smaller GPC M_n values than the theoretical M_n. These deviations from the theoretical M_n values may be partially caused by the differences between the GPC calibration standards (polystyrene) and P2VP, and potentially partially protonated pyridine groups on the P2VP polymer chains. Nevertheless, **Figure 4.4** shows that the GPC chromatograms of the resulting macro-CTAs were unimodal with relatively narrow molar mass distributions ($M_w/M_n < 1.2$). Given the two P2VP homopolymers underwent relatively well-controlled RAFT polymerisation to produce polymers with narrow molar mass distributions, they were utilised as macro-CTAs in the subsequent RAFT emulsion polymerisations using BzMA reported herein.

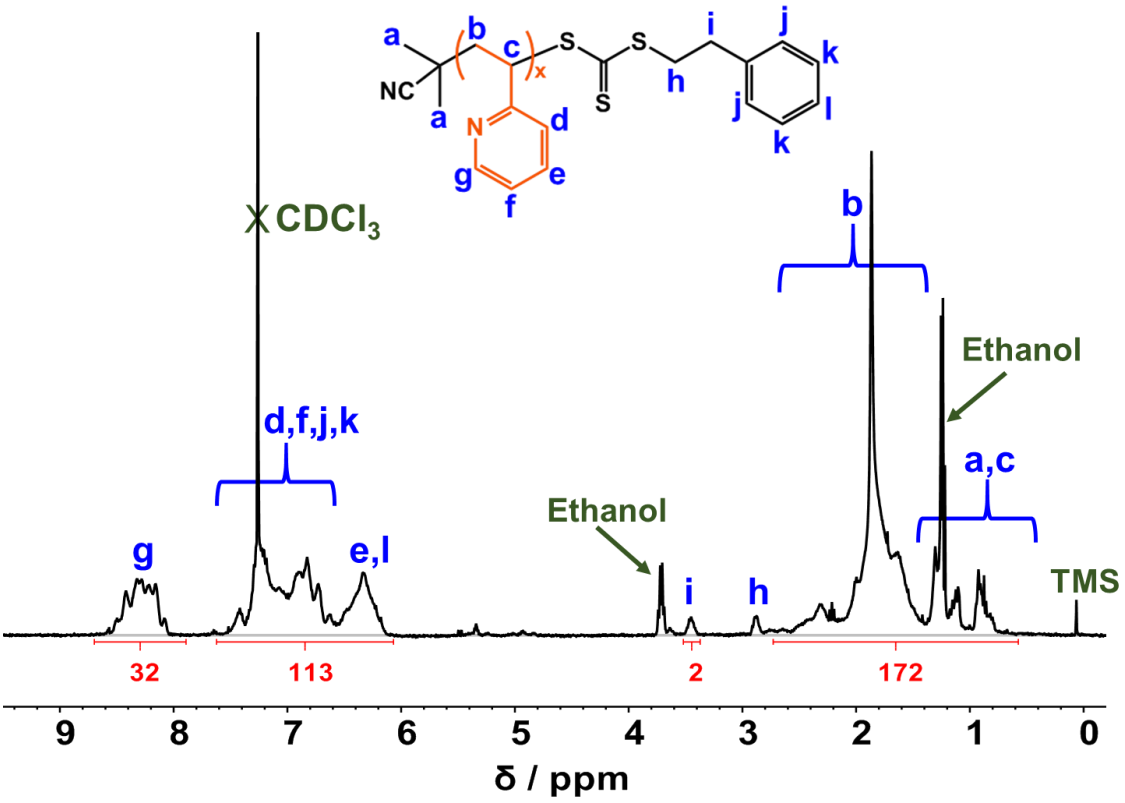

Figure 4.1. ^{1}H NMR spectrum of $P2VP_{32}$ macro-CTA. The sample was dissolved in $CDCl_3$ prior to NMR analysis. The degree of polymerisation (DP) for this macro-CTA was calculated by comparing the integrated proton signals corresponding to pyridine at 8.1–8.6 ppm (g) with that corresponding to the two protons on methylene group of the PETTCCP at 3.4–3.5 ppm (i).

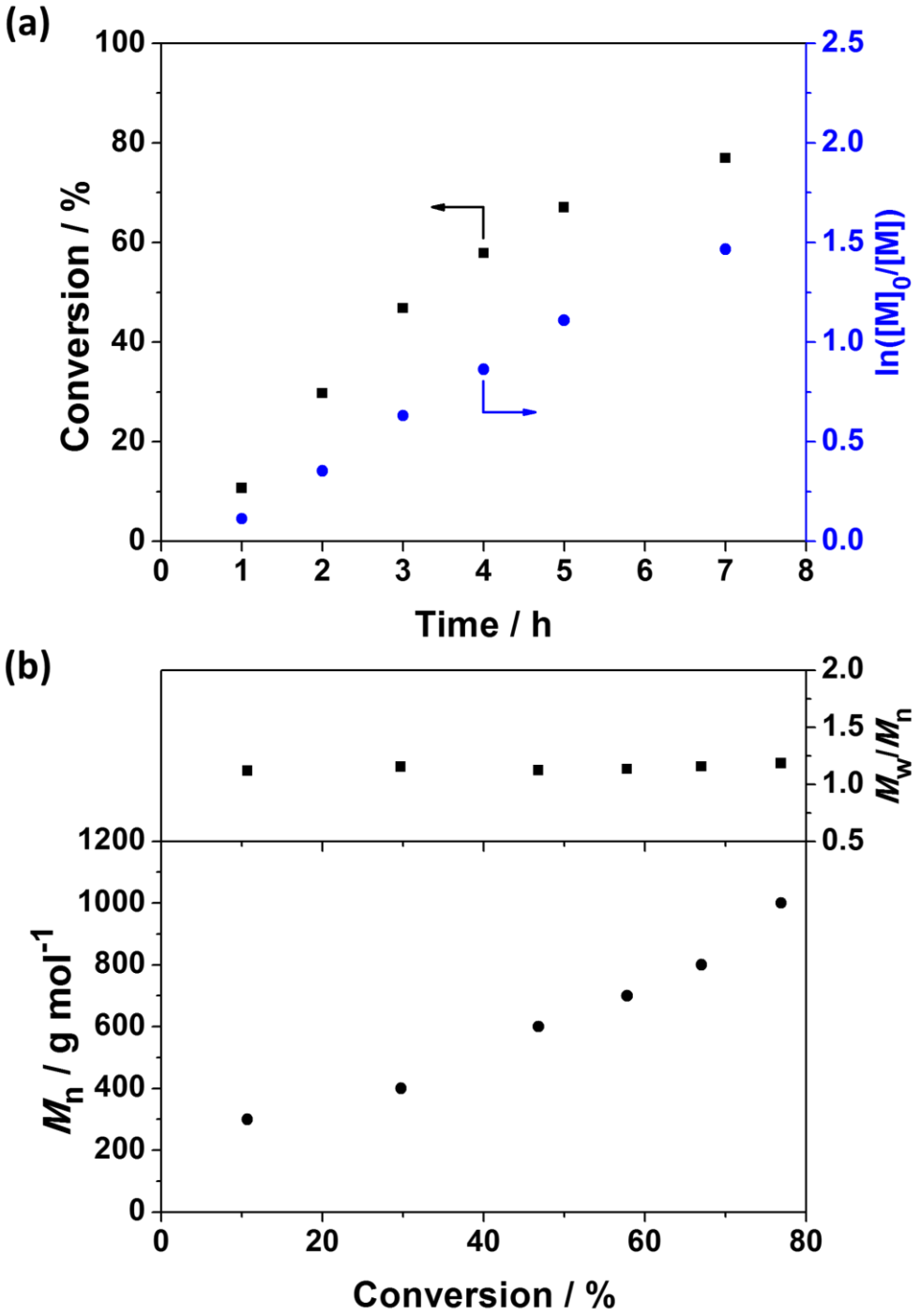

Figure 4.2. Kinetic studies for RAFT solution polymerisation of 2VP (target DP 25) using PETTCCP as a CTA in ethanol at 70 °C (15% w/w): (a) conversion and semi-logarithmic kinetics versus reaction time and (b) M_w/M_n and M_n versus monomer conversion.

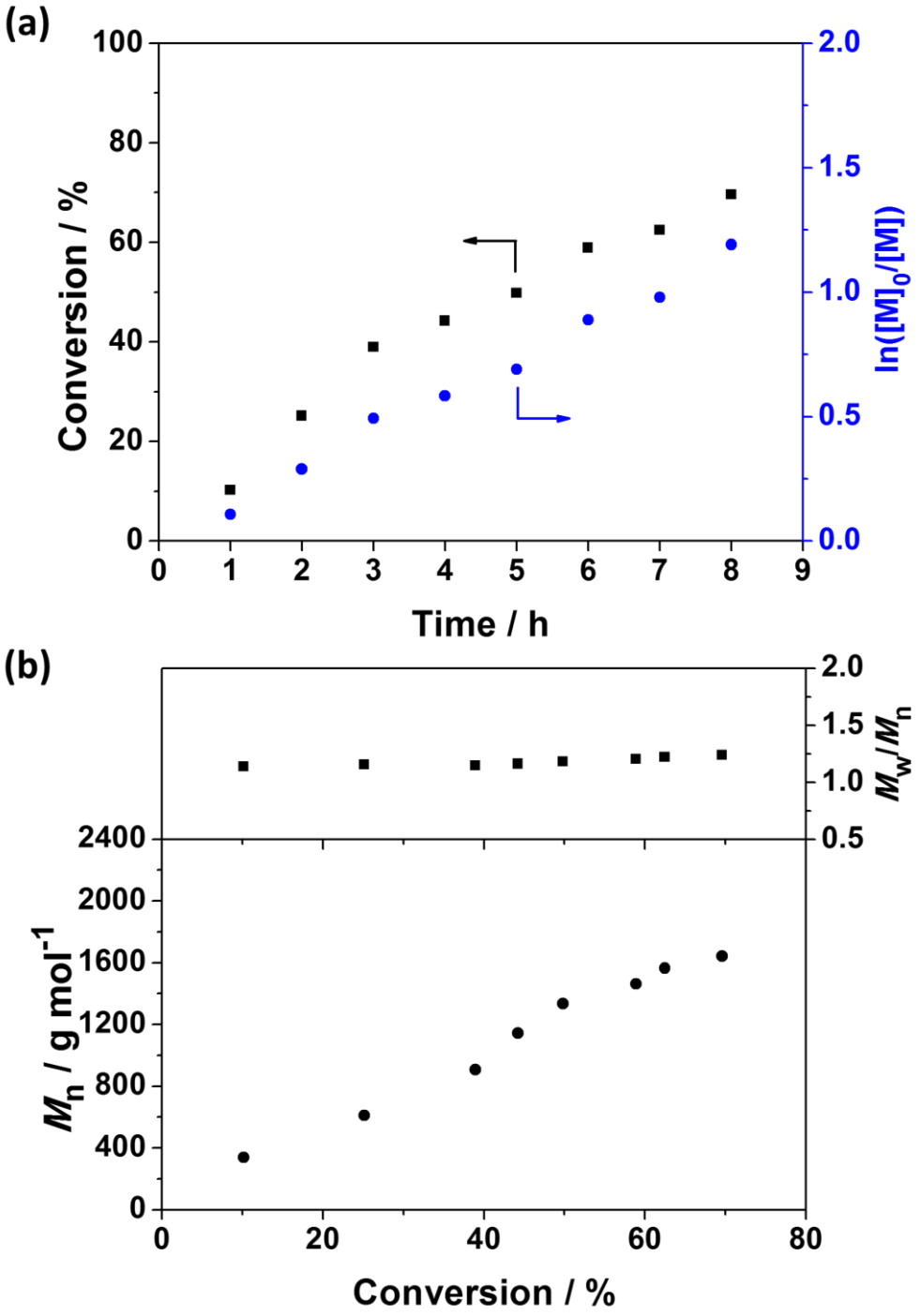

Figure 4.3. Kinetic studies for RAFT solution polymerisation of 2VP (target DP 50) using PETTCCP as a CTA in ethanol at 70 °C (15% w/w): (a) conversion and semi-logarithmic kinetics versus reaction time and (b) M_w/M_n and M_n versus monomer conversion.

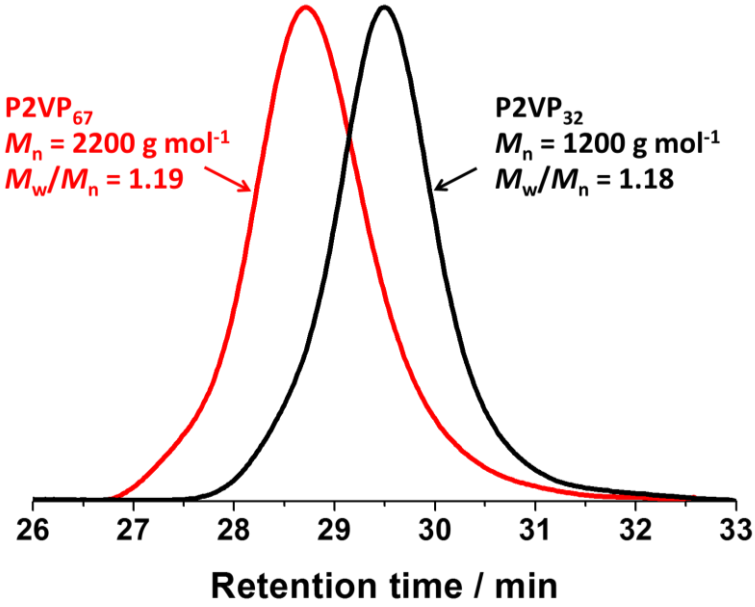

Figure 4.4. THF GPC chromatograms obtained for $P2VP_{32}$ and $P2VP_{67}$ macro-CTAs synthesised *via* RAFT solution polymerisation in ethanol at 70 °C (15% w/w). Monomer conversions of $P2VP_{32}$ and $P2VP_{67}$ macro-CTAs were 76.9% and 69.6%, respectively.

4.3.2. Characterisation of P2VP–PBzMA diblock copolymer

Cationic sterically-stabilised P2VP–PBzMA diblock copolymer nanoparticles were prepared *via* RAFT-mediated PISA under aqueous emulsion polymerisation conditions (**Scheme 4.1**). In this work, the core-forming monomer, BzMA, is insoluble in water, whereas the P2VP stabiliser is soluble in water below pH 4.2 and pH 3.8 for $P2VP_{32}$ and $P2VP_{67}$, respectively (**Figure 4.5**). This is consistent with the reported pK_a values (3.85–4.75) of related P2VP polymers.[323,419] Therefore, P2VP–PBzMA diblock copolymers were synthesised using P2VP as a macro-CTA between pH 1.0 and 3.5.

Figure 4.6 shows a representative ^{1}H NMR spectrum of $P2VP_{32}$–$PBzMA_{50}$ diblock copolymer synthesised at pH 2. The 2VP and BzMA contents in the diblock copolymer were calculated by comparison of the integration of a proton on pyridine group of P2VP at 8.1–8.6 ppm with the two protons on methylene of PBzMA at 4.5–5.0 ppm. In all cases, the calculated PBzMA DP was higher than target value. This is attributed to a combination of the P2VP chain-ends being 'more-activated', resulting in relatively low chain-extension efficiency,[85] and the presence of a small fraction of 'dead' homopolymer from the synthesis of the macro-CTA.

Figure 4.7 shows the GPC chromatograms of the V_{32} macro-CTA and V_{32}–B_{300} diblock copolymers synthesised between pH 1.0 and 3.5 (entries 1, 3, 5 and 6, **Table 4.1**).

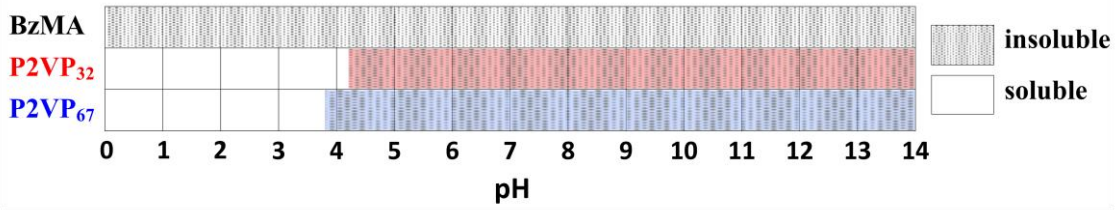

Figure 4.5. Solubility of BzMA, $P2VP_{32}$ and $P2VP_{67}$ in water at different pH. Solubility tests were conducted at 24 °C and at concentrations of 0.3 g mL^{-1} and 5 mg mL^{-1} for BzMA and $P2VP_x$, respectively.

The GPC chromatograms of all the diblock copolymers were successfully shifted to a shorter retention time, indicating that polymers with higher molar mass were obtained. However, the P2VP–PBzMA copolymers had relatively broad molar mass distributions (M_w/M_n), which were mainly a result of tailing towards lower molar mass species (**Figure 4.7**). Furthermore, an obvious low molar mass shoulder at a retention time of 28–32 min was observed in all cases. This shoulder can be attributed to the deactivated P2VP macro-CTA. It is noteworthy that the quantity of the deactivated P2VP macro-CTA decreased with decreasing solution pH, and only limited deactivated P2VP macro-CTA was observed at pH 1. This suggests that a lower degree of protonation (closer to the pK_a) results in less efficient chain extension. In contrast, at lower pH, the P2VP macro-CTA will be more ionised as a result of increased protonation of the pyridine groups (further away from pK_a). This suggested that P2VP macro-CTAs with higher degrees of protonation have better RAFT chain-extension efficiency,[93,426] and there is only a relatively small quantity of 'dead' homopolymer formed during macro-CTA synthesis. Additionally, the GPC traces of the P2VP–PBzMA diblock copolymer at a retention time of 18–27 min show a subtle shift to longer retention time (lower molar mass) with decreasing solution pH. This is consistent with the observation of less 'dead' homopolymer at lower solution pH, and therefore diblock copolymer chains with lower molar mass for a fixed quantity of BzMA monomer.[427,428] In summary, whilst the presence of a minor fraction of P2VP homopolymer is acknowledged, the preparation of P2VP–PBzMA diblock copolymers with relatively well-control molar masses and narrow molar mass distributions (M_w/M_n) was achieved.

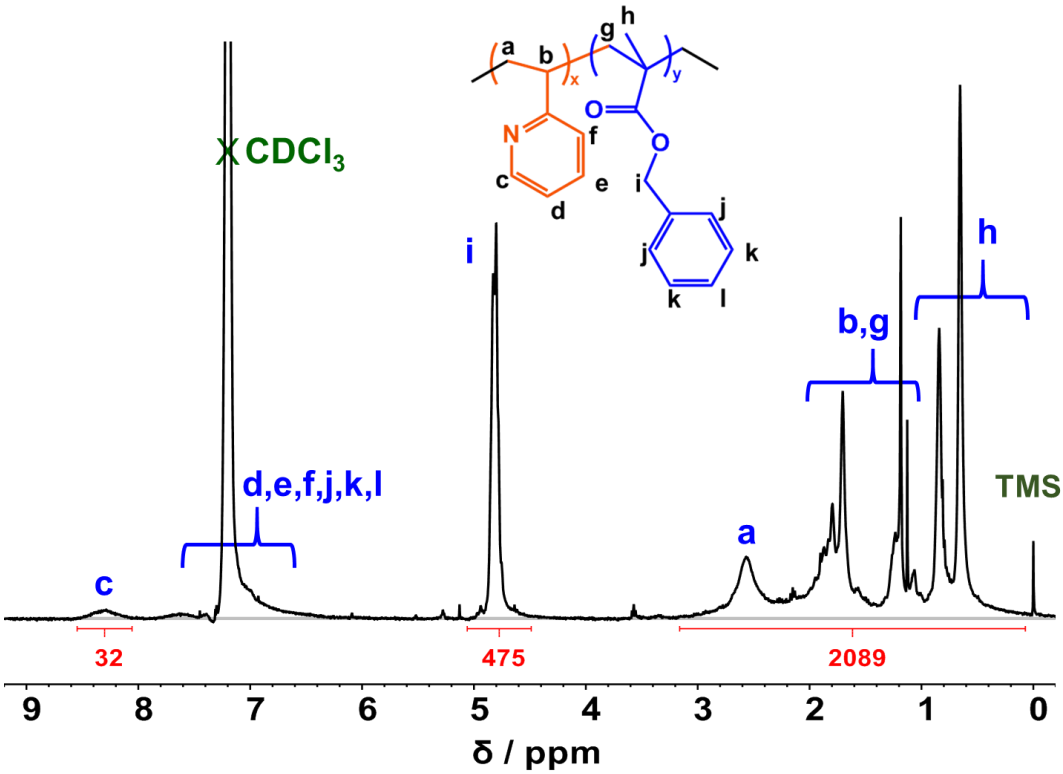

Figure 4.6. Representative ^{1}H NMR spectra of $P2VP_{32}$–$PBzMA_{50}$. The sample was dissolved in $CDCl_3$ prior to NMR analysis. The 2VP and BzMA contents in the diblock copolymer were calculated by comparison of the integration of a proton on pyridine group of P2VP at 8.1–8.6 ppm (c) with the two protons on methylene of PBzMA at 4.5–5.0 ppm (i).

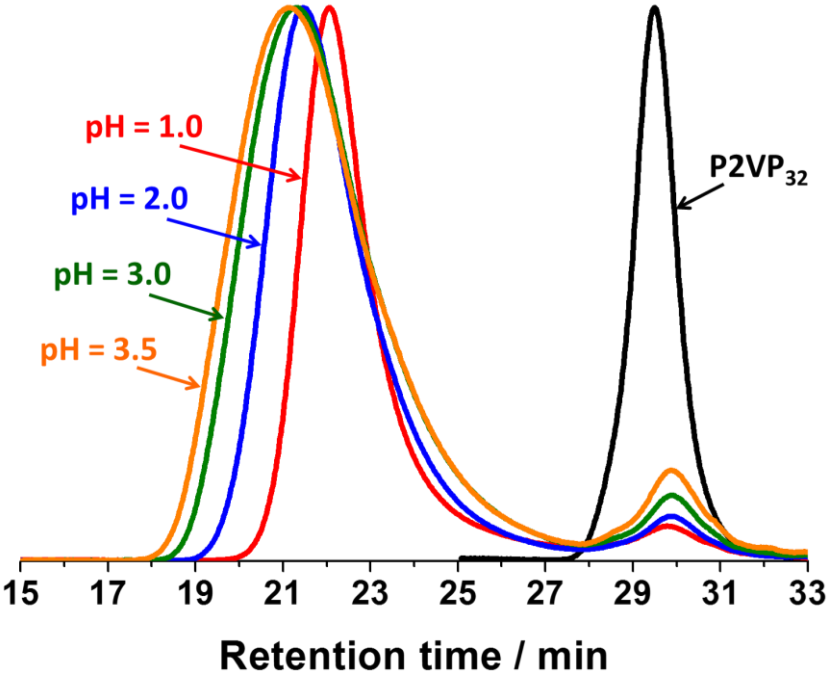

Figure 4.7. Representative GPC chromatograms of the $P2VP_{32}$ macro-CTA and $P2VP_{32}$–$PBzMA_{300}$ diblock copolymers synthesised *via* RAFT aqueous emulsion polymerisation between pH 1.0 and 3.5 (entries 1, 3, 5 and 6, **Table 4.1**).

Table 4.1. Summary of target copolymer composition, pH, mean hydrodynamic diameter, molar mass and molar mass distribution obtained for $P2VP_x$–$PBzMA_y$ (V_x–B_y) diblock copolymers synthesised at 10% w/w *via* RAFT-mediated PISA in water at 70 °C.

Entry	Target composition[a]	Solution pH	D_h[b] / nm	M_n[c] / g mol^{-1}	M_w[c] / g mol^{-1}	M_w/M_n[c]
1	V_{32}–B_{300}	1.0	74 (0.063)	40.4	55.6	1.38
2	V_{32}–B_{300}	1.5	90 (0.024)	47.8	77.1	1.61
3	V_{32}–B_{300}	2.0	113 (0.070)	47.0	79.0	1.68
4	V_{32}–B_{300}	2.5	142 (0.040)	46.0	81.6	1.77
5	V_{32}–B_{300}	3.0	162 (0.051)	48.3	102.1	2.12
6	V_{32}–B_{300}	3.5	193 (0.070)	51.6	121.2	2.35
7	V_{67}–B_{300}	1.1	59 (0.040)	18.7	25.0	1.34
8	V_{67}–B_{300}	1.5	62 (0.053)	28.4	39.1	1.38
9	V_{67}–B_{300}	2.0	74 (0.043)	29.1	43.7	1.50
10	V_{67}–B_{300}	2.3	99 (0.046)	44.5	76.6	1.72
11	V_{67}–B_{300}	3.0	147 (0.016)	57.2	98.7	1.73
12	V_{67}–B_{300}	3.5	166 (0.018)			
13	V_{32}–B_{50}	2.0	52 (0.092)			
14	V_{32}–B_{100}	2.0	63 (0.049)			
15	V_{32}–B_{300}	2.0	113 (0.070)	47.0	79.0	1.68
16	V_{32}–B_{500}	2.0	196 (0.036)	75.7	167.3	2.21
17	V_{32}–B_{700}	2.0	241 (0.041)			
18	V_{32}–B_{900}	2.0	317 (0.076)	124.8	323.0	2.59

[a] All monomer conversions determined *via* gravimetry were higher than 99% after polymerisation at 70 °C for 24 h. [b] Obtained *via* DLS analysis, where DLS polydispersity index values are indicated in brackets. Samples were diluted in water at pH 2 to minimise potential coagulation. [c] Determined *via* THF GPC analysis. Samples were diluted in deionised water, and then titrated to above pH 7 to decrease the protonation of P2VP stabiliser and increase the solubility of P2VP–PBzMA diblock copolymers in THF. The M_n and M_w/M_n values determined using the P2VP–PBzMA copolymer peaks at a retention time of 18-27 min.

4.3.3. Self-assembly behaviour of P2VP–PBzMA synthesised *via* RAFT-mediated PISA

Cationic sterically-stabilised polymeric nanoparticles with pyridine functional groups were prepared *via* RAFT-mediated PISA in water with varying solution pH (**Scheme 4.1**). **Figure 4.5** shows that the core-forming monomer, BzMA, was insoluble in water, whereas the P2VP stabiliser completely dissolves in water below pH 4.2 and pH 3.8 for $P2VP_{32}$ and $P2VP_{67,}$ respectively. This was consistent with the reported pK_a values (3.85–4.75) of related P2VP polymers.[323,419] This confirms that the protonation degree of P2VP strongly influences the solubility in water, and longer stabilisers need in more acidic conditions to dissolve.

P2VP–PBzMA (V_x–B_y) diblock copolymer nanoparticles with relatively low particle size dispersity were obtained in all cases (**Table 4.1**). **Figure 4.8** shows mean hydrodynamic diameters of V_x–B_{300} particles synthesised in water at various pH. The mean particle diameter increased with increasing solution pH. For example, in the V_{67}–B_{300} series, the mean hydrodynamic diameter increased approximately three-fold, from 59 to 166 nm, in the pH range from 1.0 to 3.5. This can be attributed to the P2VP stabilisers having different degrees of ionisation (cationic charge) resulting from increased protonation of the pyridine groups at lower solution pH.[429,430] The higher charge of the stabiliser leads to stronger electrostatic repulsion and improved electrostatic stabilisation of the resulting nanoparticles.[431] Therefore, at lower solution pH, P2VP–PBzMA nanoparticles with smaller diameters were obtained during PISA. In contrast, the protonation degree of P2VP decreases with increasing solution pH, resulting in weaker electrostatic repulsion and the formation of larger P2VP–PBzMA particles. This indicated that the degree of electrostatic repulsion in the corona (stabiliser) of the forming nanoparticles directly influences the aggregation number of polymeric chains (N_{agg}), which are incorporated into the copolymer nanoparticles and therefore the number of copolymer chains per unit surface area (S_{agg}).[353,431] These observations are similar to the preparation of the anionic sterically-stabilised PKSPMA–PBzMA and PSS–PBzMA nanoparticles described in **Chapter Two**, which were prepared *via* RAFT-mediated PISA with a fixed target diblock copolymer composition in various alcohol/water mixtures. More specifically, the repulsive interactions between

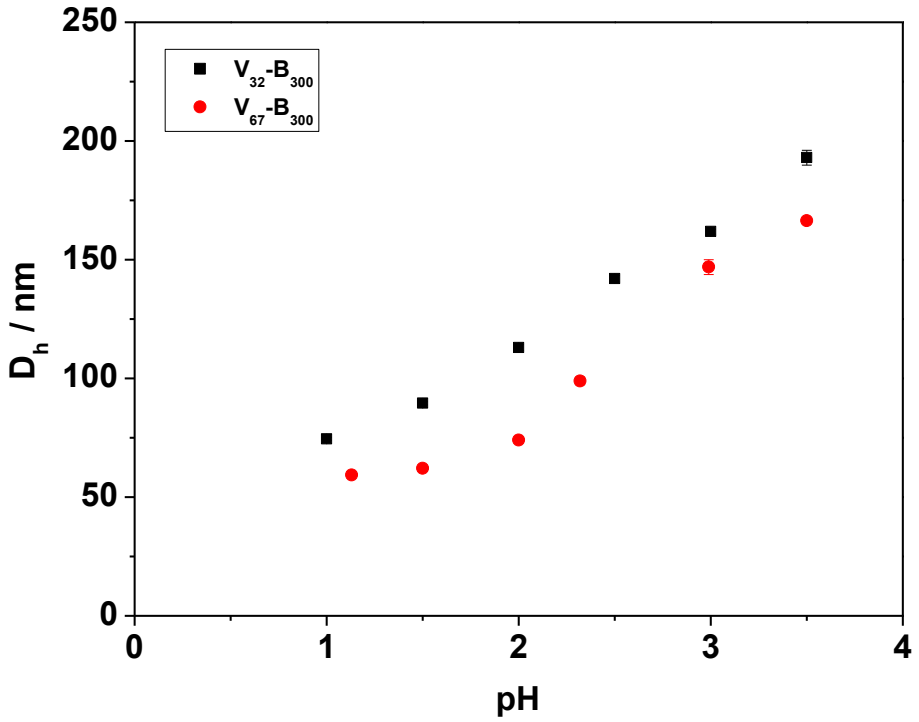

Figure 4.8. Mean hydrodynamic diameters (D_h) of $P2VP_x$–$PBzMA_{300}$ (V_x-B_{300}) diblock copolymer nanoparticles synthesised in water at varying pH at 10% w/w solids and 70 °C.

neighbouring anionic PKSPMA stabiliser chains were higher in water-rich solvent mixtures than that in alcohol-rich solvent mixtures. Therefore, the greater electrostatic repulsion between the stabiliser chains led to the self-assembly of PKSPMA–PBzMA chains into particles with comparatively lower aggregation numbers, and thus smaller particle diameters. Nevertheless, the structural parameters (N_{agg} and S_{agg}) of the P2VP–PBzMA nanoparticles may be verified by further small-angle X-ray scattering (SAXS) analysis as described in **Chapter Two** (see **section 2.3.4**) for the characterisation of PKSPMA–PBzMA nanoparticles, but data was not available at the time of writing the thesis.

For the V_{32}–B_{300} series synthesised with varying solution pH (**Figure 4.8**), a similar trend was observed as for V_{67}–B_{300}, i.e. the mean hydrodynamic diameter increased with increasing pH. When comparing the two series at a given pH, the V_{32}–B_{300} nanoparticles were consistently larger than the V_{67}–B_{300} particles. This can be attributed to the chain length (DP) of the $P2VP_{32}$ stabiliser being approximately half that of $P2VP_{67}$. Thus, the shorter P2VP stabiliser occupies a lower surface area in the corona of the nanoparticles, allowing more chains to aggregate together (higher N_{agg}) and ultimately form larger particles.[252,432]

The morphologies of the V_x–B_y diblock copolymer nanoparticles synthesised at varying solution pH were investigated *via* TEM after staining with RuO_4 (**Figure 4.9**, **Figure 4.10**, **Figure A.7** and **Figure A.8**). The RuO_4 stain typically increases the contrast of aromatic polymers (both P2VP and PBzMA blocks),[354] but it is likely to have an affinity of one block over the other, thus some of the TEM images appear to have a distinct core–shell morphology. In all cases, spherical nanoparticles were obtained, with diameters generally in agreement with DLS (**Table 4.1**). This observation agrees with previous studies, which also merely obtained spheres for P2VP–PS[422] and PKSPMA–PBzMA[69] PISA formulations using highly cationic or anionic stabilisers. This is likely due to the highly cationic character of the P2VP stabiliser preventing higher order morphology (e.g. worm, vesicle) formation.[235,252]

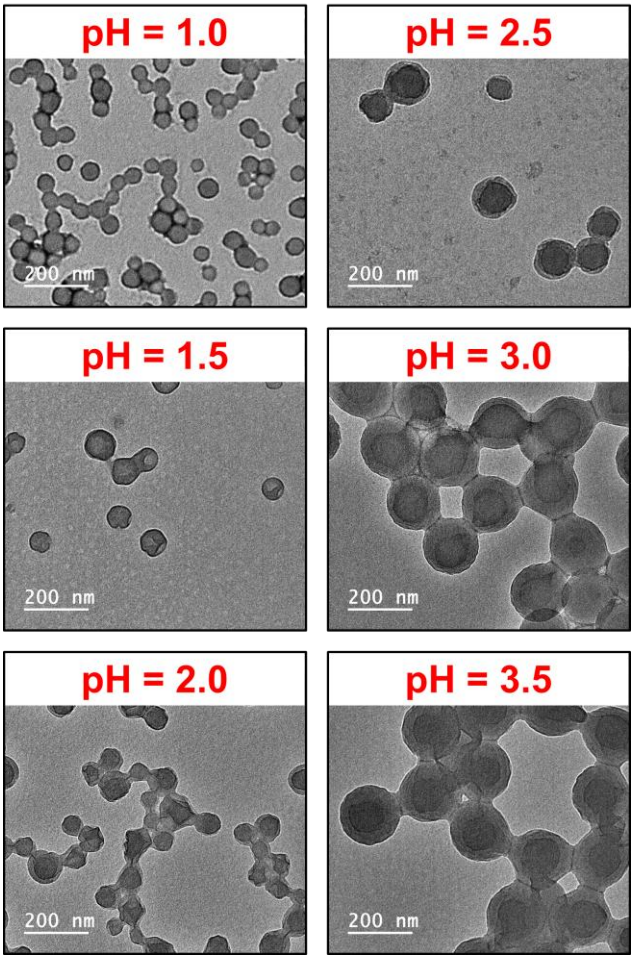

Figure 4.9. Representative TEM images of $P2VP_{32}$–$PBzMA_{300}$ diblock copolymer nanoparticles prepared at 10% w/w solids *via* RAFT-mediated PISA in water at 70 °C and varying solution pH ranging from 1.0 to 3.5 (entries 1–6, **Table 4.1**).

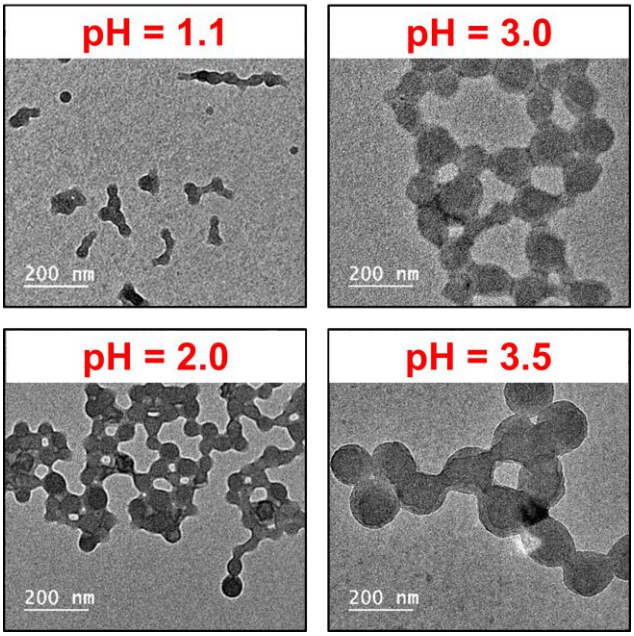

Figure 4.10. Representative TEM images of $P2VP_{67}$–$PBzMA_{300}$ diblock copolymer nanoparticles prepared at 10% w/w solids *via* RAFT-mediated PISA in water at 70 °C and varying solution pH ranging from 1.1 to 3.5 (entries 7, 9, 11 and 12, **Table 4.1**).

4.3.4. Preparation of $P2VP_x$–$PBzMA_y$ nanoparticles with varying PBzMA DP

The mean diameters of $P2VP_x$–$PBzMA_y$ (V_x–B_y) nanoparticles synthesised at fixed pH can also be tuned by simply varying the DP of PBzMA. More specifically, for a fixed $P2VP_{32}$ macro-CTA, a monotonic increase in mean hydrodynamic diameter of V_x–B_y nanoparticles was observed when increasing the DP of PBzMA from 50 to 900 at both pH 1 and pH 2. For example, in the pH 2 series, the mean hydrodynamic diameter of V_{32}–B_{50} was 52 nm, while V_{32}–B_{900} formed nanoparticles with diameters of 317 nm. Particle diameters determined by DLS (**Figure 4.11b** and **Table 4.1**) were verified by TEM (**Figure 4.11a** and **Figure A.9**), which also confirmed a spherical morphology was obtained in all cases. Furthermore, the DLS polydispersity index values remained relatively low (<0.1) even when targeting large core-forming block compositions, such as V_{32}–B_{900}.

The mean spherical diameter (D) can be correlated to the DP of the core-forming block (y) by a scaling exponent (α), as described using the equation $D = ky^{\alpha}$, where k is a constant.[355,356] **Figure 4.11c** shows a double-logarithmic plot of D against y for V_{32}–B_y nanoparticles synthesised *via* RAFT-mediated PISA in water at pH 1 and 2. Both series had a linear relationship with calculated α values of 0.55 and 0.64 for pH 1 and pH 2,

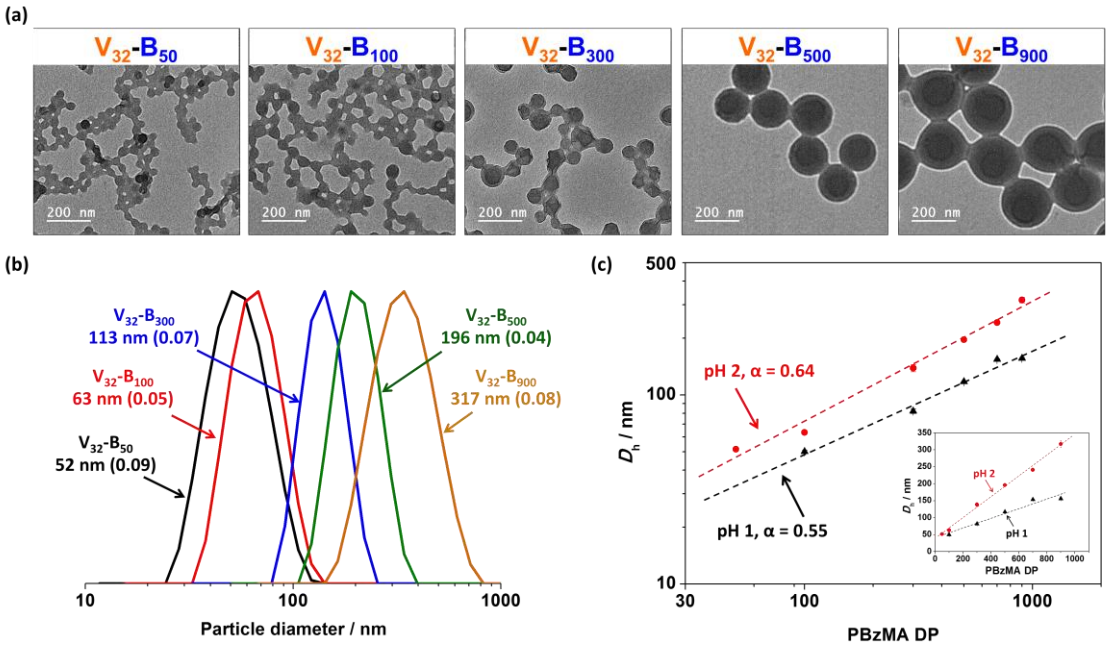

Figure 4.11. (a) Representative TEM images for $P2VP_{32}$–$PBzMA_y$ (target y = 50, 100, 300, 500 and 900) diblock copolymer nanoparticles prepared at 10% w/w solids *via* RAFT-mediated polymerisation of BzMA in water at pH 2; (b) corresponding DLS intensity-average size distributions (the number in brackets represents the DLS polydispersity index); and (c) double-logarithmic plot for mean hydrodynamic diameter (D_h) versus degree of polymerisation of the PBzMA core-forming block for $P2VP_{32}$–$PBzMA_y$ particles synthesised at pH 1 and pH 2. The inset shows the particle diameter changes using linear scales.

respectively. Both α values were close to a value of 2/3, suggesting that the PBzMA chains are in a relatively stretched configuration.[355-357] It is noteworthy that the value of α of pH 2 was about 16% greater than that at pH 1, indicating that the core-forming PBzMA block was more stretched for particles synthesised at higher solution pH. This supports the observations made in the section above in that at lower pH, the P2VP stabiliser had higher cationic charge. Thus, the greater electrostatic repulsion between the stabiliser chains results in the self-assembly of P2VP–PBzMA chains into particles with comparatively lower aggregation numbers and therefore particle diameters. Furthermore, the effect of electrostatic repulsion generated from the P2VP stabiliser was more obvious with higher target PBzMA DP. Specifically, the particle diameter of V_{32}–B_{50} prepared at pH 2 was 4% larger than same composition prepared at pH 1, whereas it was approximately 90% larger when target PBzMA DP was 900.

4.3.5. Colloidal stability of P2VP–PBzMA diblock copolymer nanoparticles

Intensity-average diameter and aqueous electrophoresis data for V_{32}–B_{300} diblock copolymer nanoparticles (entry 4, **Table 4.1**) as a function of pH are shown in **Figure 4.12**. These P2VP–PBzMA diblock copolymer nanoparticles were highly cationic with zeta potential higher than +30 mV below pH 4.5 (**Figure 4.12a**). This can be attributed to the highly protonated pyridine functional groups in acidic conditions. As the pH was increased by the addition of KOH, the zeta potential decreased, as a result of partial neutralisation of the pyridine groups in this pH range.[433] Furthermore, negative zeta potentials were recorded above the isoelectric point at pH ~9 and reached -7 mV at pH 12 (**Figure 4.12a**). It is not definitively known why negative zeta potentials occur for these particles, but this is often seen in the literature and is reported to result from the adsorption of OH^- ions on the primarily uncharged surface.[241,434,435] Similar observations were found for the other nanoparticles with longer P2VP stabiliser (e.g. V_{67}–B_{300}). The trend of zeta potential versus pH is in good agreement with the reported related PEGMA stabilised P2VP latex.[320] However, this is obviously different from the PKSPMA-stabilised PKSPMA–PBzMA diblock copolymer nanoparticles in **Chapter Two** (see **section 2.3.5**). The PKSPMA stabiliser is a strong polyelectrolyte with highly anionic charge over a wide range of pH, resulting in pH-independent zeta potentials.[69]

Figure 4.12b shows that V_x–B_y diblock copolymer nanoparticles had pH-independent behaviour at low pH and further confirms that P2VP is present within the coronas of the particles. As expected, the pyridine groups of P2VP stabiliser had higher degree of protonation in acidic solution (<pH 5), resulting in the P2VP–PBzMA nanoparticles having a high zeta potential (higher electrostatic repulsion between particles) and consistent particle diameter (~130 nm). In contrast, flocculation occurred above pH 5 as a result of P2VP chain collapse above its pK_a (reported pKa 3.85 to 4.75 for P2VP latexes[419]) and relatively low zeta potential (zeta potential <18 mV). This behaviour is clearly different from the reported PEGMA stabilised P2VP latex, where the PEGMA is a non-ionic stabiliser and the P2VP is in the core of the particles and is cross-linked.[320] More specifically, no obvious particle diameter change (no flocculation) was observed above pH 5 due to non-ionic PEGMA steric stabiliser. In contrast, the particle diameter of PEGMA stabilised P2VP latex increased significantly below pH 4.5 due to the pyridine

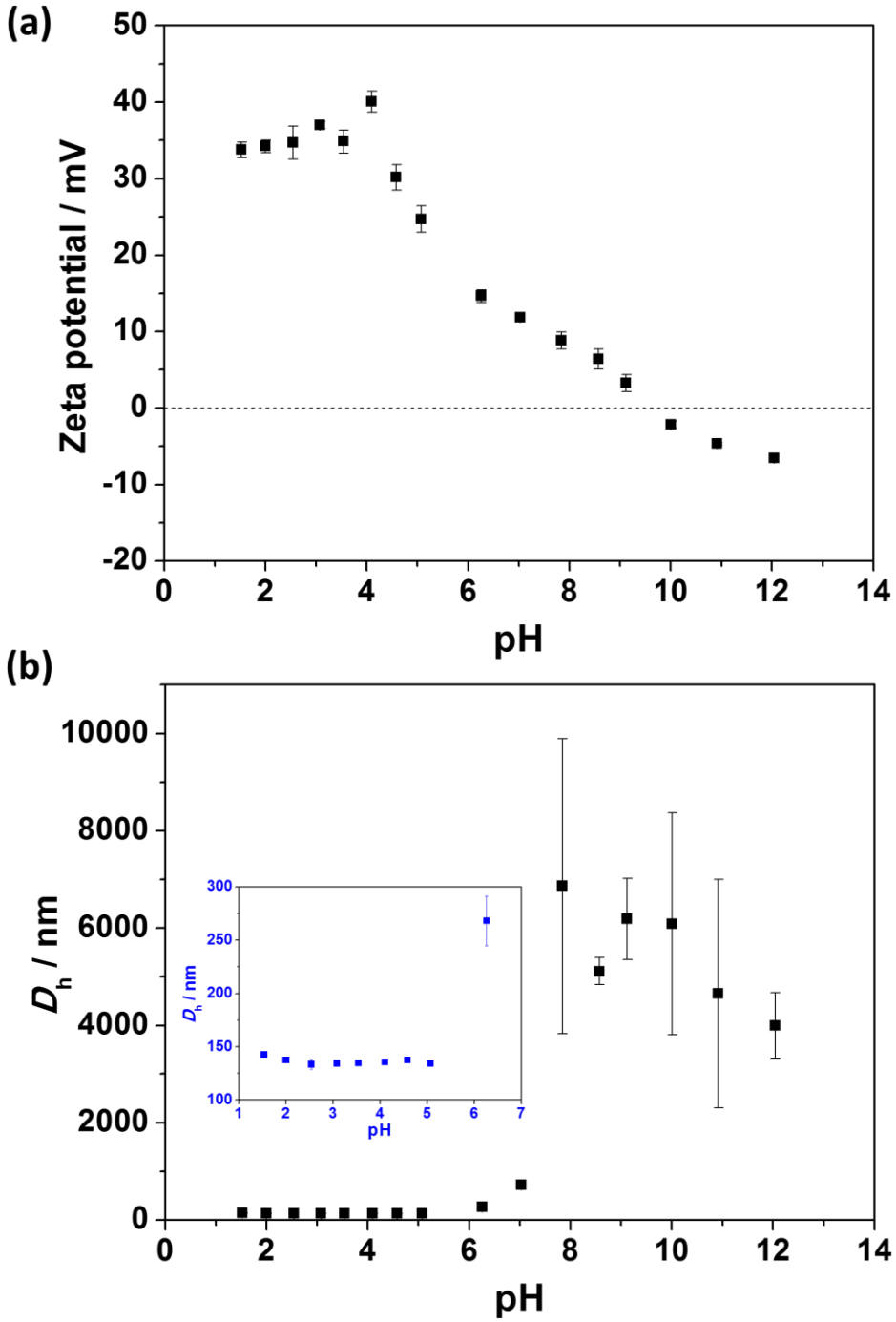

Figure 4.12. Representative (a) aqueous electrophoresis and (b) dynamic light scattering data as a function of pH obtained for $P2VP_{32}$–$PBzMA_{300}$ diblock copolymer nanoparticles (entry 4, **Table 4.1**). Measurements were conducted at a copolymer concentration of approximately 0.1% w/w with 1 mM KCl as a background electrolyte. The solution pH was initially adjusted to pH 1.5 by the addition of HCl and subsequently titrated to pH 12 using KOH. The inset shows a magnification of the particle diameter changes below pH 7.

groups on P2VP chains becoming protonated and inducing swelling of the lightly cross-linked latex particles to form microgels.

It is noteworthy that 1 mM KCl was added as background electrolyte to obtain reliable zeta potential values during this analysis. Furthermore, the dilute dispersion was titrated to approximately pH 1.5 using HCl to maintain protonation of the pyridine groups at the start of the analysis, and the pH was increased by adding KOH. However, high ionic strength (K^+ and Cl^-) can screen electrostatic interactions between nanoparticles, resulting in lower electrostatic repulsion and inducing flocculation.[436,437] In order to investigate the effects of ionic strength on the flocculation of P2VP–PBzMA nanoparticles at varying pH, $P2VP_{32}$–$PBzMA_{300}$ diblock copolymer nanoparticles (entry 4, **Table 4.1**) were directly dispersed in deionised water at pH 2, 5 and 9 without adding KCl electrolyte. The DLS histograms (**Figure 4.13**) show monomodal distributions in all cases, but relatively higher DLS dispersities were observed for nanoparticles dispersed in water at pH 5 and pH 9. Furthermore, the percentage of particles with larger sizes increased with increasing solution pH, indicating that flocculation still occurred to some extent above pH 5. However, the mean hydrodynamic diameter only increased slightly from 142 nm at pH 2 to 152 nm at pH 9, whereas the values reported by in the presence of KCl electrolyte are indicative of highly flocculated dispersions (**Figure 4.12b**).

Figure 4.14 shows particle size distributions obtained by disc centrifuge photosedimentometry (DCP) for $P2VP_{32}$–$PBzMA_{300}$ nanoparticles (entry 4, **Table 4.1**) directly dispersed in water at pH 2, 5 and 9 (i.e. in the absence of KCl electrolyte). As expected for these samples, only minor flocculation was observed (as indicated by the increasing area of the main peak and shoulder) and the mean weight average diameters were 244, 261 and 303 nm at pH 2, 5 and 9, respectively. Therefore, both DLS and DCP analysis indicated that P2VP–PBzMA nanoparticles can be well-dispersed in a wide pH range, as long as the ionic strength is kept low. This observation is important for the application of these particles in future studies (see **Chapter Five**).

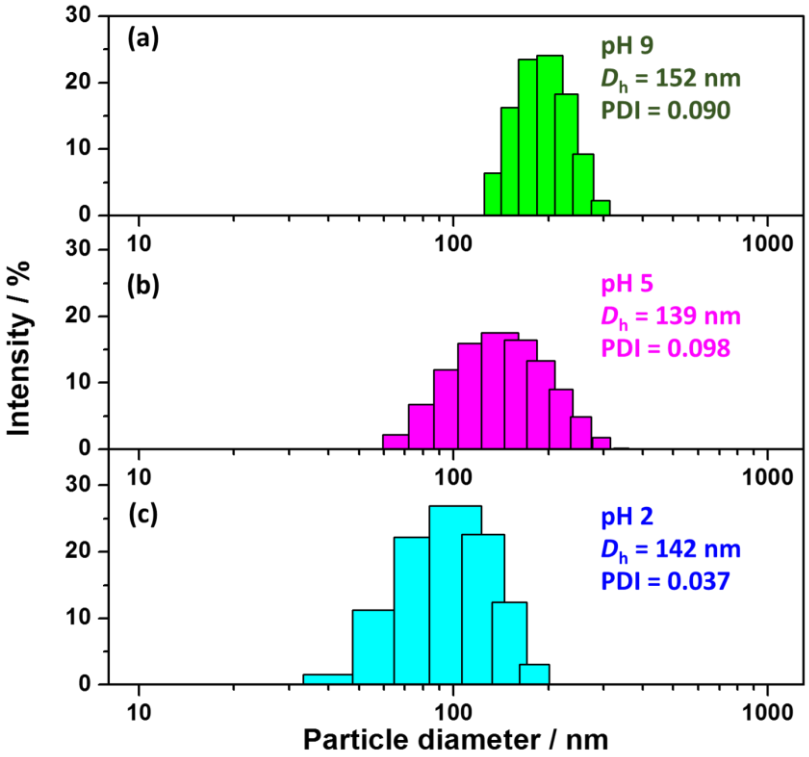

Figure 4.13. DLS histograms of $P2VP_{32}$–$PBzMA_{300}$ diblock copolymer nanoparticles prepared *via* RAFT-mediated PISA at 70 °C (entry 4, **Table 4.1**) and dispersed in water at (a) pH 9, (b) pH 5 and (C) pH 2 in the absence of KCl electrolyte. The polymer concentration was approximately 0.1% w/w.

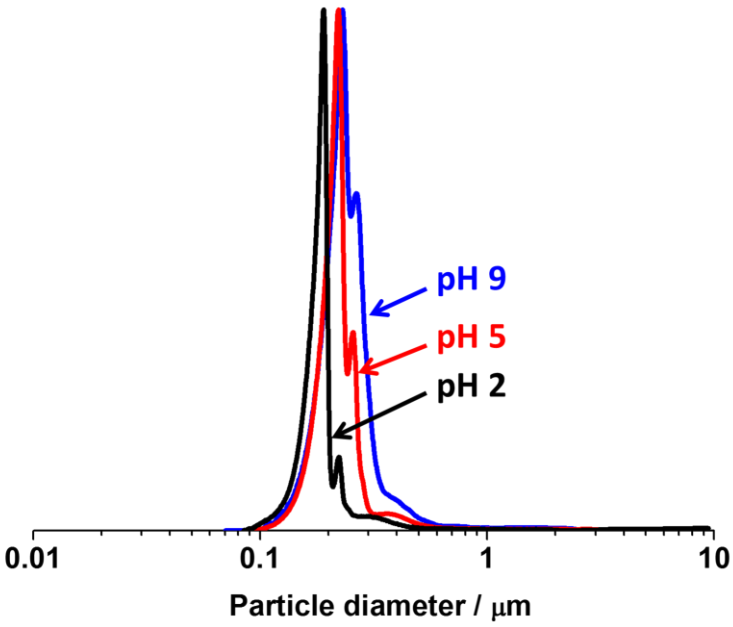

Figure 4.14. DCP particle size distributions obtained for $P2VP_{32}$–$PBzMA_{300}$ diblock copolymer nanoparticles prepared *via* RAFT-mediated PISA at 70 °C (entry 4, **Table 4.1**) and dispersed in water at pH 2, 5 and 9 in the absence of KCl electrolyte. The density of the P2VP–PBzMA particles used for these DCP measurements was taken to be 1.18 g cm^{-3}.

4.4. Conclusions

RAFT solution polymerisation affords pyridine-functional macro-CTAs, which were subsequently utilised to prepare pyridine-bearing spherical nanoparticles *via* RAFT-mediated PISA in water at low pH. Nanoparticles with tuneable diameters can be prepared by altering the DP of the stabiliser (P2VP) and/or core-forming block (PBzMA), or simply *via* varying the solution pH for a fixed target copolymer composition. This approach is highly versatile and affords the capability to prepare favoured particle diameters with varying copolymer compositions, or to obtain a desired target copolymer composition with different particle sizes. The degree of protonation of the P2VP stabiliser at different solution pH has a noticeable effect on both the aggregation of polymer chains during PISA process, and the resulting behaviour of the diblock copolymer nanoparticles. Furthermore, these P2VP–PBzMA nanoparticles had good colloidal stability and high cationic charge (>30 mV) below pH 5. However, strong ionic strength (0.1 mM KCl) led to significant flocculation above pH 5, where the pyridine functional groups had a lower degree of protonation and cationic charge. Nonetheless, when these nanoparticles were directly dispersed in solutions in absence of KCl electrolyte, only negligible flocculation was observed even at pH 9. Therefore, the capability of these highly cationic diblock copolymer nanoparticles to be dispersed within a wide pH range whilst maintaining good colloidal stability is promising for applications in future studies.

Chapter Five

Physical adsorption of graphene oxide onto polymer latexes *via* electrostatic interaction and characterisation of the resulting nanocomposite particles

5.1. Introduction

Nanocomposite particles have attracted extensive attention by both academic and industrial researchers in the past two decades.[253-255] In particular, nanocomposite particles comprising polymer and graphene have received much attention.[258-262,271] Graphene is a two-dimensional material with exceptional thermal, mechanical and electrical properties.[288-291] These exceptional properties afford tremendous possibilities for the design of advanced materials with potential applications, such as sensors,[263,264] electrode materials,[265] catalytic materials[266,267] and supercapacitors.[268-270] However, graphene has a relatively hydrophobic surface with high Van der Waals attraction between graphene sheets. This leads to the tendency for irreversible stacking-induced aggregation, hindering production, processing and storage for either research or industrial manufacturing.[294-296]

Graphene oxide (GO) has attracted attention as it is a material chemically derived graphene.[438-441] GO is commonly prepared *via* modified Hummers–Offeman methods by oxidation of graphite using strong and concentrated oxidising acids (e.g. H_2SO_4 and HNO_3).[442-445] This process results in oxygen-containing functional groups (e.g. carboxylic, hydroxyl and epoxy groups) being created and covalently attached to the basal carbon plane. Specifically, Carboxylic functionalities are mostly located at the sheet edges, whereas hydroxyl and epoxide functional groups are on the top and bottom surfaces of the GO sheets.[302,303] The presence of these functional groups significantly disturbs the planar graphene structure and facilitates exfoliation to generate single layer GO sheets as a dispersion in aqueous media.[446] Due to ionisation of the carboxylic acid and phenolic hydroxyl groups attached to the carbon skeleton, GO sheets are negatively charged across a wide pH range, with the zeta potential becoming more negative as the pH increases.[305,306] Furthermore, these oxygen-containing groups on the GO surface can be functionalised for the preparation of polymer/GO nanocomposites.

Numerous approaches have been reported for the preparation of graphene-based polymer nanocomposites using graphene related materials (e.g. graphene, graphene oxide and reduced graphene oxide) as a filler *via* solution blending[271,272] or melt processing.[272,273] The graphene oxide is usually functionalised through the carboxylic or hydroxyl groups on the basal surface *via* esterification,[447] amination,[448] isocyanate grafting[449] or polymer grafting.[450] For solution blending, the polymer is dissolved in a

selected solvent, and the GO nano fillers are dispersed in the polymer solution. Generally, more homogeneous nanocomposites can be obtained, but the residual solvents in nanocomposites are hard to remove.[271,272] In contrast, from an industrial standpoint, melt processing is potentially preferred, as it is direct and can be conducted without using solvents, and thus suitable for a wide range of polymers and nano fillers.[272,273] However, this approach needs to be conducted at relatively high temperature (>180°C)[274] and the nano fillers readily aggregate due to high surface areas, leading to poor dispersion of the nano fillers in composites and phase separation of the polymer/inorganic phase.[275]

Recently, it has been shown that GO based polymer nanocomposites can be readily prepared through hybrid latex particles on the nanoscale *via* heteroflocculation between negatively charged GO and positively charged polymer latex nanoparticles.[283-285,325-327] Pham *et al.* prepared poly(methyl methacrylate)/GO (PMMA/GO) nanocomposite by heteroflocculation between positively charged PMMA latex nanoparticle (~200 nm) and negatively charged GO sheets (from a few to 10 μm).[327] Wu *et al.*[283] reported polystyrene/GO (PS/GO) nanocomposite can be obtained by heteroflocculation between positively charged amine-modified PS latex nanoparticle (150 to 220 nm) and negatively charged GO sheets (several micrometers).[327] In those studies, the GO sheets were much larger than the size of the PMMA or PS nanoparticles, leading to several latex nanoparticles were wrapped by one large GO sheet. Both the PMMA/GO and PS/GO nanocomposite were further dried and hot pressed to obtain composite pellets. These pellets exhibited excellent electrical conductivity. In contrast, Hong *et al.* demonstrated PS/rGO nanocomposite particles with core/shell morphology can be prepared *via* a layer-by-layer heteroflocculation route using negatively charged PS latexes (~1.2 μm), positively charged rGO-NH_3^+ and negatively charged rGO-COO^- nanosheets.[325] The thickness of the rGO shell could be increased by alternating coatings of rGO-NH_3^+/rGO-COO^- layers.

However, the studies above were mainly focused on the surface morphologies of the nanocomposite particles and their bulk electric, thermal or mechanical properties. It is noteworthy that those reported polymer/GO nanocomposites were prepared using either GO sheets or latex particles at nano-size. Furthermore, to the best of our knowledge, there are no prior reports on investigating the details of

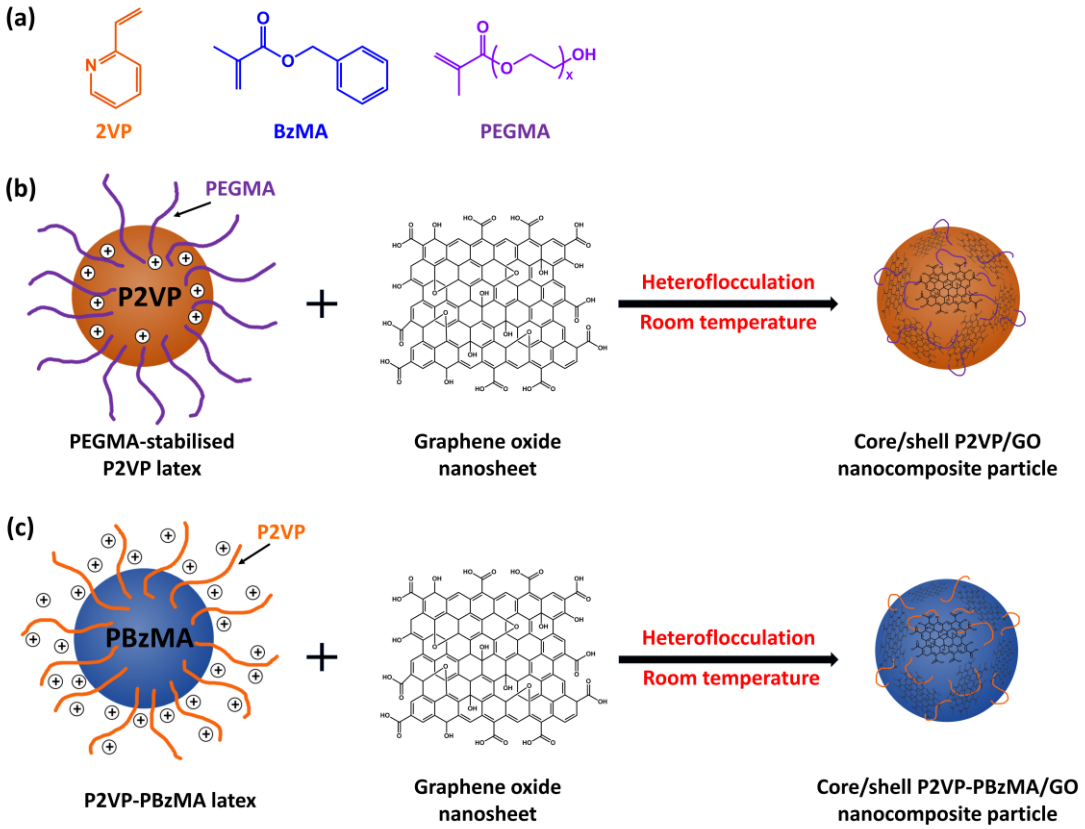

Scheme 5.1. (a) Chemical structures of 2-vinyl pyridine (2VP), benzyl methacrylate (BzMA) and poly(ethylene glycol) methacrylate (PEGMA). Schematic representation of the physical adsorption of graphene oxide nanosheets onto sterically stabilised (b) PEGMA-stabilised P2VP and (c) P2VP–PBzMA latexes *via* electrostatically-induced heteroflocculation.

electrostatically-induced heteroflocculation process between GO nanosheets and polymer latex nanoparticles prepared *via* RAFT-mediated PISA.

Herein, the preparation of polymer/GO nanocomposite particles *via* electrostatically-induced heteroflocculation is reported (**Scheme 5.1**). Specifically, cationic poly(ethylene glycol) methacrylate (PEGMA)-stabilised P2VP latex and P2VP-stabilised poly(benzyl methacrylate) (PBzMA) latex were synthesised *via* conventional and RAFT emulsion polymerisation, respectively. Polymer/GO nanocomposite particles were prepared *via* heteroflocculation at room temperature by mixing these positively charged latex nanoparticles and the negatively charged GO nanosheets. It is noteworthy that both the latexes and GO sheets used herein were at nanoscale. Furthermore, the previously prepared anionic sterically-stabilised poly(potassium 3-sulfopropyl methacrylate)-poly(benzyl methacrylate)

(PKSPMA–PBzMA, see **Chapter Two**) and non-ionic poly(benzyl methacrylate) (PBzMA, see **Chapter Three**) latexes were used to perform control heteroflocculation experiments. The polymer latexes and resulting polymer/GO nanocomposite particles were characterised *via* DLS, DCP, TEM, UV-Vis and aqueous electrophoresis. Furthermore, both the PEGMA-stabilised P2VP and P2VP–PBzMA latexes are pH responsive and have different surface charges at varying pH. Thus, the effects of solution pH on the formation of the polymer/GO nanocomposite particles prepared *via* heteroflocculation were investigated and it is shown that heteroflocculation can be achieved in either acidic (pH 2) or basic (pH 9) conditions. For the sake of brevity, a shorthand label is used throughout this chapter: PEGMA-stabilised P2VP and P2VP–PBzMA or "PEGVP" and "V–B" are utilised to denote the two types of polymer latex, respectively.

5.2. Experimental details

5.2.1. Materials

Divinylbenzene (DVB, 80 mol. % 1,4-divinyl content) and 2-vinyl pyridine (2VP, 97%) were purchased from Sigma-Aldrich (UK) and Fluka (UK), respectively, and passed through a column of activated basic alumina to remove inhibitors and impurities before use. 2,2'-Azodiisobutyramidine dihydrochloride (AIBA, 97%) and monomethoxy-capped poly(ethylene glycol) methacrylate (PEGMA) macromonomer (M_n = 2000 g mol^{-1}, M_w/M_n = 1.10; 50% w/w in H_2O) were purchased from Sigma-Aldrich (UK) and used as received. Aliquat 336 (99.9%) and dialysis tubing (regenerated cellulose, molecular weight cut-off (MWCO) = 12 kDa, diameter = 16 mm) were purchased from Fisher Scientific (UK) and used as received. Graphene oxide water dispersion (monolayer content >95%; concentration 4 mg mL^{-1}) was purchased from Graphenea (Spain) and purified by dialysis against water to remove impurities before use. Anionic poly(potassium 3-sulfopropyl methacrylate)-poly(benzyl methacrylate) (PKSPMA–PBzMA), non-ionic poly(benzyl methacrylate) (PBzMA) and cationic poly(2-vinyl pyridine)-poly(benzyl methacrylate) (P2VP–PBzMA) latexes were prepared in house, as described in **Chapters Two, Three** and **Four**, respectively. Deionised water was used in all experiments.

5.2.2. Synthesis of PEGMA-stabilised P2VP latex *via* conventional emulsion polymerisation

The synthesis of PEGMA-stabilised P2VP latexes has been described in detail elsewhere.[320,324,419] A typical protocol for the synthesis of P2VP *via* conventional emulsion polymerisation was as follows. Aliquat 336 surfactant (0.5 g) and PEGMA stabiliser (1.0 g of a 50% w/w aqueous PEGMA solution) were dissolved in deionised water (38.5 g) in a 100 mL a round-bottomed flask with stirring. A comonomer mixture of 2VP (4.95 g) and DVB (0.05 g) was added and the sealed reaction vessel was deoxygenated *via* five vacuum/nitrogen cycles using a Schlenk line at room temperature. After deoxygenation, the vessel was immersed into a preheated oil bath at 60 °C with stirring for 20 min. A portion of the initiator solution (10 mg of AIBA dissolved in 5 g of degassed water) was added, corresponding to time zero of the polymerisation. The reaction was heated at 60 °C for 24 h and magnetically stirred at 250 rpm. Polymerisations were quenched by cooling to room temperature and exposing to air. The latex particles were initially purified by dialysis against water to remove the majority of excess Aliquat 336 surfactant and non-grafted PEGMA stabiliser. The initially purified latex particles were further purified using repeated centrifugation/redispersion cycles for three times. During each cycle, the supernatant was carefully decanted and replaced with fresh water to remove residual 2VP monomer, Aliquat 336 surfactant and PEGMA stabiliser.

5.2.3. Preparation of core/shell polymer/GO nanocomposite particles *via* heteroflocculation

Aqueous dispersions of GO and latex particles were diluted separately using deionised water. The solutions were adjusted to pH 2, 5 or 9 using HCl or KOH and then water was added to adjust the solids content to 0.1% w/w. An appropriate volume of the latex particle dispersion was added to the GO dispersion with stirring using IKA vortex mixer for 60 seconds. These samples were allowed to equilibrate using a roller mixer at room temperature for 48 hours.

5.2.4. Characterisation

5.2.4.1. Dynamic light scattering

Dynamic light scattering (DLS) studies were performed using a Malvern Zetasizer Nano ZS instrument equipped with a He–Ne solid-state laser operating at 633 nm and back-scattered light at a scattering angle of 173°. Latex dispersions were diluted to approximately 0.1% w/w using deionised water. DLS samples were analysed at 25 °C using disposable plastic cuvettes and data were averaged over three consecutive measurements.

5.2.4.2. Aqueous electrophoresis

Aqueous electrophoresis studies were performed using the same Malvern Zetasizer Nano ZS instrument described above. For analysis of the PEGMA-stabilised P2VP latexes and GO, the solution pH was initially adjusted to 12 using KOH in the presence of 1.0 mM KCl. The solution pH was then manually decreased from 12 to 2 by addition of HCl as required. For analysis of the P2VP–PBzMA latexes, the solution pH was initially adjusted to 2 using HCl in the presence of 1.0 mM KCl. The solution pH was then manually increased from 2 to 12 by addition of KOH as required. Aqueous dispersions (approximately 0.1% w/w) were analysed at 25 °C using disposable folded capillary cells (Malvern DTS1017) and data were averaged over three consecutive measurements.

5.2.4.3. Gravimetry

Monomer conversions were determined by gravimetry. Aliquots were withdrawn and weighed (approximately 1.0 g) in 7 mL vials. After weighing, the samples were immediately quenched with approximately 10 µL of 1% w/w hydroquinone in an ice-water bath. The specimens were placed in an oven and dried at 60 °C to constant weight. Conversions were calculated from the measured dry residue.

5.2.4.4. Transmission electron microscopy

Transmission electron microscopy (TEM) images were recorded using a FEI Tecnai G2 20 instrument operating at an accelerating voltage of 200 kV and connected to a Gatan 1k CCD camera. Samples for TEM observation were prepared by depositing 2 µL of diluted samples (approximately 0.1% w/w) onto 400 mesh carbon-coated copper grids.

For PEGMA-stabilised P2VP latexes and polymer/GO nanocomposite particles, the samples were dried overnight at ambient temperature. For TEM studies of the P2VP–PBzMA nanoparticles, the grids were dried for 30 min under ambient temperature, and then carefully blotted with filter paper to remove excess solution. The samples were stained in a vapour space above ruthenium tetroxide (RuO_4) solution for 7 min at ambient temperature.[349] The mean nanoparticle diameters were determined using ImageJ software and over 200 randomly selected particles were measured for each sample.

5.2.4.5. UV-Vis spectrophotometry

UV spectra were recorded using an Agilent Cary 60 UV-Vis spectrophotometer between 200 to 800 nm with a scan speed of 600 nm min^{-1}. Samples were prepared by centrifuging the heteroflocculation dispersions at 200 rpm for 5 min, and subsequently the supernatants were carefully collected. A moderate centrifuge speed was utilised to ensure that only polymer/GO nanocomposite particles settled at the bottom and free GO was still dispersed in the supernatant. The supernatants were diluted to approximately 0.05% w/w using deionised water. UV-vis samples were analysed at room temperature using quartz cuvettes. The concentration of free GO in the supernatant was calculated using Beer-Lambert's law. The calibration samples of GO were prepared at concentrations ranging from 1.0×10^{-3} mg mL^{-1} to 6.7×10^{-2} mg mL^{-1} and analysed at room temperature.

5.2.4.6. Disc centrifuge photosedimentometry

Disc centrifuge photosedimentometry (DCP) studies were conducted using a CPS DC24000 instrument to obtain particle size distributions. The disc centrifuge was operated at 22,000 rpm. The spin fluid contained a density gradient built from 12 to 4% w/w aqueous sucrose, and then 0.5 ml of *n*-dodecane was injected to prevent surface evaporation and to extend the lifetime of the gradient. The aqueous sucrose solutions were adjusted to pH 2, 5 or 9 (corresponding to the heteroflocculation dispersion pH) using HCl or KOH before use. The disc centrifuge was calibrated using a polystyrene latex standard with a mean particle diameter of 348 nm.

5.3. Results and discussion

5.3.1. Characterisation of P2VP–PBzMA and PEGMA-stabilised P2VP latex nanoparticles

Two P2VP–PBzMA (V–B) latexes with different P2VP stabiliser chain length and a PEGMA-stabilised P2VP (PEGVP) were prepared by RAFT emulsion and conventional emulsion polymerisation, respectively (**Table 5.1**). The protocol for the preparation of P2VP–PBzMA latexes *via* RAFT-mediated PISA using P2VP as macro-CTA has been discussed detailly in **Chapter Four**. Briefly, P2VP–PBzMA diblock copolymer nanoparticles with controllable particle diameters can be obtained *via* RAFT emulsion polymerisation using the same target copolymer composition at varying solution pH. Herein, P2VP–PBzMA latexes with the same core-forming PBzMA block (target DP 300) and different chain length of P2VP stabiliser were prepared. More specifically, $P2VP_{32}$–$PBzMA_{300}$ (V_{32}–B_{300}) and $P2VP_{67}$–$PBzMA_{300}$ (V_{67}–B_{300}) diblock copolymer nanoparticles were prepared *via* RAFT emulsion polymerisation of BzMA at pH 2.5 and 3.0, respectively. In both cases, high conversions (>99%) were achieved after polymerisation at 70 °C for 24 h, as determined *via* gravimetry. **Figure 5.1a** and **Figure 5.1b** show that both the V_{32}–B_{300} and V_{67}–B_{300} latex had relatively narrow particle size distributions with hydrodynamic diameters of 139 nm and 149 nm, respectively. TEM images were consistent with DLS analysis and confirm that these latexes were near-monodisperse (**Figure 5.2a-b** and **Figure A.10a-b**).

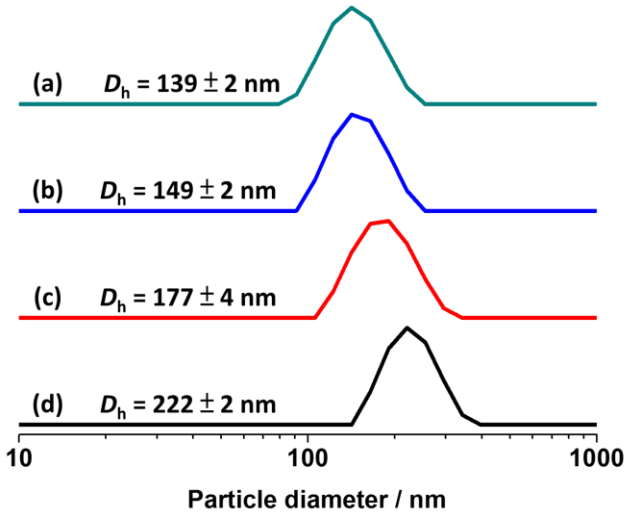

Figure 5.1. Intensity size distributions obtained *via* DLS for (a) $P2VP_{32}$–$PBzMA_{300}$, (b) $P2VP_{67}$–$PBzMA_{300}$, (c) $PKSPMA_{32}$–$PBzMA_{300}$ and (d) PEGMA-stabilised P2VP latexes. Traces (a), (b), (c) and (d) represent entries 1–4 in **Table 5.1**, respectively.

Table 5.1. Summary of the sterically-stabilised latexes used in this work.

Entry [a]	Target composition	Conversion[b] / %	D_h[c] / nm	D_{TEM}[d] / nm
1	$P2VP_{32}$–$PBzMA_{300}$	99	139 (0.098)	88 ± 7
2	$P2VP_{67}$–$PBzMA_{300}$	99	149 (0.057)	102 ± 8
3	$PKSPMA_{32}$–$PBzMA_{300}$	99	177 (0.040)	132 ± 4
4	PEGMA-stabilised P2VP	96	222 (0.052)	173 ± 5

[a] Entries 1 and 2 were prepared *via* RAFT aqueous emulsion polymerisation at 70 °C using cationic P2VP as a stabiliser at pH 2.5 and 3.0, respectively. Entry 3 was prepared *via* RAFT emulsion polymerisation at 70 °C using anionic PKSPMA as a stabiliser in methanol/water mixture at an alcohol content of 33% w/w. Entry 4 was prepared *via* conventional emulsion polymerisation at 60 °C using 10% w/w non-ionic PEGMA stabiliser, 10% w/w Aliquot 336 surfactant and 1% w/w DVB cross-linker, respectively. [b] Monomer conversions were determined *via* gravimetry. [c] Mean hydrodynamic diameter obtained *via* DLS, where DLS polydispersity index values are indicated in brackets. [d] Mean TEM particle diameters were calculated by analysing 200 particles using ImageJ software.

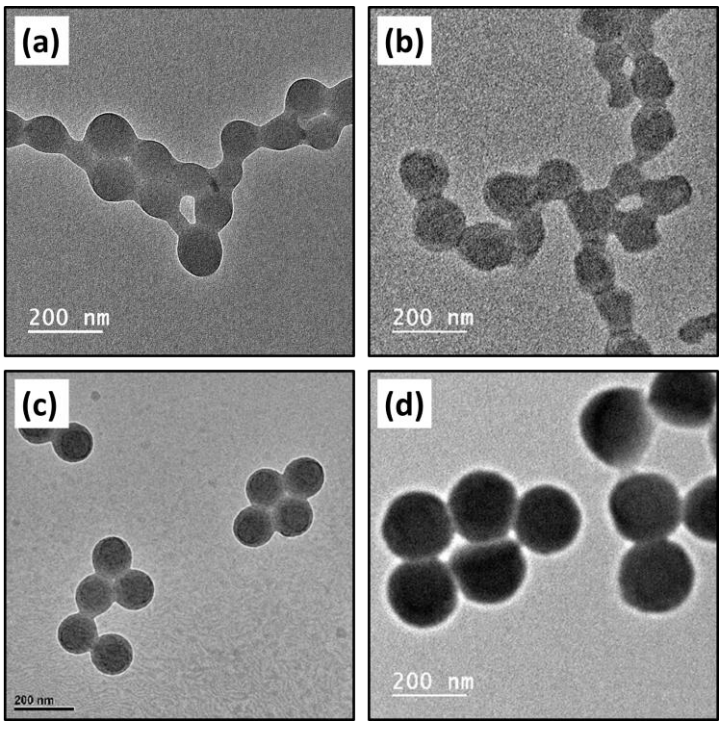

Figure 5.2. Representative TEM images for (a) $P2VP_{32}$–$PBzMA_{300}$, (b) $P2VP_{67}$–$PBzMA_{300}$, (c) $PKSPMA_{32}$–$PBzMA_{300}$ and (d) PEGMA-stabilised P2VP latex nanoparticles. (a), (b), (c) and (d) represent entries 1–4 in **Table 5.1**, respectively.

PEGMA-stabilised P2VP (PEGVP) latexes with different diameters can be prepared *via* conventional aqueous emulsion polymerisation by altering the monomer and initiator concentration.[320,324,419] According to a previously reported protocol,[324] a PEGVP latex with target hydrodynamic diameter of approximately 200 nm was prepared by conducting the polymerisation at total solids content of 11.0% w/w with 0.2% w/w AIBA initiator and 1.0% w/w DVB as cross-linker relative to monomer, respectively. After polymerisation for 24 h, high monomer conversion (96%) was achieved and all excess stabiliser (PEGMA) and surfactant (Aliquat 336) were removed by dialysis against water and three centrifugation/redispersion cycles. **Figure 5.1d** shows that the PEGVP latex had a relatively narrow particle size distribution, with a hydrodynamic diameter of 222 nm, as confirmed by TEM studies (**Figure 5.2d** and **Figure A.10d**).

Figure 5.3a shows the zeta potential as a function of pH for the PEGVP latex (entry 4, **Table 5.1**). The PEGVP particles were slightly negatively charged at pH 11, with a zeta potential of approximately -3 mV. As the solution pH was lowered by the addition of HCl, the zeta potential became more positive and reached a plateau value of approximately +25 mV at pH 4.1. This is in good agreement with reported pK_a values, ranging from 3.85 to 4.75, for P2VP latexes with different degree of cross-linking.[419] A similar trend was observed for the V_{32}–B_{300} (**Figure 5.4a**) and V_{67}–B_{300} latexes (**Figure 5.5a**). The negative zeta potentials of PEGVP and V_{32}–B_{300} latexes at high pH can be attributed to the adsorption of OH^- ions on the primarily uncharged surface.[241,434,435] It is noteworthy that the zeta potential of the V_{32}–B_{300} and V_{67}–B_{300} latexes were much higher than that of the PEGVP latex across the whole pH range studied. This is because the P2VP chains are present in the corona of the P2VP–PBzMA latexes, whereas they are in the core of the PEGVP latexes and are surrounded by non-ionic PEGMA stabiliser.

Figure 5.3b shows the mean hydrodynamic diameter (D_h) as a function of pH for the PEGVP latex (entry 4, **Table 5.1**). No obvious particle diameter change was observed between pH 11 and 5. However, the particle diameter increased significantly below pH 4.1. This can be attributed to the pyridine groups on P2VP chains becoming protonated and inducing swelling of the lightly cross-linked latex particles to form microgels. Interestingly, the observed particle diameter trend was the opposite for V_{32}–B_{300} latexes (**Figure 5.4b**) and V_{67}–B_{300} latexes (**Figure 5.5b**), with the particle diameters increasing significantly above pH 5. As the P2VP chains do not form the core

of the particle, no latex-to-microgel transition occurs. As discussed in **Chapter Four** (see **section 4.3.5**), these observations can be attributed to the relatively high ionic strength (K^+ and Cl^-), generated from the pH solution (HCl and KOH) and background electrolyte (KCl), inducing particle flocculation. Briefly, at high pH the protonation degree of P2VP stabiliser decreases, resulting in weaker positive charge and lower electrostatic repulsion among particles. Furthermore, the relatively high ionic strength screens the electrostatic repulsion and induces flocculation,[436,437] resulting in the large particle diameters reported by DLS analysis. It is noteworthy that the induced flocculation can be avoided by diluting these latexes using water at the desired pH directly to minimise the build-up of ionic strength (**Figure 4.13** and **Figure 4.14** in **Chapter Four**). Therefore, in this work, all the latex dispersions utilised for heteroflocculation with GO nanosheets were directly diluted using water at corresponding pH with no added electrolyte.

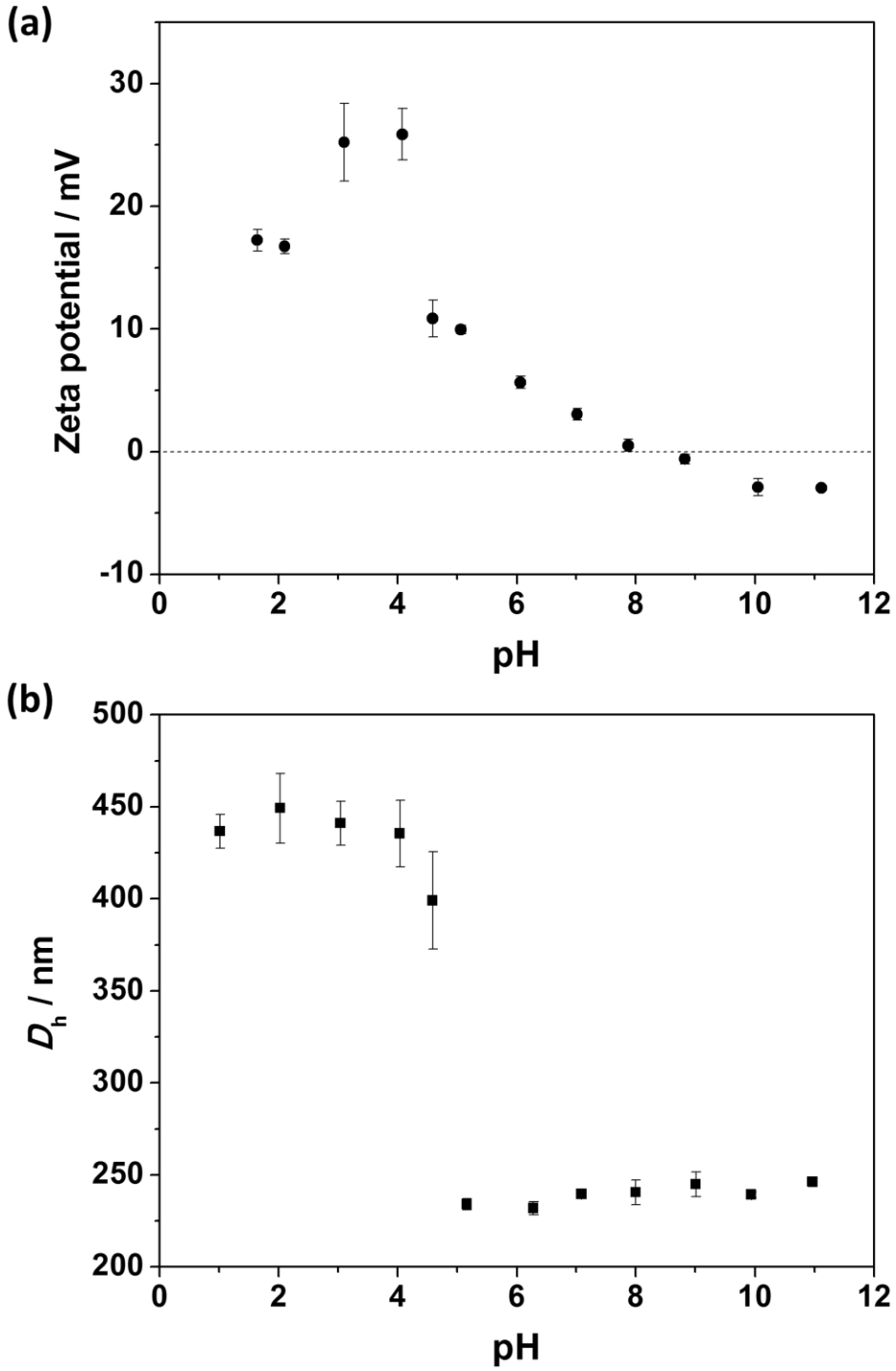

Figure 5.3. (a) Zeta potential and (b) mean hydrodynamic diameter (D_h) as a function of pH obtained for PEGVP latex (entry 4, **Table 5.1**). Measurements were conducted at a latex concentration of approximately 0.1% w/w with 1 mM KCl as a background electrolyte. The solution pH was initially adjusted to pH 11 by the addition of KOH and subsequently lowed to pH 1.0 using HCl.

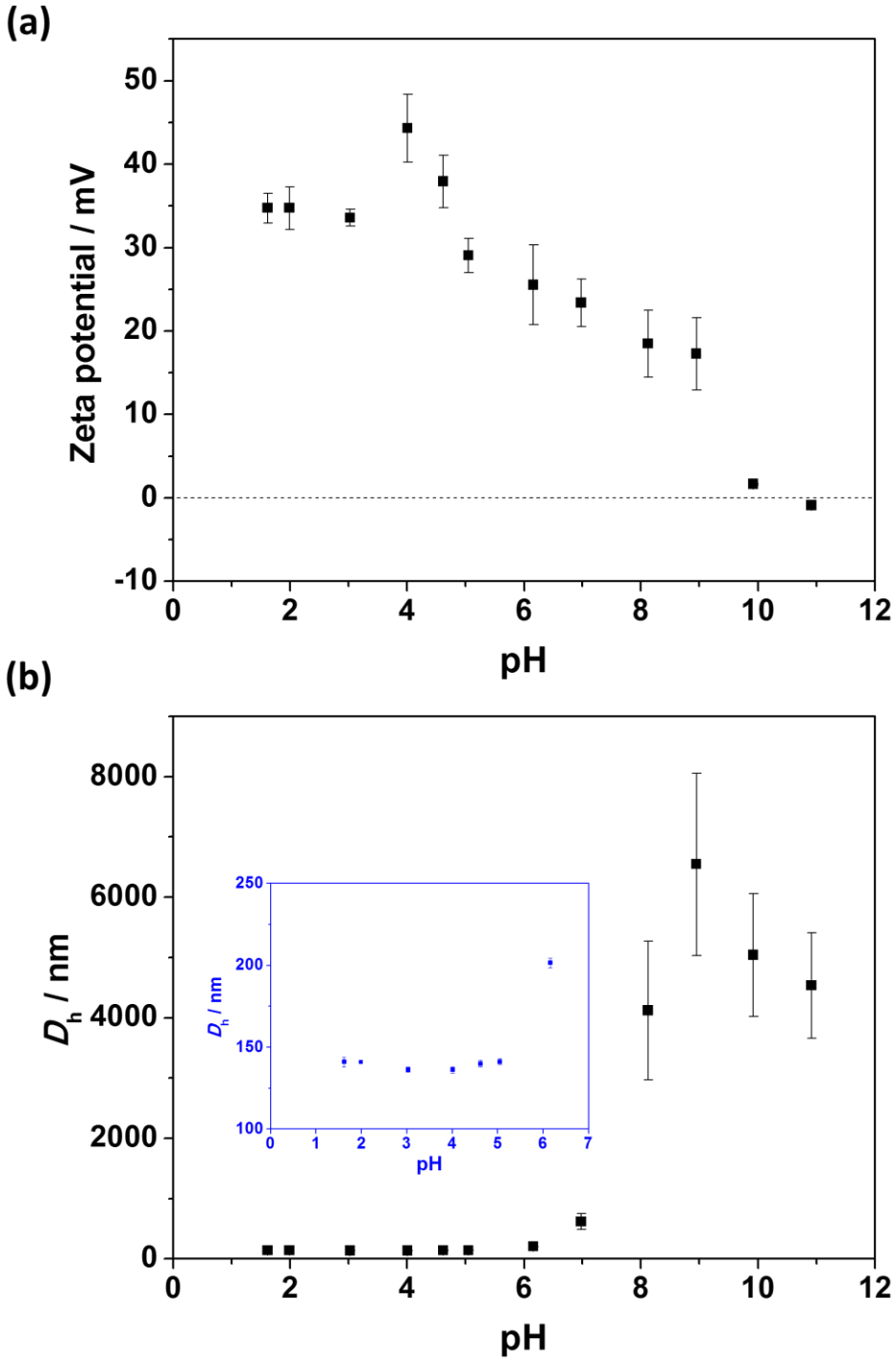

Figure 5.4. (a) Zeta potential and (b) mean hydrodynamic diameter (D_h) as a function of pH obtained for V_{32}–B_{300} latex (entry 1, **Table 5.1**). Measurements were conducted at a latex concentration of approximately 0.1% w/w with 1 mM KCl as a background electrolyte. The solution pH was initially adjusted to pH 1.5 by the addition of HCl and subsequently titrated to pH 11 using KOH. The inset shows the magnification of the particle diameter changes below pH 7.

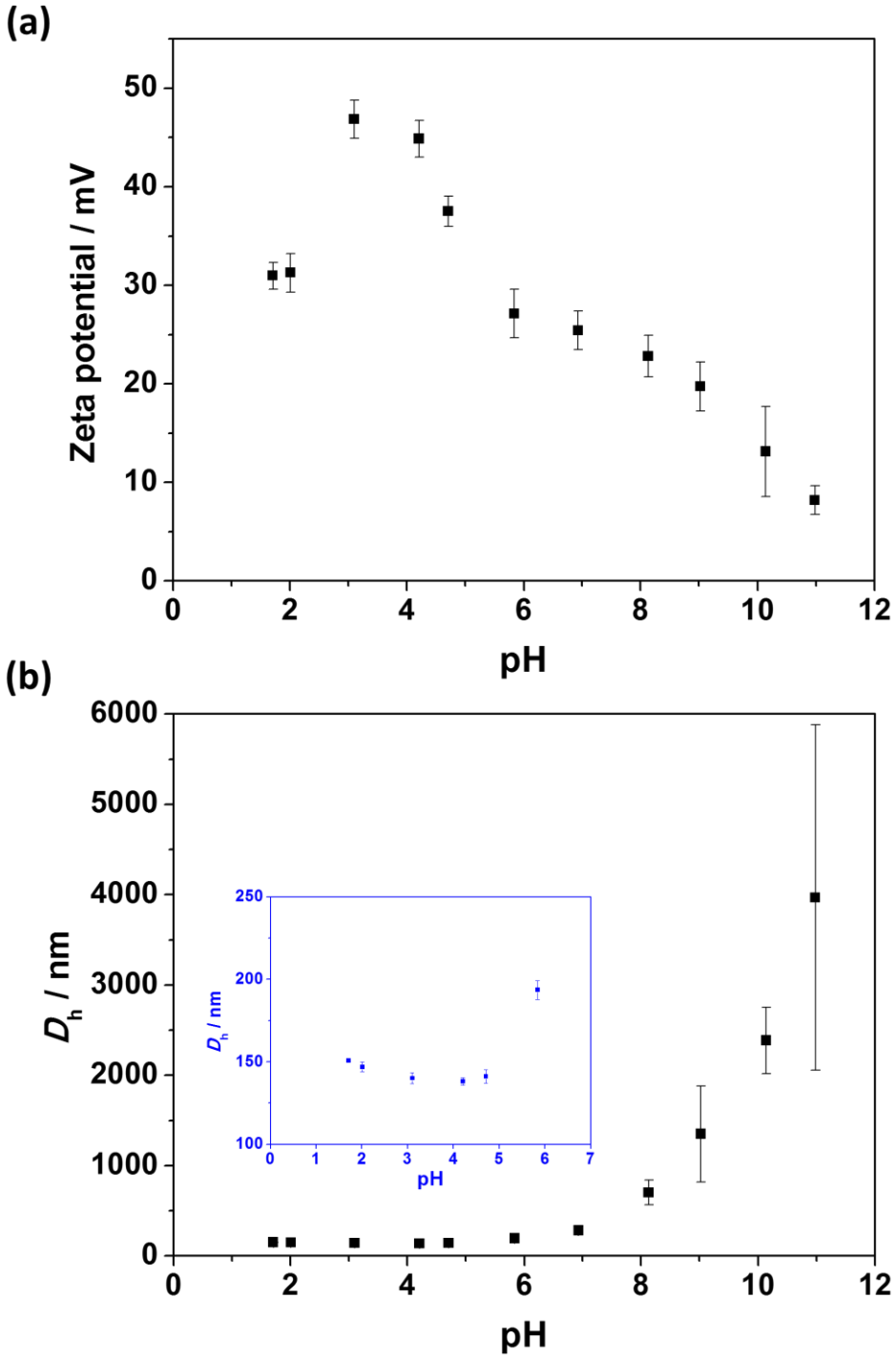

Figure 5.5. (a) Zeta potential and (b) mean hydrodynamic diameter (D_h) as a function of pH obtained for V_{67}–B_{300} latex (entry 2, **Table 5.1**). Measurements were conducted at a latex concentration of approximately 0.1% w/w with 1 mM KCl as a background electrolyte. The solution pH was initially adjusted to pH 1.5 by the addition of HCl and subsequently titrated to pH 11 using KOH. The inset shows the magnification of the particle diameter changes below pH 7.

5.3.2. Characterisation of the commercial graphene oxide dispersion

A commercial graphene oxide (GO) aqueous dispersion was used in this work. Generally, GO is prepared *via* oxidation of graphite flakes using strong concentrated acid (e.g. HNO_3 and H_2SO_4). This process results in hydroxyl (–OH) and epoxy groups being formed on the basal planes, and carboxyl (–COOH) groups present on the sheet edges of the graphite structure to form GO (**Figure 5.6a**).[441,451,452] Furthermore, the NO_3^- and SO_4^{2-} are inserted into the graphene layers and the interlayer spacing of the graphite structure is exfoliated to form GO sheets.[453] However, the GO sheets may still tend to congregate and form multilayer agglomerates during storage.[454]

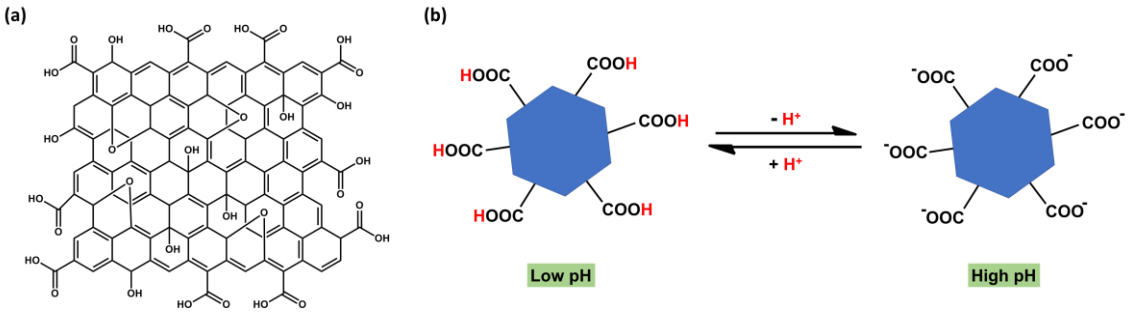

Figure 5.6. (a) Two-dimensional GO structure with hydroxyl (–OH) and epoxy groups on the basal plane and carboxyl (–COOH) groups on the edges.[451,452] (b) The –COOH groups on the edge of GO can be reversibly protonated at different pH.

Table 5.2. Summary of GO dispersions obtained using ultrasonication with varying parameters.

Entry	Amplitude / %	Process time / min	$D_{h,\,To}$[b] / nm	$D_{h,\,3D}$[c] / nm
1[a]			1448 ± 120	
2	70	5	395 ± 8	447 ± 6
3	70	10	341 ± 5	391 ± 11
4	70	30	235 ± 2	286 ± 2
5	90	5	425 ± 13	470 ± 23
6	90	10	375 ± 6	403 ± 2

[a] Commercial GO dispersion received from Graphenea without sonication. [b] Obtained *via* DLS immediately after sonication. [c] Obtained *via* DLS after storage for 3 days. The GO concentration was fixed at 4 mg mL^{-1}.

Normally, oxidised graphite is readily exfoliated using ultrasonication to generate GO nanosheets.[455,456] In order to obtain relatively uniform GO nanosheets, the commercial GO aqueous dispersions (4 mg mL^{-1}) was sonicated using an ultrasonic probe at various amplitudes (70% or 90%) and process times (5, 10 or 30 min, see **Table 5.2**). Although GO is not a spherical material, the mean hydrodynamic diameter determined *via* DLS analysis still can be used for qualitative quantification of the changes in GO size.[457,458] DLS reported that the diameter of GO after sonication decreased significantly from approximately 1500 nm to 230–430 nm (**Figure 5.7** and **Table 5.2**). Furthermore, the reported diameter of GO decreased with increasing process time at a fixed amplitude. For example, the diameter was approximately 395 nm after ultrasonication at 70% amplitude for 5 min, whereas the diameter was 235 nm (about 41% less) for 30 min. However, the GO diameters did not become increasingly smaller when using higher amplitude (90%) for a fixed process time. For instance, after ultrasonication for 10 min, the diameter was 340 nm when using 70% amplitude, whereas the diameter was 375 nm when using 90% amplitude. Furthermore, the degree of aggregation of GO after ultrasonication was monitored *via* DLS (**Figure 5.7**). In all cases, only minor increases in particle diameter were observed during storage for 3 days.

Aqueous electrophoresis measurements performed on the commercial GO aqueous dispersion after sonication at 70% aptitude for 30 min (entry 4, **Table 5.2**) as a function of pH is shown in **Figure 5.8**. The zeta potential of GO in the range of pH 2 to pH 12 was between -18 mV to -38 mV, which is in agreement with the reported values in the literature.[446,459-461] As pH increases, the GO becomes more negative due to the deprotonation of carboxylic acid on the sheet edges (**Figure 5.6b**).[462]

To further investigate the effect of solution pH, aqueous GO dispersions were diluted using water and adjusted to pH 2, 5 and 9 prior to sonication at 70% amplitude for 30 min. As expected, the size of the GO sheets became smaller after sonication than the original GO dispersion (**Figure 5.9**) and TEM studies indicated that the GO dispersed at higher pH resulted in smaller GO sheets after sonication (**Figure 5.9b** and **Figure 5.9c**).

Disc centrifuge photosedimentometry (DCP) was also used to investigate the particle size distributions of the GO dispersions before and after sonication. DCP is a powerful technique to evaluate particle size distributions as it separates the particle population during analysis based on the size and relative density of the material.

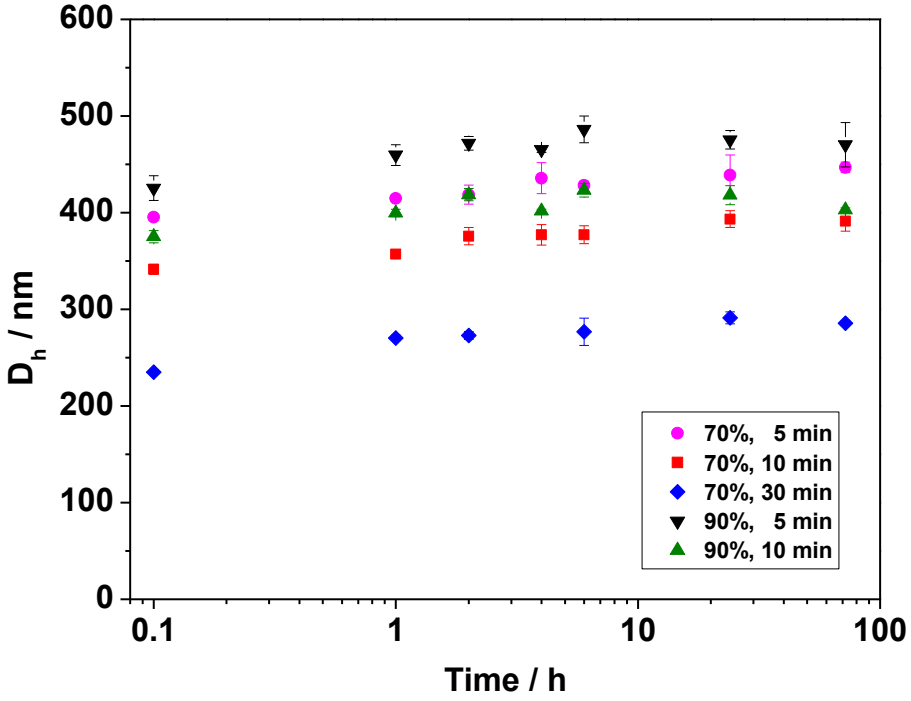

Figure 5.7. Mean hydrodynamic diameter (D_h) of GO sheets obtained after ultrasonication using various parameters [amplitude (70% or 90%) and process time (5, 10 or 30 min)] and over the course of being monitored for 3 days.

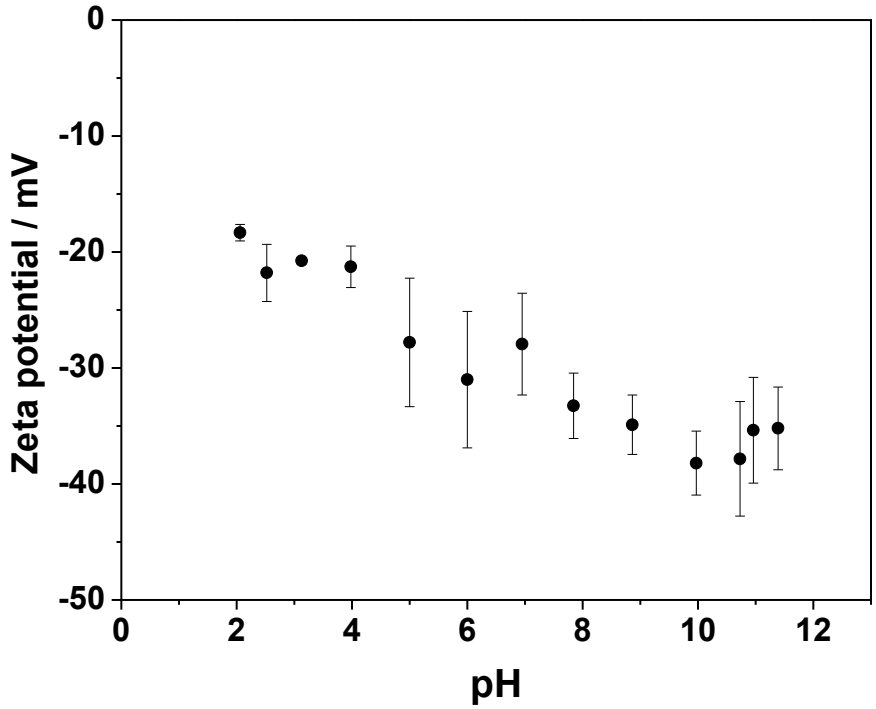

Figure 5.8. Aqueous electrophoresis data as a function of pH obtained for a GO dispersion (entry 4, **Table 5.2**) at a concentration of approximately 0.1% w/w in the presence of 1 mM KCl as a background electrolyte. The solution pH was initially adjusted to pH 2 by the addition of HCl and subsequently titrated to pH 12 using KOH.

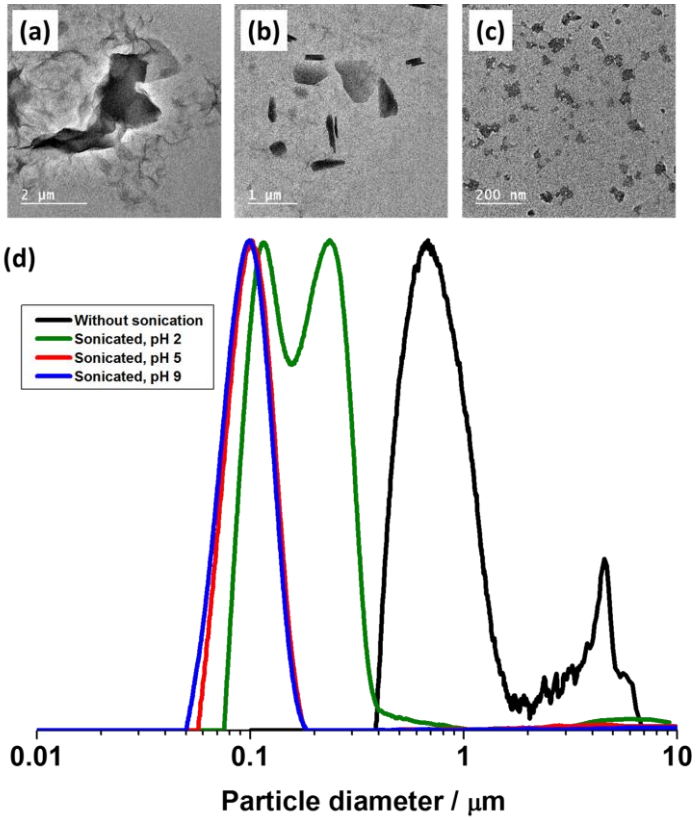

Figure 5.9. Representative TEM images of (a) commercial GO sheets as received and GO nanosheets obtained *via* sonication at 70% amplitude for 30 min in aqueous solution at (b) pH 2 and (c) pH 5. (d) DCP particle size distributions obtained for corresponding GO sheets. The density of the GO used in these measurements was taken as 1.2 g cm^{-3}.[463]

However, in order to provide accurate values for particle diameter, the technique assumes a spherical morphology and a single value for particle density.[464-466] For GO, these assumptions are unlikely to be valid and as such the reported weight-average diameter should only be interpreted qualitatively. Nevertheless, for a given range of samples the relative shape and position of the peaks reported by DCP can be used to interpret differences in particle diameter, number of particle populations and degree of flocculation.

Figure 5.9d shows the particle size distributions for the commercial GO before and after sonication at pH 2, pH 5 and pH 9. Before sonication, the GO had a much broader size distribution with particle sizes up to 7 µm, suggesting the GO was aggregated to some extent and not well dispersed during storage. In contrast, the peaks observed after sonication at pH 5 and pH 9 were clearly shifted from the non-sonicated peak. Furthermore, the particle size distributions were monomodal and narrower, with no evidence of flocculation. This indicated that well dispersed GO sheets with smaller

particle sizes were obtained. It is noteworthy that the peak of GO sonicated at pH 2 was still clearly shifted from non-sonicated peak, but the primary peak at approximately 0.1 µm was slightly shifted to a larger size and a broader particle size distribution with two peaks was observed. This implies some degree of flocculation occurred after sonication. This can be attributed to a higher degree of protonation of the carboxyl groups at the GO sheet edges, resulting in lower charge repulsion. These observations are consistent with TEM studies (**Figure 5.9a-c**) and as such provides confidence in the use of DCP technique to analyse GO-containing dispersions.

5.3.3. Control heteroflocculation experiments using anionic or non-ionic latex nanoparticles

Following the characterisation of the polymer latexes and the GO dispersions, polymer/GO nanocomposite particles were prepared by heteroflocculation. Normally, there are four situations to consider for latex-GO mixtures: (i) the quantity of GO is insufficient to cover all of the surfaces latex particles; (ii) GO adsorbs onto the latex at monolayer coverage; (iii) GO is in excess, leading to the latex particles being fully coated, with excess GO either being present as a multilayer or remaining free in solution; and (iv) GO do not adsorb onto the latex, leading to the GO and latex co-existing in the dispersion.

Control heteroflocculation experiments were conducted to demonstrate the latter situation, where no adsorption was expected between negatively charged GO nanosheets and a negatively charged $PKSPMA_{32}$–$PBzMA_{300}$ latex (entry 3, **Table 5.1**). **Figure 5.10** shows DCP data for the anionic PKSPMA–PBzMA latex before and after addition of up to 20% w/w GO at pH 2 and pH 5. A very narrow monomodal particle size distribution was observed for the PKSPMA–PBzMA latex. With the addition of GO nanosheets, no changes in the peak related to the polymer latex at approximately 0.2 µm were observed. However, broad shoulders at approximately 0.1 µm were observed and the relative weight of this shoulder increased with increasing GO concentration. The small peak observed at approximately 0.1 µm is due to free GO and indicates that the latex particles and GO simply formed a binary mixture of noninteracting particles. Similar observations were recorded for heteroflocculation between GO and non-ionic PBzMA (described in **Chapter Three**, **Figure 5.11**) or highly anionic PSS–PBzMA (described in **Chapter Two**, **Figure A.11**) latex nanoparticles.

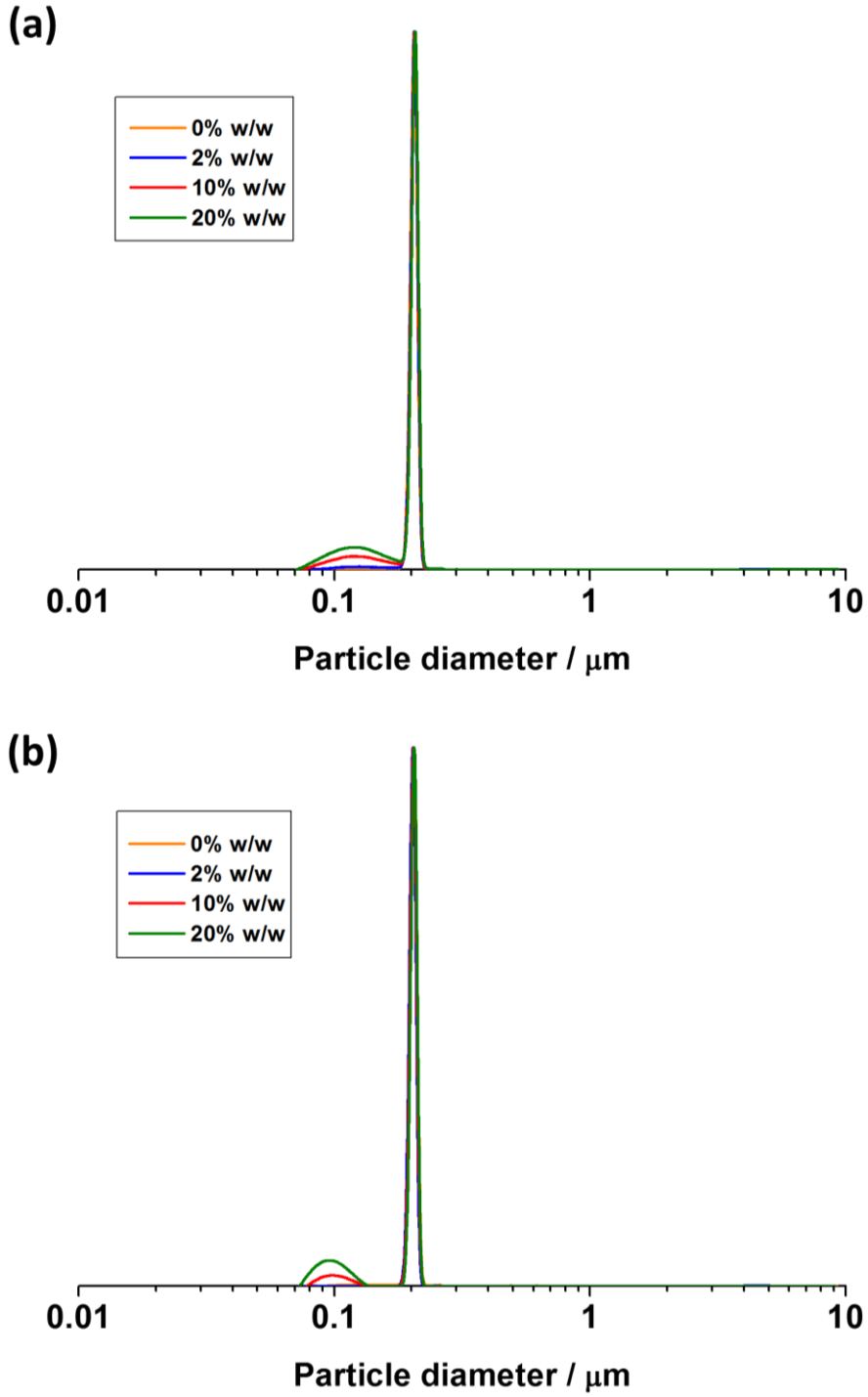

Figure 5.10. DCP particle size distributions obtained for anionic sterically-stabilised $PKSPMA_{32}$–$PBzMA_{300}$ latex (entry 3, **Table 5.1**) before and after heteroflocculation with addition of varying GO content (2 to 20% w/w relative to latex) at (a) pH 2 and (b) pH 5. In both cases, GO did not adsorb onto the surface of the anionic PKSPMA–PBzMA particles, and thus the particle size traces of latexes were identical. The density used to calculate these particle size distributions was taken as 1.18 g cm^{-3}.

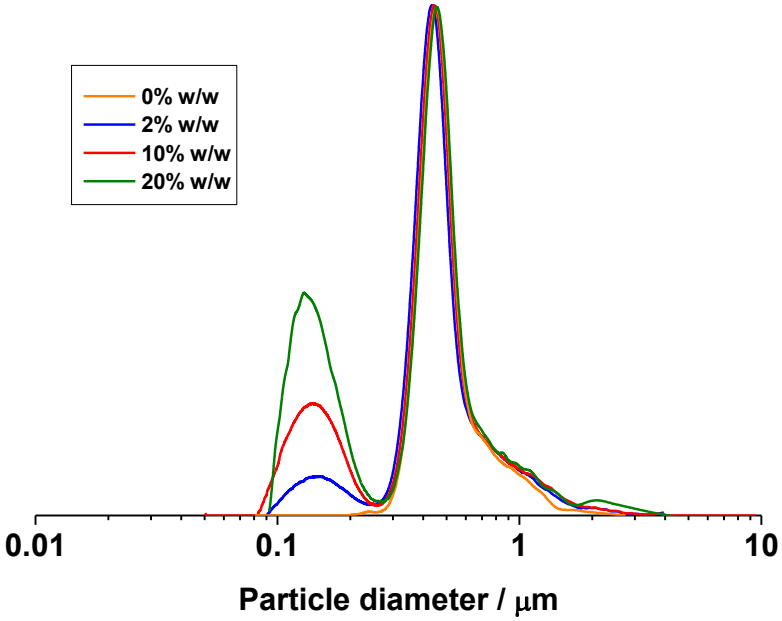

Figure 5.11. DCP particle size distributions obtained for non-ionic $PBzMA_{300}$ latex nanoparticles (311 nm, entry 3 in **Table 3.4**) before and after heteroflocculation with addition of varying GO content (2 to 20% w/w relative to latex) at pH 9. In all cases, the anionic GO were not adsorbed onto the surface of the non-ionic PBzMA particles, and thus the particle size traces of latexes were identical. The density used to calculate these particle size distributions was taken as 1.18 g cm^{-3}.

5.3.4. Preparation of polymer/GO nanocomposite particles *via* heteroflocculation using PEGMA-stabilised P2VP latex

Polymer/GO nanocomposite particles with core/shell morphology were prepared *via* heteroflocculation between cationic PEGMA-stabilised P2VP latex (PEGVP) and anionic GO nanosheets at room temperature (**Scheme 5.1b**). The PEGVP had relatively high positive surface charge (approximately +20 mV) at pH 2, and was approximately 0 mV at pH 9 (**Figure 5.3a**). In contrast, the GO was highly negatively charged (-20 to -40 mV) over a wide pH range (**Figure 5.8**) due to the presence of carboxylic acids on the sheet edges.[467] Therefore, in this work, heteroflocculation between GO and the PEGVP latexes was investigated at pH 2, 5 and 9 by the addition of PEGVP latexes (0.1% w/w) to a stirred aqueous GO dispersion (0.1% w/w), see **Table 5.3**. The solutions were mixed vigorously for 60 seconds and allowed to equilibrate using a roller mixer at room temperature for 48 hours before analysis.

Table 5.3. Summary of polymer/GO nanocomposite particles prepared *via* heteroflocculation between 222 nm PEGVP latex nanoparticles and GO nanosheets at varying pH in dilute aqueous solution at room temperature. The solids content was fixed at 0.1% w/w.

Entry	Solution pH	$D_{h,\ GO}$[a] / nm	GO content[b] / % w/w	Free GO[c] / %	Zeta potential[d] / mV
1	2	292	1		+17 ± 1
2	2	292	2		+18 ± 1
3	2	292	10		+16 ± 1
4	2	292	20	21	+17 ± 1
5	2	292	100	2	-10 ± 1
6	2	292	500	82	-21 ± 0
7	2	292	1000	75	-20 ± 1
8	5	111	1		+21 ± 2
9	5	111	2		+2 ± 1
10	5	111	10	2	-11 ± 4
11	5	111	20	36	-29 ± 0
12	5	111	100	88	-30 ± 1
13	5	111	500	>99	-37 ± 0
14	5	111	1000	>99	-38 ± 2
15	9	103	1		-6 ± 1
16	9	103	2		-3 ± 4
17	9	103	10	10	-29 ± 0
18	9	103	20	73	-32 ± 0
19	9	103	100	>99	-34 ± 1
20	9	103	500	>99	-38 ± 0
21	9	103	1000	>99	-40 ± 1

[a] Mean hydrodynamic diameter of GO determined *via* DLS analysis. [b] Concentration relative to latex. [c] Mass fraction of free GO relative to GO added, as determined by UV-Vis analysis. [d] Determined *via* aqueous electrophoresis analysis at the corresponding solution pH.

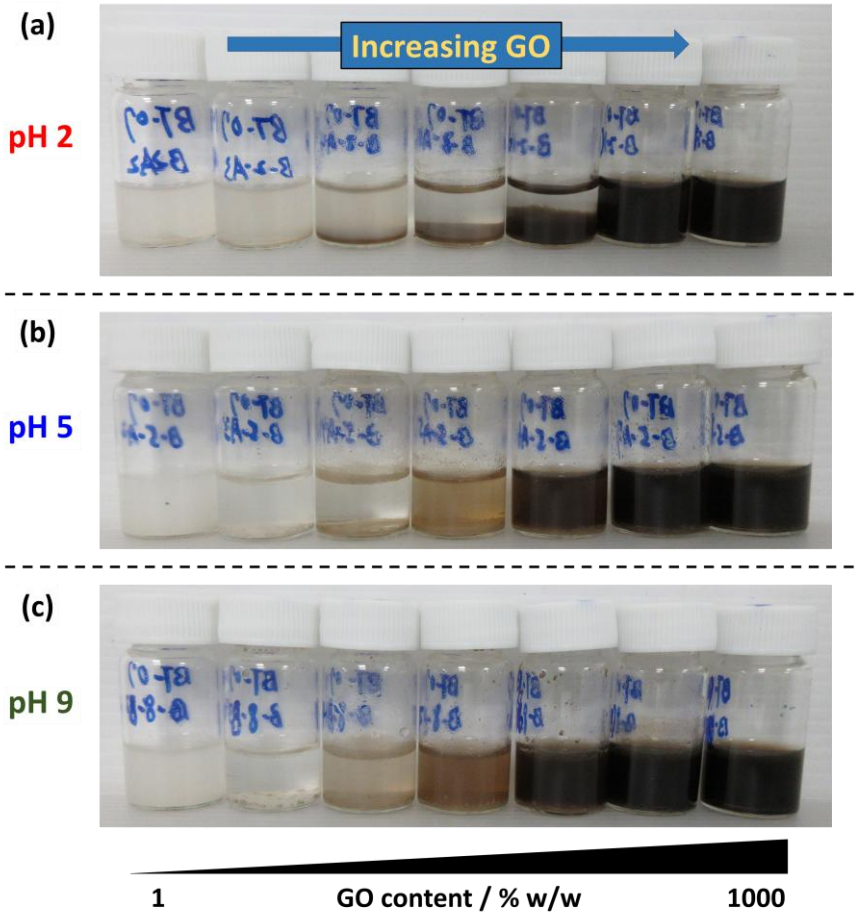

Figure 5.12. Digital photographs of vials containing PEGVP latex mixed with increasing quantities of GO nanosheets at (a) pH 2, (b) pH 5 and (c) pH 9 after standing overnight (entries 1–21, **Table 5.3**). The GO contents of the heteroflocculation dispersions from left to right are 1, 2, 10, 20, 100, 500 and 1000% w/w relative to latex, respectively. The solids content was fixed at 0.1% w/w.

As the PEGVP latex was gradually added into the GO dispersion, aggregation was observed immediately, implying that the latex particles and GO sheets were interacting due to the opposite surface charges. **Figure 5.12** shows digital photographs for various heteroflocculation experiments with varying GO content using PEGVP latex (entry 4, **Table 5.1**). Upon standing, sedimentation occurred for most samples within 1 hour, implying the GO sheets were adsorbed onto the latex surfaces and causing bridging flocculation. At lower GO contents (<10% w/w, left two vials), most of the latex remained dispersed in the solution, but some sedimentation occurred, indicating the GO sheets were adsorbed onto the latex but not providing colloidal stability. Furthermore, with increasing GO content, the colour of solution changed from white to transparent to dark. Darker colouration meant that there was more free GO dispersed in the solution. For

PEGVP/GO prepared at pH 5 and pH 9, relatively clear solutions occurred at GO contents of 20% w/w and 10% w/w (**Figure 5.12b** and **Figure 5.12c**). However, at pH 2 (**Figure 5.12a**), clear solutions were observed at GO contents up to 100% w/w. This difference can be attributed to the PEGVP latexes being in their microgel form at pH 2 (**Figure 5.3**) resulting in a stronger electrostatic interaction and larger surface area for GO adsorption.

The degree of flocculation of the polymer/GO nanocomposite particles can be assessed by comparing the DCP particle size distributions of latexes before and after the heteroflocculation process. Unfortunately, only one density can be used as an input in the DCP software for calculating the weight-average particle size, and thus only one accurate weight-average diameter can be determined per measurement. In the case of a binary particle mixture (latex and GO), this will inevitably lead to a relative error for one of the particle size distribution populations recorded. Furthermore, if heteroflocculation occurs, both the density and size of the original latex and resulting nanocomposite particles will necessarily be different, also leading to non-exact weight average particle sizes. Nevertheless, if a single density value is used in all measurements, the relative positions/shifts of the peaks in the particle size distributions can be used to deduce whether heteroflocculation did occur to form individual nanocomposite particles, and qualitatively assess the amount of free latex, free GO and the degree of bridging flocculation.

Figure 5.13 shows DCP data for the PEGVP latex (entry 4, **Table 5.1**) before and after the addition of GO at pH 9. **Figure 5.13h** shows that the particle size distribution of the PEGVP latex was relatively narrow, which a small shoulder attributed to a small population of dimers. With the addition of GO nanosheets, the narrow particle size distribution of the PEGVP latex became broader and the mean particle diameter significantly increases, indicating the formation of polymer/GO nanocomposite particles. Similar observations have been previously reported for P2VP/titania nanocomposite particles.[324] **Figure 5.13g** shows that significant flocculation of PEGVP latexes occurred and only a small amount of free latex was observed even after only adding 1% w/w GO based on latex. This indicated that the GO strongly adsorbed onto the latexes but caused bridging flocculation. With increasing GO contents (**Figure 5.13b-f**), no free PEGVP latexes were observed and large polymer/GO nanocomposite aggregates formed.

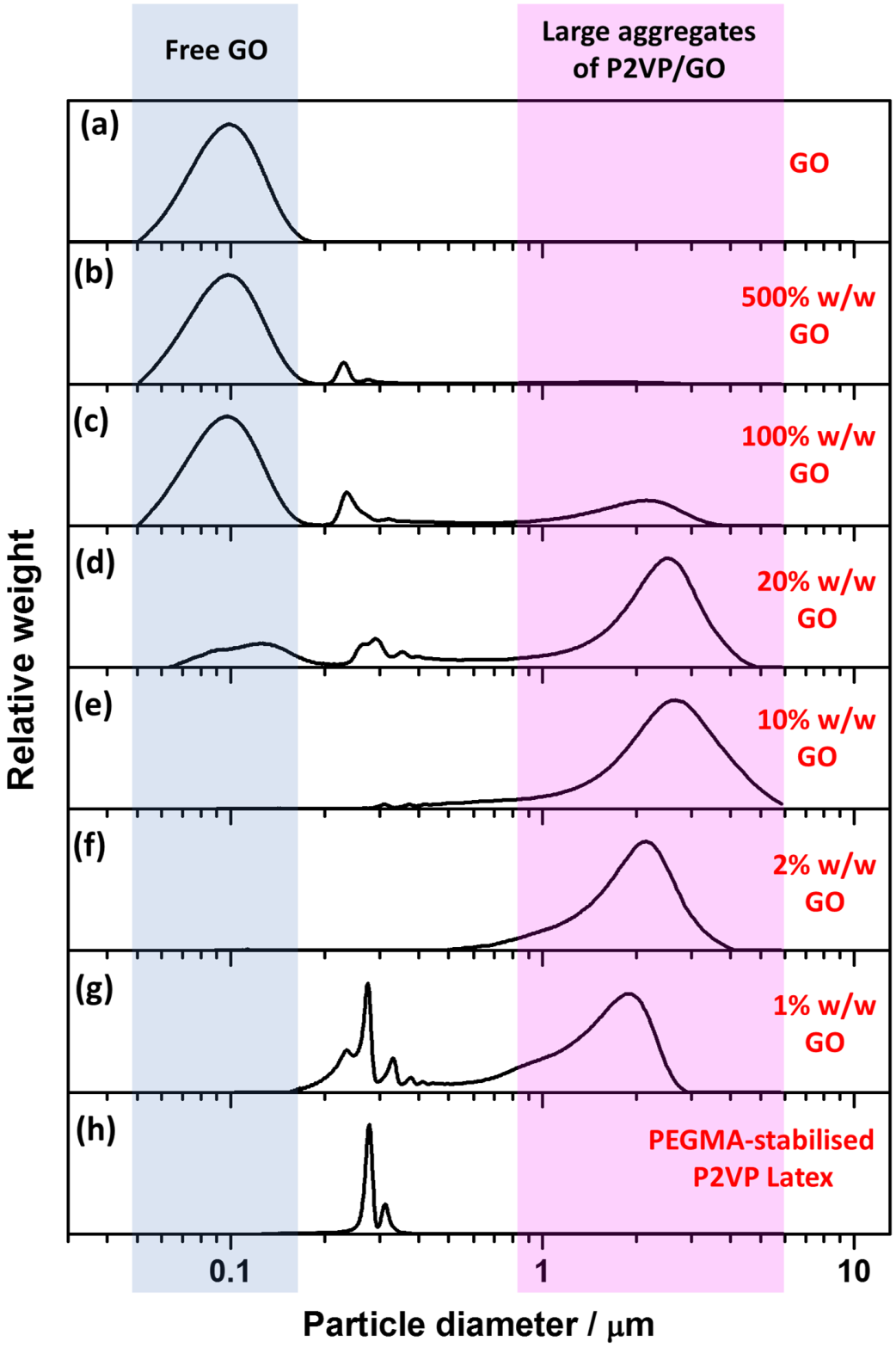

Figure 5.13. DCP particle size distributions obtained for PEGVP/GO nanocomposite particles prepared *via* heteroflocculation with varying GO content at pH 9. The density used to calculate this data was taken as 1.11 g cm^{-3}. (a) represents GO nanosheets obtained *via* sonication at 70% amplitude for 30 min. (b) – (g) represent entries 15–20 from **Table 5.3**, whereas (h) shows data obtained for entry 4 in **Table 5.1**.

Furthermore, with GO contents higher than 20% w/w (**Figure 5.13b-d**), the free GO peak at 0.1 μm is more obvious, indicating that the latex particles were fully covered by GO and free GO nanosheets were dispersed in the solution. In contrast, only a small free GO peak was observed at 10% w/w (**Figure 5.13e**), indicating that the GO content may be below or equal to the amount GO needed to cover the surface of the latex particles present. Therefore, the optimal quantity to form a monolayer of GO on the surface of the 222 nm PEGVP latex was between 10 and 20% w/w.

It is noteworthy that small peaks with a similar size to the PEGVP latexes were observed at GO content higher than 20% w/w (**Figure 5.13b-d**). These small peaks can be ascribed to a population of non-aggregated individual PEGVP/GO nanocomposite particles. Specifically, the PEGVP latexes were wrapped by GO to form larger PEGVP/GO nanocomposite particles with core/shell morphology (**Figure 5.14** and **Figure A.12**). As mentioned above, only one density can be used as an input in the DCP software for calculating the weight-average particle size. As the GO shell would be very hydrated, the individual PEGVP/GO nanocomposite particles would have a lower effective density than pristine PEGVP latexes,[341] and therefore the particle size determined by the DCP software may not accurately reflect the actual particle diameter.

Figure 5.14 and **Figure A.12** shows representative TEM images for the PEGVP/GO nanocomposite particles prepared *via* heteroflocculation with varying GO content at pH 2, 5 and 9. Nanocomposite particles with core/shell morphology were obtained at pH 5 and pH 9 with the GO content of 10% w/w (**Figure 5.14d**, **Figure 5.14g**, **Figure A.12d**, and **Figure A.12g**). This indicated that even though the latexes had a relatively low surface charge at pH 9, the GO could still adsorb onto the latexes *via* electrostatic interactions. It is noteworthy that there was no free GO observed on the TEM grids and the latex surface appeared to be fully coated with GO nanosheets. This suggested that the samples can be categorised as approximately monolayer coverage. However, the core/shell morphology was not formed well when using higher GO contents, and the latexes appeared to simply imbed or load onto the GO sheets.

It is noteworthy that the zeta potential values of nanocomposite particles were generally between the zeta potential value of the GO and PEGVP latex nanoparticles (**Table 5.3**). Furthermore, when comparing the samples with the same GO content, the nanocomposite particles prepared at higher solution pH had a higher surface charge. For

example, the zeta potential value of PEGVP/GO prepared using 10% w/w GO at pH 5 and pH 9 were -11 mV and -29 mV, respectively. This can be attributed to the adsorbed GO sheets on the surface of the latexes being more negatively charged at higher pH.

At pH 2, the core/shell morphology was not well-defined even at a GO content of 10% w/w (**Figure 5.14a**, **Figure A.12a**, entry 3 in **Table 5.3**). This may be attributed to the GO having a relatively low negative charge at pH 2, leading to aggregation of the GO sheets (**Figure 5.9**). Alternatively, the microgel form of these latexes at this pH may also hinder the observation of these particles when dried and observed under the high vacuum conditions of an electron microscope. Overall, for the preparation of PEGVP/GO nanocomposite particles, the relatively optimal conditionals can be considered to be a solution pH of 5 or 9 with a GO content between 10% w/w to 20% w/w.

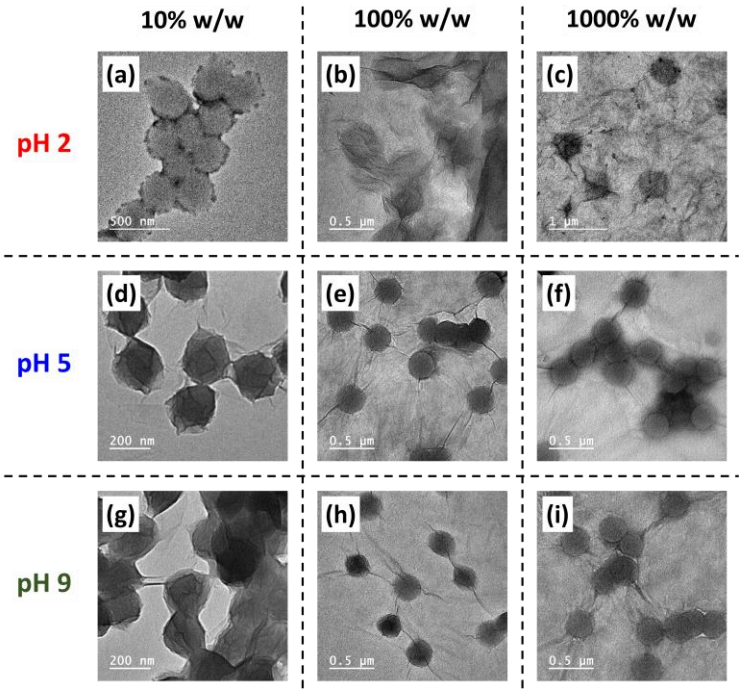

Figure 5.14. Representative TEM images for polymer/GO nanocomposite particles prepared *via* heteroflocculation between PEGVP latex and GO with varying content (10% w/w, 100% w/w and 1000% w/w). Images (a–c), (d–f) and (g–i) correspond to heteroflocculation conducted in aqueous solution at pH 2, 5 and 9, respectively (entries 3, 5, 7, 10, 12, 14, 17, 19 and 21, **Table 5.3**).

5.3.5. Preparation of polymer/GO nanocomposite particles *via* heteroflocculation using P2VP–PBzMA latex

Polymer/GO nanocomposite particles were prepared *via* heteroflocculation between cationic sterically-stabilised P2VP–PBzMA latex nanoparticles and GO nanosheets (**Scheme 5.1c**). Similar to the PEGMA-stabilised P2VP latex discussed above, the P2VP–PBzMA latexes were pH-stimuli responsive. More specifically, the latexes are highly positively charged at low pH (**Figure 5.4a** and **Figure 5.5a**) due to the higher protonation degree of the pyridine groups on the P2VP stabiliser. Therefore, electrostatic interaction between positively charged P2VP–PBzMA and negatively charged GO sheets is possible. This also implied that polymer/GO nanocomposite particles can be potentially prepared *via* electrostatically-induced heteroflocculation using block copolymer nanoparticles with P2VP as the stabiliser.

As the latex was gradually added into the GO dispersions, coagulation was observed immediately, indicating that the latex particles and GO sheets were associating due to the oppositely charged surfaces. **Figure 5.15** and **Figure 5.16** show similar appearances for both V_{32}–B_{300}/GO and V_{67}–B_{300}/GO nanocomposite particles prepared *via* heteroflocculation at pH 2, 5 and 9. This was generally consistent with the heteroflocculation between PEGVP and GO (**Figure 5.12**) as follows: (i) upon standing, sedimentation occurred within 1 hour; (ii) at lower GO content (1% w/w and 2% w/w, left two vials), most of the latexes still remained dispersed, but sedimentation occurred due to bridging flocculation; (iii) relatively clear solutions were obtained with the GO content of 20% w/w and 10% w/w at pH 5 and pH 9; and (iv) at pH 2, clear solutions were observed at GO contents up to 100% w/w.

Figure 5.17 shows DCP data obtained for V_{32}–B_{300} latex nanoparticles (entry 1, **Table 5.1**) before and after the addition of the GO at pH 5. The particle size distribution obtained for the bare latex was relatively narrow (**Figure 5.17h**). Similar to the observation for the electrostatically-induced heteroflocculation between PEGVP latexes and GO, with the addition of GO nanosheet, the narrow particle size distribution of the P2VP–PBzMA latex became broader and the mean weight-average particle diameter increased. At GO contents higher than 2% w/w (**Figure 5.17b-f**), the particle size distribution became much broader than that of the primary latex, indicating that the

Table 5.4. Summary of polymer/GO nanocomposite particles prepared *via* heteroflocculation between 139 nm V_{32}–B_{300} latex nanoparticles and GO nanosheets at varying pH in dilute aqueous solution at room temperature. The solids content was fixed at 0.1% w/w.

Entry	Solution pH	$D_{h,\ GO}$[a] / nm	GO content[b] / % w/w	Free GO[c] / %	Zeta potential[d] / mV
1	2	292	1		+34 ± 3
2	2	292	2		+33 ± 1
3	2	292	10	14	+26 ± 1
4	2	292	20	34	+23 ± 1
5	2	292	100		-6 ± 1
6	2	292	500	74	-19 ± 1
7	2	292	1000	75	-20 ± 0
8	5	111	1		+12 ± 3
9	5	111	2		-3 ± 2
10	5	111	10	9	-18 ± 5
11	5	111	20	5	-23 ± 1
12	5	111	100	74	-31 ± 1
13	5	111	500	98	-34 ± 1
14	5	111	1000	>99	-37 ± 1
15	9	103	1		-19 ± 9
16	9	103	2		-20 ± 2
17	9	103	10	4	-21 ± 3
18	9	103	20	50	-26 ± 2
19	9	103	100	>99	-34 ± 0
20	9	103	500	>99	-35 ± 2
21	9	103	1000	>99	-39 ± 2

[a] Mean hydrodynamic diameter of GO determined *via* DLS analysis. [b] Concentration relative to latex. [c] Mass fraction of free GO relative to GO added, as determined by UV-Vis analysis. [d] Determined *via* aqueous electrophoresis analysis at the corresponding solution pH.

Table 5.5. Summary of polymer/GO nanocomposite particles prepared *via* heteroflocculation between 149 nm V_{67}–B_{300} latex nanoparticles and GO nanosheets at varying pH in dilute aqueous solution at room temperature. The solid content was fixed at 0.1% w/w.

Entry	Solution pH	$D_{h,\ GO}$[a] / nm	GO content[b] / % w/w	Free GO[c] / %	Zeta potential[d] / mV
1	2	292	1		+31 ± 1
2	2	292	2		+23 ± 1
3	2	292	10		+25 ± 1
4	2	292	20	60	+27 ± 1
5	2	292	100	5	+13 ± 3
6	2	292	500	62	+15 ± 1
7	2	292	1000	45	+17 ± 1
8	5	111	1		-14 ± 3
9	5	111	2		-17 ± 2
10	5	111	10	9	-25 ± 0
11	5	111	20	7	-29 ± 0
12	5	111	100	44	-31 ± 1
13	5	111	500	91	-37 ± 0
14	5	111	1000	>99	-35 ± 0
15	9	103	1	33	+12 ± 3
16	9	103	2	30	+8 ± 1
17	9	103	10	69	-14 ± 3
18	9	103	20	>99	-17 ± 5
19	9	103	100	>99	-33 ± 1
20	9	103	500	>99	-31 ± 1
21	9	103	1000	>99	-38 ± 1

[a] Mean hydrodynamic diameter of GO determined *via* DLS analysis. [b] Concentration relative to latex. [c] Mass fraction of free GO relative to GO added, as determined by UV-Vis analysis. [d] Determined *via* aqueous electrophoresis analysis at the corresponding solution pH.

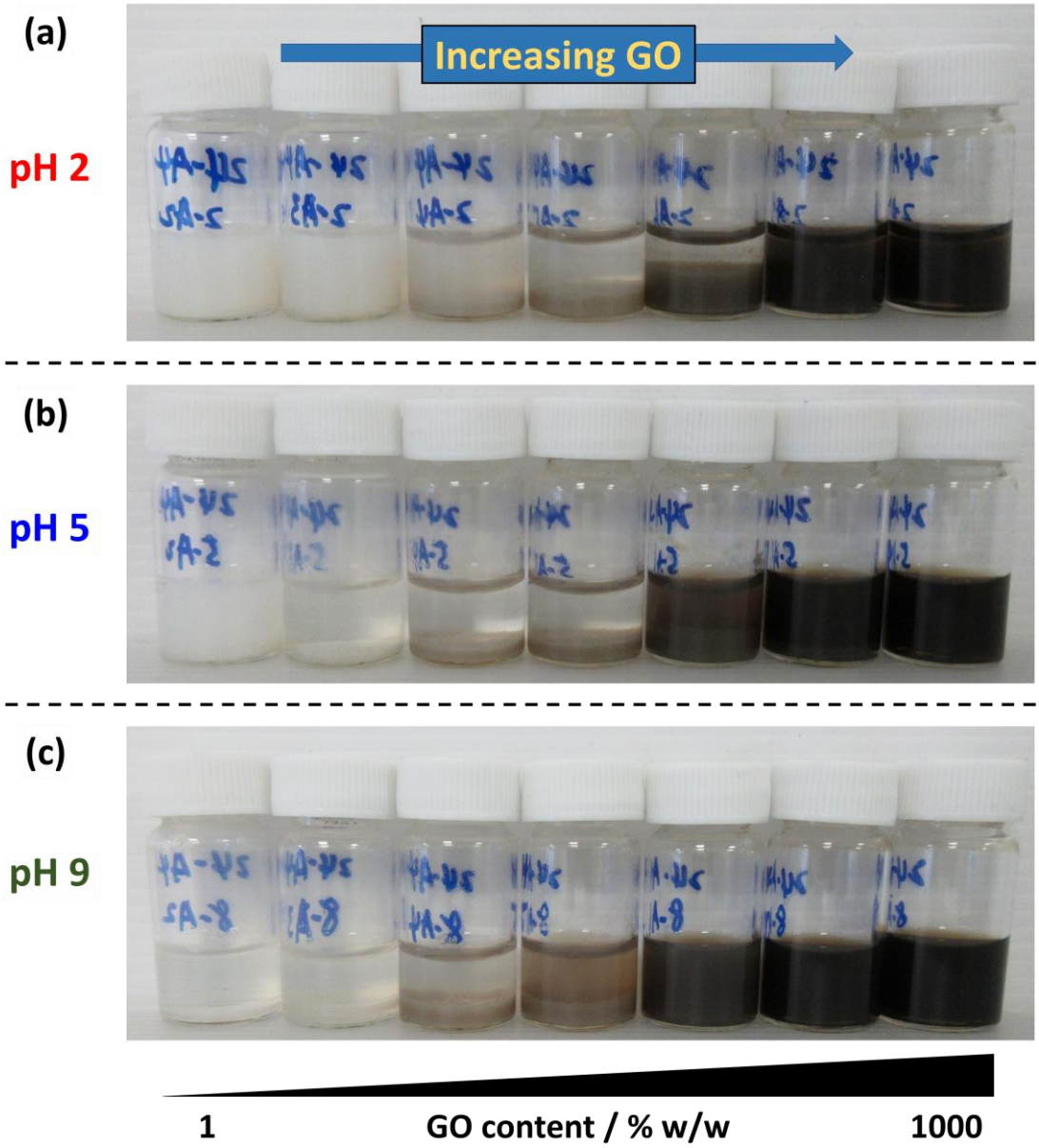

Figure 5.15. Digital photographs of vials containing V_{32}–B_{300} latex nanoparticles and increasing quantities of GO nanosheets at (a) pH 2, (b) pH 5 and (c) pH 9 after standing overnight (entries 1–21, **Table 5.4**). The GO contents of the heteroflocculation dispersions from left to right are 1, 2, 10, 20, 100, 500 and 1000% w/w relative to latex, respectively. The solids content was fixed at 0.1% w/w.

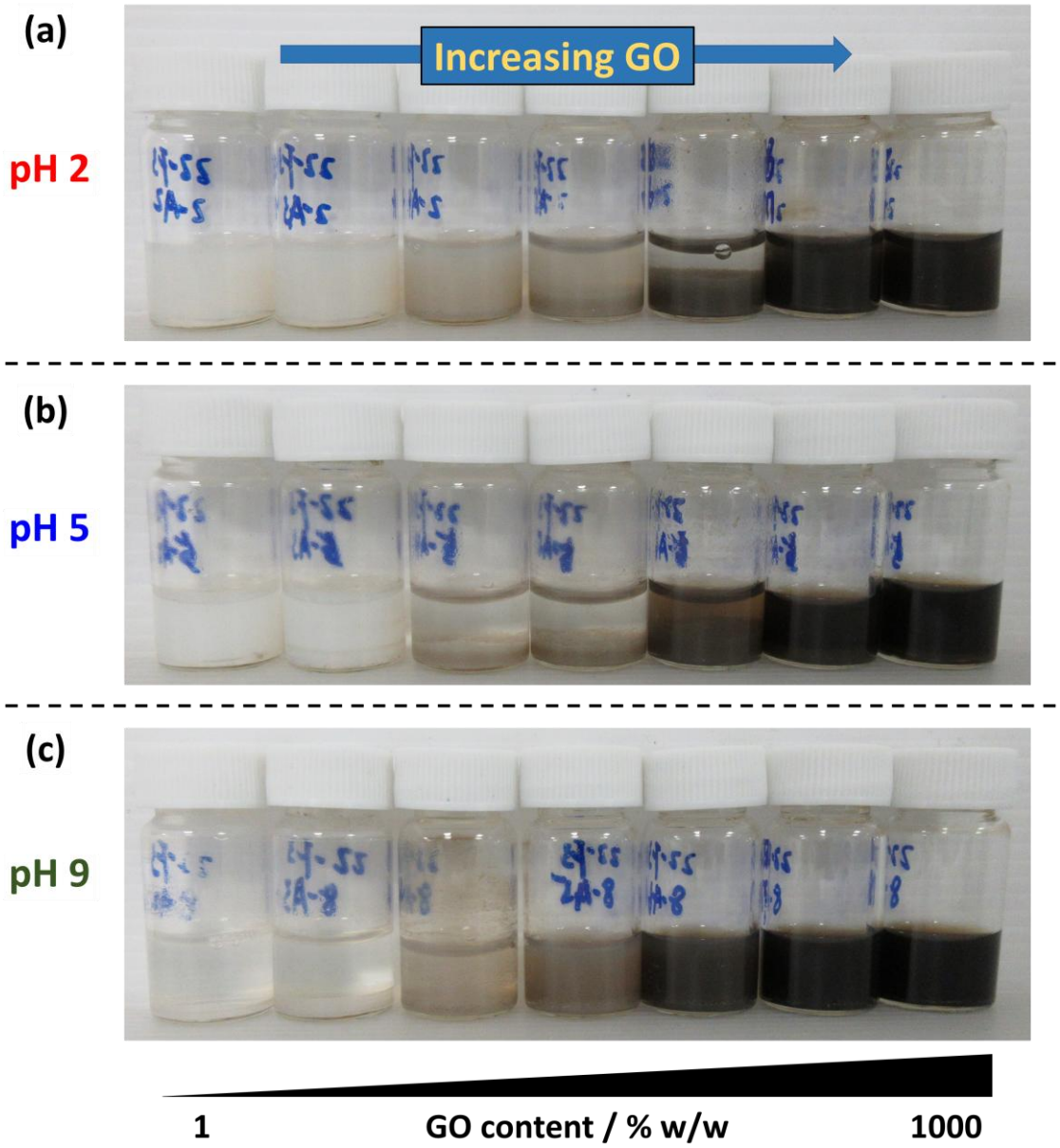

Figure 5.16. Digital photographs of vials containing V_{67}–B_{300} latex nanoparticles and increasing quantities of GO nanosheets at (a) pH 2, (b) pH 5 and (c) pH 9 after standing overnight (entries 1–21, **Table 5.5**). The GO contents of the heteroflocculation dispersions from left to right are 1, 2, 10, 20, 100, 500 and 1000% w/w relative to latex, respectively. The solids content was fixed at 0.1% w/w.

P2VP–PBzMA/GO nanocomposite aggregates were formed. Furthermore, **Figure 5.17e** shows that only a negligible primary peak of P2VP–PBzMA latex at 200 nm was observed when using 10% w/w GO, implying that the most latex particles were fully covered with GO. Furthermore, obvious peaks of individual P2VP–PBzMA/GO nanocomposite particles were observed at GO content higher than 20% w/w (**Figure 5.17b-d**). Similar observations were made for the V_{32}–B_{300}/GO (**Figure 5.18**) and V_{67}–B_{300}/GO (**Figure A.13**) nanocomposite particles obtained *via* heteroflocculation at pH 2. However, GO nanosheets are aggregated to some extend at pH 2 due to relatively low negative charge, making it relatively difficult to clearly distinguish bridging flocculation from individual nanocomposite particles and free GO (**Figure 5.18** and **Figure A.13**). Nevertheless, the broad DCP distributions (**Figure 5.18** and **Figure A.13**) and TEM studies (**Figure 5.19**, **Figure 5.20**, **Figure A.14** and **Figure A.15**) suggested that the P2VP–PBzMA/GO nanocomposite particles were obtained in both cases.

Morphologies of V_{32}–B_{300}/GO and V_{67}–B_{300}/GO nanocomposite particles prepared *via* heteroflocculation at pH 2, 5 and 9 are shown in **Figure 5.19**, **Figure 5.20**, **Figure A.14** and **Figure A.15**. The P2VP–PBzMA/GO nanocomposite particles with core/shell morphology were obtained at the GO content of 10% w/w. Moreover, the zeta potential values of nanocomposite particles were generally between the zeta potential value of the GO and P2VP–PBzMA latex nanoparticles (**Table 5.4** and **Table 5.5**). Similar to PEGVP/GO (**Figure 5.14a** and **Figure A.12a**), the core/shell morphology of P2VP–PBzMA/GO nanocomposite particles prepared using 10% w/w GO at pH 2 was not well-defined (**Figure 5.19a**, **Figure 5.20a, Figure A.14a** and **Figure A.15a**). As previously discussed, this may be attributed to the GO having a relatively low negative charge at pH 2, leading to aggregation among GO sheets (**Figure 5.9**). Therefore, only small amount of GO can be adsorbed as sheets on the latex surface.

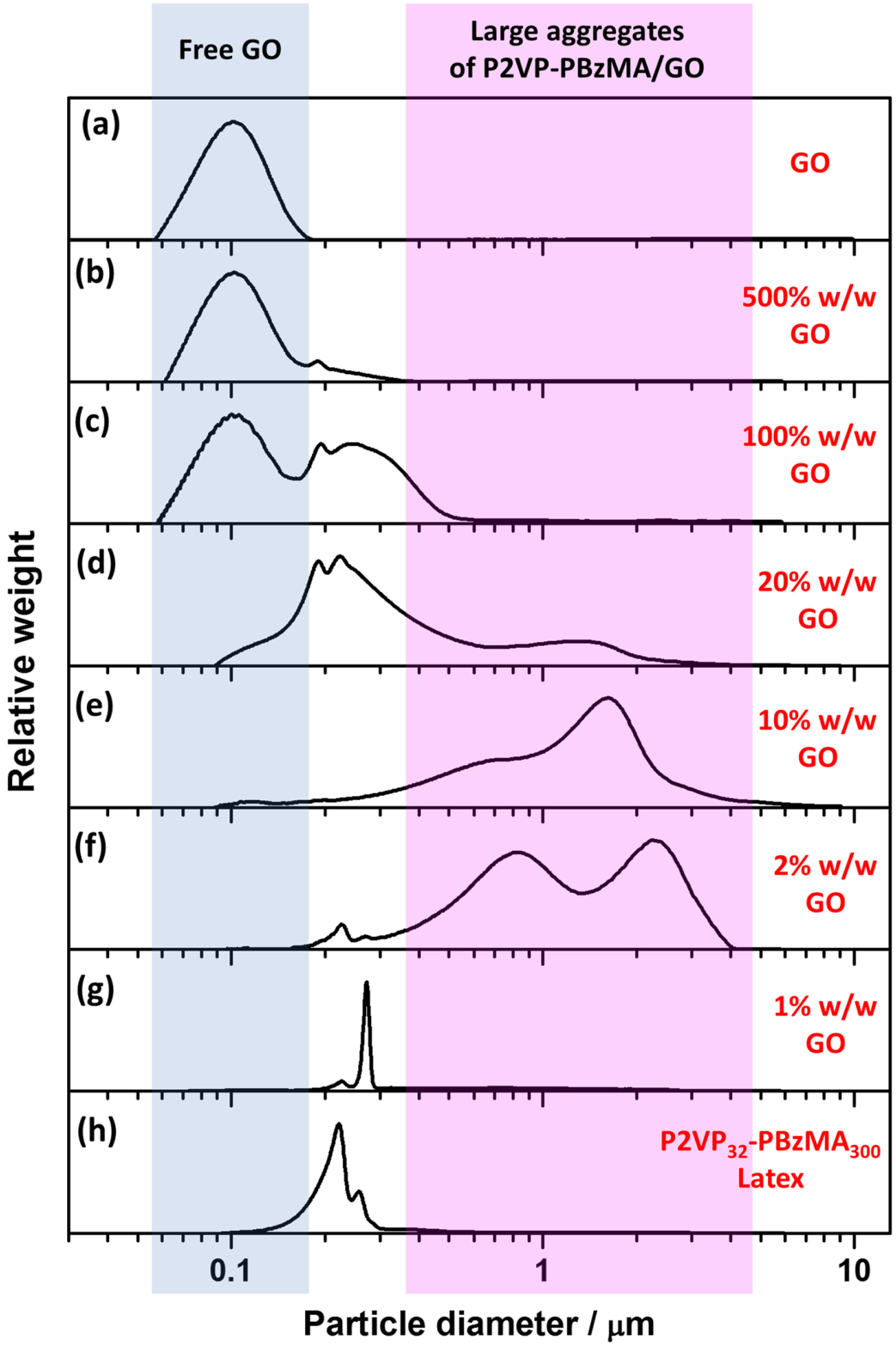

Figure 5.17. DCP particle size distributions obtained for V_{32}–B_{300}/GO nanocomposite particles prepared *via* heteroflocculation with varying GO content at pH 5. The density of the latex and nanocomposite particles used was taken as 1.18 g cm^{-3}. (a) represents GO nanosheets obtained *via* sonication at 70% amplitude for 30 min. (b) – (g) represent entries 8–13 from **Table 5.4**, whereas (h) shows data obtained for entry 1 in **Table 5.1**.

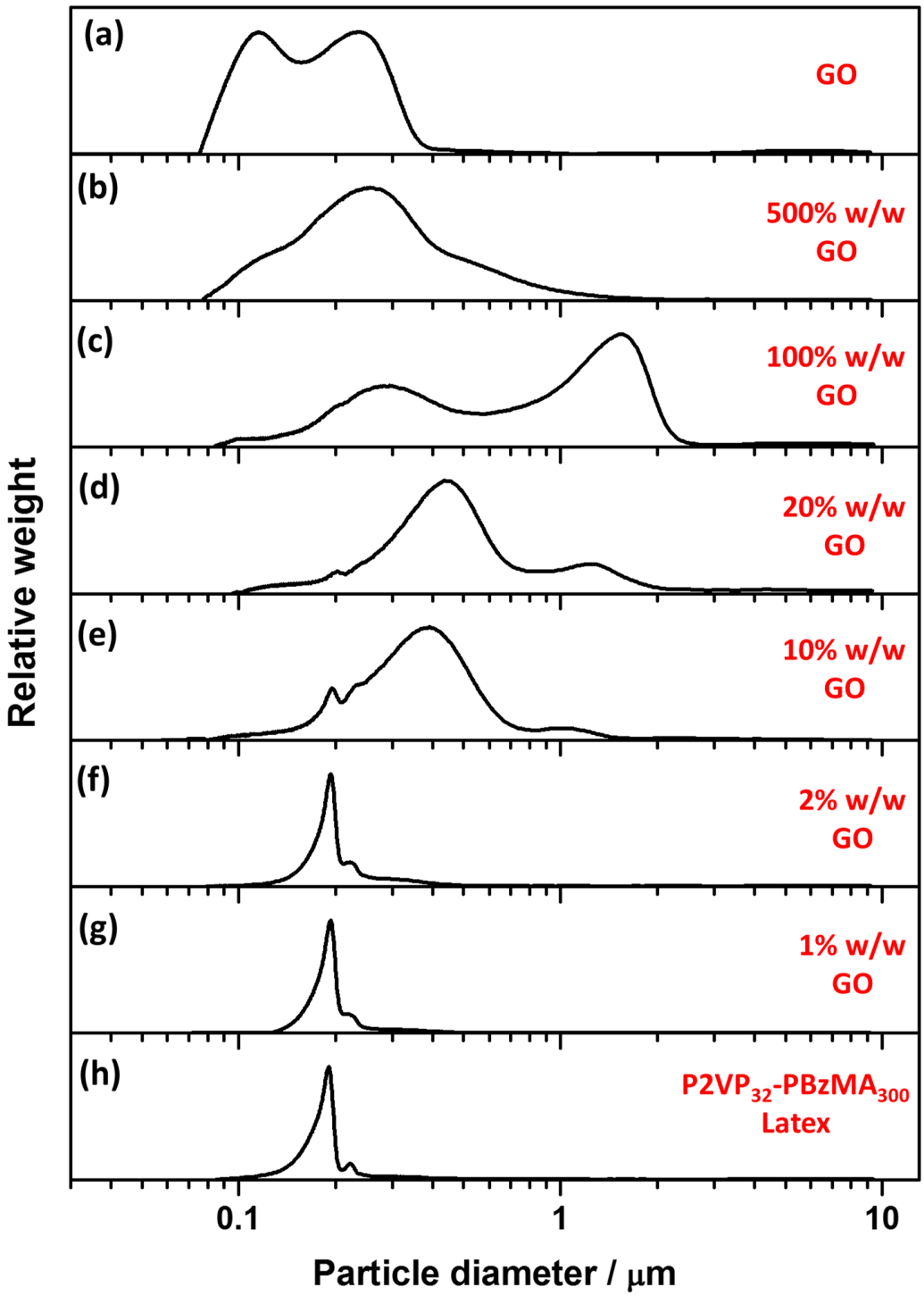

Figure 5.18. DCP particle size distributions obtained for V_{32}–B_{300}/GO nanocomposite particles prepared *via* heteroflocculation with varying GO content at pH 2. The density of the latex and nanocomposite particles used was taken as 1.18 g cm^{-3}. (a) represents GO nanosheets obtained *via* sonication at 70% amplitude for 30 min. (b) – (g) represent entries 1–6 from **Table 5.4**, whereas (h) shows data obtained for entry 1 in **Table 5.1**.

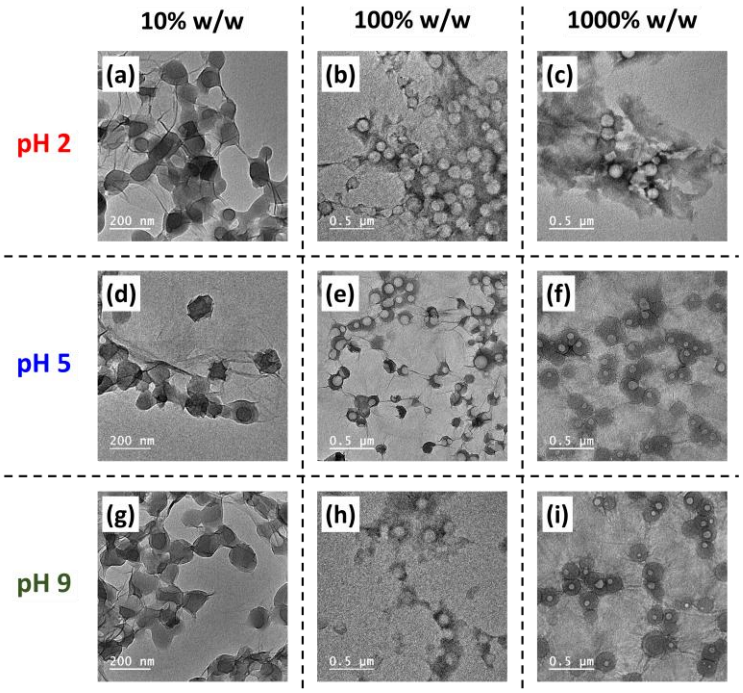

Figure 5.19. Representative TEM images for polymer/GO nanocomposite particles prepared *via* heteroflocculation between V_{32}–B_{300} latex and GO with varying content (10% w/w, 100% w/w and 1000% w/w). Images (a–c), (d–f) and (g–i) correspond to heteroflocculation conducted in aqueous solution at pH 2, 5 and 9, respectively (entries 3, 5, 7, 10, 12, 14, 17, 19 and 21, **Table 5.4**).

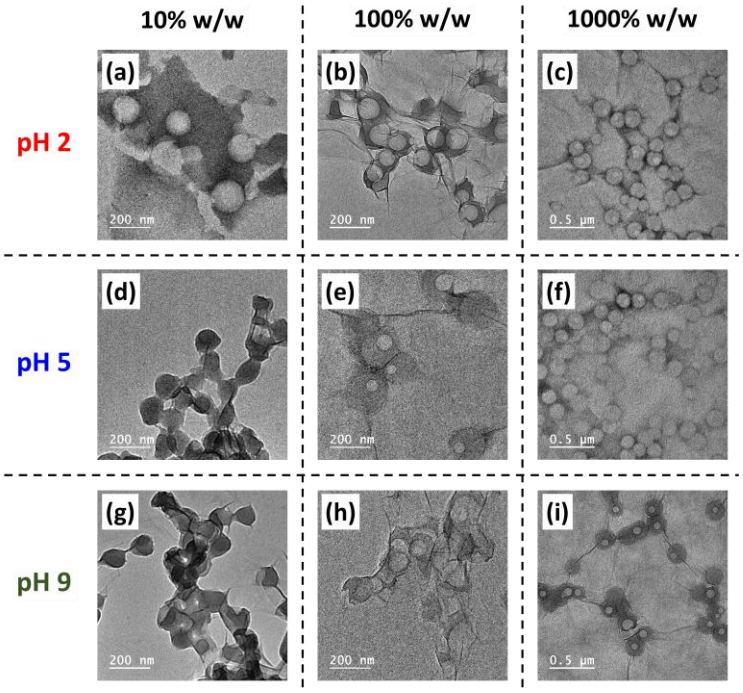

Figure 5.20. Representative TEM images for polymer/GO nanocomposite particles prepared *via* heteroflocculation between V_{67}–B_{300} latex and GO with varying content (10% w/w, 100% w/w and 1000% w/w). Images (a–c), (d–f) and (g–i) correspond to heteroflocculation conducted in aqueous solution at pH 2, 5 and 9, respectively (entries 3, 5, 7, 10, 12, 14, 17, 19 and 21, **Table 5.5**).

5.3.6. Determination of free GO after heteroflocculation using UV-Vis technique

It is well known that GO can be well dispersed in an aqueous phase due to the numerous hydroxyl and carboxyl groups on the basal planes and edges.[305,310,311] **Figure 5.21a** shows UV–vis absorbance spectra of GO aqueous dispersions at varying concentration, ranging from 0.001 to 0.067 mg mL^{-1}. The spectra indicated that the GO is a strong UV absorber, and the wavelength of maximum absorption peak was at approximately 235 nm, which is consistent to previously reported values.[454] Therefore, a linear calibration curve was constructed at 235 nm using the Beer-Lambert equation (**Equation 5.1**):

$$A = \varepsilon cL \qquad \textbf{Equation 5.1}$$

where A is the measured absorbance, ε is the coefficient of absorbance determined from Beer-Lambert plot, c is the concentration of the GO dispersions and L is the path length through the sample, which is 1 cm.

Figure 5.21b shows a linear relationship between the absorbance and the GO concentration. This indicated that the GO dispersions obey the Beer-Lambert law with the coefficient of absorbance (ε) calculated to be 47 mL mg^{-1} cm^{-1}. Therefore, the mass fraction of free GO nanosheets dispersed in the solutions after the heteroflocculation process could be determined using UV-Vis spectroscopy.[454] More specifically, the heteroflocculation solutions were centrifuged at moderate speed (200 rpm) for 5 min. At this low speed, the polymer/GO nanocomposite particles would sediment and the free GO nanosheets would still be dispersed in the supernatant. The supernatants were carefully collected and diluted using water at the corresponding pH. The diluted supernatants were analysed *via* UV-Vis spectroscopy to determine the quantity of free GO, i.e. which was not adsorbed onto the latexes.

Figure 5.22a shows UV-Vis spectra of the diluted supernatant obtained from solutions of V_{32}–B_{300} latex mixed with varying GO amounts at pH 5 (entries 8–14, **Table 5.4**). Strong UV signals at approximately 220 nm for latexes were observed, especially for the formulations using lower GO content (e.g. 1% w/w and 2% w/w). In contrast, stronger UV signals for GO at 235 nm were observed for the formulations using higher GO content, whereas the latexes peaks were negligible. For example, the UV

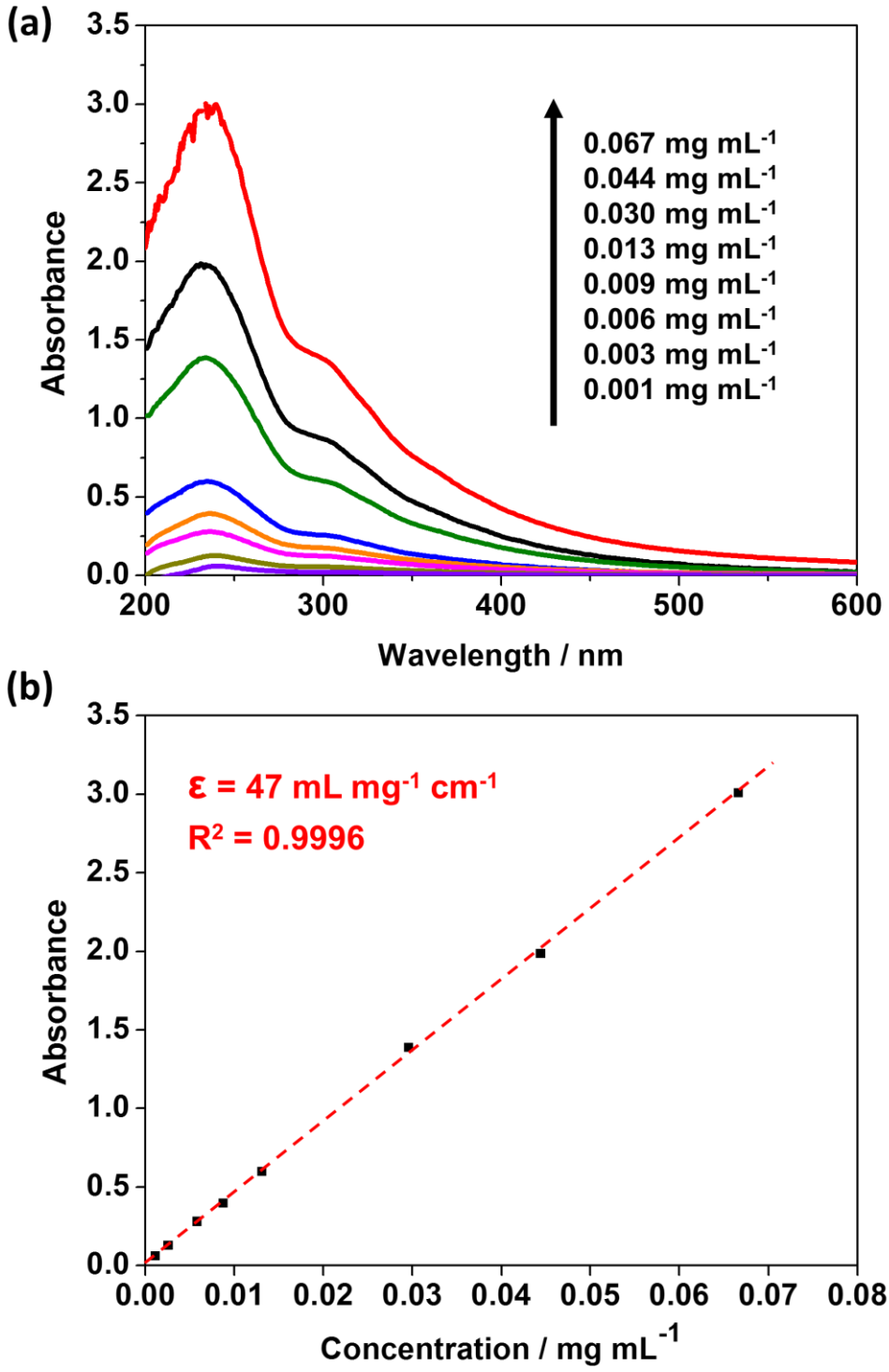

Figure 5.21. (a) UV-Vis spectra obtained for GO aqueous dispersions ranging from 0.001 to 0.067 mg mL^{-1} and (b) Beer-Lambert plot for GO recorded in deionised water. The plot shows a linear relationship between the absorbance per unit path length and the GO concentration.

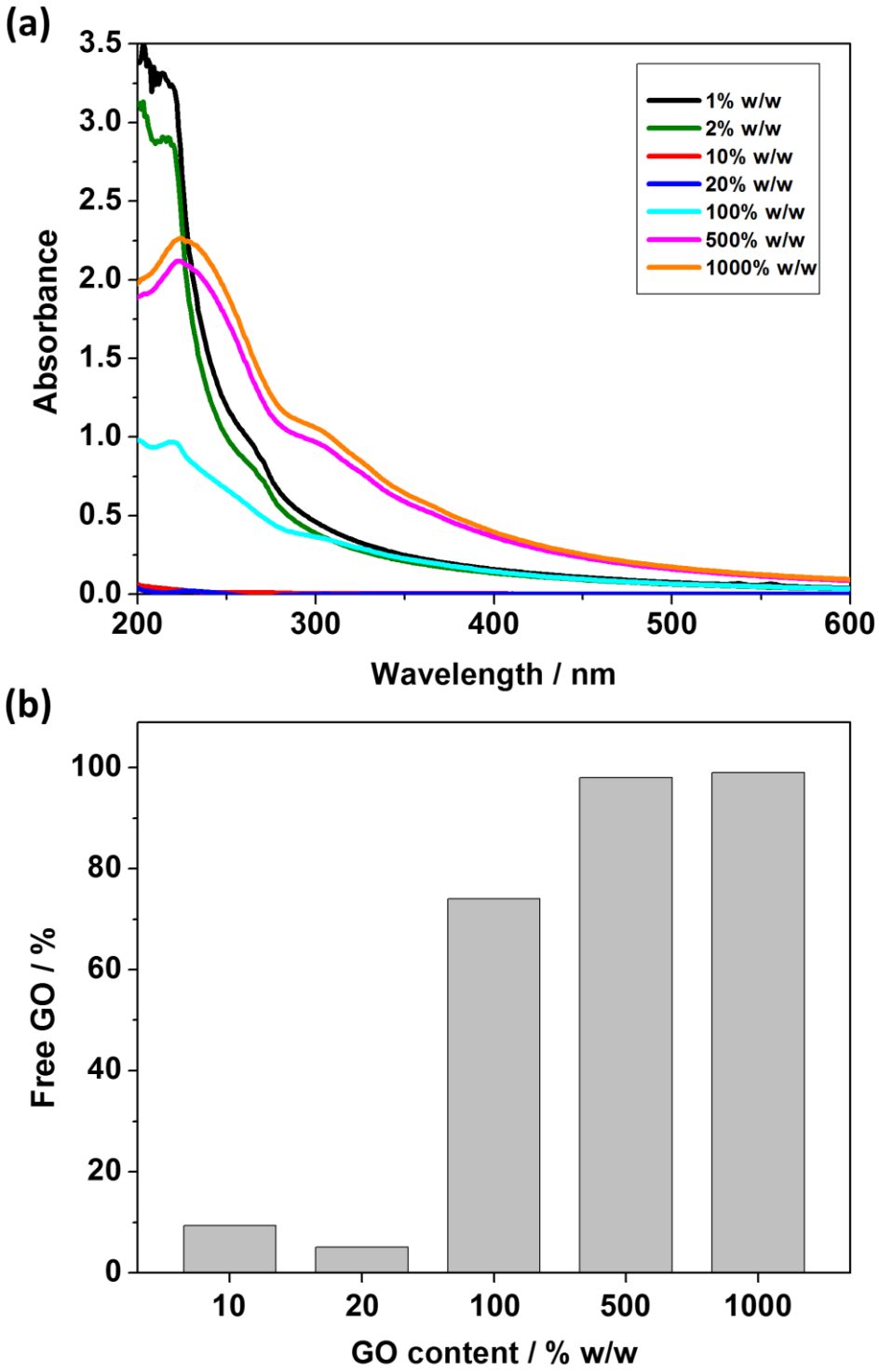

Figure 5.22. (a) UV-Vis spectra for the diluted supernatants obtained from centrifuged heteroflocculation samples prepared using V_{32}–B_{300} latexes with varying GO content at pH 5 (entries 8–14, **Table 5.4**). (b) Calculated mass fraction of free GO for corresponding heteroflocculation samples.

signal for V_{32}–B_{300} latex was obvious at GO contents below 10% w/w, whereas signals of free GO were more obvious when the content was above 20% w/w. It is noteworthy that UV signals of both the latex and GO were negligible at the GO content of 10% w/w and 20% w/w, indicating only limited free latex and free GO remained dispersed in the supernatants. This observation was consistent with the digital photographs (**Figure 5.15b**), DCP analysis (**Figure 5.17d-e**) and the TEM images (**Figure 5.19d** and **Figure A.14d**).

For V_{32}–B_{300}/GO samples with UV signals of free GO, the lowest mass fraction of free GO was approximately 5% for the formulation using 20% w/w GO (**Figure 5.22b** and entry 11 in **Table 5.4**). This indicated that most of the GO nanosheets were adsorbed on the latexes surface and only limited residual GO is still dispersed in the solution. This also implied that V_{32}–B_{300}/GO nanocomposite particles with monolayer coverage were achieved at the GO content of approximately 20% w/w.

5.3.7. Investigating the electrostatic interaction strength between latex and GO nanosheets after heteroflocculation

The strength of electrostatic interaction between latex nanoparticles and GO nanosheets was assessed by comparing the DCP particle size distributions before and after sonication. More specifically, dispersions conducted using GO contents of 10% w/w and 20% w/w, based on latex, were sonicated at a fixed frequency of 37 Hz for 60 seconds and subsequently analysed *via* DCP.

Figure 5.23 shows DCP particle size distributions obtained for PEGVP/GO nanocomposite particles before (solid line) and after (dashed line) sonication. After sonication, the distributions were still broader than primary latex peak. However, the distributions obviously shifted to a smaller size after sonication, indicating that the aggregates significantly decreased in size and some individual PEGVP/GO nanocomposite particles peaks (at approximately 0.25 μm) were observed (**Figure 5.23a** and **Figure 5.23b**). This implied that the bridging flocculation of PEGVP/GO nanocomposite particles can be disrupted using sonication. It is noteworthy that the PEGVP latex was stabilised by non-ionic PEGMA stabiliser, which can screen the positive charge generated by cationic P2VP core. This led to the electrostatic interaction between PEGVP latex and GO nanosheet being relatively weak. Therefore, it is likely that some GO coated on the

PEGVP latexes becomes detached during sonication. More specifically, a small free GO peak at approximately 0.1 μm becomes apparent after sonication of PEGVP/GO (**Figure 5.23a** and **Figure 5.23b**).

Similar observations were made for V_{32}–B_{300}/GO (**Figure 5.24**) and V_{67}–B_{300}/GO (**Figure 5.25**) nanocomposite particles before (solid line) and after (dashed line) sonication. At a GO content of 10% w/w, the particle size decreased significantly and the individual P2VP–PBzMA/GO nanocomposite particles peaks (at approximately 0.2 μm) were observed. This indicated that the bridging flocculation of these nanocomposite particles can also be disrupted by sonication. It is noteworthy that a relatively minor particle size distribution change was observed for the P2VP–PBzMA/GO nanocomposite particles prepared using 20% w/w GO after sonication (**Figure 5.24a** and **Figure 5.25a**). This implied that most of the P2VP–PBzMA/GO nanocomposite particles generally remained the same size as individual nanocomposite particles. Furthermore, compared to PEGVP/GO, a relatively small amount of free GO nanosheets (at approximately 0.1 μm) were generated, implying that only a limited quantity of coated GO was detached from the surface of the P2VP–PBzMA latexes after sonication. This indicated that the electrostatic interaction between P2VP–PBzMA latex and GO nanosheet was stronger than that between PEGMA-stabilised P2VP latex nanoparticles and GO nanosheets.

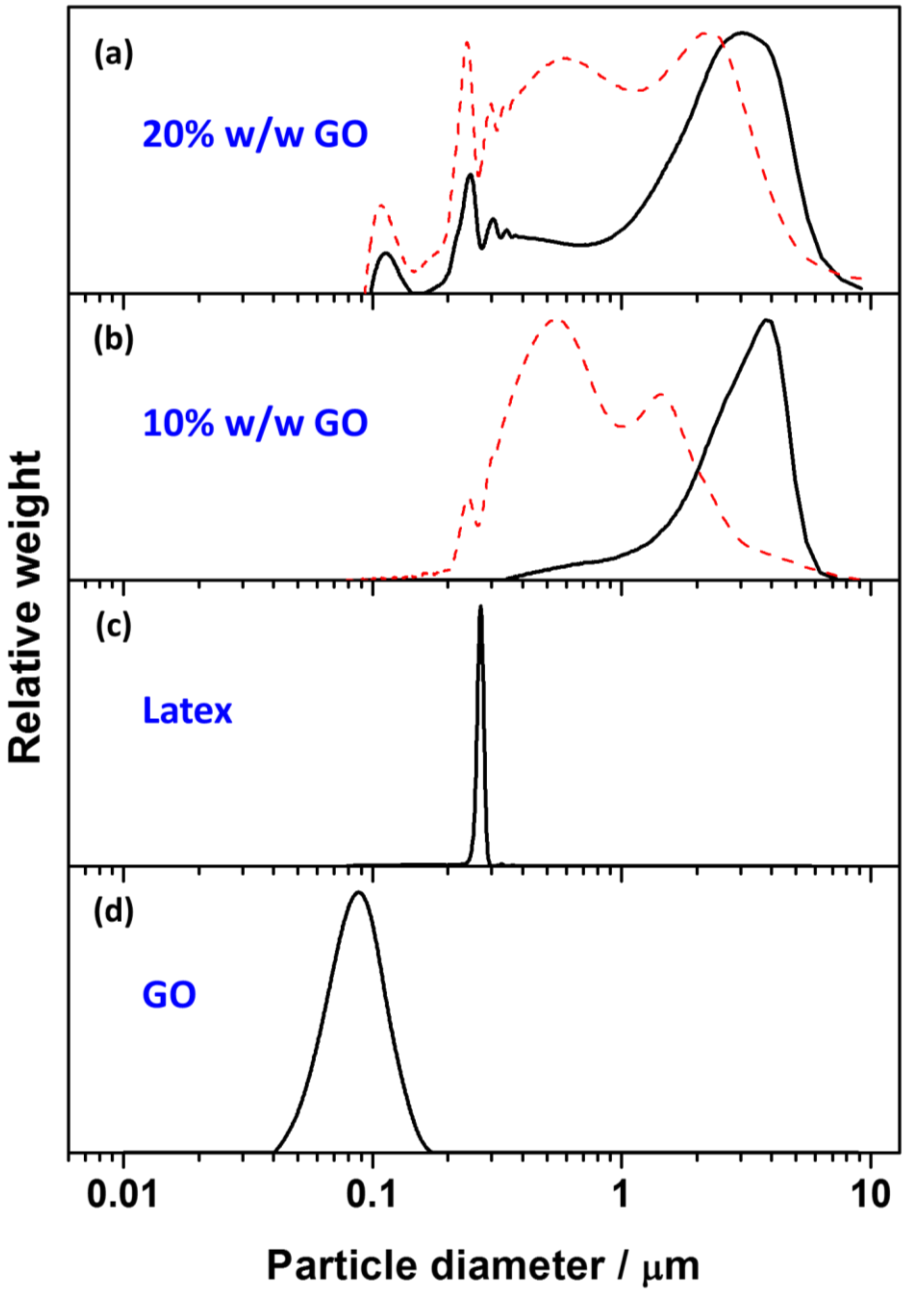

Figure 5.23. DCP particle size distributions obtained before (solid line) and after (dashed line) sonication for PEGVP/GO nanocomposite particles prepared at pH 5 with GO content of (a) 20% w/w (entry 11, **Table 5.3**) and (b) 10% w/w (entry 10, **Table 5.3**), (c) PEGVP latex (entry 4, **Table 5.1**) and (d) GO nanosheets obtained *via* sonication at 70% amplitude for 30 min in aqueous solution at pH 5. In order to do comparison, the density of all DCP analysis used was taken as 1.11 g cm^{-3}.

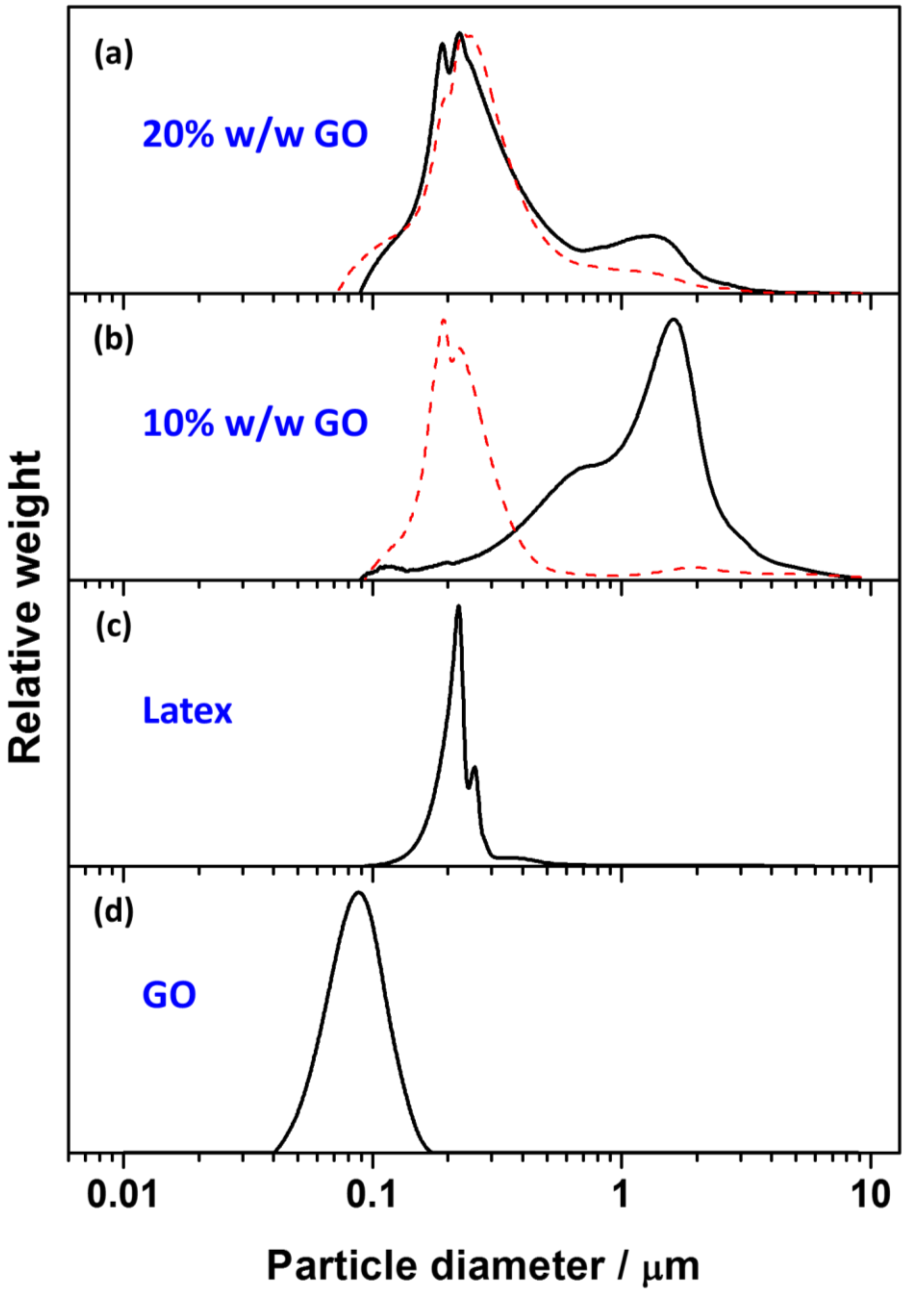

Figure 5.24. DCP particle size distributions obtained before (solid line) and after (dashed line) sonication for V_{32}–B_{300}/GO nanocomposite particles prepared at pH 5 with GO content of (a) 20% w/w (entry 11, **Table 5.4**) and (b) 10% w/w (entry 10, **Table 5.4**), (c) V_{32}–B_{300} latex (entry 1, **Table 5.1**) and (d) GO nanosheets obtained *via* sonication at 70% amplitude for 30 min in aqueous solution at pH 5. In order to do comparison, the density of all DCP analysis used was taken as 1.18 g cm^{-3}.

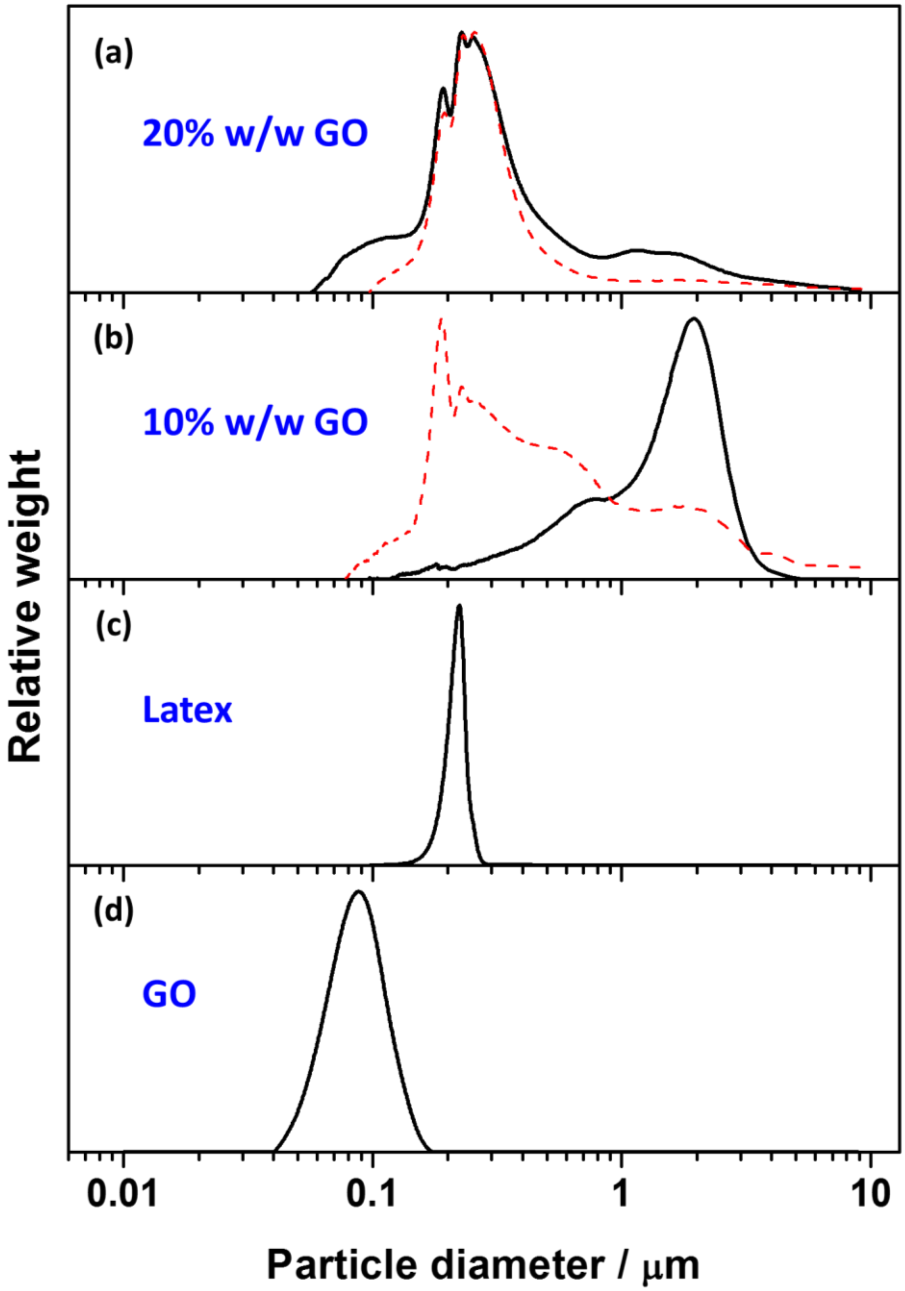

Figure 5.25. DCP particle size distributions obtained before (solid line) and after (dashed line) sonication for V_{67}–B_{300}/GO nanocomposite particles prepared at pH 5 with GO content of (a) 20% w/w (entry 11, **Table 5.5**) and (b) 10% w/w (entry 10, **Table 5.5**), (c) V_{67}–B_{300} latex (entry 2, **Table 5.1**) and (d) GO nanosheets obtained *via* sonication at 70% amplitude for 30 min in aqueous solution at pH 5. In order to do comparison, the density of all DCP analysis used was taken as 1.18 g cm^{-3}.

5.4. Conclusions

This work demonstrated that the polymer/GO nanocomposite particles with a core/shell morphology can be readily prepared *via* electrostatically-induced heteroflocculation in aqueous medium at room temperature. The heteroflocculation experiments were conducted using positively charged latex nanoparticles (PEGMA-stabilised P2VP or P2VP–PBzMA) and negatively charged GO nanosheets in water at a wide pH range. Both the PEGMA-stabilised P2VP and P2VP–PBzMA latexes are pH responsive and have different surface charge at varying pH, with a higher positive charge at lower pH. Therefore, the solution pH can influence the formation of the polymer/GO nanocomposite particles prepared *via* heteroflocculation. Digital photographs, DCP, TEM, UV-Vis and aqueous electrophoresis studies showed that heteroflocculation can be achieved in either acidic (pH 2) or basic (pH 9) conditions.

DCP studies indicated that polymer/GO nanocomposite particles were successfully formed either using PEGMA-stabilised P2VP or P2VP–PBzMA latexes, and the optimal GO loading was approximately 20% w/w based on latex. This was consistent with the calculated mass fraction of free GO determined *via* UV-Vis analysis. TEM studies confirmed that the GO nanosheets were adsorbed on the latex surface and formed core/shell morphologies, especially at pH 5 and pH 9. Aqueous electrophoresis showed that the zeta potential values of nanocomposite particles were generally between the zeta potential values of the GO and latex nanoparticles. Furthermore, when comparing the samples with the same GO content, the nanocomposite particles prepared at higher solution pH had a higher surface charge, indicating the GO sheets were adsorbed on the surface of the latexes.

The strength of electrostatic interaction between latex nanoparticles and GO nanosheets was assessed by comparing the DCP particle size distributions before and after sonication. The distributions obviously shifted to a smaller size after sonication, indicating that the bridging flocculation of polymer/GO nanocomposite particles can be readily disrupted by sonication. Furthermore, a smaller amount of free GO nanosheets were generated after sonication of P2VP–PBzMA/GO than PEGVP/GO nanocomposite particles. This suggested that the electrostatic interaction between P2VP–PBzMA latex and GO nanosheet was stronger than that between PEGMA-stabilised P2VP and GO.

In this chapter, several reported results (e.g. TEM images, zeta potential values) were not as expected. This could be because specimens were not taken from purified polymer/GO dispersions. Therefore, in order to investigate this approach further, a purification procedure should be developed and applied in the future. Nevertheless, considering that the cationic P2VP–PBzMA diblock copolymer nanoparticles is a model polymer latex, the preparation of the polymer/GO nanocomposite particles *via* electrostatically-induced heteroflocculation at room temperature is a promising approach and could be substantially extended using other cationic polymer nanoparticles prepared *via* RAFT-mediated PISA.

Chapter Six

Conclusions and Prospect

6.1. Conclusions

In this thesis, sterically-stabilised polymer nanoparticles with varying surface charge have been prepared *via* RAFT polymerisation. A wide range of topics regarding these polymer nanoparticles has been investigated in this work, including synthesis, characterisation and potential applications. Importantly, this thesis provides a deeper understanding of the design rules required to prepare nanoparticles with desired particle diameters, copolymer composition and surface characteristics. Furthermore, the positively charged nanoparticles were selected to demonstrate the capability for the preparation of polymer/GO nanocomposite particles *via* electrostatically-induced heteroflocculation.

Anionic sterically-stabilised sulfonate-bearing PKSPMA–PBzMA and PSS–PBzMA diblock copolymer nanoparticles were synthesised *via* RAFT-mediated PISA in alcohol/water mixtures using PKSPMA and PSS macro-CTAs as steric stabilisers. It was shown that nanoparticles with controllable diameters can be prepared *via* changing the DP of the stabiliser and/or core-forming block, or simply by varying the alcohol/water co-solvent composition for a fixed target copolymer composition. Generally, nanoparticles with larger diameter can be obtained *via* RAFT-mediated PISA at higher alcohol contents. This shows that the solvency of both the stabiliser (PKSPMA) and core-forming block (PBzMA) has a noticeable effect on both the aggregation of polymer chains during self-assembly and the resulting nanoparticles morphology. The DLS and aqueous electrophoresis studies indicates that these nanoparticles remain colloidally stable and highly anionic over a wide pH range from 4 to 10.

It was demonstrated for the first time that non-ionic sterically-stabilised PBzMA homopolymer nanoparticles with controlled particle diameters and polymer molar mass can be prepared *via* RAFT aqueous miniemulsion polymerisation. This was achieved by using a relatively hydrophobic chain transfer agent (PETTCCP) and non-ionic Lutensol TO 20 surfactant. The effect of the surfactant, hydrophobe, initiator and chain transfer agent concentrations on the particle diameter, particle number, rate of polymerisation and molar mass in the final PBzMA latexes was systematically investigated. More specifically, increasing the hydrophobe (HD) concentration increased the number of particles per unit volume, indicating that more droplets can be stabilised against Ostwald ripening effects. The initiator (AIBN) concentration significantly affected the overall

polymerisation rate (R_p), which followed a power-law relationship R_p α [AIBN]$^{1/2}$. However, no obvious changes in molar mass, molar mass dispersity and particle diameter were observed when varying the initiator concentration. In contrast, when using higher RAFT agent concentration, smaller latex diameters and faster overall rates of polymerisation were observed. Additionally, the approximately linear relationship of ln([M]$_0$/[M]) versus reaction time, unimodal GPC chromatograms, relatively narrow molar mass distributions and high self-blocking efficiency indicated that these were well-controlled RAFT miniemulsion polymerisations.

Cationic sterically-stabilised pyridine-bearing P2VP–PBzMA diblock copolymer nanoparticles can be prepared *via* RAFT-mediated PISA in water at low pH using P2VP macro-CTAs as a steric stabiliser. Nanoparticles with tuneable diameters were prepared by varying the DP of the stabiliser (P2VP) and/or core-forming block (PBzMA), or simply by altering the solution pH for a fixed target copolymer composition. The P2VP stabiliser was water-soluble below pH 4 because of protonation of the pyridine functional groups in acidic solution. Nanoparticles with smaller diameters were obtained *via* RAFT-mediated PISA at lower solution pH and *vice versa*. This indicated that the degree of protonation of the P2VP stabiliser at varying solution pH has a noticeable effect on both the aggregation of polymer chains during the PISA process and the resulting morphology of the diblock copolymer nanoparticles. Electrophoresis studies indicated that these P2VP–PBzMA diblock copolymer nanoparticles had pH-dependent zeta potentials and DLS studies indicated high colloidal stability below pH 5. However, significant flocculation occurred above pH 5 due to lower surface charge of P2VP stabiliser and relatively high ionic strength. Nevertheless, flocculation could be minimised if the P2VP–PBzMA nanoparticles were directly dispersed in corresponding pH solution without KCl electrolyte.

Polymer/GO nanocomposite particles with core/shell morphology were prepared *via* electrostatically-induced heteroflocculation at room temperature using cationic latex nanoparticles and anionic GO nanosheets over a wide pH range. Both the P2VP–PBzMA and PEGMA-stabilised P2VP latexes are pH responsive with higher positive charge at lower pH, whereas the GO nanosheets are highly negatively charged between pH 2 to 14. With the addition of latex to the GO dispersions, coagulation occurred immediately indicating that the oppositely charged particles facilitate the adsorption of anionic GO

nanosheets on the surface of cationic latexes and form core/shell nanocomposite aggregates. In summary, this approach represents significant progress in the synthesis, characterisation and potential applications of these sterically-stabilised nanoparticles to obtain nanocomposite particles.

6.2. Prospect

In this thesis, the procedures for the preparation of polymer nanoparticles with various surface charge (anionic, non-ionic and cationic) and polymer/GO nanocomposite particles have been established. Unfortunately, due to time constraints and the extraordinary global circumstances of the COVID-19 pandemic, some intended research was not brought to completion. Suggested future work to follow on from the work described in this thesis includes further characterisation of these nanoparticles, additional studies into the preparation of polymer/inorganic material nanocomposite particles and their potential applications, as follows.

As highlighted in **Chapter Two**, small-angle X-ray scattering (SAXS) is a powerful technique for the investigation of structural parameters of block copolymer nanoparticles. Thus, it is pertinent to characterise the anionic PSS–PBzMA and cationic P2VP–PBzMA nanoparticles to provide additional structural parameters, such as mean radius of the micelle core, radius of gyration of the stabiliser chains, average solvent fraction in the core, mean aggregation number and average number of copolymer chains per unit surface area.

In **Chapter Two**, highly anionic sulfonate-functional diblock copolymer nanoparticles (PKSPMA–PBzMA and PSS–PBzMA) have been successfully synthesised *via* RAFT-mediated PISA. It is reported that sulfonate functional groups are frequently present in biologically important macromolecules, which can have potential antiviral applications.[334,335] Therefore, a series of these nanoparticles with varying particle diameter, stabiliser chain length and stabiliser density, have been selected and provided to internal collaborators from the Jones group to determine whether these types of nanoparticles behave as virustatic or virucidal materials. Furthermore, Ning *et al.* showed that highly anionic block copolymer nanoparticles can be used to modify the growth of inorganic crystals (e.g. calcite and ZnO) *via* occlusion processes.[336] This implies that the highly anionic PKSPMA–PBzMA and PSS–PBzMA nanoparticles can potentially be used to

investigate occlusion with inorganic materials, such as noble nanoparticles (e.g. Ag, Pt, Pd) and functional crystals (e.g. Cu_2O, Fe_3O_4, MnO_2, TiO_2), to produce a wide range of novel functional hybrid nanocomposite materials.

As discussed in **Chapter Three**, the PBzMA homopolymer latexes synthesised *via* RAFT miniemulsion polymerisation still had high chain-end stability and fidelity over a 12-month storage period, as examined *via* self-blocking experiments. This indicated that the majority of the trithiocarbonate RAFT chain-ends remained intact and that these PBzMA latexes could undergo efficient chain extension to form second blocks with other monomers to form block copolymer latexes. Therefore, these PBzMA homopolymers are expected to be readily chain-extended with various stabilisers, such as PKSPMA, PSS and P2VP, to form block copolymer nanoparticles with different surface functionality.

In **Chapter Five**, core/shell polymer/GO aggregates were prepared *via* electrostatically-induced heteroflocculation using cationic polymer latexes (e.g. P2VP–PBzMA and PEGMA-stabilised P2VP). According to the TEM studies, the latex particles were relatively fully covered by GO when using 222 nm PEGMA-stabilised P2VP. Therefore, it is also worthy to prepare P2VP–PBzMA/GO nanocomposite using P2VP–PBzMA with larger particle diameter (e.g. >300 nm). Recently, several reports have shown that polymer/rGO (reduced graphene oxide) nanocomposite particles exhibit excellent electrical (e.g. electrical conductivity) and thermomechanical properties (e.g. storage modulus, T_g).[468] Therefore, the prepared P2VP–PBzMA/GO nanocomposite particles could be reduced with hydrazine (e.g. GO/hydrazine 1:10 w/w) to obtain P2VP–PBzMA/rGO nanocomposites. The resulting P2VP–PBzMA/rGO nanocomposite particles could be characterised to investigate their morphologies (SEM, TEM), electrical resistances (four-point probe method), thermal properties (TGA, DSC), or dynamic mechanical properties (dynamic mechanical analyzer, DMA). Afterwards, the development of scaled-up procedures for the preparation of polymer/GO nanocomposite particles *via* heteroflocculation could be pursued.

Chapter Seven

References

1. L. Zhang and A. Eisenberg, *Science*, 1995, **268**, 1728-1731.
2. Y. Mai and A. Eisenberg, *Chemical Society Reviews*, 2012, **41**, 5969-5985.
3. S. L. Canning, G. N. Smith and S. P. Armes, *Macromolecules*, 2016, **49**, 1985-2001.
4. F. Ouhib, A. Dirani, A. Aqil, K. Glinel, B. Nysten, A. M. Jonas, C. Jerôme and C. Detrembleur, *Polymer Chemistry*, 2016, **7**, 3998-4003.
5. C. Fong, T. Le and C. J. Drummond, *Chemical Society Reviews*, 2012, **41**, 1297-1322.
6. B. Karagoz, L. Esser, H. T. Duong, J. S. Basuki, C. Boyer and T. P. Davis, *Polymer Chemistry*, 2014, **5**, 350-355.
7. B. Charleux, G. Delaittre, J. Rieger and F. D'Agosto, *Macromolecules*, 2012, **45**, 6753-6765.
8. M. J. Derry, L. A. Fielding and S. P. Armes, *Progress in Polymer Science*, 2016, **52**, 1-18.
9. N. J. Warren and S. P. Armes, *Journal of the American Chemical Society*, 2014, **136**, 10174-10185.
10. F. d'Agosto, J. Rieger and M. Lansalot, *Angewandte Chemie International Edition*, 2020, **59**, 8368-8392.
11. M. Semsarilar, V. Ladmiral, A. Blanazs and S. Armes, *Langmuir*, 2012, **29**, 7416-7424.
12. A. Hanisch, P. Yang, A. N. Kulak, L. A. Fielding, F. C. Meldrum and S. P. Armes, *Macromolecules*, 2015, **49**, 192-204.
13. M. Williams, N. Penfold and S. Armes, *Polymer Chemistry*, 2016, **7**, 384-393.
14. Y. Li and S. P. Armes, *Angewandte Chemie International Edition*, 2010, **49**, 4042-4046.
15. A. Blanazs, A. Ryan and S. Armes, *Macromolecules*, 2012, **45**, 5099-5107.
16. N. J. Warren, O. O. Mykhaylyk, D. Mahmood, A. J. Ryan and S. P. Armes, *Journal of the American Chemical Society*, 2014, **136**, 1023-1033.
17. W. Zhou, Q. Qu, Y. Xu and Z. An, *ACS Macro Letters*, 2015, **4**, 495-499.
18. W. Shen, Y. Chang, G. Liu, H. Wang, A. Cao and Z. An, *Macromolecules*, 2011, **44**, 2524-2530.
19. V. Ladmiral, M. Semsarilar, I. Canton and S. P. Armes, *Journal of the American Chemical Society*, 2013, **135**, 13574-13581.
20. Y. Jiang, N. Xu, J. Han, Q. Yu, L. Guo, P. Gao, X. Lu and Y. Cai, *Polymer Chemistry*, 2015, **6**, 4955-4965.
21. K. E. Doncom, N. J. Warren and S. P. Armes, *Polymer Chemistry*, 2015, **6**, 7264-7273.
22. S. Sugihara, A. Blanazs, S. P. Armes, A. J. Ryan and A. L. Lewis, *Journal of the American Chemical Society*, 2011, **133**, 15707-15713.
23. V. Ladmiral, A. Charlot, M. Semsarilar and S. P. Armes, *Polymer Chemistry*, 2015, **6**, 1805-1816.
24. W. Cai, W. Wan, C. Hong, C. Huang and C. Pan, *Soft Matter*, 2010, **6**, 5554-5561.
25. M. Semsarilar, E. R. Jones, A. Blanazs and S. P. Armes, *Advanced Materials*, 2012, **24**, 3378-3382.
26. M. Semsarilar, E. R. Jones and S. P. Armes, *Polymer Chemistry*, 2014, **5**, 195-203.
27. J. Rieger, C. Grazon, B. Charleux, D. Alaimo and C. Jérôme, *Journal of Polymer Science Part A: Polymer Chemistry*, 2009, **47**, 2373-2390.
28. L. Houillot, C. Bui, M. Save, B. Charleux, C. Farcet, C. Moire, J.-A. Raust and I. Rodriguez, *Macromolecules*, 2007, **40**, 6500-6509.
29. L. A. Fielding, M. J. Derry, V. Ladmiral, J. Rosselgong, A. M. Rodrigues, L. P. Ratcliffe, S. Sugihara and S. P. Armes, *Chemical Science*, 2013, **4**, 2081-2087.
30. L. A. Fielding, J. A. Lane, M. J. Derry, O. O. Mykhaylyk and S. P. Armes, *Journal of the American Chemical Society*, 2014, **136**, 5790-5798.
31. L. H. Sperling, *Introduction to physical polymer science*, John Wiley & Sons, 2005.
32. G. Odian, *Principles of polymerization*, John Wiley & Sons, 2004.
33. P. A. Lovell, M. S. El-Aasser and P. Lovell, *Emulsion polymerization and emulsion polymers*, Wiley New York, 1997.
34. J. Brandrup, E. H. Immergut, E. A. Grulke, A. Abe and D. R. Bloch, *Polymer handbook*, Wiley New York, 1999.

35. P. C. Hiemenz and T. P. Lodge, *Polymer chemistry*, CRC press, 2007.
36. K. Matyjaszewski, Y. Gnanou and L. Leibler, *Macromolecular Engineering: Precise Synthesis, Materials Properties, Applications*, 2007, 1-6.
37. R. J. Young and P. A. Lovell, *Introduction to polymers*, CRC press, 2011.
38. G. Moad, E. Rizzardo and S. H. Thang, *Accounts of chemical research*, 2008, **41**, 1133-1142.
39. W. A. Braunecker and K. Matyjaszewski, *Progress in Polymer Science*, 2007, **32**, 93-146.
40. D. Solomon, E. Rizzardo and P. Cacioli, Polymerization Process and Polymers Produced Thereby, US Patent, 4581429, 1986.
41. M. K. Georges, R. P. Veregin, P. M. Kazmaier and G. K. Hamer, *Macromolecules*, 1993, **26**, 2987-2988.
42. J. Nicolas, Y. Guillaneuf, C. Lefay, D. Bertin, D. Gigmes and B. Charleux, *Progress in Polymer Science*, 2013, **38**, 63-235.
43. M. C. Davies, J. V. Dawkins and D. J. Hourston, *Polymer*, 2005, **46**, 1739-1753.
44. D. Benoit, C. J. Hawker, E. E. Huang, Z. Lin and T. P. Russell, *Macromolecules*, 2000, **33**, 1505-1507.
45. E. S. Park, M. N. Kim, I. M. Lee, H. S. Lee and J. S. Yoon, *Journal of Polymer Science Part A: Polymer Chemistry*, 2000, **38**, 2239-2244.
46. C. J. Hawker, A. W. Bosman and E. Harth, *Chemical reviews*, 2001, **101**, 3661-3688.
47. R. B. Grubbs, *Polymer Reviews*, 2011, **51**, 104-137.
48. M. Kato, M. Kamigaito, M. Sawamoto and T. Higashimura, *Macromolecules*, 1995, **28**, 1721-1723.
49. J.-S. Wang and K. Matyjaszewski, *Journal of the American Chemical Society*, 1995, **117**, 5614-5615.
50. P. Krol and P. Chmielarz, *Progress in Organic Coatings*, 2014, **77**, 913-948.
51. J. Ran, L. Wu, Z. Zhang and T. Xu, *Progress in Polymer Science*, 2014, **39**, 124-144.
52. Y. Kwak, R. Nicolaÿ and K. Matyjaszewski, *Australian journal of chemistry*, 2009, **62**, 1384-1401.
53. K. Matyjaszewski, *Macromolecules*, 2012, **45**, 4015-4039.
54. W. Tang, N. V. Tsarevsky and K. Matyjaszewski, *Journal of the American Chemical Society*, 2006, **128**, 1598-1604.
55. N. Chan, M. F. Cunningham and R. A. Hutchinson, *Macromolecular Reaction Engineering*, 2010, **4**, 369-380.
56. V. T. Huynh, D. Nguyen, C. H. Such and B. S. Hawkett, *Journal of Polymer Science Part A: Polymer Chemistry*, 2015, **53**, 1413-1421.
57. F. di Lena and K. Matyjaszewski, *Progress in Polymer Science*, 2010, **35**, 959-1021.
58. C.-H. Peng, M. Zhong, Y. Wang, Y. Kwak, Y. Zhang, W. Zhu, M. Tonge, J. Buback, S. Park and P. Krys, *Macromolecules*, 2013, **46**, 3803-3815.
59. W. Jakubowski and K. Matyjaszewski, *Macromolecules*, 2005, **38**, 4139-4146.
60. W. Jakubowski, K. Min and K. Matyjaszewski, *Macromolecules*, 2006, **39**, 39-45.
61. M. A. Mballa Mballa, S. I. Ali, J. P. Heuts and A. M. van Herk, *Polymer International*, 2012, **61**, 861-865.
62. C. Barner-Kowollik, *Handbook of RAFT polymerization*, John Wiley & Sons, 2008.
63. J. McLeary, F. Calitz, J. McKenzie, M. Tonge, R. Sanderson and B. Klumperman, *Macromolecules*, 2005, **38**, 3151-3161.
64. D. Taton, A. Z. Wilczewska and M. Destarac, *Macromolecular Rapid Communications*, 2001, **22**, 1497-1503.
65. M. Destarac, C. Brochon, J. M. Catala, A. Wilczewska and S. Z. Zard, *Macromolecular Chemistry and Physics*, 2002, **203**, 2281-2289.
66. M. Destarac, W. Bzducha, D. Taton, I. Gauthier-Gillaizeau and S. Z. Zard, *Macromolecular Rapid Communications*, 2002, **23**, 1049-1054.
67. G. Moad, E. Rizzardo and S. H. Thang, *Chemistry–An Asian Journal*, 2013, **8**, 1634-1644.

68. Y. Zhao and S. Perrier, *Macromolecules*, 2006, **39**, 8603-8608.
69. S.-P. Wen, J. G. Saunders and L. A. Fielding, *Polymer Chemistry*, 2020, **11**, 3416-3426.
70. L. A. Fielding, C. T. Hendley IV, E. Asenath-Smith, L. A. Estroff and S. P. Armes, *Polymer Chemistry*, 2019, **10**, 5131-5141.
71. N. B. Pramanik, P. Mondal, R. Mukherjee and N. K. Singha, *Polymer*, 2017, **119**, 195-205.
72. Y. Qu, S. Wang, H. Khan, C. Gao, H. Zhou and W. Zhang, *Polymer Chemistry*, 2016, **7**, 1953-1962.
73. X. Guo, T. Zhang, Y. Wu, W. Shi, B. Choi, A. Feng and S. H. Thang, *Polymer Chemistry*, 2020, **11**, 6794-6802.
74. S. Xu, T. Zhang, R. P. Kuchel, J. Yeow and C. Boyer, *Macromolecular rapid communications*, 2020, **41**, 1900493.
75. S. Cosson, M. Danial, J. R. Saint-Amans and J. J. Cooper-White, *Macromolecular rapid communications*, 2017, **38**, 1600780.
76. J. Hu, R. Qiao, M. R. Whittaker, J. F. Quinn and T. P. Davis, *Australian Journal of Chemistry*, 2017, **70**, 1161-1170.
77. B. Xu, X. Sun, C. Wu, J. Hu and X. Huang, *Polymer Chemistry*, 2017, **8**, 7499-7506.
78. D. Shen, B. Xu, X. Huang, Q. Zhuang and S. Lin, *Polymer Chemistry*, 2018, **9**, 2821-2829.
79. S. L. Banerjee, P. Saha, R. Ganguly, K. Bhattacharya, U. Kalita, A. Pich and N. K. Singha, *Journal of Colloid and Interface Science*, 2020, **589**, 110-126.
80. H. T. Lord, J. F. Quinn, S. D. Angus, M. R. Whittaker, M. H. Stenzel and T. P. Davis, *Journal of Materials Chemistry*, 2003, **13**, 2819-2824.
81. G. Moad, E. Rizzardo and S. H. Thang, *Australian Journal of Chemistry*, 2009, **62**, 1402-1472.
82. G. Moad, E. Rizzardo and S. H. Thang, *Australian Journal of Chemistry*, 2006, **59**, 669-692.
83. G. Moad, E. Rizzardo and S. H. Thang, *Australian journal of chemistry*, 2005, **58**, 379-410.
84. C. Boyer, V. Bulmus, T. P. Davis, V. Ladmiral, J. Liu and S. Perrier, *Chemical reviews*, 2009, **109**, 5402-5436.
85. G. Moad, *Polymer Chemistry*, 2017, **8**, 177-219.
86. D. J. Keddie, *Chemical Society Reviews*, 2014, **43**, 496-505.
87. S. Perrier, *Macromolecules*, 2017, **50**, 7433-7447.
88. H. Fischer, *Chemical reviews*, 2001, **101**, 3581-3610.
89. A. Goto and T. Fukuda, *Progress in Polymer Science*, 2004, **29**, 329-385.
90. J. F. Quinn, L. Barner, E. Rizzardo and T. P. Davis, *Journal of Polymer Science Part A: Polymer Chemistry*, 2002, **40**, 19-25.
91. S. Muthukrishnan, E. H. Pan, M. H. Stenzel, C. Barner-Kowollik, T. P. Davis, D. Lewis and L. Barner, *Macromolecules*, 2007, **40**, 2978-2980.
92. A. J. Convertine, B. S. Sumerlin, D. B. Thomas, A. B. Lowe and C. L. McCormick, *Macromolecules*, 2003, **36**, 4679-4681.
93. A. Goto, K. Sato, Y. Tsujii, T. Fukuda, G. Moad, E. Rizzardo and S. H. Thang, *Macromolecules*, 2001, **34**, 402-408.
94. D. J. Keddie, G. Moad, E. Rizzardo and S. H. Thang, *Macromolecules*, 2012, **45**, 5321-5342.
95. G. Moad and E. Rizzardo, *Polymer International*, 2020, **69**, 658-661.
96. Y. Chong, J. Krstina, T. P. Le, G. Moad, A. Postma, E. Rizzardo and S. H. Thang, *Macromolecules*, 2003, **36**, 2256-2272.
97. J. Chiefari, R. T. Mayadunne, C. L. Moad, G. Moad, E. Rizzardo, A. Postma, M. A. Skidmore and S. H. Thang, *Macromolecules*, 2003, **36**, 2273-2283.
98. G. Moad, E. Rizzardo and S. H. Thang, *Australian Journal of Chemistry*, 2012, **65**, 985-1076.
99. M. Destarac, *Polymer reviews*, 2011, **51**, 163-187.
100. G. Moad, *Journal of Polymer Science Part A: Polymer Chemistry*, 2019, **57**, 216-227.
101. M. P. Stevens, *Polymer chemistry: an introduction*, Oxford University Press New York, 1990.

102. W. D. Harkins, *Journal of the American Chemical Society*, 1947, **69**, 1428-1444.
103. W. D. Harkins, *The Journal of Chemical Physics*, 1945, **13**, 381-382.
104. W. V. Smith and R. H. Ewart, *The journal of chemical physics*, 1948, **16**, 592-599.
105. J. L. Gardon, *Journal of Polymer Science Part A-1: Polymer Chemistry*, 1968, **6**, 623-641.
106. R. G. Gilbert, *Emulsion polymerization: a mechanistic approach*, Academic press, 1995.
107. K. Luettgen, Process for Continuous Emulsion Polymerization, US Patent, 9296851B2, 2016.
108. A. J. Morse, D. Dupin, K. L. Thompson, S. Armes, K. Ouzineb, P. Mills and R. Swart, *Langmuir*, 2012, **28**, 11733-11744.
109. W. Priest, *The Journal of Physical Chemistry*, 1952, **56**, 1077-1082.
110. C. P. Roe, *Industrial & Engineering Chemistry*, 1968, **60**, 20-33.
111. C. Miller, E. Sudol, C. Silebi and M. El-Aasser, *Macromolecules*, 1995, **28**, 2754-2764.
112. V. Mittal, *Miniemulsion polymerization technology*, John Wiley & Sons, 2011.
113. Y. Chou, M. El-Aasser and J. Vanderhoff, *Journal of Dispersion Science and Technology*, 1980, **1**, 599-618.
114. J. Ugelstad, M. El-Aasser and J. Vanderhoff, *Journal of Polymer Science: Polymer Letters Edition*, 1973, **11**, 503-513.
115. G. H. Al-Ghamdi, E. D. Sudol, V. L. Dimonie and M. S. El-Aasser, *Journal of applied polymer science*, 2006, **101**, 3479-3486.
116. Y. Huang and D. Paul, *Journal of Polymer Science Part B: Polymer Physics*, 2007, **45**, 1390-1398.
117. R. Udagama, E. Degrandi-Contraires, C. Creton, C. Graillat, T. F. McKenna and E. Bourgeat-Lami, *Macromolecules*, 2011, **44**, 2632-2642.
118. A. Lopez, E. Degrandi-Contraires, E. Canetta, C. Creton, J. L. Keddie and J. M. Asua, *Langmuir*, 2011, **27**, 3878-3888.
119. R. Jovanović and M. A. Dubé, *Journal of applied polymer science*, 2001, **82**, 2958-2977.
120. A. Agirre, C. d. l. Heras-Alarcón, T. Wang, J. L. Keddie and J. M. Asua, *ACS applied materials & interfaces*, 2010, **2**, 443-451.
121. M. Aguirre, M. Paulis and J. R. Leiza, *Journal of Materials Chemistry A*, 2013, **1**, 3155-3162.
122. N. Sankarakumar and Y. W. Tong, *Journal of Materials Chemistry B*, 2013, **1**, 2031-2037.
123. L. B. Fonseca, M. Nele, N. M. Volpato, R. C. Seiceira and J. C. Pinto, *Macromolecular Reaction Engineering*, 2013, **7**, 54-63.
124. J. Ramos and J. Forcada, *Langmuir*, 2011, **27**, 7222-7230.
125. G. Baier, A. Musyanovych, V. Mailänder and K. Landfester, *The International journal of artificial organs*, 2012, **35**, 77-83.
126. F. J. Schork, Y. Luo, W. Smulders, J. P. Russum, A. Butté and K. Fontenot, *Polymer particles*, Springer, 2005.
127. J. M. Asua, *Progress in polymer science*, 2002, **27**, 1283-1346.
128. M. Antonietti and K. Landfester, *Progress in polymer science*, 2002, **27**, 689-757.
129. J. M. Asua, *Progress in polymer science*, 2014, **39**, 1797-1826.
130. K. Landfester, *Annual Review of Materials Research*, 2006, **36**, 231-279.
131. H. Huang, H. Zhang, J. Li, S. Cheng, F. Hu and B. Tan, *Journal of applied polymer science*, 1998, **68**, 2029-2039.
132. J. Soma and K. D. Papadopoulos, *Journal of colloid and interface science*, 1996, **181**, 225-231.
133. K. Landfester, N. Bechthold, F. Tiarks and M. Antonietti, *Macromolecules*, 1999, **32**, 5222-5228.
134. M. S. El-Aasser and C. M. Miller, *Polymeric dispersions: Principles and applications*, Springer, 1997.

135. Y. Choi, M. El-Aasser, E. Sudol and J. Vanderhoff, *Journal of Polymer Science: Polymer Chemistry Edition*, 1985, **23**, 2973-2987.
136. T. F. Tadros, *Applied surfactants: principles and applications*, John Wiley & Sons, 2006.
137. K. Landfester, N. Bechthold, F. Tiarks and M. Antonietti, *Macromolecules*, 1999, **32**, 2679-2683.
138. L. L. Hecht, A. Schoth, R. Muñoz-Espí, A. Javadi, K. Köhler, R. Miller, K. Landfester and H. P. Schuchmann, *Macromolecular Chemistry and Physics*, 2013, **214**, 812-823.
139. J. Valle-Delgado, J. Molina-Bolivar, F. Galisteo-Gonzalez and M. Gálvez-Ruiz, *Colloid and Polymer Science*, 2003, **281**, 708-715.
140. G. N. Smith, S. D. Finlayson, S. E. Rogers, P. Bartlett and J. Eastoe, *The journal of physical chemistry letters*, 2017, **8**, 4668-4672.
141. P. Elworthy and A. Florence, *Journal of Pharmacy and Pharmacology*, 1969, **21**, 79S-90S.
142. E. Grządka and J. Matusiak, *Carbohydrate polymers*, 2017, **175**, 192-198.
143. P. M. Claesson, J. C. Eriksson, C. Herder, B. A. Bergenståhl, E. Pezron, I. Pezron and P. Stenius, *Faraday Discussions of the Chemical Society*, 1990, **90**, 129-142.
144. F. J. Schork, G. Poehlein, S. Wang, J. Reimers, J. Rodrigues and C. Samer, *Colloids and Surfaces A: Physicochemical and Engineering Aspects*, 1999, **153**, 39-45.
145. M. H. Stenzel, L. Zhang and W. T. Huck, *Macromolecular rapid communications*, 2006, **27**, 1121-1126.
146. L. L. Hecht, C. Wagner, K. Landfester and H. P. Schuchmann, *Langmuir*, 2011, **27**, 2279-2285.
147. L. I. Ronco, R. J. Minari and L. M. Gugliotta, *Brazilian Journal of Chemical Engineering*, 2015, **32**, 191-200.
148. N. Bechthold and K. Landfester, *Macromolecules*, 2000, **33**, 4682-4689.
149. K. Landfester, *Colloid chemistry II*, 2003, **227**, 75-123.
150. K. Landfester, N. Bechthold, S. Förster and M. Antonietti, *Macromolecular rapid communications*, 1999, **20**, 81-84.
151. C. Miller, E. Sudol, C. Silebi and M. El-Aasser, *Journal of Polymer Science Part A: Polymer Chemistry*, 1995, **33**, 1391-1408.
152. N. Kim, E. D. Sudol, V. L. Dimonie and M. S. El-Aasser, *Macromolecules*, 2004, **37**, 2427-2433.
153. I. Aizpurua and M. a. J. Barandiaran, *Polymer*, 1999, **40**, 4105-4115.
154. M. Lansalot, T. P. Davis and J. P. Heuts, *Macromolecules*, 2002, **35**, 7582-7591.
155. K. Matyjaszewski, J. Qiu, N. V. Tsarevsky and B. Charleux, *Journal of Polymer Science Part A: Polymer Chemistry*, 2000, **38**, 4724-4734.
156. M. F. Cunningham, M. Xie, K. B. McAuley, B. Keoshkerian and M. K. Georges, *Macromolecules*, 2002, **35**, 59-66.
157. D. Kukulj, T. P. Davis and R. G. Gilbert, *Macromolecules*, 1997, **30**, 7661-7666.
158. M. Lansalot, C. Farcet, B. Charleux, J.-P. Vairon and R. Pirri, *Macromolecules*, 1999, **32**, 7354-7360.
159. M. Khan, T. R. Guimarães, D. Zhou, G. Moad, S. Perrier and P. B. Zetterlund, *Journal of Polymer Science Part A: Polymer Chemistry*, 2019, **57**, 1938-1946.
160. G. Qi and F. J. Schork, *Langmuir*, 2006, **22**, 9075-9078.
161. X. Zhou, P. Ni and Z. Yu, *Polymer*, 2007, **48**, 6262-6271.
162. S. W. Prescott, M. J. Ballard, E. Rizzardo and R. G. Gilbert, *Macromolecules*, 2002, **35**, 5417-5425.
163. R. W. Simms, T. P. Davis and M. F. Cunningham, *Macromolecular rapid communications*, 2005, **26**, 592-596.
164. J. G. Tsavalas, F. J. Schork, H. de Brouwer and M. J. Monteiro, *Macromolecules*, 2001, **34**, 3938-3946.
165. Y. Luo, B. Liu, Z. Wang, J. Gao and B. Li, *Journal of Polymer Science Part A: Polymer Chemistry*, 2007, **45**, 2304-2315.

166. L. Yang, Y. Luo and B. Li, *Polymer*, 2006, **47**, 751-762.
167. M. Park, K. Kim, A. K. Mohanty, H. Y. Cho, H. Lee, Y. Kang, B. Seo, W. Lee, H. B. Jeon and H. j. Paik, *Macromolecular Rapid Communications*, 2020, **41**, 2000399.
168. Z. Huang, P. Pan and Y. Bao, *Journal of Polymer Science Part A: Polymer Chemistry*, 2016, **54**, 2092-2101.
169. A. V. Fuchs and K. J. Thurecht, *Macromolecular Chemistry and Physics*, 2015, **216**, 1271-1281.
170. J. Vosloo, D. De Wet-Roos, M. Tonge and R. Sanderson, *Macromolecules*, 2002, **35**, 4894-4902.
171. A. Butté, G. Storti and M. Morbidelli, *Macromolecules*, 2000, **33**, 3485-3487.
172. J. McLeary, M. Tonge, D. De Wet Roos, R. Sanderson and B. Klumperman, *Journal of Polymer Science Part A: Polymer Chemistry*, 2004, **42**, 960-974.
173. C. Miller, E. Sudol, C. Silebi and M. El-Aasser, *Macromolecules*, 1995, **28**, 2772-2780.
174. B. T. Pham, D. Nguyen, C. J. Ferguson, B. S. Hawkett, A. K. Serelis and C. H. Such, *Macromolecules*, 2003, **36**, 8907-8909.
175. A. Guyot and K. Tauer, *Polymer Synthesis*, Springer, 1994.
176. A. Guyot, K. Tauer, J. Asua, S. Van Es, C. Gauthier, A. Hellgren, D. Sherrington, A. Montoya-Goni, M. Sjoberg and O. Sindt, *Acta Polymerica*, 1999, **50**, 57-66.
177. I. Uzulina, A. Zicmanis, C. Graillat, J. Claverie and A. Guyot, *Macromolecular Chemistry and Physics*, 2001, **202**, 3126-3135.
178. A. Butté, G. Storti and M. Morbidelli, *Macromolecules*, 2001, **34**, 5885-5896.
179. G. Moad, J. Chiefari, Y. K. Chong, J. Krstina, R. T. A. Mayadunne, A. Postma, E. Rizzardo and S. H. Thang, *Polymer International*, 2000, **49**, 993-1001.
180. A. J. van Zyl, R. F. Bosch, J. B. McLeary, R. D. Sanderson and B. Klumperman, *Polymer*, 2005, **46**, 3607-3615.
181. R. Nagarajan, *Surfactant Science and Technology, Retrospects and Prospects*, CRC Press, 2014.
182. J. McBain, *Transactions of the Faraday Society*, 1913, **9**, 99-112.
183. I. Climie and E. White, *Journal of Polymer Science*, 1960, **47**, 149-156.
184. S. Krause, *The Journal of Physical Chemistry*, 1964, **68**, 1948-1955.
185. D. Lombardo, M. A. Kiselev, S. Magazù and P. Calandra, *Advances in Condensed Matter Physics*, 2015, **2015**.
186. R. Zana, *Dynamics of surfactant self-assemblies: micelles, microemulsions, vesicles and lyotropic phases*, CRC press, 2005.
187. J. N. Israelachvili and D. J. Mitchell, *Biochimica et Biophysica Acta (BBA)-Biomembranes*, 1975, **389**, 13-19.
188. J. N. Israelachvili, D. J. Mitchell and B. W. Ninham, *Journal of the Chemical Society, Faraday Transactions 2: Molecular and Chemical Physics*, 1976, **72**, 1525-1568.
189. J. N. Israelachvili, D. J. Mitchell and B. W. Ninham, *Biochimica et Biophysica Acta (BBA)-Biomembranes*, 1977, **470**, 185-201.
190. J. Israelachvili, S. Marčelja and R. G. Horn, *Quarterly reviews of biophysics*, 1980, **13**, 121-200.
191. J. N. Israelachvili, *Intermolecular and surface forces*, Academic press, 2015.
192. A. Blanazs, S. P. Armes and A. J. Ryan, *Macromolecular rapid communications*, 2009, **30**, 267-277.
193. J. Rodriguez-Hernandez, F. Chécot, Y. Gnanou and S. Lecommandoux, *Progress in polymer science*, 2005, **30**, 691-724.
194. N. S. Cameron, M. K. Corbierre and A. Eisenberg, *Canadian journal of chemistry*, 1999, **77**, 1311-1326.
195. L. Zhang and A. Eisenberg, *Journal of the American Chemical Society*, 1996, **118**, 3168-3181.
196. L. Zhang, K. Yu and A. Eisenberg, *Science*, 1996, **272**, 1777-1779.

197. J. Van Hest, D. Delnoye, M. Baars, M. Van Genderen and E. Meijer, *Science*, 1995, **268**, 1592-1595.
198. E. L. Thomas, D. M. Anderson, C. S. Henkee and D. Hoffman, *Nature*, 1988, **334**, 598.
199. F. S. Bates, *Science*, 1991, **251**, 898-905.
200. L. Zhang and A. Eisenberg, *Macromolecules*, 1999, **32**, 2239-2249.
201. Y. Yu, L. Zhang and A. Eisenberg, *Macromolecules*, 1998, **31**, 1144-1154.
202. P. Bhargava, J. X. Zheng, P. Li, R. P. Quirk, F. W. Harris and S. Z. Cheng, *Macromolecules*, 2006, **39**, 4880-4888.
203. R. T. Pearson, N. J. Warren, A. L. Lewis, S. P. Armes and G. Battaglia, *Macromolecules*, 2013, **46**, 1400-1407.
204. J. R. Howse, R. A. Jones, G. Battaglia, R. E. Ducker, G. J. Leggett and A. J. Ryan, *Nature materials*, 2009, **8**, 507.
205. V. Bütün, S. Armes and N. Billingham, *Polymer*, 2001, **42**, 5993-6008.
206. S. Sugihara, K. Sugihara, S. P. Armes, H. Ahmad and A. L. Lewis, *Macromolecules*, 2010, **43**, 6321-6329.
207. S. Sugihara, S. P. Armes and A. L. Lewis, *Angewandte Chemie International Edition*, 2010, **49**, 3500-3503.
208. K. H. Kim, J. Kim and W. H. Jo, *Polymer*, 2005, **46**, 2836-2840.
209. E. Groison, S. g. n. Brusseau, F. D'Agosto, S. p. Magnet, R. Inoubli, L. Couvreur and B. Charleux, *ACS Macro Letters*, 2011, **1**, 47-51.
210. G. Delaittre, J. Nicolas, C. Lefay, M. Save and B. Charleux, *Chemical communications*, 2005, 614-616.
211. S. g. n. Brusseau, F. D'Agosto, S. Magnet, L. Couvreur, C. Chamignon and B. Charleux, *Macromolecules*, 2011, **44**, 5590-5598.
212. Y. Chong, T. P. Le, G. Moad, E. Rizzardo and S. H. Thang, *Macromolecules*, 1999, **32**, 2071-2074.
213. J.-T. Sun, C.-Y. Hong and C.-Y. Pan, *Soft Matter*, 2012, **8**, 7753-7767.
214. J.-T. Sun, C.-Y. Hong and C.-Y. Pan, *Polymer Chemistry*, 2013, **4**, 873-881.
215. J. Rieger, *Macromolecular rapid communications*, 2015, **36**, 1458-1471.
216. G. Moad, J. Chiefari, K. C. BY and J. Krstina, *Polymer International*, 2000, **49**, 993.
217. M. R. Hill, R. N. Carmean and B. S. Sumerlin, *Macromolecules*, 2015, **48**, 5459-5469.
218. J. Chiefari, Y. Chong, F. Ercole, J. Krstina, J. Jeffery, T. P. Le, R. T. Mayadunne, G. F. Meijs, C. L. Moad and G. Moad, *Macromolecules*, 1998, **31**, 5559-5562.
219. E. Chernikova, E. Lysenko, N. Serkhacheva and N. Prokopov, *Polymer Science, Series C*, 2018, **60**, 192-218.
220. C. A. Figg, A. Simula, K. A. Gebre, B. S. Tucker, D. M. Haddleton and B. S. Sumerlin, *Chemical science*, 2015, **6**, 1230-1236.
221. S. W. Prescott, M. J. Ballard, E. Rizzardo and R. G. Gilbert, *Australian journal of chemistry*, 2002, **55**, 415-424.
222. M. J. Derry, L. A. Fielding and S. P. Armes, *Polymer Chemistry*, 2015, **6**, 3054-3062.
223. A. Guyot, *Current opinion in colloid & Interface science*, 1996, **5**, 580-586.
224. C. J. Ferguson, R. J. Hughes, B. T. Pham, B. S. Hawkett, R. G. Gilbert, A. K. Serelis and C. H. Such, *Macromolecules*, 2002, **35**, 9243-9245.
225. C. J. Ferguson, R. J. Hughes, D. Nguyen, B. T. Pham, R. G. Gilbert, A. K. Serelis, C. H. Such and B. S. Hawkett, *Macromolecules*, 2005, **38**, 2191-2204.
226. D. E. Ganeva, E. Sprong, H. De Bruyn, G. G. Warr, C. H. Such and B. S. Hawkett, *Macromolecules*, 2007, **40**, 6181-6189.
227. S. Boissé, J. Rieger, K. Belal, A. Di-Cicco, P. Beaunier, M.-H. Li and B. Charleux, *Chemical communications*, 2010, **46**, 1950-1952.
228. W. Zhang, F. D'Agosto, O. Boyron, J. Rieger and B. Charleux, *Macromolecules*, 2012, **45**, 4075-4084.

229. J. Rieger, W. Zhang, F. o. Stoffelbach and B. Charleux, *Macromolecules*, 2010, **43**, 6302-6310.
230. I. Chaduc, W. Zhang, J. Rieger, M. Lansalot, F. D'Agosto and B. Charleux, *Macromolecular rapid communications*, 2011, **32**, 1270-1276.
231. J. Rieger, G. Osterwinter, C. Bui, F. Stoffelbach and B. Charleux, *Macromolecules*, 2009, **42**, 5518-5525.
232. J. Rieger, F. Stoffelbach, C. Bui, D. Alaimo, C. Jérôme and B. Charleux, *Macromolecules*, 2008, **41**, 4065-4068.
233. V. J. Cunningham, A. M. Alswieleh, K. L. Thompson, M. Williams, G. J. Leggett, S. P. Armes and O. M. Musa, *Macromolecules*, 2014, **47**, 5613-5623.
234. W. Zhang, F. D'Agosto, P.-Y. Dugas, J. Rieger and B. Charleux, *Polymer*, 2013, **54**, 2011-2019.
235. J. Ma, H. M. Andriambololona, D. Quemener and M. Semsarilar, *Journal of Membrane Science*, 2018, **548**, 42-49.
236. Y. Li and S. P. Armes, *Angewandte Chemie*, 2010, **122**, 4136-4140.
237. M. Semsarilar, V. Ladmiral, A. Blanazs and S. Armes, *Langmuir*, 2012, **28**, 914-922.
238. M. Semsarilar, V. Ladmiral, A. Blanazs and S. Armes, *Langmuir*, 2013, **29**, 7416-7424.
239. W.-M. Wan and C.-Y. Pan, *Macromolecules*, 2010, **43**, 2672-2675.
240. W. M. Wan, X. L. Sun and C. Y. Pan, *Macromolecular rapid communications*, 2010, **31**, 399-404.
241. E. R. Jones, M. Semsarilar, A. Blanazs and S. P. Armes, *Macromolecules*, 2012, **45**, 5091-5098.
242. M. Semsarilar, V. Ladmiral, A. Blanazs and S. P. Armes, *Polymer Chemistry*, 2014, **5**, 3466-3475.
243. M. Semsarilar, N. J. Penfold, E. R. Jones and S. P. Armes, *Polymer Chemistry*, 2015, **6**, 1751-1757.
244. W. Zhao, G. Gody, S. Dong, P. B. Zetterlund and S. Perrier, *Polymer Chemistry*, 2014, **5**, 6990-7003.
245. A. P. Lopez-Oliva, N. J. Warren, A. Rajkumar, O. O. Mykhaylyk, M. J. Derry, K. E. Doncom, M. J. Rymaruk and S. P. Armes, *Macromolecules*, 2015, **48**, 3547-3555.
246. Q. Zhang and S. Zhu, *ACS Macro Letters*, 2015, **4**, 755-758.
247. H. Zhou, C. Liu, C. Gao, Y. Qu, K. Shi and W. Zhang, *Journal of Polymer Science Part A: Polymer Chemistry*, 2016, **54**, 1517-1525.
248. K. Nieswandt, P. Georgopanos and V. Abetz, *Polymer Chemistry*, 2021, **12**, 2210-2221.
249. X. Xiao, S. He, M. Dan, Y. Su, F. Huo and W. Zhang, *Journal of Polymer Science Part A: Polymer Chemistry*, 2013, **51**, 3177-3190.
250. X. Zhang, J. Rieger and B. Charleux, *Polymer Chemistry*, 2012, **3**, 1502-1509.
251. E. Jones, M. Semsarilar, P. Wyman, M. Boerakker and S. Armes, *Polymer Chemistry*, 2016, **7**, 851-859.
252. Y. Ning, L. A. Fielding, L. P. Ratcliffe, Y.-W. Wang, F. C. Meldrum and S. P. Armes, *Journal of the American Chemical Society*, 2016, **138**, 11734-11742.
253. S. Pourhashem, F. Saba, J. Duan, A. Rashidi, F. Guan, E. G. Nezhad and B. Hou, *Journal of Industrial and Engineering Chemistry*, 2020.
254. Y. Yan, G. Yang, J.-L. Xu, M. Zhang, C.-C. Kuo and S.-D. Wang, *Science and Technology of Advanced Materials*, 2020, **21**, 768-786.
255. A. Kausar, *Polymer-Plastics Technology and Materials*, 2020, **59**, 895-909.
256. H. Zou and S. Zhai, *Polymer Chemistry*, 2020, **11**, 3370-3392.
257. S. C. Thickett and G. H. Teo, *Polymer Chemistry*, 2019, **10**, 2906-2924.
258. R. Shah, A. Kausar, B. Muhammad and S. Shah, *Polymer-Plastics Technology and Engineering*, 2015, **54**, 173-183.
259. Z. U. Khan, A. Kausar, H. Ullah, A. Badshah and W. U. Khan, *Journal of plastic film & sheeting*, 2016, **32**, 336-379.

260. A. Kausar, *Polymer-Plastics Technology and Materials*, 2019, **58**, 821-842.
261. B. Tan and N. L. Thomas, *Journal of Membrane Science*, 2016, **514**, 595-612.
262. F. Pena-Pereira, V. Romero, I. de la Calle, I. Lavilla and C. Bendicho, *TrAC Trends in Analytical Chemistry*, 2021, 116303.
263. M. Dehghani, N. Nasirizadeh and M. E. Yazdanshenas, *Materials Science and Engineering: C*, 2019, **96**, 654-660.
264. S. Alexander, P. Baraneedharan, S. Balasubrahmanyan and S. Ramaprabhu, *Materials Science and Engineering: C*, 2017, **78**, 124-129.
265. S. Mondal, U. Rana and S. Malik, *The Journal of Physical Chemistry C*, 2017, **121**, 7573-7583.
266. P. Pattanayak, N. Pramanik, P. Kumar and P. P. Kundu, *international journal of hydrogen energy*, 2018, **43**, 11505-11519.
267. M. Adeel, M. Bilal, T. Rasheed, A. Sharma and H. M. Iqbal, *International journal of biological macromolecules*, 2018, **120**, 1430-1440.
268. J. Zhang, Z. Zhang, Y. Jiao, H. Yang, Y. Li, J. Zhang and P. Gao, *Journal of Power Sources*, 2019, **419**, 99-105.
269. Q. Meng, K. Cai, Y. Chen and L. Chen, *Nano Energy*, 2017, **36**, 268-285.
270. A. Olabi, M. A. Abdelkareem, T. Wilberforce and E. T. Sayed, *Renewable and Sustainable Energy Reviews*, 2021, **135**, 110026.
271. V. Mittal, *Macromolecular Materials and Engineering*, 2014, **299**, 906-931.
272. R. Verdejo, M. M. Bernal, L. J. Romasanta and M. A. Lopez-Manchado, *Journal of Materials Chemistry*, 2011, **21**, 3301-3310.
273. R. Scaffaro and A. Maio, *Chemical Engineering Journal*, 2017, **308**, 1034-1047.
274. L. Zhang, S. Tu, H. Wang and Q. Du, *Composites Science and Technology*, 2018, **154**, 1-7.
275. D. Han, L. Yan, W. Chen, W. Li and P. Bangal, *Carbohydrate Polymers*, 2011, **83**, 966-972.
276. E. Bourgeat-Lami, *Journal of nanoscience and nanotechnology*, 2002, **2**, 1-24.
277. Y. Fadil, F. Jasinski, T. W. Guok, S. C. Thickett, H. Minami and P. B. Zetterlund, *Polymer Chemistry*, 2018, **9**, 3368-3378.
278. S. N. Tripathi, P. Saini, D. Gupta and V. Choudhary, *Journal of materials science*, 2013, **48**, 6223-6232.
279. E. Bourgeat-Lami, J. Faucheu and A. Noel, *Polymer Chemistry*, 2015, **6**, 5323-5357.
280. I. Tissot, C. Novat, F. Lefebvre and E. Bourgeat-Lami, *Macromolecules*, 2001, **34**, 5737-5739.
281. T. Selvan, J. P. Spatz, H. A. Klok and M. Möller, *Advanced Materials*, 1998, **10**, 132-134.
282. L. Wang and D. Chen, *Chemistry letters*, 2004, **33**, 1010-1011.
283. C. Wu, X. Huang, G. Wang, L. Lv, G. Chen, G. Li and P. Jiang, *Advanced Functional Materials*, 2013, **23**, 506-513.
284. W. Fan, C. Zhang, W. W. Tjiu and T. Liu, *Journal of Materials Research*, 2013, **28**, 611.
285. P. Zhao, Y. Luo, J. Yang, D. He, L. Kong, P. Zheng and Q. Yang, *Materials Letters*, 2014, **121**, 74-77.
286. K. S. Novoselov, A. K. Geim, S. V. Morozov, D. Jiang, Y. Zhang, S. V. Dubonos, I. V. Grigorieva and A. A. Firsov, *science*, 2004, **306**, 666-669.
287. K. S. Novoselov and A. Geim, *Nature materials*, 2007, **6**, 183-191.
288. M. D. Stoller, S. Park, Y. Zhu, J. An and R. S. Ruoff, *Nano letters*, 2008, **8**, 3498-3502.
289. A. A. Balandin, *Nature materials*, 2011, **10**, 569-581.
290. A. A. Balandin, S. Ghosh, W. Bao, I. Calizo, D. Teweldebrhan, F. Miao and C. N. Lau, *Nano letters*, 2008, **8**, 902-907.
291. D. G. Papageorgiou, I. A. Kinloch and R. J. Young, *Progress in Materials Science*, 2017, **90**, 75-127.
292. V. Chabot, D. Higgins, A. Yu, X. Xiao, Z. Chen and J. Zhang, *Energy & Environmental Science*, 2014, **7**, 1564-1596.
293. A. Zurutuza and C. Marinelli, *Nature nanotechnology*, 2014, **9**, 730-734.

294. G. Klimchitskaya and V. Mostepanenko, *Physical Review B*, 2013, **87**, 075439.
295. J. H. Lee, A. Avsar, J. Jung, J. Y. Tan, K. Watanabe, T. Taniguchi, S. Natarajan, G. Eda, S. Adam and A. H. Castro Neto, *Nano letters*, 2015, **15**, 319-325.
296. G. Gómez-Santos, *Physical Review B*, 2009, **80**, 245424.
297. J. W. Suk, R. D. Piner, J. An and R. S. Ruoff, *ACS nano*, 2010, **4**, 6557-6564.
298. K. Krishnamoorthy, M. Veerapandian, K. Yun and S.-J. Kim, *Carbon*, 2013, **53**, 38-49.
299. L. Stobinski, B. Lesiak, A. Malolepszy, M. Mazurkiewicz, B. Mierzwa, J. Zemek, P. Jiricek and I. Bieloshapka, *Journal of Electron Spectroscopy and Related Phenomena*, 2014, **195**, 145-154.
300. O. C. Compton, B. Jain, D. A. Dikin, A. Abouimrane, K. Amine and S. T. Nguyen, *ACS nano*, 2011, **5**, 4380-4391.
301. B. C. Brodie, *Philosophical transactions of the Royal Society of London*, 1859, 249-259.
302. E. Aliyev, V. Filiz, M. M. Khan, Y. J. Lee, C. Abetz and V. Abetz, *Nanomaterials*, 2019, **9**, 1180.
303. D. Zaharie-Butucel, M. Potara, A. Craciun, R. Boukherroub, S. Szunerits and S. Astilean, *Physical Chemistry Chemical Physics*, 2017, **19**, 16038-16046.
304. W. S. Hummers Jr and R. E. Offeman, *Journal of the american chemical society*, 1958, **80**, 1339-1339.
305. D. Konios, M. M. Stylianakis, E. Stratakis and E. Kymakis, *Journal of colloid and interface science*, 2014, **430**, 108-112.
306. M. Wang, Y. Niu, J. Zhou, H. Wen, Z. Zhang, D. Luo, D. Gao, J. Yang, D. Liang and Y. Li, *Nanoscale*, 2016, **8**, 14587-14592.
307. M. Singh, A. Yadav, S. Kumar and P. Agarwal, *Applied Surface Science*, 2015, **326**, 236-242.
308. S. Wang, Y. Dong, C. He, Y. Gao, N. Jia, Z. Chen and W. Song, *RSC advances*, 2017, **7**, 53643-53652.
309. D. Sutar, G. Singh and V. Divakar Botcha, *Applied Physics Letters*, 2012, **101**, 103103.
310. J. Paredes, S. Villar-Rodil, A. Martínez-Alonso and J. Tascon, *Langmuir*, 2008, **24**, 10560-10564.
311. O. C. Compton and S. T. Nguyen, *small*, 2010, **6**, 711-723.
312. D. Chen, H. Feng and J. Li, *Chemical reviews*, 2012, **112**, 6027-6053.
313. V. H. Pham, T. V. Cuong, S. H. Hur, E. Oh, E. J. Kim, E. W. Shin and J. S. Chung, *Journal of Materials Chemistry*, 2011, **21**, 3371-3377.
314. V. Georgakilas, J. N. Tiwari, K. C. Kemp, J. A. Perman, A. B. Bourlinos, K. S. Kim and R. Zboril, *Chemical reviews*, 2016, **116**, 5464-5519.
315. V. Mittal, *Polymer-graphene nanocomposites*, Royal Society of Chemistry, 2012.
316. S. Wang, D. Yu, L. Dai, D. W. Chang and J.-B. Baek, *ACS nano*, 2011, **5**, 6202-6209.
317. Y. Li, C. Deng and M. Yang, *Sensors and Actuators B: Chemical*, 2014, **194**, 51-58.
318. K. Maruyama, M. Kawaguchi and T. Kato, *Colloids and Surfaces A: Physicochemical and Engineering Aspects*, 2001, **189**, 211-223.
319. J. L. Luna-Xavier, A. Guyot and E. Bourgeat-Lami, *Polymer international*, 2004, **53**, 609-617.
320. J. A. Balmer, E. C. Le Cunff, S. P. Armes, M. W. Murray, K. A. Murray and N. S. Williams, *Langmuir*, 2010, **26**, 13662-13671.
321. J. A. Balmer, O. O. Mykhaylyk, S. P. Armes, J. P. A. Fairclough, A. J. Ryan, J. Gummel, M. W. Murray, K. A. Murray and N. S. Williams, *Journal of the American Chemical Society*, 2011, **133**, 826-837.
322. J. A. Balmer, O. O. Mykhaylyk, A. Schmid, S. P. Armes, J. P. A. Fairclough and A. J. Ryan, *Langmuir*, 2011, **27**, 8075-8089.
323. J. A. Balmer, S. P. Armes, P. W. Fowler, T. Tarnai, Z. Gáspár, K. A. Murray and N. S. Williams, *Langmuir*, 2009, **25**, 5339-5347.

324. L. A. Fielding, S. P. Armes, P. Staniland, R. Sayer and I. Tooley, *Journal of colloid and interface science*, 2014, **426**, 170-180.
325. J. Hong, K. Char and B.-S. Kim, *The Journal of Physical Chemistry Letters*, 2010, **1**, 3442-3445.
326. S. A. Ju, K. Kim, J.-H. Kim and S.-S. Lee, *ACS applied materials & interfaces*, 2011, **3**, 2904-2911.
327. V. H. Pham, T. T. Dang, S. H. Hur, E. J. Kim and J. S. Chung, *ACS applied materials & interfaces*, 2012, **4**, 2630-2636.
328. S. Jain and F. S. Bates, *Science*, 2003, **300**, 460-464.
329. R. K. O'Reilly, C. J. Hawker and K. L. Wooley, *Chemical Society Reviews*, 2006, **35**, 1068-1083.
330. M. Antonietti and S. Förster, *Advanced Materials*, 2003, **15**, 1323-1333.
331. X. Zhang, S. Boisse, W. Zhang, P. Beaunier, F. D'Agosto, J. Rieger and B. Charleux, *Macromolecules*, 2011, **44**, 4149-4158.
332. M. Manguian, M. Save and B. Charleux, *Macromol. Rapid Commun.*, 2006, **27**, 399-404.
333. J. Zhou, H. Yao and J. Ma, *Polymer Chemistry*, 2018, **9**, 2532-2561.
334. V. Cagno, P. Andreozzi, M. D'Alicarnasso, P. J. Silva, M. Mueller, M. Galloux, R. Le Goffic, S. T. Jones, M. Vallino and J. Hodek, *Nature materials*, 2018, **17**, 195.
335. M. Ramstedt, N. Cheng, O. Azzaroni, D. Mossialos, H. J. Mathieu and W. T. Huck, *Langmuir*, 2007, **23**, 3314-3321.
336. C. T. Hendley IV, L. A. Fielding, E. R. Jones, A. J. Ryan, S. P. Armes and L. A. Estroff, *Journal of the American Chemical Society*, 2018, **140**, 7936-7945.
337. M. Semsarilar, V. Ladmiral, A. Blanazs and S. Armes, *Langmuir*, 2011, **28**, 914-922.
338. Y. Ning, L. Han, M. J. Derry, F. C. Meldrum and S. P. Armes, *Journal of the American Chemical Society*, 2019, **141**, 2557-2567.
339. Z. Ding, C. Gao, S. Wang, H. Liu and W. Zhang, *Polymer Chemistry*, 2015, **6**, 8003-8011.
340. J. Tan, J. He, X. Li, Q. Xu, C. Huang, D. Liu and L. Zhang, *Polymer Chemistry*, 2017, **8**, 6853-6864.
341. B. Akpinar, L. A. Fielding, V. J. Cunningham, Y. Ning, O. O. Mykhaylyk, P. W. Fowler and S. P. Armes, *Macromolecules*, 2016, **49**, 5160-5171.
342. Y.-Y. Kim, L. A. Fielding, A. N. Kulak, O. Nahi, W. Mercer, E. R. Jones, S. P. Armes and F. C. Meldrum, *Chemistry of Materials*, 2018, **30**, 7091-7099.
343. C. Gonzato, M. Semsarilar, E. R. Jones, F. Li, G. J. Krooshof, P. Wyman, O. O. Mykhaylyk, R. Tuinier and S. P. Armes, *Journal of the American Chemical Society*, 2014, **136**, 11100-11106.
344. L. Zhang and A. Eisenberg, *Macromolecules*, 1996, **29**, 8805-8815.
345. Y. Ning, L. Fielding, T. Andrews, D. Growney and S. Armes, *Nanoscale*, 2015, **7**, 6691-6702.
346. J. V. Herráez and R. Belda, *Journal of Solution Chemistry*, 2006, **35**, 1315-1328.
347. E. J. Wensink, A. C. Hoffmann, P. J. van Maaren and D. van der Spoel, *The Journal of chemical physics*, 2003, **119**, 7308-7317.
348. G. Akerlof, *Journal of the American Chemical Society*, 1932, **54**, 4125-4139.
349. L. A. Fielding, J. A. Lane, M. J. Derry, O. O. Mykhaylyk and S. P. Armes, *Journal of the American Chemical Society*, 2014, **136**, 5790-5798.
350. J. Ilavsky and P. R. Jemian, *Journal of Applied Crystallography.*, 2009, **42**, 347-353.
351. J. S. Pedersen, *Journal of Applied Crystallography*, 2000, **33**, 637-640.
352. V. Cunningham, S. Armes and O. Musa, *Polymer chemistry*, 2016, **7**, 1882-1891.
353. J. Raula, H. Eerikäinen and E. I. Kauppinen, *International journal of pharmaceutics*, 2004, **284**, 13-21.
354. E. Pedraza and M. Soucek, *Polymer*, 2005, **46**, 11174-11185.
355. F. S. Bates and G. H. Fredrickson, *Annual review of physical chemistry*, 1990, **41**, 525-557.

356. S. Förster, M. Zisenis, E. Wenz and M. Antonietti, *The Journal of chemical physics*, 1996, **104**, 9956-9970.
357. M. W. Matsen and F. S. Bates, *Macromolecules*, 1996, **29**, 1091-1098.
358. K. Yu, L. Zhang and A. Eisenberg, *Langmuir*, 1996, **12**, 5980-5984.
359. M. J. Derry, L. A. Fielding, N. J. Warren, C. J. Mable, A. J. Smith, O. O. Mykhaylyk and S. P. Armes, *Chemical science*, 2016, **7**, 5078-5090.
360. Y. Yu and A. Eisenberg, *Journal of the American Chemical Society*, 1997, **119**, 8383-8384.
361. E. Jones, O. Mykhaylyk, M. Semsarilar, M. Boerakker, P. Wyman and S. Armes, *Macromolecules*, 2016, **49**, 172-181.
362. Y. Y. Kim, M. Semsarilar, J. D. Carloni, K. R. Cho, A. N. Kulak, I. Polishchuk, C. T. Hendley IV, P. J. Smeets, L. A. Fielding and B. Pokroy, *Advanced Functional Materials*, 2016, **26**, 1382-1392.
363. J. Qiu, B. Charleux and K. Matyjaszewski, *Progress in Polymer Science*, 2001, **26**, 2083-2134.
364. M. F. Cunningham, *Progress in Polymer Science*, 2002, **27**, 1039-1067.
365. N. Corrigan, K. Jung, G. Moad, C. J. Hawker, K. Matyjaszewski and C. Boyer, *Progress in Polymer Science*, 2020, 101311.
366. K. Matyjaszewski, S. Gaynor and J.-S. Wang, *Macromolecules*, 1995, **28**, 2093-2095.
367. Y. Kwak, A. Goto, Y. Tsujii, Y. Murata, K. Komatsu and T. Fukuda, *Macromolecules*, 2002, **35**, 3026-3029.
368. M. J. Monteiro and H. de Brouwer, *Macromolecules*, 2001, **34**, 349-352.
369. S. Jousset, J. Qiu, K. Matyjaszewski and C. Granel, *Macromolecules*, 2001, **34**, 6641-6648.
370. P. B. Zetterlund, Y. Kagawa and M. Okubo, *Chemical reviews*, 2008, **108**, 3747-3794.
371. M. F. Cunningham, *Progress in polymer science*, 2008, **33**, 365-398.
372. P. B. Zetterlund, S. C. Thickett, S. Perrier, E. Bourgeat-Lami and M. Lansalot, *Chemical reviews*, 2015, **115**, 9745-9800.
373. D. Crespy and K. Landfester, *Beilstein journal of organic chemistry*, 2010, **6**, 1132-1148.
374. J. Hu, M. Chen and L. Wu, *Polymer Chemistry*, 2011, **2**, 760-772.
375. K. Landfester, *Angewandte Chemie International Edition*, 2009, **48**, 4488-4507.
376. F. J. Schork, Y. Luo, W. Smulders, J. P. Russum, A. Butté and K. Fontenot, *Advances in Polymer Science*, Springer, 2005.
377. D. Mouran, J. Reimers and F. J. Schork, *Journal of Polymer Science Part A: Polymer Chemistry*, 1996, **34**, 1073-1081.
378. C. Chern and T. Chen, *Colloid and polymer science*, 1997, **275**, 546-554.
379. Y. Gnanou, L. Leibler and K. Matyjaszewski, *Macromolecular Engineering: Precise Synthesis, Materials Properties, Applications*, Wiley-VCH, 2007.
380. A. H. Milani, L. A. Fielding, P. Greensmith, B. R. Saunders, D. J. Adlam, A. J. Freemont, J. A. Hoyland, N. W. Hodson, M. A. Elsawy and A. F. Miller, *Chemistry of Materials*, 2017, **29**, 3100-3110.
381. Z. Li, H. Tam, L. Xu and Q. Zhang, *Optics letters*, 2005, **30**, 1117-1119.
382. N. Chaix, C. Gourgon, S. Landis, C. Perret, M. Fink, F. Reuther and D. Mecerreyes, *Nanotechnology*, 2006, **17**, 4082.
383. L. J. Guo, *Journal of Physics D: Applied Physics*, 2004, **37**, R123.
384. C. González-Chomón, M. Silva, A. Concheiro and C. Alvarez-Lorenzo, *Acta biomaterialia*, 2016, **41**, 302-311.
385. H. Li, J. Liu, L. Lin, Q. Mu, X. Sun and X. Liu, *Polymer Science Series B*, 2014, **56**, 855-862.
386. J. Ou, G. T. Gibson and R. D. Oleschuk, *Journal of Chromatography A*, 2010, **1217**, 3628-3634.
387. C. Yoon, H. S. Kwon, J. S. Yoo, H. Y. Lee, J. H. Bae and J. H. Choi, *Coloration Technology*, 2015, **131**, 2-8.
388. A. Aqel, K. Yusuf, Z. A. Al-Othman, A. Y. Badjah-Hadj-Ahmed and A. A. Alwarthan, *Analyst*, 2012, **137**, 4309-4317.

389. A. Aqel, Z. A. ALOthman, K. Yusuf, A. Y. Badjah-Hadj-Ahmed and A. A. Alwarthan, *Journal of chromatographic science*, 2014, **52**, 201-210.
390. A. Kharel, C. Hall, P. Černoch, P. Stepanek and T. P. Lodge, *Macromolecules*, 2020, **53**, 885-894.
391. K. Hashimoto, Y. Kobayashi, H. Kokubo, T. Ueki, K. Ohara, K. Fujii and M. Watanabe, *The Journal of Physical Chemistry B*, 2019, **123**, 4098-4107.
392. T. Ueki, *Polymer Journal*, 2014, **46**, 646-655.
393. M. Kocik, O. Mykhaylyk and S. Armes, *Soft Matter*, 2014, **10**, 3984-3992.
394. M. S. Musa, A. H. Milani, P. Shaw, G. Simpson, P. A. Lovell, E. Eaves, N. Hodson and B. R. Saunders, *Soft Matter*, 2016, **12**, 8112-8123.
395. M. G. Prolongo, C. Arribas, C. Salom and R. M. Masegosa, *Polymer Engineering & Science*, 2010, **50**, 1820-1830.
396. G. N. Smith, V. J. Cunningham, S. L. Canning, M. J. Derry, J. Cooper, A. Washington and S. P. Armes, *Soft matter*, 2019, **15**, 17-21.
397. I. Benito, M. Garcia, C. Monge, J. Saz and M. Marina, *Colloids and Surfaces A: Physicochemical and Engineering Aspects*, 1997, **125**, 221-224.
398. S. Nilsson, *Macromolecules*, 1995, **28**, 7837-7844.
399. L. Zhang, X. Zhang, P. Zhang, Z. Zhang, S. Liu and B. Han, *Colloids and Surfaces A: Physicochemical and Engineering Aspects*, 2018, **553**, 225-229.
400. Z. Ujhelyi, F. Fenyvesi, J. Varadi, P. Feher, T. Kiss, S. Veszelka, M. Deli, M. Vecsernyes and I. Bacskay, *European Journal of Pharmaceutical Sciences*, 2012, **47**, 564-573.
401. A. J. van Zyl, D. de Wet-Roos, R. D. Sanderson and B. Klumperman, *European polymer journal*, 2004, **40**, 2717-2725.
402. S. Garnier and A. Laschewsky, *Macromolecules*, 2005, **38**, 7580-7592.
403. D. B. Thomas, A. J. Convertine, L. J. Myrick, C. W. Scales, A. E. Smith, A. B. Lowe, Y. A. Vasilieva, N. Ayres and C. L. McCormick, *Macromolecules*, 2004, **37**, 8941-8950.
404. C. Barner-Kowollik, J. F. Quinn, T. U. Nguyen, J. P. Heuts and T. P. Davis, *Macromolecules*, 2001, **34**, 7849-7857.
405. P. B. Zetterlund and D. R. D'hooge, *Macromolecules*, 2019, **52**, 7963-7976.
406. H. Tobita, *Macromolecular theory and simulations*, 2009, **18**, 108-119.
407. Y. Luo, R. Wang, L. Yang, B. Yu, B. Li and S. Zhu, *Macromolecules*, 2006, **39**, 1328-1337.
408. J. Yeow and C. Boyer, *Advanced Science*, 2017, **4**, 1700137.
409. G. Moad, Y. Chong, A. Postma, E. Rizzardo and S. H. Thang, *Polymer*, 2005, **46**, 8458-8468.
410. W.-D. He, X.-L. Sun, W.-M. Wan and C.-Y. Pan, *Macromolecules*, 2011, **44**, 3358-3365.
411. C. De las Heras Alarcón, S. Pennadam and C. Alexander, *Chemical Society Reviews*, 2005, **34**, 276-285.
412. A. E. Smith, X. Xu and C. L. McCormick, *Progress in polymer science*, 2010, **35**, 45-93.
413. J. Hu, G. Zhang, Z. Ge and S. Liu, *Progress in Polymer Science*, 2014, **39**, 1096-1143.
414. A. S. Hoffman, *Advanced drug delivery reviews*, 2013, **65**, 10-16.
415. S. Dai, P. Ravi and K. C. Tam, *Soft Matter*, 2008, **4**, 435-449.
416. G. Kocak, C. Tuncer and V. Bütün, *Polymer Chemistry*, 2017, **8**, 144-176.
417. S. Förster and M. Antonietti, *Advanced Materials*, 1998, **10**, 195-217.
418. V. Pinkrah, M. Snowden, J. Mitchell, J. Seidel, B. Chowdhry and G. Fern, *Langmuir*, 2003, **19**, 585-590.
419. D. Dupin, S. Fujii, S. P. Armes, P. Reeve and S. M. Baxter, *Langmuir*, 2006, **22**, 3381-3387.
420. J.-F. Gohy, S. Antoun and R. Jérôme, *Macromolecules*, 2001, **34**, 7435-7440.
421. M. Zamfir, C. S. Patrickios, F. Montagne, C. Abetz, V. Abetz, L. Oss-Ronen and Y. Talmon, *Journal of Polymer Science Part A: Polymer Chemistry*, 2012, **50**, 1636-1644.
422. K. Nieswandt, P. Georgopanos and V. Abetz, *Polymer Chemistry*, 2021.
423. K. Nieswandt, P. Georgopanos, C. Abetz, V. Filiz and V. Abetz, *Materials*, 2019, **12**, 3145.
424. S. Demirci, S. Kinali-Demirci and T. Caykara, *Polymer*, 2013, **54**, 5345-5350.

425. C. Barner-Kowollik, J. F. Quinn, D. R. Morsley and T. P. Davis, *Journal of Polymer Science Part A: Polymer Chemistry*, 2001, **39**, 1353-1365.
426. K. H. Wong, T. P. Davis, C. Barner-Kowollik and M. H. Stenzel, *Polymer*, 2007, **48**, 4950-4965.
427. P. B. Zetterlund, G. Gody and S. Perrier, *Macromolecular Theory and Simulations*, 2014, **23**, 331-339.
428. C. H. Hornung, X. Nguyen, S. Kyi, J. Chiefari and S. Saubern, *Australian Journal of Chemistry*, 2013, **66**, 192-198.
429. D.-J. Liaw, K.-L. Wang and F.-C. Chang, *Macromolecules*, 2007, **40**, 3568-3574.
430. S. Kappaun, S. Horner, A. M. Kelterer, K. Waich, F. Grasse, M. Graf, L. Romaner, F. Niedermair, K. Müllen and A. C. Grimsdale, *Macromolecular chemistry and physics*, 2008, **209**, 2122-2134.
431. W. Sun, W. Tian, Y. Zhang, J. He, S. Mao and L. Fang, *Nanomedicine: Nanotechnology, Biology and Medicine*, 2012, **8**, 460-467.
432. R. Gibson, S. Armes, O. Musa and A. Fernyhough, *Polymer Chemistry*, 2019, **10**, 1312-1323.
433. L. Zha, J. Hu, C. Wang, S. Fu and M. Luo, *Colloid and Polymer Science*, 2002, **280**, 1116-1121.
434. A. Drechsler, A. Synytska, P. Uhlmann, M. M. Elmahdy, M. Stamm and F. Kremer, *Langmuir*, 2010, **26**, 6400-6410.
435. S. North, E. Jones, G. Smith, O. Mykhaylyk, T. Annable and S. Armes, *Langmuir*, 2017, **33**, 1275-1284.
436. T. W. Healy, A. Homola, R. O. James and R. J. Hunter, *Faraday Discussions of the Chemical Society*, 1978, **65**, 156-163.
437. D. Sato, M. Kobayashi and Y. Adachi, *Colloids and Surfaces A: Physicochemical and Engineering Aspects*, 2005, **266**, 150-154.
438. D. A. Dikin, S. Stankovich, E. J. Zimney, R. D. Piner, G. H. Dommett, G. Evmenenko, S. T. Nguyen and R. S. Ruoff, *Nature*, 2007, **448**, 457-460.
439. J. Shen, Y. Hu, M. Shi, X. Lu, C. Qin, C. Li and M. Ye, *Chemistry of materials*, 2009, **21**, 3514-3520.
440. D. C. Marcano, D. V. Kosynkin, J. M. Berlin, A. Sinitskii, Z. Sun, A. Slesarev, L. B. Alemany, W. Lu and J. M. Tour, *ACS nano*, 2010, **4**, 4806-4814.
441. A. T. Dideikin and A. Y. Vul, *Frontiers in Physics*, 2019, **6**, 149.
442. S. William, J. Hummers and R. E. Offeman, *Journal of the American Chemical Society*, 1958, **80**, 1339-1339.
443. H. C. Schniepp, J.-L. Li, M. J. McAllister, H. Sai, M. Herrera-Alonso, D. H. Adamson, R. K. Prud'homme, R. Car, D. A. Saville and I. A. Aksay, *The Journal of Physical Chemistry B*, 2006, **110**, 8535-8539.
444. L. Shahriary and A. A. Athawale, *International Journal of Renewable Energy and Environmental Engineering*, 2014, **2**, 58-63.
445. J. Guerrero-Contreras and F. Caballero-Briones, *Materials Chemistry and Physics*, 2015, **153**, 209-220.
446. B. Konkena and S. Vasudevan, *The journal of physical chemistry letters*, 2012, **3**, 867-872.
447. T. A. Pham, N. A. Kumar and Y. T. Jeong, *Synthetic Metals*, 2010, **160**, 2028-2036.
448. J.-Y. Wang, S.-Y. Yang, Y.-L. Huang, H.-W. Tien, W.-K. Chin and C.-C. M. Ma, *Journal of Materials Chemistry*, 2011, **21**, 13569-13575.
449. P. G. Ren, D. X. Yan, T. Chen, B. Q. Zeng and Z. M. Li, *Journal of Applied Polymer Science*, 2011, **121**, 3167-3174.
450. Y. Lin, J. Jin and M. Song, *Journal of Materials Chemistry*, 2011, **21**, 3455-3461.
451. A. Lerf, H. He, M. Forster and J. Klinowski, *The Journal of Physical Chemistry B*, 1998, **102**, 4477-4482.
452. T. Nakajima and Y. Matsuo, *Carbon*, 1994, **32**, 469-475.

453. H. He, T. Riedl, A. Lerf and J. Klinowski, *The Journal of physical chemistry*, 1996, **100**, 19954-19958.
454. G. Wang, B. Wang, J. Park, J. Yang, X. Shen and J. Yao, *carbon*, 2009, **47**, 68-72.
455. X. Qi, T. Zhou, S. Deng, G. Zong, X. Yao and Q. Fu, *Journal of materials science*, 2014, **49**, 1785-1793.
456. G. T. Le, N. Chanlek, J. Manyam, P. Opaprakasit, N. Grisdanurak and P. Sreearunothai, *Chemical Engineering Journal*, 2019, **373**, 1212-1222.
457. J. Ma, J. Liu, W. Zhu and W. Qin, *Colloids and Surfaces A: Physicochemical and Engineering Aspects*, 2018, **538**, 79-85.
458. R. Kurapati, J. Russier, M. A. Squillaci, E. Treossi, C. Ménard-Moyon, A. E. Del Rio-Castillo, E. Vazquez, P. Samorì, V. Palermo and A. Bianco, *Small*, 2015, **11**, 3985-3994.
459. D. Li, M. B. Müller, S. Gilje, R. B. Kaner and G. G. Wallace, *Nature nanotechnology*, 2008, **3**, 101-105.
460. X. Wang, H. Bai and G. Shi, *Journal of the American Chemical Society*, 2011, **133**, 6338-6342.
461. F. Baskoro, C.-B. Wong, S. R. Kumar, C.-W. Chang, C.-H. Chen, D. W. Chen and S. J. Lue, *Journal of Membrane Science*, 2018, **554**, 253-263.
462. J. Kim, L. J. Cote, F. Kim, W. Yuan, K. R. Shull and J. Huang, *Journal of the American Chemical Society*, 2010, **132**, 8180-8186.
463. G. Bocharov, A. Eletskii and V. Mel'Nikov, *Nanosystems: Physics, Chemistry, Mathematics*, 2018, **9**, 98-101.
464. D. N. Tran, S. Kabiri and D. Losic, *Carbon*, 2014, **76**, 193-202.
465. A. A. Novikova, V. E. Burlakova, V. N. Varavka, I. E. Uflyand, E. G. Drogan and V. A. Irkha, *Journal of Molecular Liquids*, 2019, **284**, 1-11.
466. M. Markovic, I. Andelkovic, J. Shuster, L. Janik, A. Kumar, D. Losic and M. J. McLaughlin, *Chemosphere*, 2020, **245**, 125640.
467. A. Arzac, G. P. Leal, J. C. de la Cal and R. Tomovska, *Macromolecular Materials and Engineering*, 2017, **302**, 1600315.
468. V. H. Pham, T. T. Dang, S. H. Hur, E. J. Kim and J. S. Chung, *ACS Appl Mater Interfaces*, 2012, **4**, 2630-2636.

Chapter Eight

Appendices

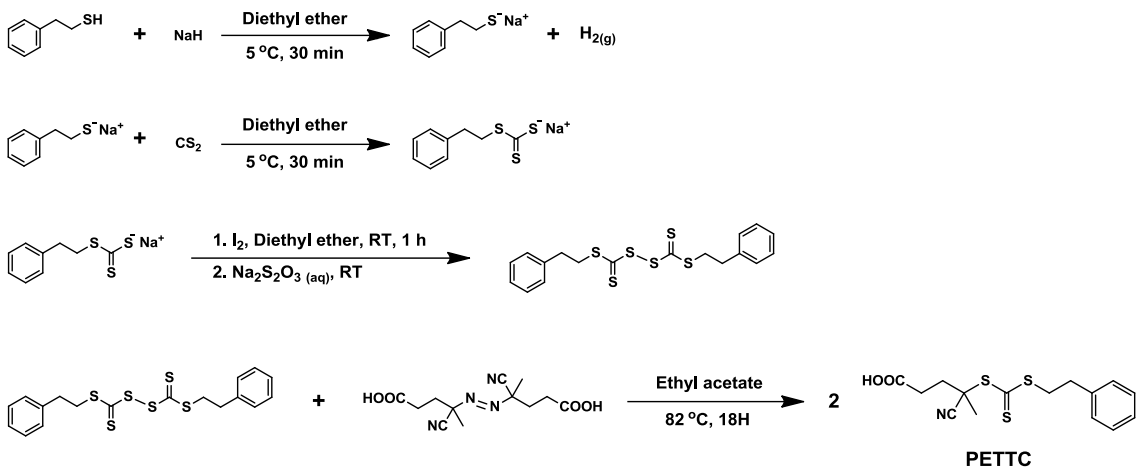

Scheme A.1. Synthesis of 4-cyano-4-(2-phenylethane sulfanylthiocarbonyl) sulfanylpentanoic acid (PETTC) RAFT agent.

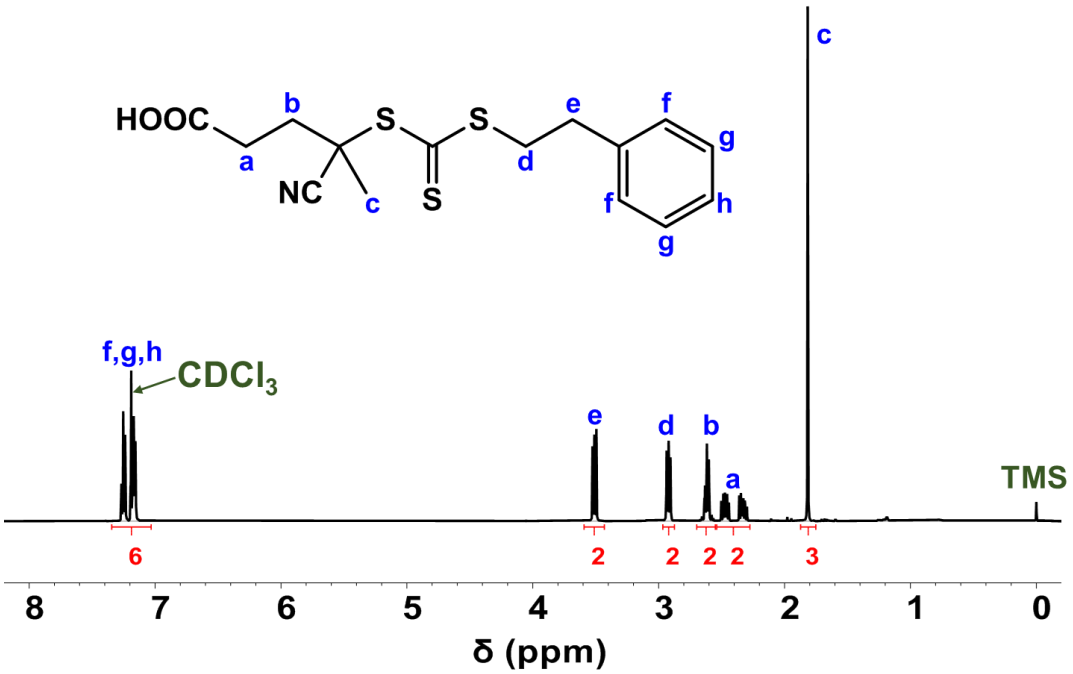

Figure A.1. ^{1}H NMR spectrum of 4-cyano-4-(2-phenylethane sulfanylthiocarbonyl) sulfanylpentanoic acid (PETTC) RAFT agent. The sample was dissolved in $CDCl_3$ prior to analysis.

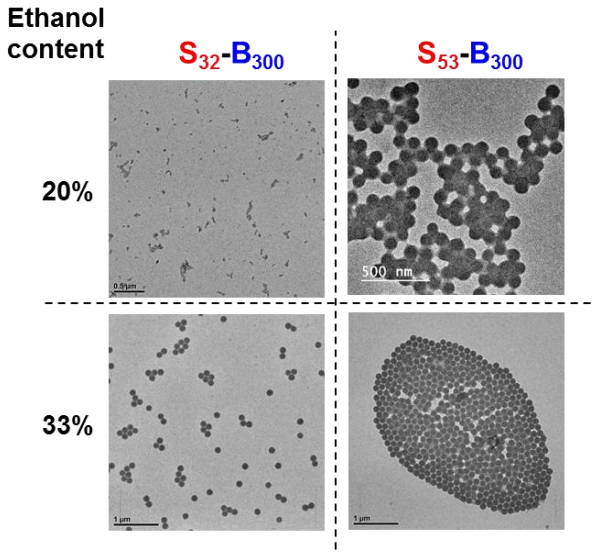

Figure A.2. Representative TEM images of S_{32}–B_{300} and S_{53}–B_{300} diblock copolymer nanoparticles prepared at 10% w/w solids *via* RAFT-mediated PISA in ethanol/water mixtures at 70 °C.

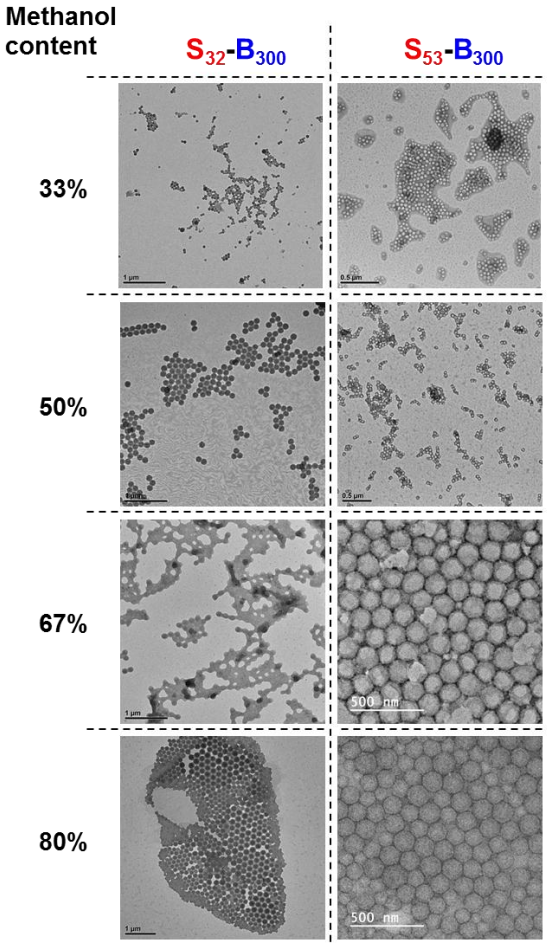

Figure A.3. Representative TEM images of S_{32}–B_{300} and S_{53}–B_{300} diblock copolymer nanoparticles prepared at 10% w/w solids *via* RAFT-mediated PISA in methanol/water mixtures at 70 °C.

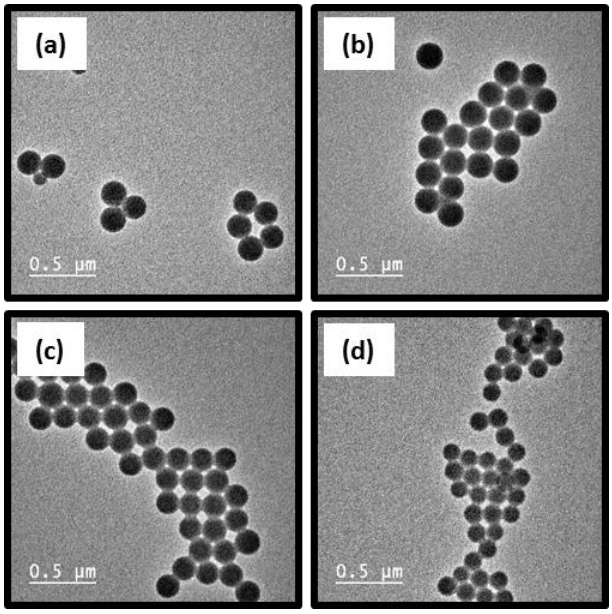

Figure A.4. Representative TEM images for (a) PSS_{13}–$PBzMA_{100}$, (b) PSS_{23}–$PBzMA_{100}$, (c) PSS_{54}–$PBzMA_{100}$ and (d) PSS_{111}–$PBzMA_{100}$ diblock copolymer nanoparticles synthesised *via* RAFT-mediated PISA at 70 °C in methanol/water at 20% w/w methanol. The [macro-CTA]:[ACVA] ratio was fixed at 3:1 and polymerisations were conducted at a solids content of 10% w/w.

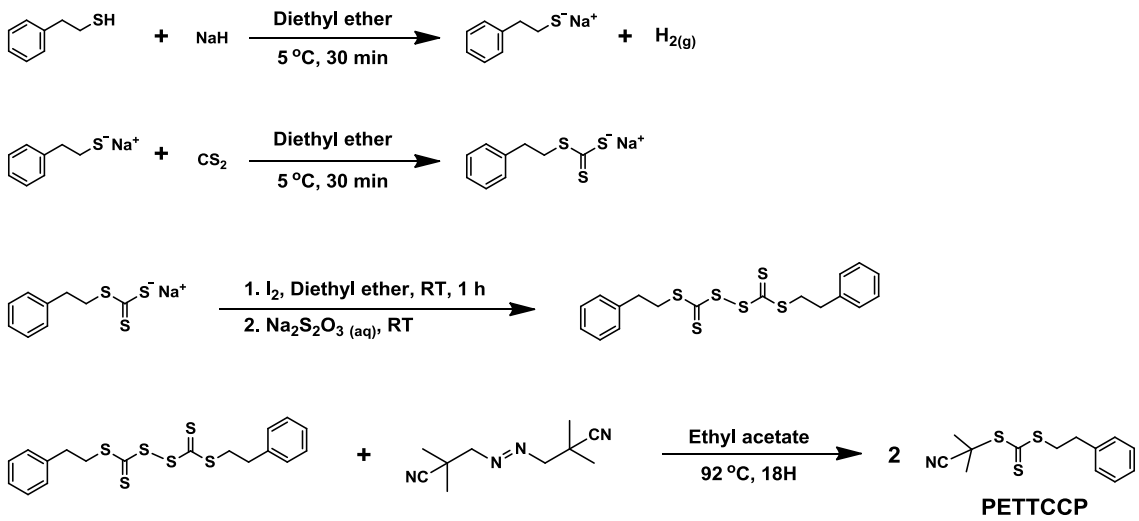

Scheme A.2. Synthesis of 2-cyano-2-propyl phenethyl trithiocarbonate (PETTCCP) RAFT agent.

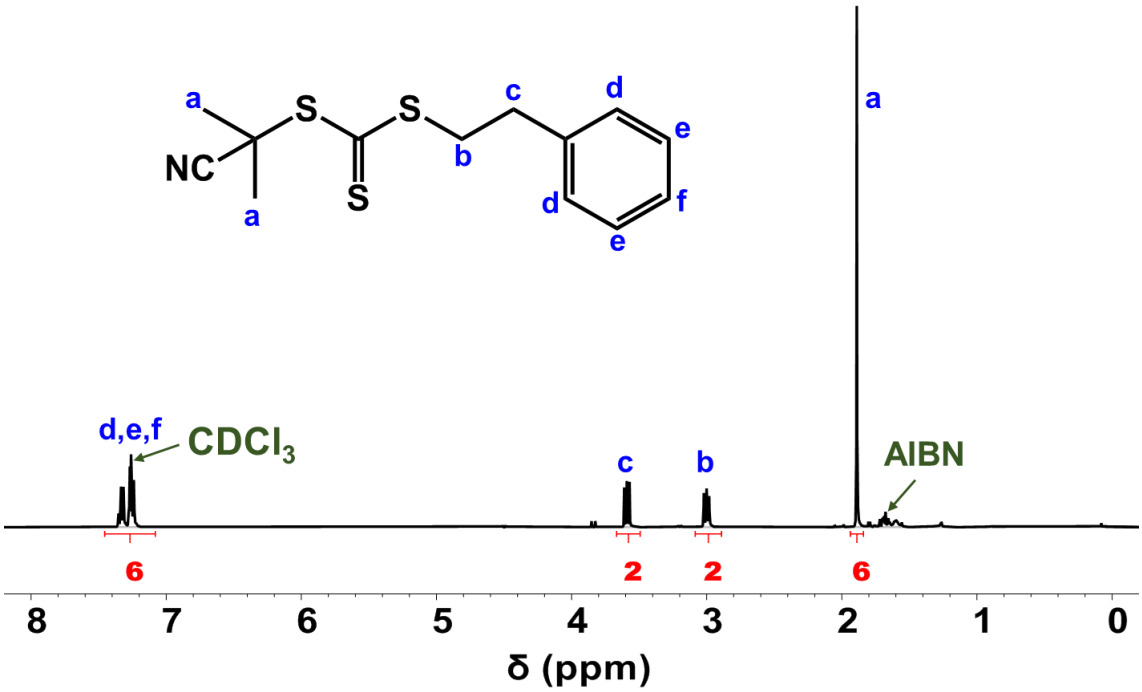

Figure A.5. ^{1}H NMR spectrum of 2-cyano-2-propyl phenethyl trithiocarbonate (PETTCCP) RAFT agent. The sample was dissolved in $CDCl_3$ prior to analysis.

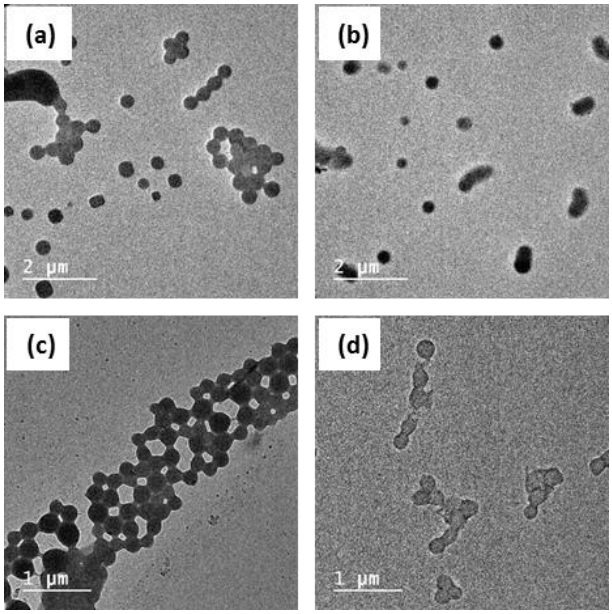

Figure A.6. Representative TEM images for PBzMA latexes synthesised *via* RAFT miniemulsion polymerisation at 70 °C with varying target DP: (a) 200, (b) 400, (c) 700 and (d) 800. The [PETTCCP]:[AIBN] ratio was fixed at 5:1 and polymerisations were conducted at a dispersed phase content of 20% w/w, with the concentration of HD and TO 20 fixed at 2.4% w/w and 7.8% w/w relative to BzMA, respectively.

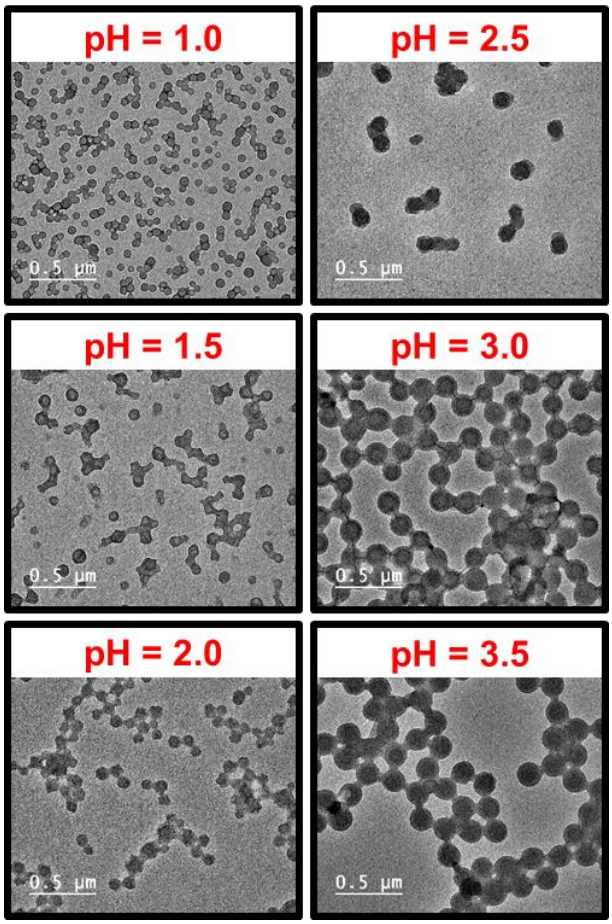

Figure A.7. Representative TEM images of $P2VP_{32}$–$PBzMA_{300}$ diblock copolymer nanoparticles prepared at 10% w/w solids *via* RAFT-mediated PISA in water at 70 °C and varying solution pH ranging from 1.0 to 3.5 (entries 1–6, **Table 4.1**).

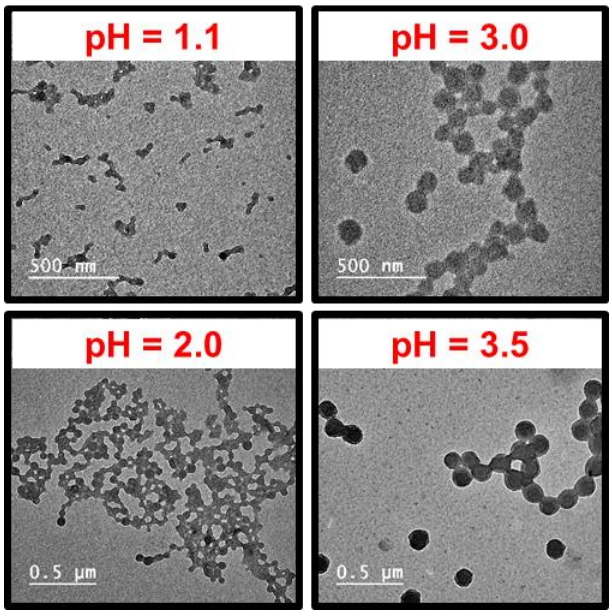

Figure A.8. Representative TEM images of $P2VP_{67}$–$PBzMA_{300}$ diblock copolymer nanoparticles prepared at 10% w/w solids *via* RAFT-mediated PISA in water at 70 °C and varying solution pH ranging from 1.1 to 3.5 (entries 7, 9, 11 and 12, **Table 4.1**).

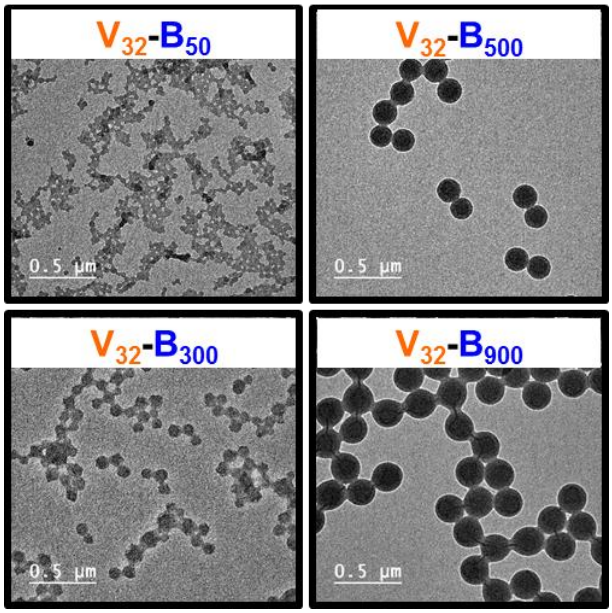

Figure A.9. Representative TEM images for P2VP$_{32}$–PBzMA$_y$ (target y = 50, 300, 500 and 900) diblock copolymer nanoparticles prepared at 10% w/w solids *via* RAFT-mediated polymerisation of BzMA in water at pH 2 (entries 13, 15, 16 and 18, **Table 4.1**).

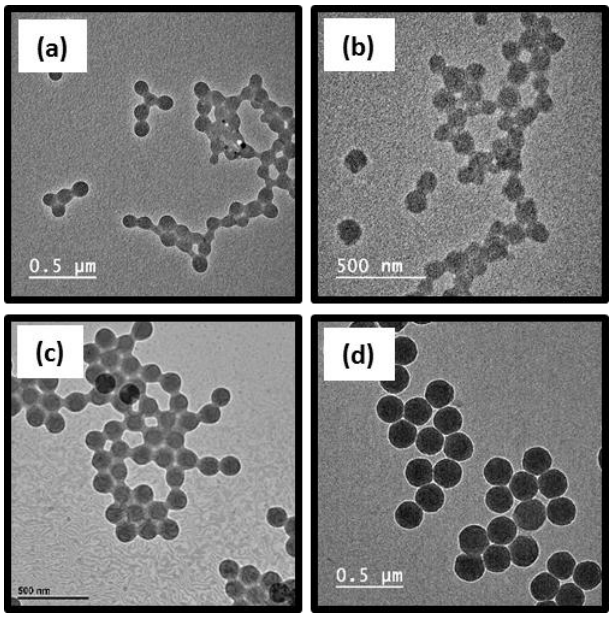

Figure A.10. Representative TEM images for (a) P2VP$_{32}$–PBzMA$_{300}$, (b) P2VP$_{67}$–PBzMA$_{300}$, (c) PKSPMA$_{32}$–PBzMA$_{300}$ and (d) PEGMA-stabilised P2VP latex nanoparticles. (a), (b), (c) and (d) represent entries 1–4 in **Table 5.1**, respectively.

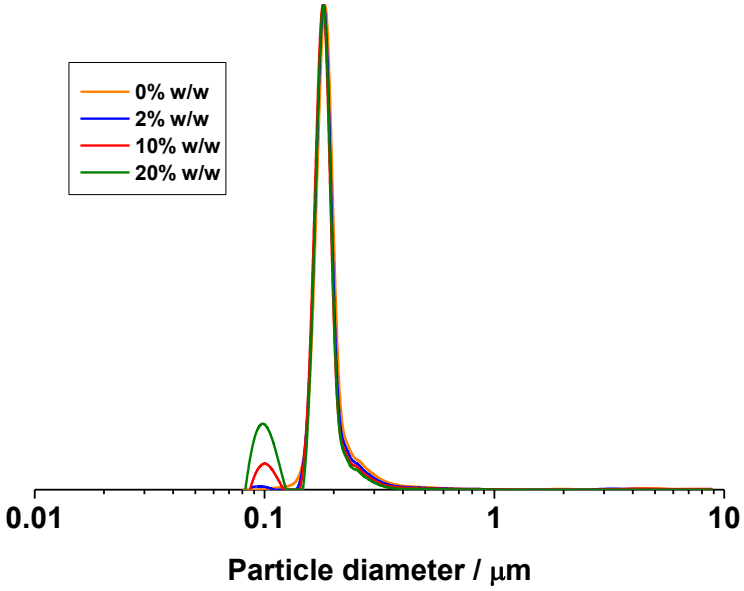

Figure A.11. DCP particle size distributions obtained for anionic sterically-stabilised PSS_{32}–$PBzMA_{300}$ latex (168 nm) before and after heteroflocculation with addition of varying GO content (2 to 20% w/w relative to latex) at pH 5. In all cases, the anionic GO were not adsorbed onto the surface of the anionic PSS–PBzMA particles, and thus the particle size traces of latexes were identical. The density used to calculate these particle size distributions was taken as 1.18 g cm^{-3}.

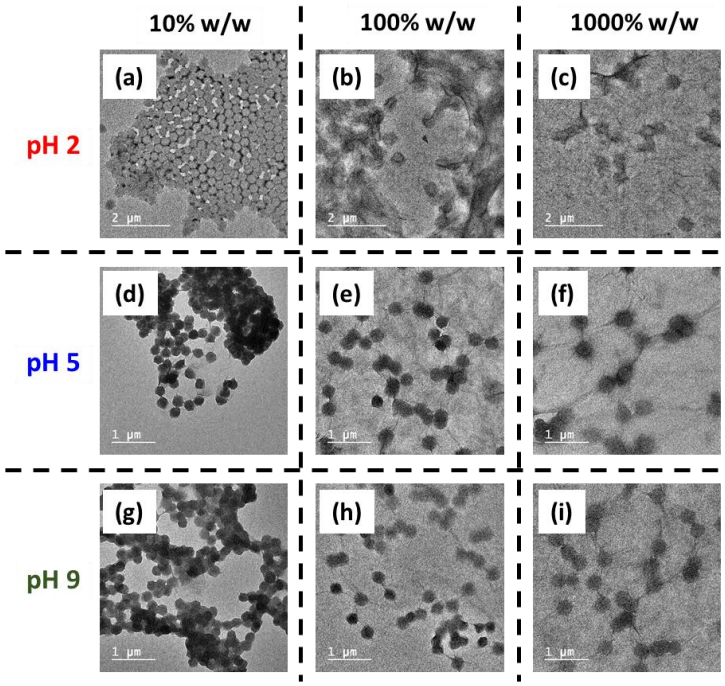

Figure A.12. Representative TEM images for polymer/GO nanocomposite particles prepared *via* heteroflocculation between PEGVP latex and GO with varying content (10% w/w, 100% w/w and 1000% w/w). Images (a–c), (d–f) and (g–i) correspond to heteroflocculation conducted in aqueous solution at pH 2, 5 and 9, respectively (entries 3, 5, 7, 10, 12, 14, 17, 19 and 21, **Table 5.3**).

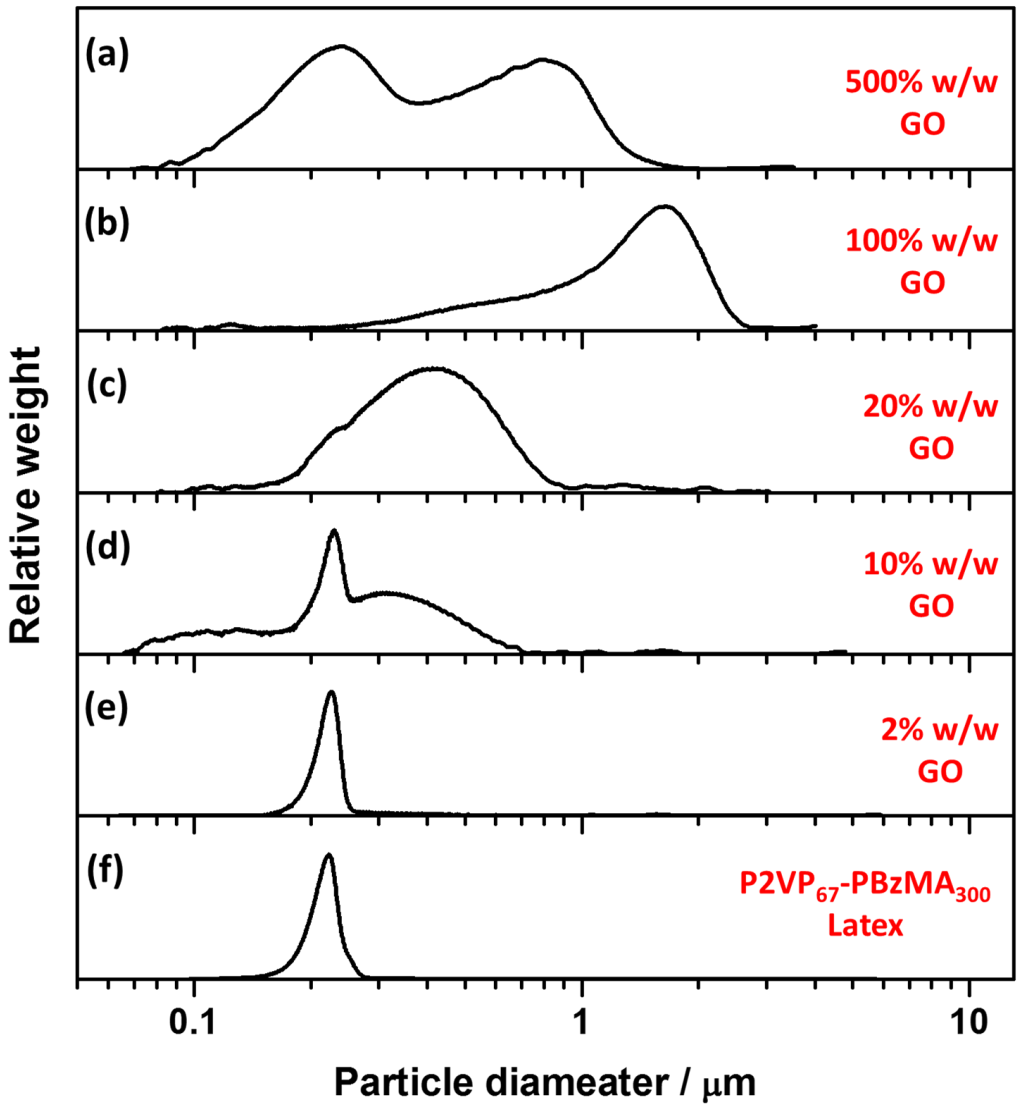

Figure A.13. DCP particle size distributions obtained for V_{67}–B_{300}/GO nanocomposite particles prepared *via* heteroflocculation with varying GO content at pH 2. The density of the latex and nanocomposite particles used was taken as 1.18 g cm^{-3}. (a) – (e) represent entries 2–6 from **Table 5.5**, whereas (f) shows data obtained for entry 2 in **Table 5.1**.

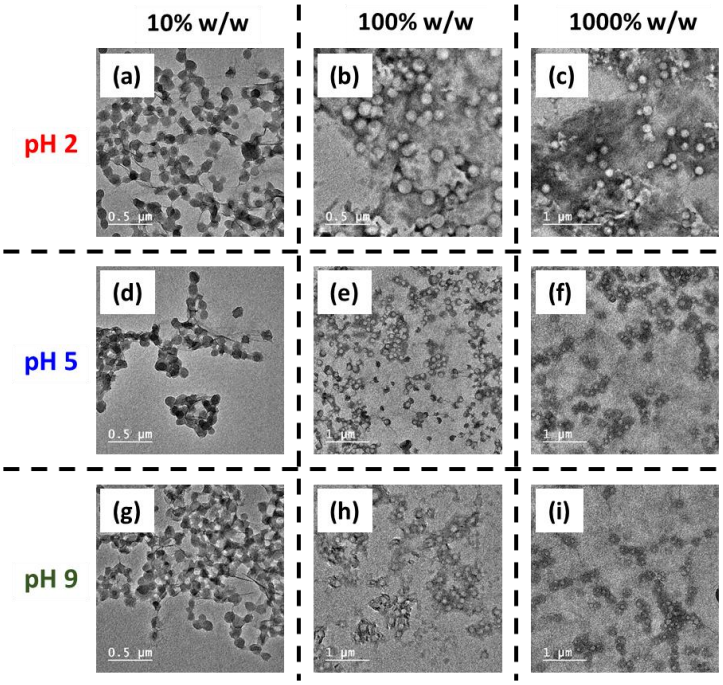

Figure A.14. Representative TEM images for polymer/GO nanocomposite particles prepared *via* heteroflocculation between V_{32}–B_{300} latex and GO with varying content (10% w/w, 100% w/w and 1000% w/w). Images (a–c), (d–f) and (g–i) correspond to heteroflocculation conducted in aqueous solution at pH 2, 5 and 9, respectively (entries 3, 5, 7, 10, 12, 14, 17, 19 and 21, **Table 5.4**).

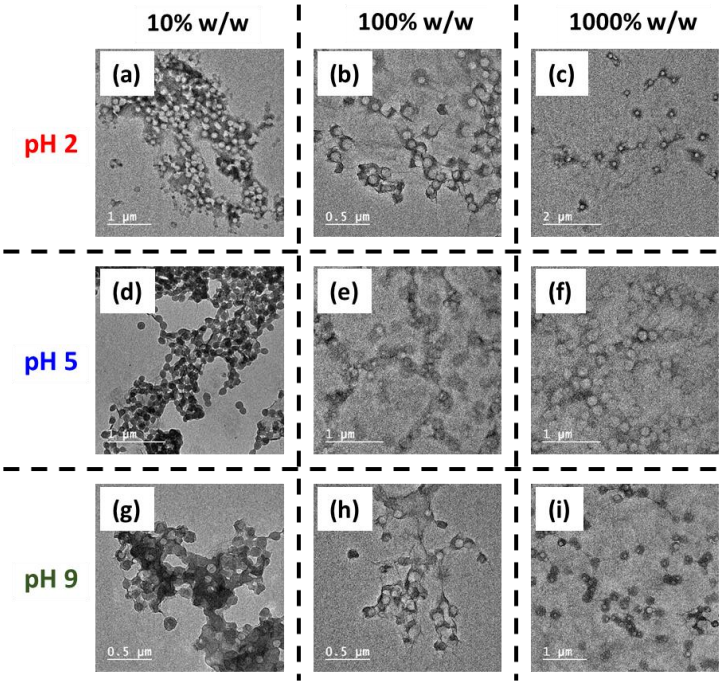

Figure A.15. Representative TEM images for polymer/GO nanocomposite particles prepared *via* heteroflocculation between V_{67}–B_{300} latex and GO with varying content (10% w/w, 100% w/w and 1000% w/w). Images (a–c), (d–f) and (g–i) correspond to heteroflocculation conducted in aqueous solution at pH 2, 5 and 9, respectively (entries 3, 5, 7, 10, 12, 14, 17, 19 and 21, **Table 5.5**).